

**Computational Mathematics Elucidates the
Dependence of Brain Perfusion on Microcirculation**

BY

IAN GOPAL GOULD
B.S., Case Western Reserve University, 2007

THESIS

Submitted as partial fulfillment of the requirements
for the degree of Doctor of Philosophy in Bioengineering
in the Graduate College of the
University of Illinois at Chicago, 2018

Chicago, Illinois

Defense Committee:

Andreas A. Linninger, Bioengineering, Chair and Advisor

Ali Alaraj, Neurosurgery

Simon Alford, Anatomy and Cell Biology

Urmila Diwekar, Bioengineering

Richard Magin, Bioengineering

This thesis is dedicated to my fellow travelers in spiritual recovery and my higher power, without whom this journey never would have been started let alone completed.

ACKNOWLEDGEMENTS

I would like to thank my thesis committee – Andreas Linninger, Ali Alaraj, Richard Magin, Urmila Diwekar and Simon Alford – for their support and assistance. I would like to especially thank Professors Alford and Alaraj for guiding a young researcher to ask the big questions. I cannot thank my committee chair Professor Andreas Linninger enough for his unwavering support, persistence and mentorship over the years. His fortitude and patience taught me that there is no obstacle that cannot be overcome.

There are a great number of my fellow students whose friendship, collegiate rivalry and wit brought joy to research – Kevin Tangen, Dr. Sukhi Basati, Dr. Chih-Yang Hsu, Ying Hsu, Dr. Andy Pelzmann, Maurice Chojecki, Joel Buishas, Dr. Eric Leuschen, Mahsa Ghaffari, and Grant Hartung. And thank you Dr. Brian Sweetman for your mentorship and the wisdom you shared with me, “There were days when I left early and I should have stayed late, and there were days when I stayed late and I should have left early.”

IGG

CONTRIBUTION OF AUTHORS STATEMENT

Chapter I is an overview of the entire dissertation that highlights the findings of my research and ties each chapter together as a coherent investigation of oxygen transport and blood flow modeling in the brain.

Chapter II is a reprinting of a published manuscript (Linninger, Andreas A., I. G. Gould, T. Marrinan, C-Y. Hsu, M. Chojecki, and Ali Alaraj. "Cerebral microcirculation and oxygen tension in the human secondary cortex." *Annals of biomedical engineering* 41, no. 11 (2013): 2264-2284.) for which I was the second author, performed and analyzed the simulations, designed the figures and write the main text. My research mentor, Professor Linninger, heavily edited the manuscript, designed the architecture on which the simulations were run, and closely guided the design of the paper message, figures and revisions. My colleague Dr. Marrinan designed the visualization software that rendered many of the figures. Dr. Hsu contributed to the editing of the manuscript and producing the full brain visualization shown in Figure 1. Maurice Chojecki assisted in the statistical analysis of the structure show in Figure 2. Dr. Alaraj was key in developing the message of the paper and was heavily involved in the editing of the manuscript.

Chapter III is a reprinting of a published manuscript (Gould, Ian G., and Andreas A. Linninger. "Hematocrit distribution and tissue oxygenation in large microcirculatory networks." *Microcirculation* 22, no. 1 (2015): 1-18.) for which I was the first author. Professor Linninger was a co-creator of the KPSM model and contributed to the writing and editing of the manuscript.

Chapter IV is a reprinting of a published manuscript (Gould, Ian Gopal, Philbert Tsai, David Kleinfeld, and Andreas Linninger. "The capillary bed offers the largest hemodynamic resistance to the cortical blood supply." *Journal of Cerebral Blood Flow & Metabolism* 37, no. 1 (2017): 52-68.) for which I was the first author. Two-photon microscopy images, data filtering and construction of the microcirculation topology for all four data sets were performed by Professor

Kleinfeld and Dr. Tsai at University of California San Diego. Computational simulations, figure design and text are credited to Professor Linninger and myself at University of Illinois Chicago. Both groups contributed to the technical content of this manuscript.

Chapter V is an expanded Appendix that was dropped from the publication of Chapter IV, which compares the performance of two model reduction strategies of the cerebral microcirculation. The conceptualized of the conductive plate model was realized over many conversations with me adviser Professor Linninger, who also suggested the blood flow response investigation study as testing criterion between the two models.

Chapter VI is an unpublished report created in preparation for Chapter VII. This investigation determined the best integration technique for solving the dynamic FSI problem over a distributed network. My colleague Jagan Jimmy assisted in implementing the Linear Finite Difference with Euler Integrator solver and running simulations.

Chapter VII is an unpublished manuscript which I contributed the text, simulation and figure design. Professor Linninger assisted with literature review, figure design, manuscript editing and the contributed the automatically generated simplified cerebral microcirculatory network. I anticipate that this line of research will be continued in the laboratory after I leave and that this work will ultimately be published as part of a co- authored manuscript.

TABLE OF CONTENTS

I. OVERVIEW.....	1
II. CEREBRAL MICROCRICULTION AND OXYGEN TENSION IN THE HUMAN SECONDARY CORTEX.....	7
Abstract	7
Introduction.....	8
Materials and Methods.....	12
Microvasculature Construction	14
Arterioles and Veins	14
Capillaries	17
Hemodynamics	19
Oxygen Perfusion from the Cerebral Microvasculature to the Cortical Tissue	22
Results	27
Morphometrics	27
Flow and Oxygen Exchange in the Entire Subsection	27
Microvascular Blood Pressure.....	30
Blood Flow and Velocity Predictions	30
Hemodynamic State Changes Along Multiple Erythrocyte Paths.....	31
Simulated Transit Times.....	31
Axial Oxygen Gradients	34
Radial Oxygen Perfusion Profiles.....	34
Discussion	35
Supplemental 1.....	40
Supplemental 2.....	44
Supplemental 3.....	47
Cited Literature	52
III. HEMATOCRIT DISTRIBUTION AND TISSUE OXYGENATION IN LARGE MICROCIRCULATORY NETWORKS	61
Abstract	61
Introduction.....	62
Microscopic forces cause biphasic flow and the creation of the endothelial surface layer	62
Macroscopic behavior of tube and discharge hematocrit in a single channel.....	63
Plasma skimming at bifurcations	64
Materials and Methods.....	69
Bulk Blood Flow	69
Model 1	69
Model 2	70
Model 3.....	70
Model 3 Parameterization of the Drift Parameter M.....	73
Iterative solution method for the plasma skimming models.....	75
Network Effects may lead to Hemoconcentration more than unity	76
Tissue Oxygenation	79
Results	79
Hematocrit distribution in single bifurcations.....	79
Hematocrit distribution in the rat mesentery network	82
Hierarchical distribution of hematocrit.....	87
Tissue oxygen supply in the rat mesentery network	87
The effect of low-hematocrit capillaries on oxygen tension.....	89
Hematocrit distribution in the cremaster muscle	93

TABLE OF CONTENTS (continued)

Discussion	95
Supplemental 1.....	104
Supplemental 2.....	107
Supplemental 3.....	109
Cited Literature	111
IV. THE CAPILLARY BED OFFERS THE LARGEST HEMODYNAMIC RESISTANCE TO THE CORTICAL BLOOD SUPPLY	119
Abstract	119
Introduction.....	120
Materials and Methods.....	121
Data acquisition	121
Biphasic blood flow computations	123
Oxygen convection in erythrocytes and plasma	124
Tissue oxygen diffusion and metabolism.....	126
Results	130
Morphological statistical analysis	130
Hemodynamics	136
Oxygen exchange	138
Prediction of intracellular oxygen gradients	140
Path analysis.....	142
Discussion	147
Hemodynamics and variability along microcirculatory paths.....	147
Microcirculatory resistance distribution.....	149
Limitations.....	149
Future work.....	151
Supplemental 1.....	153
Supplemental 2.....	154
Supplemental 3.....	155
Supplemental 4.....	157
Supplemental 5.....	159
Cited Literature	161
V. MORPHOLOGICALLY CONSISTENT MODEL REDUCTION OF BRAIN MICROCIRCULATION ACCURATELY COMPUTES CEREBRAL BLOOD FLOW RESPONSE	171
Abstract	171
Introduction.....	172
Methods.....	176
Cerebral microcirculatory angioarchitecture	176
Network blood flow simulations	176
Resistance computation for each vascular group	177
Serial resistance configuration	178
Conductive plate network.....	180
Results	188
Resistance distribution	188
Blood flow response.....	189
Discussion	194
Model Construction	194
Resistance variation lower in the <i>plat network</i>	195
Conductive plate blood flow response matches full simulation	195
Comparison of model reduction strategies	196

TABLE OF CONTENTS (continued)

Future Work	197
Cited Literature	198
VI. LARGE SCALE ONE-DIMENSIONAL FLUID STRUCTURE INTERACTION MODELS OF THE CEREBRAL VASCULATURE	200
Introduction	200
Methods	201
Derivation of 1D Mass Conservation Balance	202
Derivation of 1D Momentum Conservation	204
Tube Law	209
Inflow Boundary Conditions	210
Outflow Boundary Conditions	211
Reflection Coefficient	215
Integration Methods	216
Linear and Nonlinear Finite Difference with Euler Integrator	216
Lax-Wendroff	218
Collocation Method with Euler Integrator/Method of Weighted Residuals	220
Results	225
Canine Aorta Case Study	225
Bifurcation	238
Network Simulations	243
Validation of Continuously Differentiable Signal	249
Discussion	252
Phase Lag between Pressure and Flow	252
Determining Outlet RCR Parameters	253
Blood Flow Control	254
Future Work	260
Supplemental 1	261
Special Considerations at the Boundaries	264
Special Considerations at the Boundaries	265
Parallel Computations	266
CFL Condition	266
Supplemental 2	268
Bifurcations	268
Unions	272
Narrowing or Widening Channels	275
Supplemental 3	278
Cited Literature	280
VII. MODELING HEMODYNAMIC RESPONSE AND DIVERSION OF BLOOD FLOW FOLLOWING FUNCTIONAL HYPEREMIA IN THE CEREBRAL MICROCIRCULATION	285
Abstract	285
Introduction	286
Changes in cerebral microcirculation compartments following functional hyperemia	287
Mathematical modeling	288
Modeling fMRI BOLD signal	289
Modeling presented in this work	289
Materials and Methods	290
Model Generation	290
Mathematical Formulation	293
Boundary Conditions	295
Results	297

TABLE OF CONTENTS (continued)

Steady State	297
Harmonic Equilibrium	298
Blood Flow at Harmonic Equilibrium.....	300
Simulating Vasodilation	301
Discussion	307
Baseline microcirculation hemodynamics.....	307
Vasodilation Study	308
Limitations.....	312
Future Work	313
Cited Literature	315
Supplemental 1.....	321
APPENDICES.....	326
APPENDICE A.....	326
Publisher Permissions for Chapter II	326
Publisher Permissions for Chapter III	329
Publisher Permissions for Chapter IV.....	335
CURRICULUM VITAE.....	337
Education.....	337
Awards and Honors	337
Industrial Experience	337
Publications	337
Refereed Proceedings Articles.....	337
Abstract, Posters and Presentations at Technical Conferences and Meetings.....	338

LIST OF TABLES

Table I Overview of microvascular simulation models and their features	11
Table II Morphometrics of the computer network compared to prior work.....	25
Table III Boundary Conditions	26
Table IV Parameters of distribution using the Krogh model	51
Table V List of biphasic mathematical models for phase separation and plasma skimming	67
Table VI Comparison of H_d and partial pressure (pO_2) to model predictions in rat mesentery	85
Table VII Drawbacks to models predicting the spatial distribution of discharge hematocrit	99
Table VIII Summary of boundary conditions used in the microcirculatory perfusion computations	125
Table IX Cerebral oxygen transport parameters used in this work	127
Table X Comparison of model predictions against experimental measurements	137
Table XI Percent surface area fraction.....	156
Table XII Morphological and Hemodynamic Parameters of each mouse	175
Table XIII Hemodynamic parameters of each vessel structure	181
Table XIV Fractional vascular resistance of the <i>Serial Resistance Configuration</i>	182
Table XV Fractional vascular resistance of the <i>Conductive Plate Model</i>	190
Table XVI Canine Aorta Case Study Parameters	226
Table XVII Sheep Pulmonary Artery Case Study Parameters	239
Table XVIII Values of physiologic parameters.....	296

LIST OF FIGURES

Figure 1 Overall multi-scale hierarchy of the human cerebral circulation. (a) Sagittal view of the full brain vasculature model generated *in silico* by combining image data with constrained constructive optimization. (b) Magnified section of the secondary cortex next to the collateral sulcus in the right temporal lobe, showing the arrangement of the network of pial arteries and veins at the cortical surface. (c) Isolated view of the territories of two draining pial veins supplied by six penetrating arterioles. (d) The construction principles for the computer aided construction and analysis of cerebral blood flow networks. This article is limited to structures ranging from the pial arterioles to the pial veins are discussed. 9

Figure 2 Summary and validation of morphometric properties and blood rheology of the microvessels of the secondary cortex next to the collateral sulcus in the right temporal lobe. Closed symbols show measured morphological properties with best fit solid line, open symbols show morphometrics of our artificially constructed microvessel structure. Panels a–d compare this work against morphological analysis of confocal microscopy work of the human secondary cortex.^{12,38} (a) Diameter distribution of all vessels in the microvascular network. (b) Length distribution of all vessels in the network. (c) Normal distribution of capillary vessels diameter with a mean diameter of 6 μm . (d) Histogram of distance to nearest capillary vessel in the cortical tissue, solid line shows polynomial best-fit. (e) Laminar distribution of volume fraction for vessels in cortical subsection, Triangles (Δ) indicate the total vessel pattern, squares (\square) represent only the capillary spectra, compared with laminar network morphometrics obtained by scanning electron microscopy of corrosion casts of the macaque visual cortex.⁷⁶ The volume density for the synthetic human microvasculature is lower than the macaque, as reflected in the values reported in Table 2. (f) Diameter dependent viscosity as determined by the Fahraeus–Lindqvist equation (eq. 4) in comparison to values reported by Boas⁴ and Takahashi.⁶⁸ In the simulations, we used $Hd = 0.45$13

Figure 3 Schematic of a single vessel segment addition using the modified Constrained Constructive Growth (CCO) algorithm.⁶³ Segment addition begins with the selection and connection of a point in the domain to the existing tree. The position of this connection point, highlighted in red, is optimized to create a tree with the smallest luminal volume. During the optimization, the diameters d_i and d_j , as well as the lengths l_i and l_j of the two daughter branches, are selected so that all terminal leaves discharge equal blood flow F . N is the number of segments belonging to the tree. The application of these *optimization principles* leads to networks with topological features similar to vascular structures.16

Figure 4 Partial view of the territories drained by two penetrating venules with their six descending arterioles as well as the capillary bed, cut out from the 27 mm³ subsection of the secondary cortex for better visibility. The six cortical layers of the extravascular space are occupied by brain tissue. The extravascular space is modeled as a porous medium into which oxygen is transported from the blood and metabolized by brain cells. (a) The nodal balance envelope encompasses the sum of half of the cylindrical volumes connected to it (red semi-cylinders). Blood convects oxygen with concentration C_{in} into a nodal volume and out with concentration C_b (red arrows) with flow Q . Oxygen exchange (purple arrow) occurs between the blood volume (node volume at C_b) and the extravascular tissue cell (tetrahedral cell at C_t). Oxygen can also diffuse freely inside the extravascular space (blue arrows). Oxygen diffusion and metabolism is solved by a finite volume method using an unstructured tetrahedral mesh. (b) Close up of microcirculatory pre-capillaries arterioles feeding the capillary bed, the site of oxygen mass exchange. (c). Detail of the continuous extravascular space composed of an unstructured tetrahedral mesh.20

Figure 5 Visualization of a relatively large 27 mm³ subsection of the secondary cortex with computed steady state blood pressure, volumetric flow rate, and oxygen profiles projected onto the vessel architecture. Top row—larger vessels (capillary bed without showing small vessels,

$d < 10 \mu\text{m}$). Bottom row—all vessels, including capillary bed, are shown. (a) Blood pressure, (b) Oxygen tension, and (c) Volumetric blood flow value profiles.21

Figure 6 Detailed study of hemodynamics of a typical vascular territory of a single draining vein with its associated arterioles and capillaries. (a) Blood pressure distribution. (b) Blood flow velocity. (c) Blood oxygen tension. (d) Volumetric blood flow rate. Analysis of twelve distinct paths a single red blood cell may take when traveling from a feeding descending arteriole to a nearby draining venule. Panels 1–3 each depict four typical sample paths chosen randomly, colored blue, green, yellow, and red. In total there are >236,000 number of paths for a single territory.....29

Figure 7 Radial oxygen gradient as a function of cortical depth 400 μm (A), 1 mm (B), and 2 mm (C) below the cortical surface. Top row also shows the oxygen tension gradient in the molecular layer (a) as a vector field at 400 μm and 1 mm. In-plane radial oxygen gradients of three arterials (I–III) are displayed in the left hand column (Panels A1, B1, C1). The right hand column shows in-plane oxygen tension as a function of distance to arterioles. The simulated oxygen gradient agrees with trends observed *in vivo* in the rat cortex in panels A2 to C2.33

Figure 8 Mesh independence study and blood pressure validation. (A) Model prediction of extravascular oxygen gradient in the capillary-depleted cylinder surrounding a descending arteriole (I)—discussed in detail in Figure 6—as a function of mesh density. Predicted oxygen tension stabilized after increasing the number of tetrahedral elements from 400,000 to 600,000. All results are reported for the 400,000 element mesh. (B) Microvasculature pressure gradients of multiple paths (paths 1–4 introduced in Figure 6) from a penetrating arteriole to its corresponding draining venule of our subsection of the secondary cortex, compared to point measurements made to animal and computational models. The chosen pressure boundary conditions or pial arterioles ($P_{\text{arterial}} = 65 \text{ mmHg}$) to the draining venule ($P_{\text{venous}} = 18 \text{ mmHg}$) govern the pressure drop of the model. Trends compares well against empirical results⁸² and models4 with similar boundary conditions.36

Figure 9 Stepwise construction of capillary beds. (A) Delaunay triangulation of the space between the terminal nodes of the arteriole tree (a_1 , and a_2) and the venous tree (v_1). Mesh density (shown as triangles for clarity) controls the segment length of the desired capillary bed. (B) Construction of Voronoi tessellation, which is the dual of the Delaunay mesh. (C) Connection of arterial and venous terminal to the closest neighbor capillary node. (D) Bezier curve approximation of capillary segments to adjust desired degree of tortuosity. (E) Network flow simulation yields a pressure field to determine the mean capillary pressure, P . Segments within a desired pressure range, $P \pm 2\sigma_F$, are assigned the smallest capillary diameter, $D_{\min} = 3 \mu\text{m}$. (F) Diameters of capillary segments are according to an iterative averaging scheme, producing smooth transitions from the pre-capillary arterioles to the post-capillary venules. Steps E to F can be repeated to eliminate sharp diameter transitions at the inlets and outlets of the capillary bed.....43

Figure 10 Bezier Curve adjustment of capillary tortuosity. (A) Depiction of a Bezier curve between endpoints, P_0 , P_1 and control points, C_0 , C_1 . (B) Automatic generation of control points based on segments connected to the current Bezier segment. (C) Straight line segments. (D) Tortuous capillary segment with Bezier curve parameter, $\alpha = 0.25$46

Figure 11 Krogh cylinder solution of tissue oxygen perfusion from a single vessel, comparison of analytical and discrete methods. (a) Analytical solution of a Krogh cylinder with capillary radius ($r_C = 5 \mu\text{m}$) and capillary length ($L = 1000 \mu\text{m}$) and surrounding tissue radius ($r_T = 40 \mu\text{m}$) and a constant injection of solute ($C_0 = 5 \mu\text{mole/mL}$). This radial distribution was determined at $z = 570 \mu\text{m}$. (b) Solution of the same system using the discrete approach described in this paper. (c) Discrete radial concentration of solute compared to realizations of the analytical solution for $z = 569 \text{ mm}$ and $z = 571 \text{ mm}$ (d) axial distribution of oxygen between the analytical and the discrete solution.....50

Figure 12 Tube and discharge hematocrit along a narrowing vessel. As the channel narrows, the CFL occupies an increasingly larger fraction of the cross sectional area, causing the RBC phase velocity u to increase relative to the plasma velocity v . Also, the drift velocity between the phases, v_{Drift} , becomes large. In effect, the tube hematocrit, H_t , decreases along the flow direction, while the discharge hematocrit, H_d , stays constant. The radius of the blood vessel occupied by RBCs, R_e , is defined by the difference between the radius of the vessel lumen, R_p , and the thickness of the CFL.....65

Figure 13 Schematic of a bifurcating vessel carrying biphasic blood flow composed of RBC and plasma phase. Branch 3 receives more bulk blood, Q_3 , and disproportionately more RBCs, $Q_3 H_3$, than the weaker branch 2.71

Figure 14 Correlation of the plasma skimming coefficient θ for each daughter branch diameter as a function of different drift parameters M . As M increases, θ tends towards unity for all diameter ratios. $M < 1$ are inadmissible74

Figure 15 Flowchart describing the implementation for each of the models to solve for the bulk blood flow, Q , and discharge hematocrit, H_d ; **A.** Model 1, **B.** Model 2, and **C.** Model 3. Since Model 1 requires knowledge of the upstream hematocrit to compute the RBC split at a bifurcation, the inner loop is non-linear. In contrast, Model 2 and 3 have a linear inner loop. D is the vessel diameter, α is the flow resistance, and the tolerance is $\epsilon = 10^{-5}$78

Figure 16 The RBC flux split fraction as a function of the fractional bulk blood flow, γ , on the ordinate in a single bifurcation in the rat mesentery⁴⁶. Circles show observed RBC split for varying flow rates forced by gradually constricting the thinner branch shown with open circles ($d_1 = 6\mu\text{m}$). Closed circles are used for the thicker branch ($d_2 = 8\mu\text{m}$). Solid lines show numerical results for the thin (black) and thick (gray) branches as predicted by **A.** Model 1, **B.** Model 2, and **C.** Model 3 ($M = 1.13$). The residual sum of squares, RSS , is reported. Model 1 shows the best match to empirical data. Plasma-skimming pattern is observed both in Model 1 and the

Model 3. The grey dashed line represents a well-mixed contrast agent dividing equally between the two daughter branches.....81

Figure 17 Spatial distribution of discharge hematocrit as predicted by three models. **A.** Image of the network shown in microscopic monochromatic images^{34,51}, with arrow indicating the arterial inlet. A large vessel trunk spans the microvessel image from right to left, bifurcating near the inlet to form a side branch that curves downwards. As the main trunk near advances towards the right portion of the image, it bifurcates into two smaller branches that follow a tortuous path toward the edge of the domain. **B.** Manual reconstruction of the image captured vessel morphology features and diameter distributions. Histogram shows matching diameter spectra between original image and reconstruction. Vessels of interest were identified at key side branches (B_1 - B_5) and along the main arterial trunk (A_1 - A_6). Spatial distribution of discharge hematocrit (H_d) as computed by **C.** Model 1, **D.** Model 2, and **E.** Model 3. Vessels empty of RBCs are shown in yellow. Model 1 predicts many capillaries without any RBCs. Both Model 1 and Model 3 show hemoconcentration in the arteriole trunk from left to right, Model 2 shows hemodilution in main vessels in direct opposition to the plasma skimming experiments. Numerical values are listed in Table VI. Frame A reproduced from original work³⁴ with publisher permission.83

Figure 18 Distribution of discharge hematocrit in small vessels as predicted by **A.** Model 1 and **B.** Model 3. Bars shown in white indicate vessels with no RBCs. Model 1 has a high incidence of zero RBC vessels, which are mostly capillaries. Model 3 predicts no RBC-free vessels.....88

Figure 19 Tissue oxygen distribution to the mesentery tissue. Contour maps of oxygen tension in the mesentery tissue computed using 77,500 square mesh cells with 20 μ m side length. **A.** Model 1, and **B.** Model 3, with respective vessel oxygen tension. Arrows indicate *measured* physiologic tissue oxygen tension of 34.1 \pm 7.8mmHg⁵⁰ and *predicted* average tissue oxygen tension for Model 1 (pO_2 =24.4 \pm 5.2mmHg) and Model 3 (pO_2 =29.1 \pm 3.1mmHg).....90

Figure 20 The sensitivity of effect of oxygen exchange on small vessel hematocrit. **A.** The percent of oxygen exchange duty by vessels grouped by diameter. Mean oxygen exchange values in mmol/s are reported in bold, and their corresponding percent are shown underneath. Vessels with diameter less than 20 μ m accounted for more than 95% of the total network oxygen exchange. **B.** A comparison of Model 1 and 3 predictions of H_d/H_{sys} against rat mesentery measurements³⁴, as grouped by diameter. The collected mesentery data is shown as dark grey bars, the predictions of Model 3 as light grey speckled bars, and the predictions of Model 1 as white bars. For vessels with diameter less than 30 μ m, the large error between Model 1 predictions and measured mesentery data has a statistically significant p -value ($p<0.01$), denoted by an asterisk.92

Figure 21 Measured and computed RBC flux split as a function of volumetric blood flow. Empty circles showing measurements from the hamster cremaster muscle⁶¹ are compared against numerical predictions shown as filled circles from, **A.** Model 1, and **B.** Model 3. The *logit* function proposed by Klitzman⁶¹ is shown as a solid black line in **C.** While the experiments show no RBC free vessels, Model 1 includes many vessels carrying no RBCs marked as gray circles. Model 3 predicts no vessels with zero hematocrit in agreement with the experiment, as does the *logit* function.94

Figure 22 Computed tissue oxygenation in a 3x3x3mm section of the secondary human cortex predicted by Model 3. **A.** Predicted blood pressures, red marks high arterial, blue lower venous pressure regions. **B.** Hematocrit distribution in a small subsection supplied by six penetrating arterioles and three draining veins. Oxygen perfusion to tissue in three layers of the cerebral cortex **C.** 0.30mm, **D.** 1.35mm, and **E.** 2.40mm. Average oxygen tension in the three layers was 41.76 \pm 0.07mmHg (0.30mm), 41.76 \pm 0.06mmHg (1.35mm), and 40.84 \pm 0.06mmHg (2.40mm). Cerebral tissue near the surface of the cortex is well supplied. Model 3 predicts physiologic oxygenation in deeper layers (2.40mm) due to hemoconcentration in the penetrating

arterioles. In contrast, constant hematocrit computations gave lower oxygen tension in deep tissue ($30.25 \pm 1.93 \text{ mmHg}$, computations not shown).101

Figure 23 Flow profile integration of the bulk and hematocrit phase. Established laminar flow profile for the blood bulk, $v_z(r)$, and the plug flow profile $H_t(r)$ for the RBC phase with a local volume concentration of H_{core} . The RBC phase radially exists from $r=0$ to $r=r_0-\delta$, where δ is the thickness of the CFL and r_0 is the radius of the cylindrical vessel lumen. CFL thickness evaluated as $0.8 \mu\text{m}$105

Figure 24 Construction of mass conservation equations using Model 3. The discharge hematocrit of the upstream vessel is H_1 , and the volumetric bulk flow for each vessel, Q , is known. The plasma skimming coefficient, θ , for each daughter branch is computed using eq. 24, for **A.** a bifurcation, and **B.** a trifurcation. The adjusted hematocrit, H^* , for both case studies is computed by mass conservation. The daughter branch discharge hematocrit is the product of its plasma skimming coefficient θ for each branch and the adjusted hematocrit, H^*110

Figure 25 Vectorized data of the multi-scale vascular and cellular morphology of the mouse cerebral cortex. **A.** Illustration of the multiscale resolution of the murine cerebral vasculature from the cortical surface vessels down to the cellular level. (Whole brain snapshot taken from the NIH supported KOMP Phenotyping Pilot project⁴⁵). **B.** Full view of the microvascular network with cerebral arterioles in red, draining veins in blue, and capillaries in purple. Neuronal cells are displayed in yellow and glial cells in green at the 0.5 mm resolution. (Frames **B₁** to **B₃** show data in increasing magnification **B₁**. $1.0 \text{ mm} \times 1.0 \text{ mm} \times 1.2 \text{ mm}$, **B₂**. $200 \mu\text{m} \times 200 \mu\text{m} \times 200 \mu\text{m}$, and **B₃**. $25 \mu\text{m} \times 25 \mu\text{m} \times 25 \mu\text{m}$. At the finest resolution in **B₃**, cell bodies of neurons and glial cells were added for clarity). Histogram of cell to capillary distance for **C.** neurons and **D.** glial cells.132

Figure 26 Statistical analysis of the four primary somatosensory cortical mouse data sets with superimposed hemodynamic simulation results. Probability density functions of anatomical parameters: **A.** vessel diameter, **B.** vessel length, and **C.** the number of capillaries located at a

given depth. Distributions for pial arteries (PiaA), pial veins (PiaV), penetrating arterioles (PenA), penetrating venules (PenV) and capillaries (Cap) with respect to **D.** surface area, and **E.** lumen volume fraction. **F.** Probability density function of neuronal density at a given depth. **G-I.** Computational results for blood pressure, hematocrit, and RBC saturation. Color-coding for **G.** blood pressure from red (120mmHg) to blue (5mmHg), **H.** hematocrit from orange (0.99) to green (0.11), and **I.** RBC saturation from red (90%) to orange (2%).135

Figure 27 Depiction of the anatomical hierarchy of arterial, venous and capillary microvessels in the primary somatosensory cortex for the first data set. Vessels are painted in colors corresponding to the blood pressure depicting arteries in red and veins in blue. Large surface pial vessels distribute blood along the surface of the cortex, and feed penetrating arterioles. Penetrating arterioles divert blood into deeper cortical layers. The capillary bed distributes blood uniformly in all directions. Venules collect the blood from the capillary bed and return it to the cortical surface. Pial veins convey the venous blood from the surface to the sinuses.....139

Figure 28 Comparison of predicted hematocrit distribution, RBC velocity and RBC oxygen tension to measured data. **A.** The predicted capillary RBC velocity matches measurements acquired with high-speed camera laser-scanning confocal microscopy⁶⁸. Both simulation and experiment show that more than 88% of RBCs travel at speeds below 2mm/s. **B.** The PDF for capillary hematocrit shows that the majority of capillaries have a hematocrit between 0.25-0.50 comparing well to two-photon measurements.⁶⁰ **C.** Mean RBC oxygen tension at different depths from the cortical surface (50-500 μ m). Bars indicate arterial (red), capillary (gray) and venous (blue) RBC oxygen tension compared to measured data⁶⁰ drawn as lines with connected dots in red for arteries and veins in blue.141

Figure 29 Oxygen tension in the murine cortical tissue. **A.** Average oxygen tension in the arterioles, tissue and venules in all four data sets, standard deviation as capped lines. The tissue is an oxygen sink and therefore lower than both arteries and veins. **B.** Oxygen

metabolism as a function of proximity to penetrating vessel. Oxygen tension along a ray passing through the center of each of the four data sets (**C-F**) in the x-direction, y-direction, and z-direction. Dotted vertical lines illustrate the position of penetrating arterioles (red) and penetrating venules (blue), gray box indicates experimentally measured oxygen tension in the murine cortex (18-40mmHg).144

Figure 30 Predicted tissue, cellular, and intercellular oxygen gradients. Mitochondria were spatially distributed to different location with the respect to the cell nucleus according to a cell-specific PDF: **A.** PDF for mitochondria location around glial nucleus ($x=0\text{mm}$) **B.** PDF of mitochondria in neurons. **C₁-C₄.** Oxygen tension gradient between ECS and neuronal cytoplasm (ΔEN), neuronal cytoplasm and mitochondria (ΔNM), ECS and glial cell cytoplasm (ΔEG), and glial cell cytoplasm to glial mitochondria (ΔGM) are reported for cortical layers I-IV. **D.** Illustration of the differences between the ECS, neuronal cell cytoplasm (N), glial cell cytoplasm (G) and mitochondrial oxygen tension.....146

Figure 31 Path analysis in a representative data set (mouse one). **A.** Anatomy of the cortical microcirculation with five typical flow paths. Each path follows the blood flow from an inlet pial artery through the capillary bed returning to the surface via draining venules. **B₁-B₄.** Mean pressure paths and range of microcirculatory blood pressure shown for all four data sets. Light gray shaded box indicates the capillary bed (vessels with diameter $<10\mu\text{m}$), where the main pressure drop occurs. This shaded region includes pre-capillary arterioles, capillaries and post-capillary venules. **C-F.** The computed hemodynamic trajectory of each flow path is reported for **C.** blood pressure, **D.** discharge hematocrit, **E.** RBC saturation, and **F.** plasma pO_2 . Upper and lower ranges of all paths (only five individual paths are shown) are drawn as a gray shaded region, illustrating the heterogeneity of the capillary bed. Averages of all paths are drawn as a black line. Note that averages do not well characterize the wide variety of hemodynamic state transitions that occur in the capillary bed.....148

Figure 32 Mesh Independence Study. Oxygen extraction and profiles (data not shown) was computed for different edge lengths for each data set. In coarse meshes (50-100 μ m), oxygen extraction was sensitive to edge length. As the computational domain for solving the reaction-diffusion equations was gradually refined, oxygen transport was no longer affected. For all four data sets mesh independence was achieved between 2.5-3.0 million equations corresponding to an approximate mesh edge length of 6.6 μ m.158

Figure 33 Morphological and hydraulic characteristics of the capillary bed as a function of branch order. Average values shown as a red box, distribution of values at each branch order shown in blue. **A.** Diameter of arterioles and capillaries as a function of branch order from the penetrating arteriole. The mean capillary diameter of 5 μ m decreases slightly with increasing branching order. **B.** Hydraulic resistance of individual vessels as a function of branch order. Mean capillary hydraulic resistance near the feeding arteriole is an order of magnitude lower than vessels with a branch order of 4th or higher.160

Figure 34. The angioarchitecture and hierarchy of cortical microcirculation; the surface pial arteries, penetrating arterioles (PA), capillaries, ascending venules (AV), and pial surface veins in one of the murine data sets. Vessel color corresponds with blood pressure from arterial inlets (red) to venous outlets (blue). Surface pial arteries travel along the cortical surface, narrowing until they descend into the parenchyma as penetrating arterioles. These PA feed the capillary bed, which is in turn drained by ascending venules. The AV journey back to the cortical surface where they empty into the cortical surface veins.174

Figure 35. Generation of simplified blood flow models. **A.** Schematic of the *serial resistor configuration* and **B.** the *conductive plate network*. Resistances were fitted at nominal conditions of arterial inlet pressure of 120mmHg and venous outlet pressure of 5mmHg for all groups; surface pial arteries, penetrating arterioles, capillaries, ascending venules and surface pial veins.179

Figure 36. Linear regression of vascular resistance of penetrating vessels as a function of root diameter: **A.** penetrating arterioles ($N=92$) **B.** penetrating venules ($N=325$). Regression formula and R^2 shown in boxed insets. The regression formula was used to assign penetrating arteriole and venule resistances in the *conductive plate network*.183

Figure 37. Capillary plate conductance optimized to match the inlet arterial blood flow between the conductive plate model, Q , and the full microcirculation network, Q . Plate conduction was varied by adjusting the uniform capillary diameter of the plate network until $|R|<0.10$. Final optimized capillary plate conduction was 165.79 (Mouse 1), 99.69 (Mouse 2), 296.85 (Mouse 3), and 597.33.14fL/mmHg/s/ μm (Mouse 4). The dependent control variable of the optimization routine is reported independent of cylinder length, i.e. conduction / arc length.186

Figure 38. Optimized length independent capillary plate conductance as a function of **A.** number of PA and AV, **B.** number of PA, **C.** cortical surface area, and **D.** the cortical volume of each data set. The linear fit of number of PA and AV to capillary plate conductance is the tightest fit ($R^2=0.9738$).....187

Figure 39. Fractional resistance distribution between the five microcirculatory vascular compartments determined by the *serial resistor configuration*. The *serial* model gives different values for each group including the capillary resistance in the four data sets. The average resistance of each vascular compartment does not adequately represent any of the four data sets.191

Figure 40. The distribution of fractional resistance as determined by the *conductive plate* network. The *plate* model gives similar values for each group with most of the vascular resistance residing in the capillary bed for all four data sets. The average resistance value of each vascular compartment accurately characterizes all four of the mouse data sets.192

Figure 41. Cortical perfusion as a function of arterial inlet blood pressure for the full network (blue), *serial resistor configuration* (red) and *conductive plate network* (green). Changing blood flow response for the full network model and both model reduction approaches are shown for **A.** Mouse 1, **B.** Mouse 2, **C.** Mouse 3, and **D.** Mouse 4. The perfusion predictions of the *plate model* are consistently closer to the results of the full network than the blood perfusion computed by the *serial configuration*.....193

Figure 42 Effects of reflective outlet boundary condition on the pressure wave. Applying a single inlet pressure impulse through a short 16cm vessel causes reflections that bounce from inlet to outlet, lessening in intensity due to the loss of energy from viscous friction. These results were computed with the collocation method.....212

Figure 43 Schematic of the outlet non-reflective RCR circuit, also known as the Windkessel balloon model. The first resistor, R_1 , must be low enough to ensure that flow and pressure leave the vessel and enter the capacitor, C , which acts as a distensible balloon. The second resistor, R_2 , must be much lower than R_1 so that as the capacitor releases energy it leaves the system toward the terminal pressure, P_{term} , and not back into the blood vessel.....214

Figure 44 Lagrangian polynomials and indexing scheme for the calculation of continuous *splines*. Each vessel section is represented by a single 3rd order polynomial, and C0 continuity is enforced by the definition of Lagrangian polynomials as shown above. Each section is indexed locally, and a global index is shown beneath the cylinder schematic.....224

Figure 45 Validation of numerical methods against measurements from the canine aorta. An inlet pressure wave collected from *in vivo* measurements was applied to a single straight distensible vessel and wall displacement was computed using the **A.** nonlinear and **B.** linear finite difference method, **C.** the two-step Lax Wendroff method, and **D.** the implicitly integrated collocation method..228

Figure 46 Effects of using consecutive splines with the collocation method using **A.** 1, **B.** 2, **C.** 5, and **D.** 10 segments. By increasing the number of 3rd order Lagrangian polynomials to represent the canine aorta, outlet boundary reflections were eliminated and the numerical simulation approached the measured values. No significant change in RSS was detected between 5 and 10 segments.229

Figure 47 Dynamic oscillatory results of the four integrators at the proximal (red), 33% (blue), 66% (green), and distal segments (black) of a single vessel. Integrators are, from top row to bottom; Lax-Wendroff, Linear Finite Difference (FD), Collocation, Nonlinear FD. The spatial signal propagation is nearly immediate for the Nonlinear FD method as evidence by the lack of time lapse between the four colored lines. Similarly, the time lapse of signal propagation from inlet to outlet is longest when calculated by the Collocation method.....231

Figure 48 Dynamic oscillatory results of the four integrators at t=17.1ms (red), t=145.6ms (blue), t=307.8ms (green), and t=614.0ms (black) of a single vessel. Integrators are, from top row to bottom; Lax Wendroff, Linear Finite Difference, Collocation, Nonlinear Finite Difference. The axial profile of the Collocation method appears to be more rigid than the other three methods.....233

Figure 49 State space comparison of all four methods (Lax Wendroff, Linear Finite Difference, Collocation, Nonlinear Finite Difference) using the linear tube law.234

Figure 50 Sensitivity analysis of longitudinal stress, β , and damping term, κ , on the phase lag between the area and pressure, as shown in the state space diagram. The phase lag induced by the longitudinal stress term is small compared to the effects of the damping term.235

Figure 51 Comparison between damping and longitudinal stress model and viscoelastic model. A direct comparison is difficult as even the linear version of the two methods gives different results as shown in the first and second column. The pressure-radius state-space

diagram is more sensitive to small changes in the viscoelastic parameters, τ_1 and τ_2 , than the damping and longitudinal stress coefficients, κ and β237

Figure 52 Dynamic trajectory of area, pressure, and flow at the proximal ends of the parent vessel and the main trunk bifurcation in the ovine arterial pulmonary bifurcation as computed by both the Lax-Wendroff (red) and Collocation (blue) method, compared to a QLV model²⁷. As the flow does not match between the methods presented in this report and computational results provided in the literature²⁷, a mass conservation analysis was undertaken as shown in Figure 53.....240

Figure 53 Mass Conservation of sheep pulmonary artery bifurcation as computed by the Lax-Wendroff method for the parent vessel, the main trunk daughter branch, and the smaller side branch. Analysis of a small vessel section with a $dx=0.25\text{mm}$ shows residual below numerical error, the green line, for each branch. However, extending the balance envelope to the entire vessel for the computation of Q while restricting the wall deformation measurement to either the proximal or distal node, as shown in the bottom row, results in a misleading analysis.242

Figure 54 Simulation parameters and network properties of microvessel network. This cerebral microcirculatory single inlet / single outlet network model consists of a penetrating arteriole (left) a draining venule (right) and an interconnected capillary bed in the middle.245

Figure 55 Harmonic steady state analysis of oscillatory signal in microcirculatory network. Blood pressure signal at **A.** penetrating arteriole inlet and **B.** descending venule outlet were compared for period 1, 3, 5 and 7. The blood pressure signals for periods 5 and 7 overlap for both the arteriole inlet and venule outlet, indicating that harmonic steady state is achieved by period 5. As each period is 0.6s, harmonic steady state is achieved at $t=3.0\text{s}$246

Figure 56 Dynamic blood pressure, velocity and percent change in cross sectional area at **A.** The deep penetrating pre-capillary arterioles, **B.** post-arteriole and **C.** pre-venule capillaries and **D.** the ascending venules. Gray bar in velocity and area plots indicates value of zero.248

Figure 57 The dynamic blood pressure distribution in a small microcirculatory test network. Blood pressure throughout the test network was visualized at different time points as indicated by the empty circles on the input pressure signal shown in the top left corner. Blood pressure is shown from 130mmHg (red) to 80mmHg (blue) at each time point.....250

Figure 58 Investigation of signal smoothness at different sampling rates. **A.** At the coarse signal sampling rate of $\Delta t=7.5\text{ms}$, it is unclear whether the peak at $t=0.25\text{s}$ is real or an integrator artifact. Black dots indicate the actual data points extracted from the results of the Lax-Wendroff integration. **B.** A higher resolution sampling rate of $\Delta t=1.5\text{ms}$ clarifies that the signal around this peak is continuously differentiable and smooth.....251

Figure 59 The effects of vessel bifurcation on phase lag between the pressure and flow signal and accompanying state space diagrams. In the parent vessel, the flow wave follows the pressure wave slightly. In the main trunk daughter branch, the phase lag between the flow and pressure signals is decreased, while in the side branch the phase lag is increased. This alignment in phase in the main trunk daughter branch is due to the similar area of the two vessels ($d=10\text{mm}$ in the parent vessel, $d=9\text{mm}$ in the daughter branch) that allows for the pressure signal to be passed through with little reflection while the flow signal is slightly reflected by the decreased change in flow. In the side daughter branch, the flow signal is reflected similarly to its sister branch, however the pressure wave is slowed down significantly more due to the large change in area ($d=10\text{mm}$ in the parent vessel, $d=5\text{mm}$ in the side branch).255

Figure 60 Four different blood flow signals in the upper branch of the cerebral microcirculation capillary bed indicated by the arrow as shown in the left panel. Each blood flow signal shown in gray is computed in response to a pressure input signal with an offset between +0 to +30mmHg in 10mmHg increments. The period averaged signal is shown in black lines for

each flow signal. Flow increases by 4.37nL/min from 2.39 to 6.76nL/min in response to a 30mmHg increase in penetrating arterial input pressure.256

Figure 61 Fluctuations in period averaged flow measurements in four select vessels. The average blood flow through a vessel for a period may fluctuate from period to period at harmonic steady state. Average blood flow values have a two period cycle at harmonic steady state in these four select vessels. Mass is conserved between the arteriole inlet vessel C (6.46nL/min) and the venous outlet vessel D (6.46nL/min), as well as at the union of the upper capillary A (2.46nL/min) and the lower capillary B (4.00nL/min).257

Figure 62 Dynamic blood flow response to an open-loop vasodilation event in the capillary bed at $t=6.0s$. Dilation of a capillary in the upper half of the capillary bed, shown by the black arrow, affects the dynamic blood in **A.** downstream vessels, **B.** the lower half of the capillary bed, **C.** the pre-capillary feeding arteriole, and **D.** the post-capillary draining venule. Blood flow in the downstream vessel increases in response to the widening vessel, while blood flow correspondingly drops in the sister vessel in the lower half of the capillary bed. Period to period fluctuations are flattened by the Arteriole inflow and venule outflow are unaffected259

Figure 63 Schematic of Lax Wendroff Richten-Meyer two-step indexing scheme. The bottom row, the initial state, is the known states of A , U , and P at the nodes $I = 1, 2$ and 3 . Step 1 advances these values to the off-grid points $i = 1\frac{1}{2}$ and $2\frac{1}{2}$. Finally, Step 2 determines the values of A , U , and P at every node for the full advancement in time.263

Figure 64 Schematic of bifurcation indexing scheme. Each vessel is assigned a local index from its proximal to distal end. The distal index of the parent vessel is in the same spatial position as the proximal node of both daughter branches. The value of P is the same between these three nodes, PB , however the values of the cross sectional area, A , or the blood velocity, U , may not be as described in eq. 131-133. The length of each vessel is Δx_1 , Δx_2 , and Δx_3 . .269

Figure 65 Schematic of union indexing. Each vessel is assigned a local index from proximal to distal end, where the distal index of both parent vessels has the same spatial coordinate as the proximal node of the daughter branch. The value of P is the same at all three nodes at the junction, however the values of A and U may not be. The length of each vessel is Δx_1 , Δx_2 , and Δx_3273

Figure 66 Schematic of narrowing or widening channel indexing. Each vessel is assigned a local index from proximal to distal end, where the distal index of the upstream vessels has the same spatial coordinate as the proximal node of the downstream vessel. The value of P is the same at both nodes at the junction, however the values of A and U may not be. Vessel length is Δx_1 and Δx_2276

Figure 67 Angioarchitecture of cerebral microcirculation and pressure signal at pial arteriole entrance. **A.** Cerebral microvessels are either pial surface vessels located along the cortical exterior or inferior microcirculation embedded within the tissue of the cortex. The inferior microcirculation includes PA, pre-capillary arterioles, capillaries and AV. Arrow indicates the entrance of the model. **B.** The periodic inlet pressure boundary condition for the model ($T=0.6s$) was captured using a 15 term Fourier series from patient Doppler measurements. **C.** Outlet pressure boundary condition of 5mmHg. **D.** Diameter probability distribution function (PDF) of generated microcirculation vessel network, mean diameter of $12.9\mu m$. **E.** Length PDF, mean length of $289\mu m$292

Figure 68 Schematic of microcirculatory vessel configuration and labels for **A.** pial surface arterioles, **B.** penetrating arterioles, **C.** pre-capillary arterioles, capillaries and draining ascending venules.299

Figure 69 Vasodilation of surface pial arteriole S_1 leads to a hemodynamic changes in **A.** Blood flow and **B.** CBV. Values at harmonic equilibrium are shown as a dotted line, only select vessels shown. A 30% decrease in E of the pial artery S_1 led to a 1.4% increase in **A**₁. upstream

feeding arteriole S_0 and subsequently A_3 . PA, A_4 . capillaries and A_5 . AV. Increases in CBV were not limited to B_1 - B_2 . surface pial arteries, CBV increased significantly in B_3 - B_5 . vessels embedded in the cortical parenchyma.....303

Figure 70 Vasodilation of PA P_5 leads to an increase in **A.** Blood flow and **B.** CBV.

Harmonic equilibrium values are shown as a dotted line. A 30% decrease in E of the PA P_5 leads to an increase in flow through A_1 . The upstream feeding pial artery S_0 by 1.4%, leading to an increase in A_3 . PA, and A_4 . capillaries and A_5 . AV. Increases in CBV occurred mostly at B_1 - B_2 . surface pial arteries, CBV increased slightly in B_3 . PA and B_4 . capillaries. B_5 . AV CBV did not increase appreciably.306

Figure 71 Comparison of active and passive changes in **A.** CBF and **B.** CBV for all three vasodilation scenarios, **1.** Surface pial arteries, **2.** Penetrating arterioles and **3.** Pre-capillary arterioles. Hemodynamic changes in blood flow and volume were measured for surface pial arteries, PA, capillaries and AV vessel groups. A_1 - B_1 Passive Δ CBF and Δ CBV dominated active changes during vasodilation of surface pial arteries, while active Δ CBV dominated during PA dilation as shown in B_2 . Vasodilation of pre-capillary arterioles led to the smallest Δ CBF and CBV as shown in A_3 - B_3 , and led to diversion of blood volume from capillaries that were not actively dilated, resulting in passive Δ CBV<0.309

Figure 72 Vasodilation of pre-capillary arterioles R_1 , R_2 , and R_4 leads to a slight increase in **A.** Blood flow and little change to **B.** CBV. Harmonic equilibrium values are shown as a dotted line. A 30% decrease in E of the pre-capillary arterioles R_1 , R_2 , and R_4 leads to an increase in flow A_4 . capillaries R_3 , R_4 , and R_5 only. CBV increased in capillaries embedded within the cortical parenchyma only, R_4 shown as a candidate vessel. Some vessels (such as R_2) did not increase in diameter even though E was decreased.311

Figure 73 Vasodilation of pial arteriole S_1 leads to a changes in **A.** Blood flow and **B.** CBV in select vessels. Signals displayed as values averaged over one-second intervals. Harmonic

equilibrium shown as a dotted line. A 30% decrease in E of the pial artery S_1 led to a 1.4% increase in A_1 . upstream feeding arteriole S_0 and subsequently A_3 . PA, A_4 . capillaries and A_5 . AV. CBV increases in B_1 - B_2 . surface pial arteries, were significantly higher than changes in B_3 - B_5 . vessels embedded in the cortical parenchyma.322

Figure 74 Vasodilation of PA P_5 leads to an increase in **A.** Blood flow and **B.** CBV. Signals displayed as values averaged over one-second intervals and harmonic equilibrium values are shown as a dotted line. **A.** A 30% decrease in E of P_5 increases flow through upstream feeding pial artery S_0 by 1.4%, leading to an increase in A_3 . PA, and A_4 . capillaries and A_5 . AV. Increases in CBV occurred mostly at B_1 - B_2 . surface pial arteries, and increased slightly in B_3 . PA and B_4 . capillaries. B_5 . AV CBV did not increase appreciably.323

Figure 75 Vasodilation of pre-capillary arterioles R_1 , R_2 , and R_4 leads to a slight increase in **A.** Blood flow and **B.** CBV. Signals displayed as values averaged over one-second intervals and harmonic equilibrium is shown as a dotted line. A 30% decrease in E of pre-capillary arterioles R_1 , R_2 , and R_4 increases flow A_4 . capillaries R_3 , R_4 , and R_5 only. CBV only increased in some capillaries, R_4 shown as a candidate vessel. Other capillaries, such as R_2 , did not increase in diameter even though E was decreased.324

LIST OF ABBREVIATIONS / NOMENCLATURE

BBB	Blood Brain Barrier
ATP	Adenosine Triphosphate
AV	Ascending Venule
BOLD	Blood Oxygen Level Dependent
CBF	Cerebral Blood Flow
CBV	Cerebral Blood Volume
CCO	Constrained Constructive Optimization
CFL	Cell Free Layer
CFL	Courant-Friedrichs-Lewy
CMRO	Cerebral Metabolic Rate of Oxygen
CT	Computed Tomography
CVD	Cerebrovascular Disease
DNA	Deoxyribonucleic Acid
ECS	Extracellular Space
ESL	Endothelial Surface Layer
FBU	Functional Blood Unit
fMRI	Functional Magnetic Resonance Imaging
FSI	Fluid Structure Interaction
Hb	Hemoglobin
Hd	Discharge Hematocrit
Ht	Tube Hematocrit
KPSM	Kinetic Plasma Skimming Model
MRI	Magnetic Resonance Imaging
NVU	Neurovascular Unit
OE	Oxygen Extraction
PA	Penetrating Arteriole
PDF	Probability Density Function
PQM	Phosphorescence Quenching Microscopy
QLV	Quasilinear Viscoelastic
RBC	Red Blood Cells
RSS	Residual Sum of Squares
SMC	Smooth Muscle Cells

SUMMARY

This dissertation presents a comprehensive mathematical model of microcirculatory cerebrovascular blood flow and oxygen transport to cortical tissue. As available measurements for blood flow, RBC oxygenation, RBC velocity and blood flow in cerebral blood microvessels ($\text{dia} < 100 \mu\text{m}$) in human patients are difficult to obtain, computer simulations are necessary for quantifying measurements acquired from imaging modalities, such as CT or fMRI.

A 3D model of the human cortical microcirculation is presented, including oxygen perfusion to tissue. This model is closely validated against available *in vivo* animal and *ex vivo* human measurements. The sensitivity of these models to boundary conditions is investigated as well as the apparent “flat” tissue oxygen tension gradients at deep within the cortex. This model is then augmented with a novel biphasic blood flow model, the kinetic plasma skimming model (KPSM). This novel KPSM was developed out of necessity following a comprehensive investigation of existing biphasic blood flow models which were unable to accurately reproduce the phenomena of plasma skimming observed experimentally in physiological studies of the microcirculation.

This biphasic model of blood flow, coupled with an improved nonlinear oxygen dissociation model, was deployed on four murine microcirculatory networks acquired from two-photon confocal microscopy. This study demonstrated the variability of hemodynamic properties along different “paths” through the cerebral microcirculation, and that vessels of similar types and lumen diameters may exhibit a wide variation in blood pressure, flow, hematocrit, RBC velocity or RBC oxygenation. Furthermore, the majority of the microcirculatory resistance was shown to reside between the pre-capillary arterioles and the ascending venules, and not in the descending arterioles or the surface pial arteries.

Finally, the pulsatile distensibility of the microcirculatory vessels was addressed. Several fluid structure interaction models were investigated, as well as candidate solvers to compute the solution of these nonlinear wave equations. A two-step Lax Wendroff solver was identified as a robust method for computing hemodynamics across a distributed blood flow network. Dynamical

SUMMARY

blood flow, pressure, velocity and vessel volume was computed across a 3D simplified microcirculatory network. Three functional hyperemia case studies were investigated as possible vasodilatory mechanisms in response to neuronal activation. In each scenario, a different vessel type was vasodilated exclusively; a pial artery, a penetrating arteriole, or a collection of pre-capillary arterioles. The passive network response to these vasodilatory mechanisms was compared against changes in CBV as measured by fMRI. It was determined that none of these mechanisms activated in isolation would be capable of reproducing measured CBV changes, therefore these mechanisms must work in concert during functional hyperemia.

Overall, the models presented here demonstrate that morphologically accurate, physiologically consistent models are capable of reproducing hemodynamic measurements at the micron scale within the cerebral vasculature. Furthermore, as these measurements are impossible to obtain in a distributed fashion, these computational models provide a comprehensive picture of intracranial dynamics that would otherwise be unobtainable. This model establishes the first-principles mechanistic understanding of cerebral oxygen supply and functional hyperemia that is necessary for quantifiable fMRI.

I. OVERVIEW

Cerebrovascular disease (CVD) is the fifth leading cause of death in the US, costing the healthcare system over \$33 billion annually. Treatment of fatal CVD such as stroke, aneurysm, micro-infarcts and genetic disorders heavily relies on the interpretation of indirect medical imaging modalities such as CT and MRI. Interpretation of signals extracted from these modalities is limited to qualitative comparison only, restricting the information provided to clinicians. Providing a quantitative basis for these imaging modalities requires an in-depth understanding of how blood flow, tissue oxygen tension and deoxygenated hemoglobin behave at rest and in response to neuronal activation. As a direct measurement of these phenomena in human patients is impossible, mathematical models must be relied on to provide a comprehensive basis of cerebral hemodynamics and oxygen supply. This is especially true in the cerebral microcirculation, the site of oxygen supply. By better comprehending how these hemodynamic properties relate to tissue oxygenation at rest and during healthy activity, we can better understand how to treat the brain during injury. This model is the foundation of a novel computational approach for hypothesis testing in fMRI analysis, specifically understanding the complex interactions between the BOLD signal, CBV, CBF and hemodynamic reserve. The investigation presented in this dissertation investigates both steady state and dynamical models of the microcirculation in image-reconstructed and artificially generated network models. This investigation included studies in both human and mouse models.

Chapter II addresses how network simulations of the cortical microcirculation may be accomplished without the detailed image reconstruction. Using a modified vessel generation algorithm (CCO), a 3D model of the microcirculatory system inside an subsection of the human secondary cortex was generated that includes surface pial arteries, penetrating arterioles, a capillary bed, ascending venules and surface pial veins. A realistic 3D morphology is important to understand the effects of vessel orientation, density, arrangement, and hierarchy in oxygen

distribution in the cerebral cortex. The construction principles of this vessel generation algorithm are tuned to match morphological observations measured with SEM and intravital microscopy in the human secondary cortex. A steady state single phase non-Newtonian blood flow model was deployed accounting for the inconsistency of blood viscosity as vessel caliber narrows in the inferior microcirculation. Validation of blood flow, pressure and velocity is presented. Oxygen convection, extraction and metabolism simulations are presented and analyzed to determine the distribution of oxygen between arteries and veins, the capillary bed and diffused through the tissue in different cortical layers. Analysis of extravascular oxygen gradient profiles surrounding different vessel types is presented to identify which vessel types are the main site for oxygen transport to neuronal tissue in the cerebral cortex.

Chapter III improves upon the oxygen transport presented in Chapter II with the development of a novel two-phase blood flow model. This Chapter is a modified document of a previously published manuscript, with included corrections from published Erratum. An analysis of existing biphasic blood flow microcirculatory models is presented and their limitations described and the need for a new biphasic model is determined. Specifically, no prior model can accurately capture the phenomenon of plasma skimming in realistic microcirculation vascular networks without predicting capillaries devoid of RBCs. Therefore, a novel kinetic plasma skimming (KPSM) model is presented which simulates the effect of plasma skimming if microvascular bifurcations and while simultaneously keeping all capillaries full of RBCs. This new methodology is validated thoroughly against 2D RBC concentration and oxygen measurements in the image reconstructed rat mesentery networks and the hamster cremaster muscle. A new oxygen transport model is introduced which utilizes these biphasic blood flow predictions, and the consequence of RBC-devoid vessels is demonstrated. This improved blood flow model is deployed on the human secondary cortex microcirculation network presented in Chapter II and oxygen simulations are presented. The biphasic model transports oxygen into the deeper into the cortex than was simulated using the single phase model.

Chapter IV presents a steady state simulation of oxygen transport on a microcirculatory model captured from two-photon microscopy data, rather than built using a vessel generation algorithm. Oxygen simulations are performed on four cortical microcirculatory networks obtained from different mouse subjects. The model is improved upon as well; a kinetic feature is added to simulate the nonlinear dissociation of oxygen from hemoglobin. This kinetic binding / unbinding model of oxygen captures the Hill Saturation curve of oxy-deoxygenated hemoglobin ratios in the bloodstream. Additionally, the tissue model of oxygen metabolism was improved. Oxygen metabolism models in Chapters II and III treated the extravascular tissue space as a single lumped compartment. Detailed two-photon confocal microscopy data from the four murine data sets included the spatial location of the soma of neuronal and non-neuronal extravascular cells. Assigning a cell type-specific mitochondrial probability distribution function to each cell soma allows us to build a 3D distribution of mitochondria and therefore a 3D distribution of cortical cellular metabolism. Analysis of the microvascular network structure reveals a non-uniform catalogue of paths from the surface arterial inlet to the surface venous outlet. The trajectory of hemodynamic properties (Pressure, flow, RBC velocity, RBC saturation, plasma oxygen tension) varies wildly between different paths, revealing that there is no “standard” trajectory of hemodynamic state transitions. The differentiation between hemodynamic trajectories of different paths has two consequences; 1) previously conflicting observations of RBC velocity, oxygen tension and blood pressure in the cerebral microcirculation may now be reconciled as vessel type and lumen caliper is not a reasonable basis for direct comparison, and 2) the majority of path trajectories indicate that the capillary bed is the primary site for pressure drop in the cerebral microcirculation.

Chapter V presents two model reduction methods of the complex blood flow simulations described in Chapters II-IV. Each of these approaches focuses on reducing the number of equations needed to accurately compute blood flow through the five vascular compartments; the surface pial arteries, penetrating arterioles, capillary bed, ascending venules and the surface

pial veins. The first approach is a *serial resistance configuration* which simplifies each of vascular compartments to a single resistor which are then connected in series. The second approach, the *conductive plate network*, preserves the morphology of the surface pial and venous morphology, while the penetrating arterioles and ascending venules are reduced to single resistors connected to a 2D conductive plate representing the capillary bed. A separate model was constructed for each of the four data sets described in Chapter IV. The fractional vascular resistance distribution of the *serial* model demonstrates a wide variation between data sets, whereas the *plate* model consistently attributes >85% of the fractional resistance to the capillary bed. Furthermore, an averaged *series* model was unable to accurately predict the blood flow response for a given arterial input pressure for any of the four data sets. The performance of the blood flow response using the *plate* model gave a close match against the simulation results of the full network models at 2% of the computational cost. This preliminary investigation of model reduction demonstrates that blood flow computations using the *conductive plate network* are physiologically meaningful while significantly reducing the computational cost of simulating the cerebral microcirculation.

Until Chapter VI, all previous chapters dealt with steady state simulations exclusively. This chapter introduces a dynamic model of situating blood flow as a FSI problem. This approach to modeling blood flow requires the dynamic solution of a set of nonlinear partial-differential equations. Solution of these equations over a distributed blood flow network requires an investigation of different integration and discretization techniques which are presented. A mix of implicit and explicit solvers is studied. Additionally, the effects of different tube laws (linear elastic, viscoelastic and longitudinal stress) are explored. Validation against physical measurements eliminated all but a linear elastic tube law and two solvers: the two-step Richtmeyer-Morton Lax-Wendroff scheme or the Collocation method integrated with the Implicit Euler method. These two methods were compared using canine aorta and sheep pulmonary

case studies. The Lax-Wendroff scheme was selected and preliminary simulations on an extended network are described, as well as a primitive vasodilation simulation.

The dynamic FSI problem investigated in Chapter V is deployed to a simplified 3D microcirculatory model of the human cerebral microcirculation in Chapter VI. This microcirculatory network model is constructed using the same modified vessel growth algorithm presented in Chapter II; however this simplified network is not as dense and includes a more irregular distribution of penetrating arterioles and ascending venules. Hemodynamic properties of pulsatile pressure, velocity and blood volume are investigated at harmonic equilibrium (i.e. harmonic steady state) and in response to one of three different vasodilation scenarios. Each scenario is modeled as a possible vasoactive response to neuronal activity during functional hyperemia. In each scenario, blood flow and passive CBV response in the surface pial arteries, penetrating arterioles, pre-capillary arterioles and ascending venules is recorded. Simulation results are compared to fMRI measurements, revealing that the measured changes in CBV that follow functional hyperemia at both the surface and within the parenchyma tissue are not captured by any one of the three proposed vasodilation mechanisms. It is hypothesized that the physiologically accurate mechanism of vasodilation following neuronal activity is a combination of large surface vessel dilation and relaxation of pre-capillary sphincters.

Studies of simulated CBV and blood flow response to vasodilation scenarios proposed in Chapter VI are critical for analyzing the multi-part signal that is BOLD fMRI. These distributed, multi-scale FSI simulations require a robust solver, identified by the investigation presented in Chapter V. These dynamic blood flow simulations, combined with kinetic oxygen simulations in Chapter IV, the novel plasma skimming law described in Chapter III, and the vascular growth algorithm presented in Chapter II are critical components to building a first-principle model of the relation between blood flow, oxygen metabolism, and observable deoxygenated hemoglobin. Quantifiable fMRI and CT as a clinical and research tool requires the construction of such a model to advance the understanding and treatment of CVD.

II. CEREBRAL MICROCRICULTION AND OXYGEN TENSION IN THE HUMAN SECONDARY CORTEX

(Previously published as Linninger, Andreas A., I. G. Gould, T. Marrinan, C-Y. Hsu, M. Chojecki, and Ali Alaraj. "Cerebral microcirculation and oxygen tension in the human secondary cortex." *Annals of biomedical engineering* 41, no. 11 (2013): 2264-2284.)

Abstract

The three-dimensional spatial arrangement of the cortical microcirculatory system is critical for understanding oxygen exchange between blood vessels and brain cells. A three-dimensional computer model of an $3 \times 3 \times 3\text{mm}^3$ subsection of the human secondary cortex was constructed to quantify oxygen advection in the microcirculation, tissue oxygen perfusion, and consumption in the human cortex. This computer model accounts for all arterial, capillary and venous blood vessels of the cerebral microvascular bed as well as brain tissue occupying the extravascular space. Microvessels were assembled with optimization algorithms emulating angiogenic growth; a realistic capillary bed was built with space filling procedures. The extravascular tissue was modeled as a porous medium supplied with oxygen by advection–diffusion to match normal metabolic oxygen demand. The resulting synthetic computer generated network matches prior measured morphometrics and fractal patterns of the cortical microvasculature. This morphologically accurate, physiologically consistent, multi-scale computer network of the cerebral microcirculation predicts the oxygen exchange of cortical blood vessels with the surrounding gray matter. Oxygen tension subject to blood pressure and flow conditions were computed and validated for the blood as well as brain tissue. Oxygen gradients along arterioles, capillaries and veins agreed with *in vivo* trends observed recently in imaging studies within experimental tolerances and uncertainty.

Introduction

Oxygen transport is critical for the brain to meet the rapidly changing metabolic demands during neuronal firing. Neurovascular coupling is a mechanism for matching the rise in the mitochondrial oxidative metabolism of neurons with a local increase in cerebral blood flow⁴⁵. Recent studies have begun to uncover the significance of the spatial arrangement of the cortical microvasculature for oxygen supply^{22, 25, 54}. The morphology of cerebral microcirculation appears to play a significant role in ensuring adequate oxygen transport from the blood to brain cells.

A series of anatomical and physiological studies by Duvernoy, Cassot, and Lauwers delineated the morphometrics of blood vessels in the cerebral cortex.^{6,7,12,38} Their studies uncovered the particular arrangement of cortical blood vessels centering around pial draining veins which are irrigated by three to six penetrating arterioles.¹² Recent topology studies confirmed the spatial allocation of the cortical microvasculature.^{3,22} Fresh arterial blood enters each territory through the leptomeningeal vessels depicted in Figure 1A, which discharge into descending arterioles shown in Figure 1B. From the cortical surface, descending—often also referred to as penetrating—arterioles dive into the gray matter carrying blood and oxygen deeper into the cerebral cortex. Figure 1C shows descending arterioles traversing the six cortical layers where they bifurcate into gradually narrowing binary trees, whose terminal leaves discharge into the capillary bed. The capillary bed does not conform to a binary tree, because it contains anastomoses which create loops. The multiscale morphometrics of binary arterial and venous trees as opposed to the mesh-like capillary bed was studied in detail.⁴²

A single endothelial cell layer lines the capillary wall thus creating a large mass exchange surface between oxygen-rich blood and the extravascular space. Mass transfer also occurs between arterioles and venules.^{14,75}

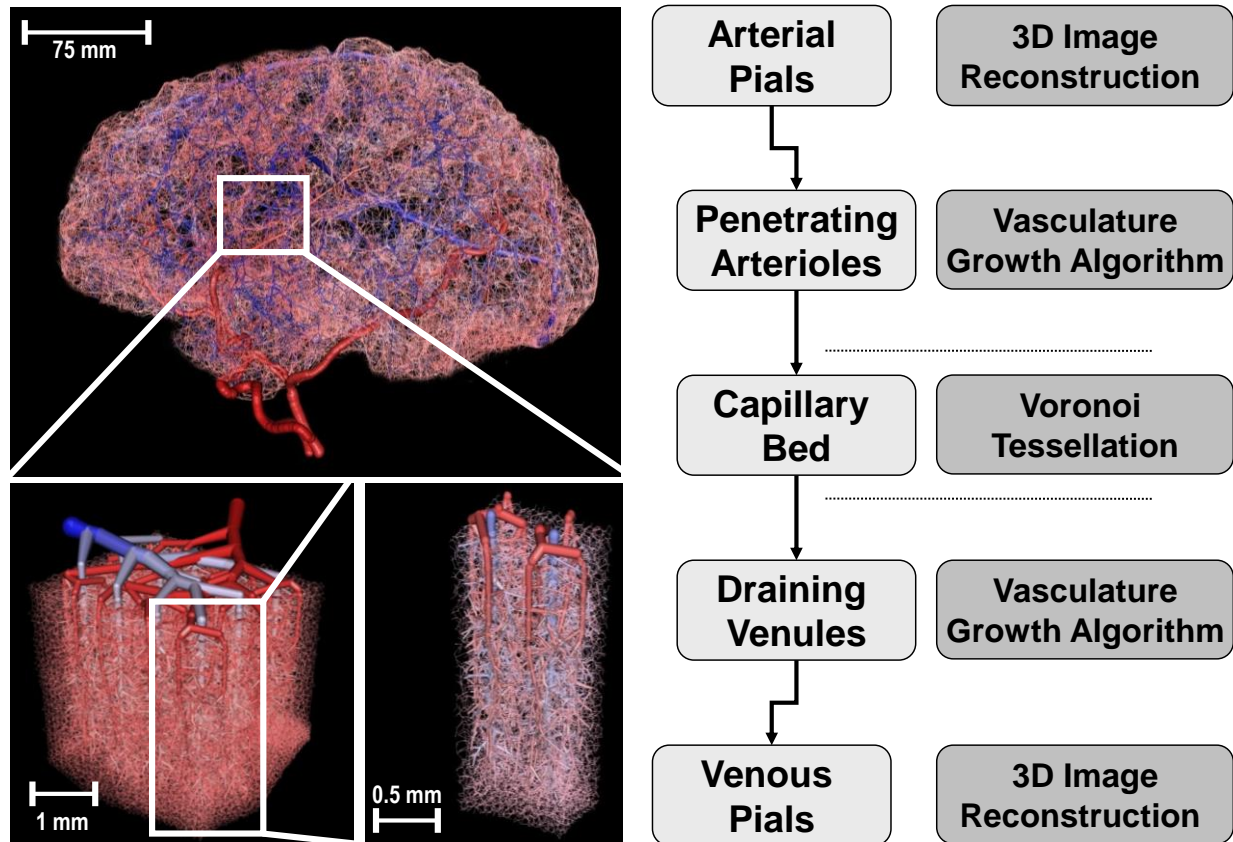


Figure 1 Overall multi-scale hierarchy of the human cerebral circulation. (a) Sagittal view of the full brain vasculature model generated *in silico* by combining image data with constrained constructive optimization. (b) Magnified section of the secondary cortex next to the collateral sulcus in the right temporal lobe, showing the arrangement of the network of pial arteries and veins at the cortical surface. (c) Isolated view of the territories of two draining pial veins supplied by six penetrating arterioles. (d) The construction principles for the computer aided construction and analysis of cerebral blood flow networks. This article is limited to structures ranging from the pial arterioles to the pial veins are discussed.

Red blood cells traveling with the blood stream carry oxyhemoglobin which can release free oxygen into the plasma. Oxyhemoglobin dissociation is facilitated by a basicity-mediated conformational change in hemoglobin. Blood pH is reduced by carbonic acid which is a byproduct of cellular respiration.³⁰ Free plasma oxygen permeates the vessel endothelial layer and diffuses to brain cells driven by concentration gradients. Due to the mitochondrial oxidative metabolism, oxygen tension in the extravascular tissue is lower than in the blood stream.

However, oxygen exchange between the microvessels and the brain cells, especially with respect to the spatial arrangement of vessels, have not been fully quantified. Goldman proved that random and tortuous blood vessel networks greatly enhance mixing and oxygen distribution compared to evenly spaced, ordered vessel configurations.¹⁸ Boas developed *in vivo* optical measurements of tissue oxygenation in relation to cerebral blood flow. Their experiments are beginning to unravel the spatiotemporal characteristics of the blood flow and oxygen responses after neuronal activation.^{4,27} Their computational models also explored the evolution of tissue oxygen tension around a single cylindrical blood vessel, as well as for a more realistic anatomical microvessel network of the rat.¹⁴ Plouraboue reconstructed microvascular networks from synchrotron CT images to investigate coupling and robustness of intra-cortical vascular territories.^{20,22} Weber emphasizes the need for topologically accurate models to investigate the effect of local vascular dilation and occlusion on the flow in the surrounding network.^{24,54,61} Lorthois, Cassot and Lauwers demonstrated the quantitative relationship between the diameter of a pial draining vein and the size of the surrounding neuronal activated area.^{38,43,44}

Anatomically and physiologically accurate computer models are an important tool for analyzing tissue metabolism coupled to micro-hemodynamics. Table I summarizes the characteristics of several recent microvasculature models.

Table I Overview of microvascular simulation models and their features

References	Species	Model characteristic	Number of vessels	Extracell. Space	Venous	Capillary bed	Oxygen tension
This work	Human	Geometric construction, 3D	256,000	600,000	•	•	•
Lorthois ⁴⁴	Human	Image Segmentation. 3D	10,318	-	•		
Safaeian ⁵⁹	Human	Geometric construction, 3D	112	-	•	•	
Lauwers ³⁸	Human	Morphometric Study, 3D ^a	359,242	-	•	•	
Zagzoule ⁷⁸	Human	Geometric construction, 3D	316,858	-	•	•	
Guibert ²⁰	Marmoset	Image Segmentation. 3D	16,000	-	•		
Weber ⁷⁶	Marmoset	Morphometric Study, 3D ^a	NS	-	•	•	
Niimi ⁴⁷	Cat	Image Segmentation. 3D	45	-			
Goldman ¹⁸	Hamster	Geometric construction, 3D	11	-		•	•
Fang ¹⁴	Rodent	Image Segmentation. 3D	NS	600,000	•		•
Blinder ³	Rat	Morphometric Study, 3D ^a	200	-			
Reichold ⁵⁴	Rat	Image Segmentation. 3D	NS	-	•	•	
Boas ⁴	Rat	Geometric construction, 3D	254	-	•	•	•
Huppert ²⁷	Rat	Geometric construction, 3D	NS	-	•	•	•
Kasischke ³⁴	Mouse	Biophysical Study, 2D	NS	-		•	•
Tsai ⁷⁰	Mouse	Morphometric Study, 3D ^a	~6,300	-	•		

NS Not stated in referenced work.

^a No Computations, morphometric studies only.

These computational methods can address the need for (i) better interpreting optical measurements acquired in open cranial windows in rodents,^{3,60} (ii) for exploring intracellular transport phenomena on length scales currently not accessible to imaging methods,^{34,35} and (iii) for making inferences for humans^{38,44} for whom invasive experimentation is not an option.

This work introduces a detailed three-dimensional computer model for cerebral microcirculation inside a subsection of the human secondary cerebral cortex. A network model was used to perform hemodynamic simulations of the microcirculation. The microvessel network was embedded inside the extravascular space to compute the oxygen exchange between blood and cortical brain tissue. Hemodynamic characteristics of blood flow, convective transport, and oxygen perfusion to the cortical tissue were predicted. In addition to computing blood oxygen tension, oxygen gradients around arteries and capillaries were predicted at different cortical depths. We validated critical morphometric and hemodynamic predictions against prior experimental studies in the open literature. Oxygen gradients predicted for a relatively large cortical domain (27 mm³ subsection of the secondary cortex in humans) matches trends observed in *in vivo* imaging studies.

Materials and Methods

A three-dimensional model of the microcirculatory system inside an $3 \times 3 \times 3\text{mm}^3$ subsection of the human secondary cortex was generated with principles illustrated in Figure 1. The morphometrics of our artificial microcirculation matched human experimental data acquired with confocal microscopy by Lauwers,³⁸ the comparison of the model with prior experiments are summarized in Figure 2. The vascular network was embedded inside the porous brain tissue. For modeling the extravascular domain, we lumped the intracellular space, neurons and glial cells of the gray matter and meshed this space as a single continuum. Oxygen exchange between the blood and the porous tissue were computed by solving for advection, diffusion and metabolism simultaneously with custom-coded computer programs.

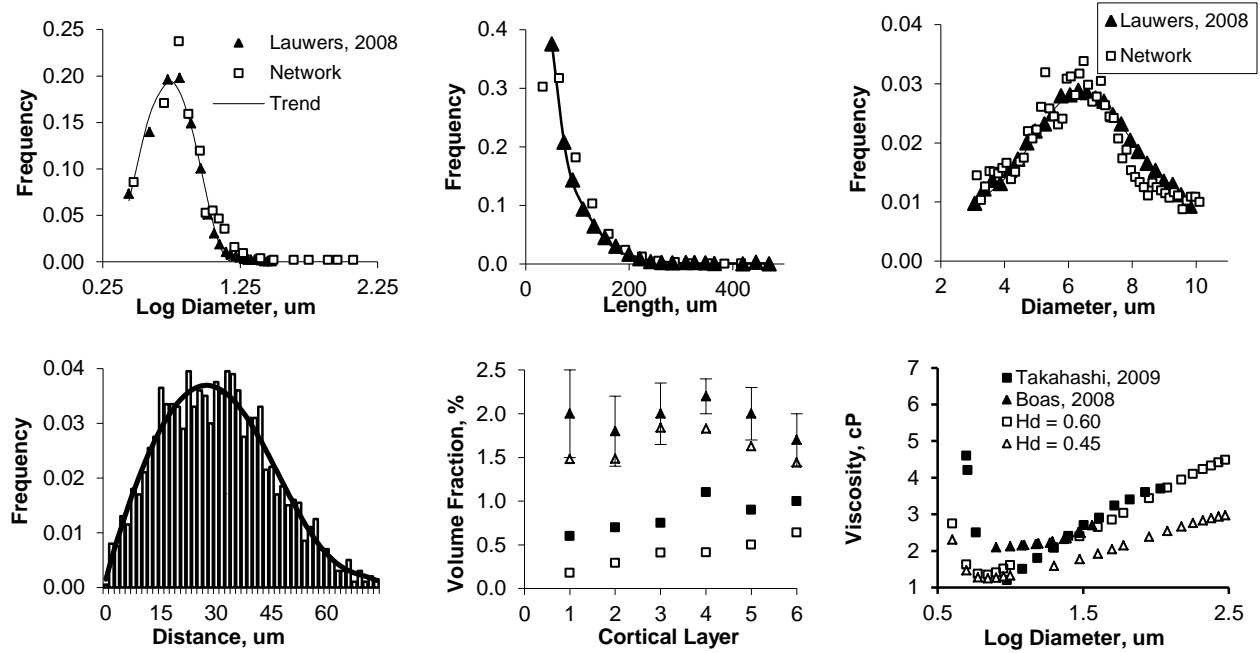


Figure 2 Summary and validation of morphometric properties and blood rheology of the microvessels of the secondary cortex next to the collateral sulcus in the right temporal lobe. Closed symbols show measured morphological properties with best fit solid line, open symbols show morphometrics of our artificially constructed microvessel structure. Panels a–d compare this work against morphological analysis of confocal microscopy work of the human secondary cortex.^{12,38} (a) Diameter distribution of all vessels in the microvascular network. (b) Length distribution of all vessels in the network. (c) Normal distribution of capillary vessels diameter with a mean diameter of 6 μm . (d) Histogram of distance to nearest capillary vessel in the cortical tissue, solid line shows polynomial best-fit. (e) Laminar distribution of volume fraction for vessels in cortical subsection, Triangles (Δ) indicate the total vessel pattern, squares (\square) represent only the capillary spectra, compared with laminar network morphometrics obtained by scanning electron microscopy of corrosion casts of the macaque visual cortex.⁷⁶ The volume density for the synthetic human microvasculature is lower than the macaque, as reflected in the values reported in Table 2. (f) Diameter dependent viscosity as determined by the Fahraeus–Lindqvist equation (eq. 4) in comparison to values reported by Boas⁴ and Takahashi.⁶⁸ In the simulations, we used $Hd = 0.45$.

Microvasculature Construction

Because the spatial arrangement and hierarchical connectivity of all cerebral microvessels inside large domains such as the proposed cortical subsection of 27 mm^3 are not easy to acquire experimentally,⁸¹ we generated an anatomically consistent computer model of cortical oxygen exchange. Customized vessel construction algorithms ensured proper topology of the microvessels and blood flow rheology. Different construction principles accounted for structural differences between arterial and venous trees, in contrast to the mesh-like capillary bed. The resulting computer model of the detailed microvascular network is a cyclic graph of logically connected cylindrical segments. Figure 1D gives an overview of the microvasculature construction principles used to generate the microcirculatory system.

Arterioles and Veins

A backbone of visible larger vessels was generated by geometric reconstruction from high resolution cortical images,¹² which matches the morphology of the pial arteries. The conversion of image data into computational meshes is executed with image analysis techniques described elsewhere.⁴⁰ Laminar microvessel density, diameter spectra, and capillary arrangement was used as the geometric basis for our model. In the model, the blood supply to the cortical subsection was provided by a single larger pial artery (inner diameter, $d_i = 150 \text{ }\mu\text{m}$) and drained by only one pial surface vein ($d_i = 180 \text{ }\mu\text{m}$), which compares well to the topological observations of the human brain.¹² The pial network bifurcated into 36 penetrating arterioles ($d_i = 40 \text{ }\mu\text{m} \pm 1 \text{ }\mu\text{m}$). The location of arteriole penetrations centered in circular patterns around 12 draining veins ($d_i = 115 \text{ }\mu\text{m} \pm 5 \text{ }\mu\text{m}$), a spatial pattern originally discovered by Duvernoy. Penetrating arterioles descended from the cortical surface about 2.5 mm deep into cortex reaching down to the gray-white matter intersection.¹²

The backbone of penetrating arterioles was extended by sprouting additional arterial bifurcations into the six cortical layers. The smaller artificially generated segments were added

using constrained constructive optimization (CCO) invented by Schreiner^{31–33,63} with desired segments-per-volume and fractal order.^{32,33} The location of the bifurcation coordinates as well as the hydraulic diameters of the two branching segment were determined, so that each terminal leaf of the emerging vascular tree discharged equal flow, yet whose blood lumen was minimal.³¹ During sequential segment addition, geometric constraints prohibit segment overlap, as well as enforce morphologically consistent bifurcation angles and smooth vessel diameter transitions.^{19,71} Optimal segment position was determined by solving the non-linear constrained optimization problem given in eq. 1. Figure 3 illustrates the geometric optimization, where \vec{x} is the optimal position of the bifurcation fork leading to the minimum tree volume, d_i and l_i are the segment diameters and lengths, ΔP is the pressure drop, and F_i is the volumetric flow rate across segment i . Equality constraints enforce that overall tree dimensions and morphology satisfy the simplified flow equations. Note that this simple flow model is only used for constructing vascular trees, the actual hemodynamic simulations are described later in eq. 2-4. Microvascular tree growth involves random segment addition and the repeated solution of global minimization problems, until the diameters of terminal leafs in the gradually thinning binary tree narrowed to about 12 μm , the physiologic diameter of the pre-capillaries. Segment addition requires repeated solutions of eq. 1 which we implemented with non-linear constrained optimization algorithms developed by our group.^{69,79,80} The resulting network is an acyclic binary graph composed of cylindrical elements, where N is the number of segments belonging to the tree.

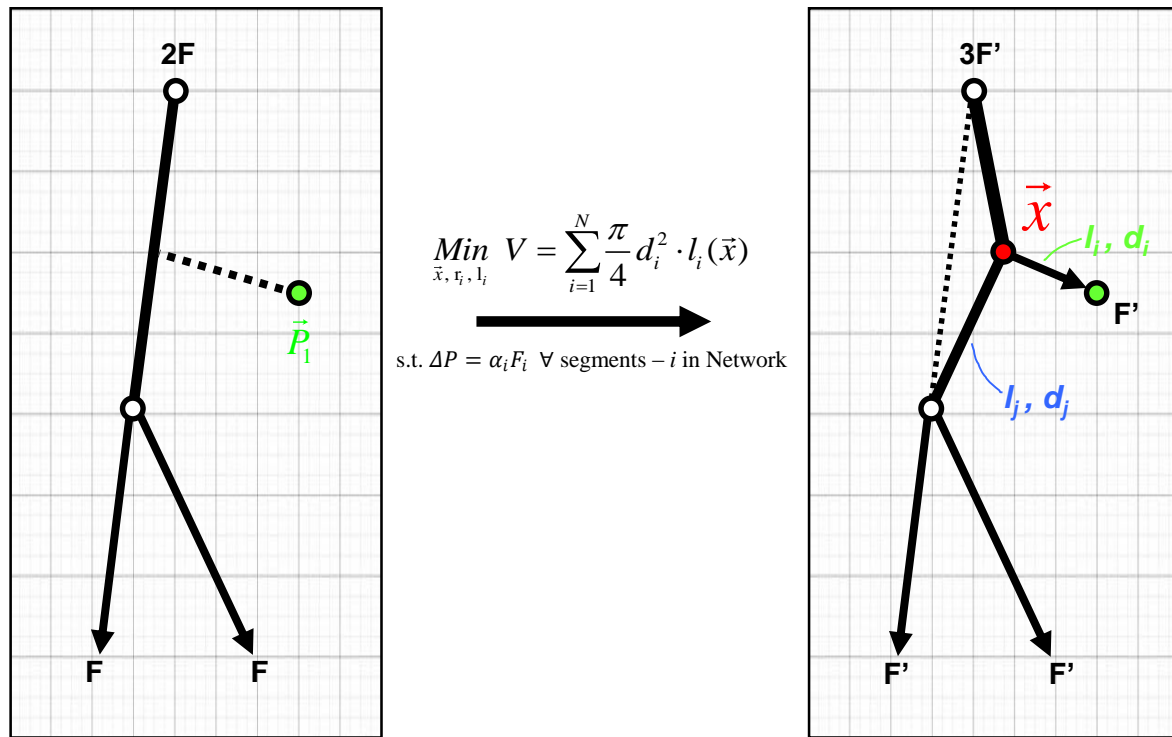


Figure 3 Schematic of a single vessel segment addition using the modified Constructive Growth (CCO) algorithm.⁶³ Segment addition begins with the selection and connection of a point in the domain to the existing tree. The position of this connection point, highlighted in red, is optimized to create a tree with the smallest luminal volume. During the optimization, the diameters d_i and d_j , as well as the lengths l_i and l_j of the two daughter branches, are selected so that all terminal leaves discharge equal blood flow F . N is the number of segments belonging to the tree. The application of these *optimization principles* leads to networks with topological features similar to vascular structures.

Minimum tree volume optimization

$$\min_{\vec{x}, r_i, l_i} V = \sum_{i=1}^N \frac{\pi}{4} d_i^2 \cdot l_i(\vec{x})$$

1

$$\text{s. t. } \Delta P = \alpha_i F_i \quad \forall \text{ segments } - i \text{ in Network}$$

For the venous drainage, tree generation was executed in reverse order until all tributary branches connected to the trunk of the single draining vein, which in turn discharged into the network of pial veins.

Capillaries

The capillary bed is not a tree, but a cyclic graph whose bifurcations and anastomoses form loops.³⁹ Existing algorithms like CCO,^{31,63} angiogenic^{61,62,67} or fractal growth⁵⁴ do not generate mesh-like capillary structures. We created anatomically realistic capillary beds by a novel triangulate-prune-smooth procedure. To build a capillary artifact with desired topology, the domain was meshed by tetrahedral Delaunay triangulation. The dual of the Delaunay mesh, known as a Voronoi mesh, was generated using TetGen.⁶⁵ The edges of the each cell of the Voronoi dual mesh constitute the preliminary capillary network, and overall mesh structure was adjusted so that average Voronoi cell edge length was approximately equal to the desired mean capillary segment length. The implementation details of the novel computational method to synthesize realistic mesh-like capillary networks are given in Supplemental 1.

Unfortunately, three-dimensional Voronoi meshes have trifurcations which occur rarely *in vivo*. To correct this, we removed one arc of each Voronoi cell, while avoiding the creation of dangling segments. This automatic pruning process ensured bifurcations in most junctions as observed in nature. In our final capillary bed, 86% of the 136,037 junctions were bifurcations. The perivascular space close to penetrating arteries exhibits a capillary-depleted zone as observed by Duvernoy¹² and Kasischke.³⁴ We accounted for a capillary-depleted zone in a radial

distance of 50 μm around the larger penetrating arteries. Capillary vessels surrounding the vicinity of penetrating arterioles were removed only in the molecular layer.

The diameters of the preliminary Voronoi edges were smoothed for implementing a hemodynamically and anatomically sound normally distributed diameter spectrum found in real capillary beds,³⁸ as shown in Figure 2A-E. Segments with pressures associated with the watershed between arterial and venous sides were assigned the smallest vessel diameters. An iterative averaging scheme was executed, resulting in smooth diameter spectra in the capillary bed according to the probability density function in Figure 2B. To further procure realistic pressure drops, the degree of tortuosity of the Voronoi tessellation can be altered by deploying Bezier interpolation of the connecting arcs. Structural parameters of the tessellation, such as vessel density and edge length were controlled to ensure accurate morphometrics and realistic hemodynamic resistance. Additional information on Bezier arcs can be found in Supplemental 2.

Furthermore, one study found that the density of microvessels does not match the strong variations in neuronal density,³⁴ other studies did report variations in vascular densities in different cortical layers in both animal models⁷⁶ and humans.³⁸ Microvasculature density is an easily adjustable model construction parameter, and was tuned to the laminar volume fraction patterns observed by Weber⁷⁶ as shown in Figure 2E.

Using the tree and mesh construction principles described above, a closed network connecting penetrating arterioles through the capillary bed to the draining vein emerged. A partial view showing only two venous territories is shown in Figure 4. Arteriole trees accounted for 8,388 segments, venous trees were composed of about 6,804 vessels, and the capillary bed is comprised of 241,697 segments. The entire microvasculature of the cortical subsection, shown in Figure 5, had 36 descending arterioles, 12 draining venules, and a dense capillary bed which altogether totaled more than 256,000 segments.

Hemodynamics

Blood flow was described using established hemodynamic network models.⁵² Flow resistance of each cylindrical segment was approximated by the Poiseuille law as given in eq. 3, where ΔP is pressure drop across a single segment, l is its length, d is the diameter, and α is the apparent blood flow resistance. The continuity equation was applied for each node shown in eq. 2, where u is the steady state flow per area entering or leaving a network node. Due to low Womersley numbers ($W_0 < 0.1$), the pulsatile nature of cortical blood micro-flow can be ignored, and a quasisteady flow assumption is reasonable.¹ Because of the low Reynolds numbers in microcirculation ($Re < 1$), inertia is also neglected in our simplified fluid flow model.¹⁶ The effect of biphasic blood rheology was approximated by the Fahraeus–Lindqvist equation in eq. 4, which predict the apparent viscosity, η_{vitro} , as a function of diameter, d , and hematocrit,⁵² Hd , as shown in Figure 2F. Hematocrit distribution was assigned a constant value ($H_d = 0.45$). Viscosity is weakly dependent on hematocrit, as predicted by the Fahraeus-Lindqvist effect, at the diameter range investigated in this paper.⁵¹ For this reason, Pries' *in vitro* model for diameter dependent viscosity was implemented instead of *in vivo* models which are very sensitive to hematocrit levels.⁵¹ Phase separation and plasma skimming are known to lead to lower hematocrit in microvessels ($d_0 < 100 \mu m$) compared to the systemic hematocrit. We chose for this study to maintain the constant hematocrit, although methods of Plouaboue²¹ can be used to compute hematocrit variations in the blood flow network.

The pressure drop was set to 47 mmHg across the microcirculation from the pial arteriole ($P_{arterial} = 65 \text{ mmHg}$)¹³ to the draining venule ($P_{venous} = 18 \text{ mmHg}$).⁸² Capillaries at the boundary of our large cortical subsection were connected to similar size vessels at another boundary in the same cortical layer, thus implementing periodic boundary conditions. Due to the size of the computational domain, penetrating arteries and draining veins did not leave the subsection, thus not requiring special boundary closures necessary in thin computational models.

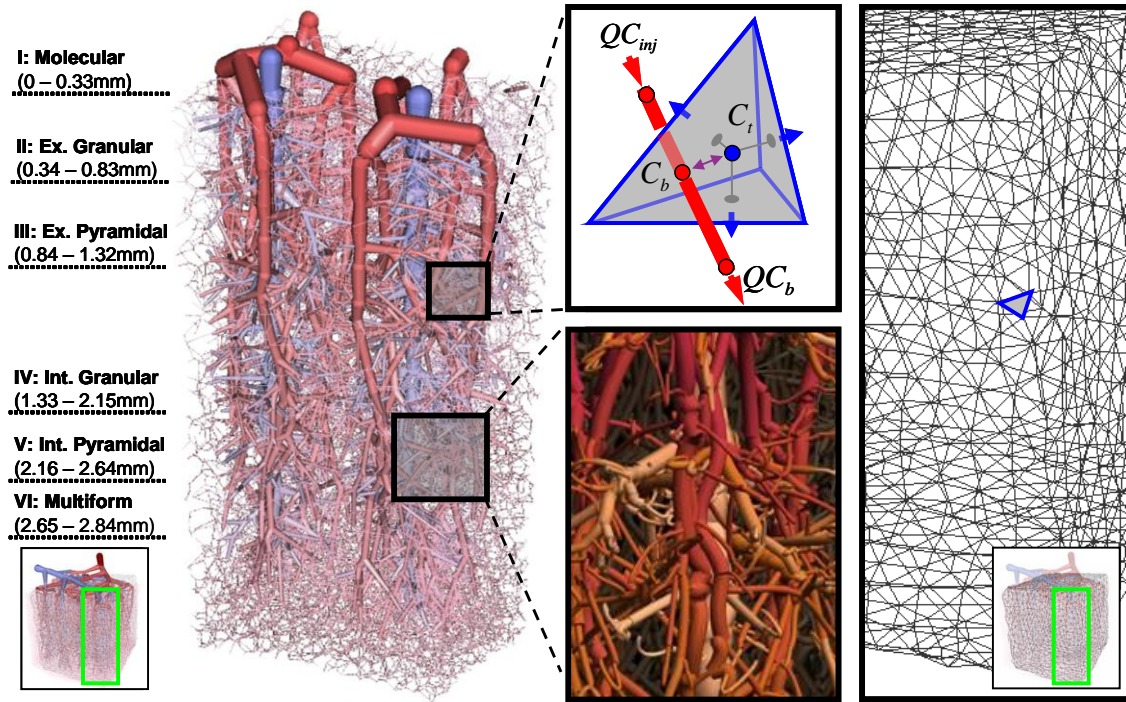


Figure 4 Partial view of the territories drained by two penetrating venules with their six descending arterioles as well as the capillary bed, cut out from the 27 mm^3 subsection of the secondary cortex for better visibility. The six cortical layers of the extravascular space are occupied by brain tissue. The extravascular space is modeled as a porous medium into which oxygen is transported from the blood and metabolized by brain cells. (a) The nodal balance envelope encompasses the sum of half of the cylindrical volumes connected to it (red semi-cylinders). Blood convects oxygen with concentration C_{in} into a nodal volume and out with concentration C_b (red arrows) with flow Q . Oxygen exchange (purple arrow) occurs between the blood volume (node volume at C_b) and the extravascular tissue cell (tetrahedral cell at C_t). Oxygen can also diffuse freely inside the extravascular space (blue arrows). Oxygen diffusion and metabolism is solved by a finite volume method using an unstructured tetrahedral mesh. (b) Close up of microcirculatory pre-capillaries arterioles feeding the capillary bed, the site of oxygen mass exchange. (c). Detail of the continuous extravascular space composed of an unstructured tetrahedral mesh.

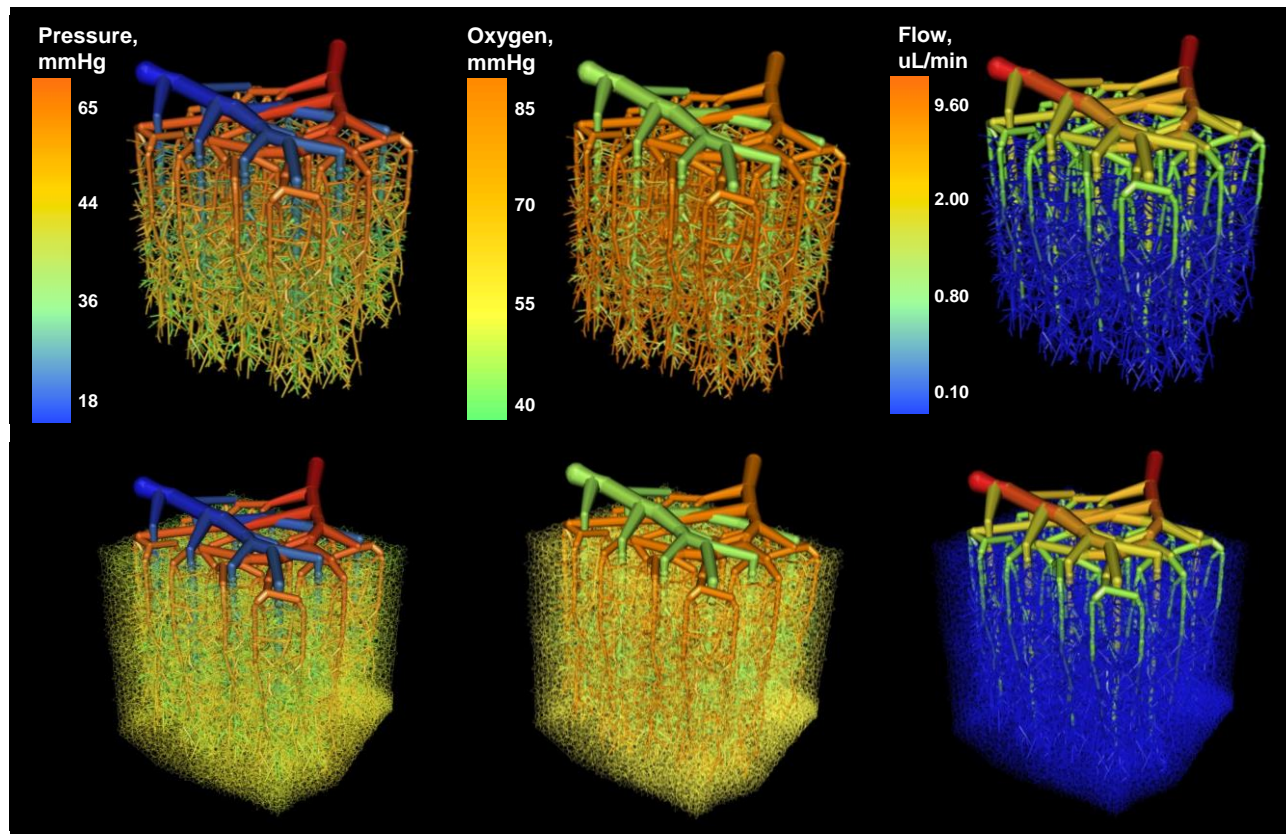


Figure 5 Visualization of a relatively large 27 mm^3 subsection of the secondary cortex with computed steady state blood pressure, volumetric flow rate, and oxygen profiles projected onto the vessel architecture. Top row—larger vessels (capillary bed without showing small vessels, $d < 10 \mu\text{m}$). Bottom row—all vessels, including capillary bed, are shown. (a) Blood pressure, (b) Oxygen tension, and (c) Volumetric blood flow value profiles.

The simultaneous solution of the discretized set of linear algebraic equations with Duff's MA48 algorithm¹⁰ gave the pressure distribution in the nodes; the blood flow velocities were determined with eq. 2 for all segments. In this first paper, we chose not to incorporate the phase separation effect in order to keep the blood flow model simple. Models for the inclusion of phase separation effects are established,²¹ but still await experimental validation in the human cortex.

Blood Flow

$$\vec{\nabla} \cdot \vec{u} = 0 \quad 2$$

$$u = \frac{1}{\alpha} \Delta P, \text{ with } \alpha = \frac{128\eta_{vitro}l}{\pi d^4} \quad 3$$

$$\eta = 1 + (\eta_{0.45} - 1) \cdot \frac{(1 - Hd)^\gamma - 1}{(1 - 0.45)^\gamma - 1}$$

$$\text{with } \eta_{0.45} = 220e^{-1.3d} + 3.2 - 2.44e^{-0.06d^{0.645}} \quad 4$$

$$\gamma = (0.8 + e^{-0.075d})(-1 + \beta) + \beta$$

$$\beta = \frac{1}{1 + 10^{-11} \cdot d^{12}}$$

Oxygen Transport

$$V_b \frac{dC_b}{dt} = \vec{u} \vec{\nabla} C_b - S_b U \Delta C_{b-t}, \text{ with } U = \frac{K_w}{w} \quad 5$$

$$V_t^* \frac{dC_t}{dt} = \left[\sum_{i=1}^M (S_{b,i} U \Delta C_{b,i-t}) \right] - V_t^* C_t CMRO + \vec{\nabla} \cdot D \vec{\nabla} C_t \quad 6$$

Oxygen Perfusion from the Cerebral Microvasculature to the Cortical Tissue

For simulating oxygen exchange between blood and surrounding brain cells with tractable problem size, we developed a novel dual mesh technique using two computational domains:

(i) a vasculature network of cylindrical segments to account for arterioles, capillaries and

venules described in the previous section and (ii) a volumetric brain mesh surrounding the vascular network to represent the cell matrix.

The vascular network contained about 256,000 segments. Blood oxygen tension was assigned to the node of each vascular segment; this choice produced a favorable staggering of the oxygen field in relation to the flow field which is computed on the edges. Each vascular network node is located in exactly one tetrahedral cell. However, a tetrahedral cell may contain multiple vascular nodes. The spatial relation between a vascular network node with oxygen tension, C_b , connecting two cylindrical vascular segments with their associated tetrahedral tissue cell with oxygen concentration, C_t , is depicted in Figure 4A. The species conservation for each network node was balanced with eq. 5, where C_b is the nodal oxygen concentration. V_b is the blood volume associated with each node, which is equal to half of the sum of the cylindrical segment volumes connected to the node, C_b . S_b is the surface area of the semi-cylindrical segments connected to node, C_b . The overall mass transfer coefficient, U , in eq. 5 is a function of wall thickness, w , and the oxygen permeability of epithelial tissue K_w with values given in Table II. Oxygen mass exchange is driven by the concentration difference between free oxygen in blood and oxygen concentration in the brain tissue, ΔC_{b-t} . All molar oxygen concentrations were reported as partial pressures, assuming a temperature of 37°C, pH = 7.4, and the empirically derived gas solubility constant of 0.003 mL O₂/100 mL/mmHg₂. The vascular network was co-registered in the same spatial domain with an unstructured tetrahedral brain mesh as seen in Figure 4. The volumetric mesh representing the extravascular space was modeled as a single continuum with extracellular and intracellular space lumped together. The brain mesh was grouped into six cortical layers with the following depths scaled from imaging data³⁸ to the depth of 2.5 mm: 0–0.33 mm (I: molecular), 0.33–0.83 mm (II: external granular), 0.83–1.32 mm (III: external pyramidal), 1.32–1.68 mm (IV: internal granular), 1.68–2.02 mm (V: internal pyramidal), and 2.02–2.50 mm (VI, multiform). The finest mesh with 600,000 tetrahedral

elements had an average edge length of 34 μm . We computed the oxygen concentration for each tissue cell, C_t , by solving the oxygen conservation balance in eq. 6. Here V_t is the volume of extravascular space, which is equal to the tetrahedral volume reduced by the outer lumen of all blood network nodes contained in the cell. Oxygen transfers from the blood into the tissue as a function of the concentration, ΔC_{b-t} . Since each tetrahedral tissue cell may contain multiple vascular network nodes, eq. 6 sums the mass transfer into the tissue cell from M vascular nodes. Oxygen is also consumed at a cellular metabolic rate. The metabolic oxygen demand for normal brain activity⁴⁵ expressed as the cerebral metabolic rate of oxygen consumption, was set to $\text{CMRO} = 8.2 \cdot 10^{-24} \text{cm}^3 \text{O}_2 / \text{cm}^3 / \text{s}$. Oxygen is further free to diffuse in the extravascular space, $\vec{\nabla} \cdot D \vec{\nabla} C_t$ with diffusion coefficient,⁴⁵ $D = 1.8 \cdot 10^{-25} \text{cm}^2 / \text{s}$. All parameters and constants are listed in Table II.

The boundary conditions for the oxygen exchange simulations include a constant pial oxygen partial pressure of, $C_{in} = 85 \text{ mmHg}$. For the gray-white matter interface we assumed zero oxygen exchange. All boundaries of the large cortical subsection were assigned symmetric boundary conditions as shown in eq. 6. Table III summarizes all types of boundary conditions and values for the vascular network and tissue domains.

Oxygen exchange between blood and tissue was solved simultaneously after full discretization of eq. 5-6 over the two domain meshes using finite volume techniques developed by our group.³⁹ Repeated simulations with increasingly fine meshes, ranging from 140,000 to 600,000 volumetric elements, established mesh-independence at 400,000 elements as shown in Figure 6A. The steady state spatial distribution of oxygen in the tissue (400,000 equations) and the vascular network (256,000 equations) was solved simultaneously (656,000 equations) with an iterative SOR²⁹ method. The simulation solved on a 2.8 GHz Intel Core 2 Duo processor in less than eight CPU minutes.

Table II Morphometrics of the computer network compared to prior work.

Parameter	This work	Literature	Animal	Ref.
Vessel Density	9,487/ mm ³	7,473–14,069/mm ³	Human	Lauwers ³⁸
		4,991–9,140/mm ³	Primate	Risser ⁵⁶
Surface Area/Volume	13.60 mm ² / mm ³	10.19–12.85 mm ² / mm ³	Human	Lauwers ³⁸
		4.04–5.84 mm ² / mm ³	Marmoset	Risser ⁵⁷
		13.3 ± 3.2 mm ² / mm ³	Cat	Pawlik ⁵⁰
		5.19–7.24 mm ² / mm ³	Rat	Risser ⁵⁷
Capillary Diameters	6.46 ± 2.7 µm	6.66 ± 1.70 µm	Human	Lauwers ³⁸
		7–9 µm	Human	Duvernoy ¹²
		5.91 ± 1.30	Human	Cassot ⁵
		5.0 µm	Cat	Zweifach ⁸²
Mean Capillary Length	56.16 µm	52.95 ± 49.75 µm	Human	Lauwers ³⁸
		57.37 ± 50.98 µm	Human	Lorthois ⁴⁴
Vascular Fraction	2.49%	2.43–3.02%	Human	Lauwers ³⁸
		3.19%	Marmoset	Risser ⁵⁶
		2.52%	Rat	Reichold ⁵⁴
Cortical Perfusion	64 mL/100 g/min	51–65 mL/100 g/min	Human	Rostrup ⁵⁸
		60 mL/100 g/min	Rat	Reichold ⁵⁴
Pial Art. Blood Velocity	14 µm /s	~14 µm /s	Cat	Lipowsky ⁴¹
		9.2 ± 4.8 mm/s	Rat	Nishimura ⁴⁸
Arterial O ₂ Tension	85 mmHg	82.4 ± 3.5 mmHg	Rat	Vovenko ⁷⁴
		94 ± 18 mmHg	Mouse	Kasischke ³⁴
Capillary O ₂ Tension	50 mmHg	50–60 mmHg	Rat	Vovenko ⁷⁴
		28 ± 11 mmHg	Mouse	Kasischke ³⁴
Pressure Drop	47 mmHg	52–78 mmHg	Human	Espagno ¹³
		50 mmHg	Cat	Guibert ²⁰
		70–35 mmHg	Cat	Zweifach ⁸²
Transit Time	0.41 s	0.61 s	Human	Sorenson ⁶⁶
		0.51–0.75 s	Human	Yang ⁷⁷
		1.1 ± 0.4 s	Human	Gjedde ¹⁷
CMRO	8.2×10–4cm ³ O ₂ /cm ³ /s	8.2×10–4cm ³ O ₂ /cm ³ /s	Human	Mintun ⁴⁵
Tissue Diffusivity (<i>D</i>)	1.8×10–5cm ² /s	1.8×10–5cm ² /s	Human	Mintun ⁴⁵
Permeability (<i>K_w</i>)	5×10–8uL/mm/s/mmHg	5×10–8uL/mm/s/mmHg	Rat	Vovenko ⁷³
Cap. Wall Thickness (<i>w</i>)	1 µm	1 µm	Human	Nolte ⁴⁹
Art. Wall Thickness (<i>w</i>)	2–10 µm	2–10 µm	Rat	Rakusan ⁵³
Ven. Wall Thickness (<i>w</i>)	0.5–1.5 µm	0.5–1.5 µm	Rabbit	Rhodin ⁵⁵
Arterial Inlet Pressure	65	60	Cat	Lipowsky ⁴¹
Venous Outlet Pressure	18	25	Cat	Lipowsky ⁴¹

Table III Boundary Conditions

Physiological description	Boundary type	Value
Pial artery inlet (P_{arterial}), $d_i = 38 \mu\text{m}$	Dirichlet	65 mmHg
Pial vein outlet (P_{venule}), $d_i = 100 \mu\text{m}$	Dirichlet	18 mmHg
Oxygen tension at pial inlet	Neumann	80 mmHg/s
Capillary bed domain edge (A)	Periodic	-
Capillary bed domain edge (B)	Neumann	Symmetry (No Flux)
Cortical tissue domain edge	Neumann	Symmetry (No Flux)

Results

Morphometrics

The statistics of Figure 2A-E summarize the morphological validation of the cortical microvasculature in terms of vessel density, diameter, and length.³⁸ The mean capillary diameter of $6.46 \pm 2.7 \mu\text{m}$ agrees well with reported values³⁸ of $6.47 \mu\text{m}$, as shown in Figure 2C. The mean distance between capillaries reported in Figure 2D is $16\text{--}46 \mu\text{m}$ compared to $24\text{--}42 \mu\text{m}$ reported in previous work.^{26,34} 73% of the tissue elements are no further than $40 \mu\text{m}$ away from the nearest blood vessel. Laminar volume fractions in Figure 2E for the cortical subsection microvasculature match vascular topology studies by Weber, however the human trends are somewhat below those found in the macaque cortex.⁷⁶ Table II lists a vascular density of 9,487 vessels/ mm^3 , compared to 7,473–14,069 vessels/ mm^3 in prior human *ex vivo* measurements.³⁸ Segment length per unit volume was $601 \text{ mm}/\text{mm}^3$, which lies within two standard deviations above an empirical *ex vivo* measurement in the human cortex.³⁸ The volume ratio of vessel lumen to surrounding extravascular space was 2.49%, comparing well to the range of 2.4–3.2% reported in other microvasculature studies shown in Table II. The capillary volume density is 1.43%; which compared well to the 1.0–1.5% capillary volume fraction reported in the literature.^{38,76} The lumen ratios between the arteriole, venous and capillary compartments were 29.4, 10.8 and 59.7%, which matches measurements in microvascular⁴ and whole brain studies.^{11,28}

Flow and Oxygen Exchange in the Entire Subsection

The simulation results for blood flow and oxygen tension in a large cortical section are summarized in Figure 5. For clarity, the top row shows only the arterial and venous tree without capillary bed, the lower depicts the same results including the capillary bed. The blood flow simulations, the pial arterial inlet pressure was set to 65 mmHg, the pial venous drain had 18 mmHg.

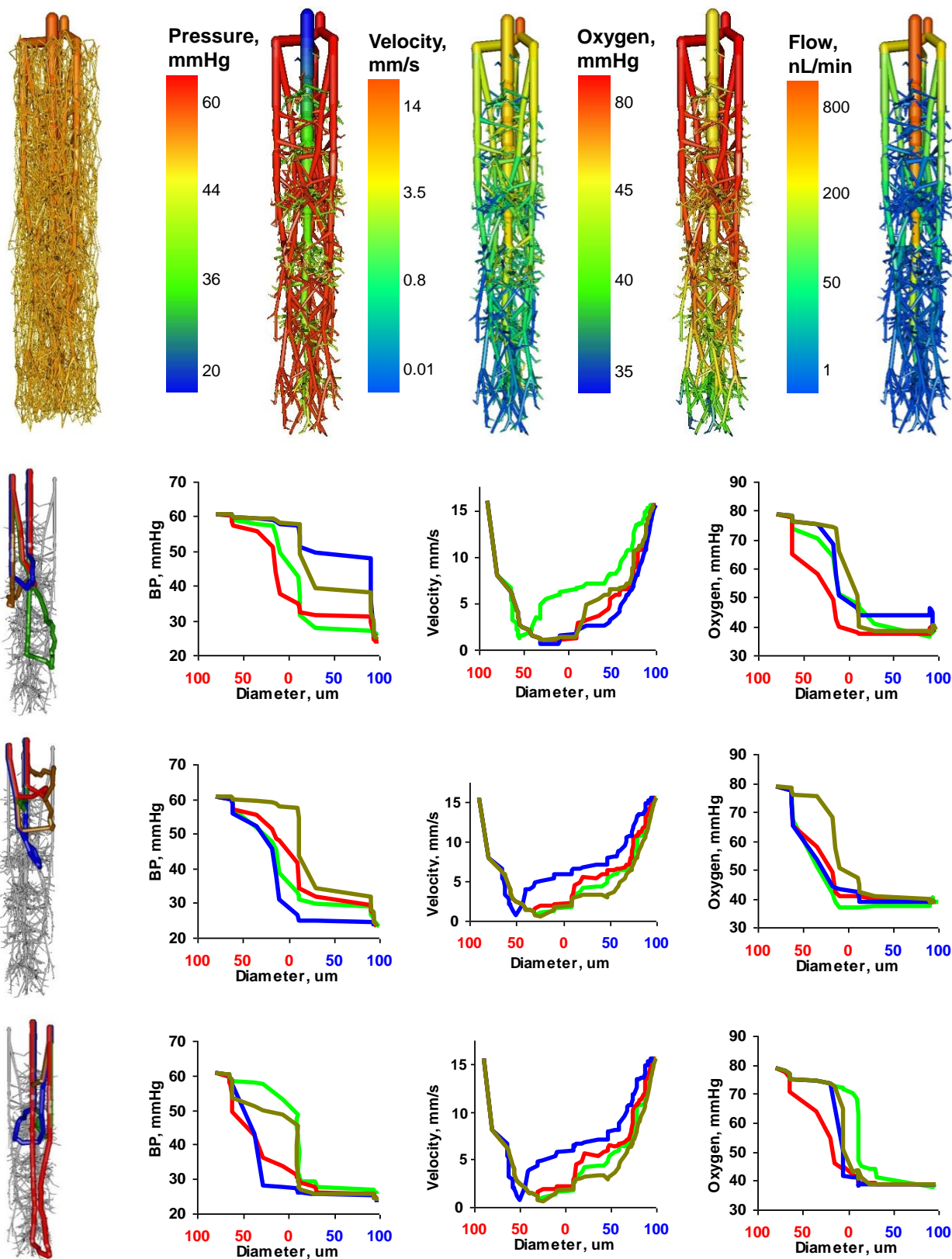


Figure 6 Detailed study of hemodynamics of a typical vascular territory of a single draining vein with its associated arterioles and capillaries. (a) Blood pressure distribution. (b) Blood flow velocity. (c) Blood oxygen tension. (d) Volumetric blood flow rate. Analysis of twelve distinct paths a single red blood cell may take when traveling from a feeding descending arteriole to a nearby draining venule. Panels 1–3 each depict four typical sample paths chosen randomly, colored blue, green, yellow, and red. In total there are >236,000 number of paths for a single territory.

Currently the experimental evidence for pial arterial pressure in humans is scarce. Espagno¹³ performed blood pressure measurement on cortical arteries of several dozen patients prior to removing cortical tumors. Averaged pressure measurements in “submillimeter” pial arteries, without precisely specifying the diameters vary over a range. The blood pressure throughout the entire microvasculature subsection of the cortex are shown in Figure 5A. A comparison of pressure drops to three models by other researchers is shown in Figure 6B. The scarcity in the experimental evidence about pial blood pressures is reflected by the wide variations among different models. However, the overall trends seem to be similar, except for choices in boundary conditions. The differences between predictions for microcirculatory models are expected to align better as soon as reliable pressure measurements become available. The volumetric blood flow rate is depicted in Figure 5C. The oxygen tension in the microvasculature of the entire domain gradually drops from 85 mmHg in the pial artery down to 40 mmHg in pial vein as depicted in Figure 5B. The redirected oxygen extraction compares well to cortical measurements.⁷³ To better analyze the flow and oxygen tension in detail, we turn next to the territory of a single draining vein in the interior of the subsection and its tributary arterioles.

Microvascular Blood Pressure

Hemodynamic simulations for a pressure drop between penetrating arterioles and draining vein of 40 mmHg are depicted in Figure 7A. Pressure drops in the territory were computed as 8.2 ± 2.1 mmHg across the arteriole tree, 20 ± 1.3 mmHg across the capillary bed, and 9.3 ± 1.6 mmHg across the venous side. Accordingly, the capillaries offer the largest flow resistance.

Blood Flow and Velocity Predictions

Blood flow through a single draining venule was predicted as 800 nL/min as shown in Figure 7D; this number equals a perfusion of 68 mL/100 g/min. This simulation blood perfusion result agrees with experimental values of 50–70 mL/100 g/min found in the open literature.⁵⁸ Blood velocity can be established as 15 $\mu\text{m/s}$ at the arteriole inlets, 0.1 $\mu\text{m/s}$ in

capillary vessels and $14 \mu\text{m/s}$ at the venous outlet as shown Figure 7B. These predictions compare well to prior velocimetry studies which measured arteriole blood velocity at $14 \mu\text{m/s}$.⁴¹

Hemodynamic State Changes Along Multiple Erythrocyte Paths

We further investigated hemodynamic state properties along multiple paths of red blood cells traveling from the penetrating arterioles to the draining vein. Alternate pathways commenced at pial surfaces then descend into the penetrating arterioles, traversed the capillary labyrinth, and finally terminated at the draining vein. At each junction, a random choice among alternative downstream paths was made, and the hemodynamic states—blood pressure, velocity, and oxygen content—along the itinerary were recorded with results visualized in Figure 7. A total of more than 236,000 different paths were identified connecting a penetrating arteriole to the draining vein. Twelve typical samples were selected as illustrated in panels 1–3 of Figure 7. Path lengths varied from 1.78 to 6.81 mm. Figure 7A demonstrates that the blood pressure decreases monotonically in all paths; yet the profiles are not identical. Figure 7B depicts that the blood flow velocity is highest in the penetrating arterioles, $v_a = 15 \mu\text{m/s}$, at a minimum in the capillaries, $v_c \sim 100 \text{ lm/s}$, and again rises in the draining vein, $v_v = 14 \mu\text{m/s}$, which has been qualitatively observed in previous studies.⁷⁸ Blood pressure dropped about 40 mmHg from the penetrating arteriole to the corresponding vein.

Simulated Transit Times

We determined dynamic trajectories of contrast agent infused into the cortical microcirculation to quantitatively analyze transit time behavior similar to a clinical angiography exam (figures not shown) with eq. 7. The mean transit time between the inlet penetrating arteriole ($d_i = 39 \mu\text{m}$) and the draining vein ($d_v = 120 \mu\text{m}$) was found to be, $s = 0.4 \text{ s}$. This value reported in Table II falls within the range of human microvasculature transit times.^{17, 66, 77}

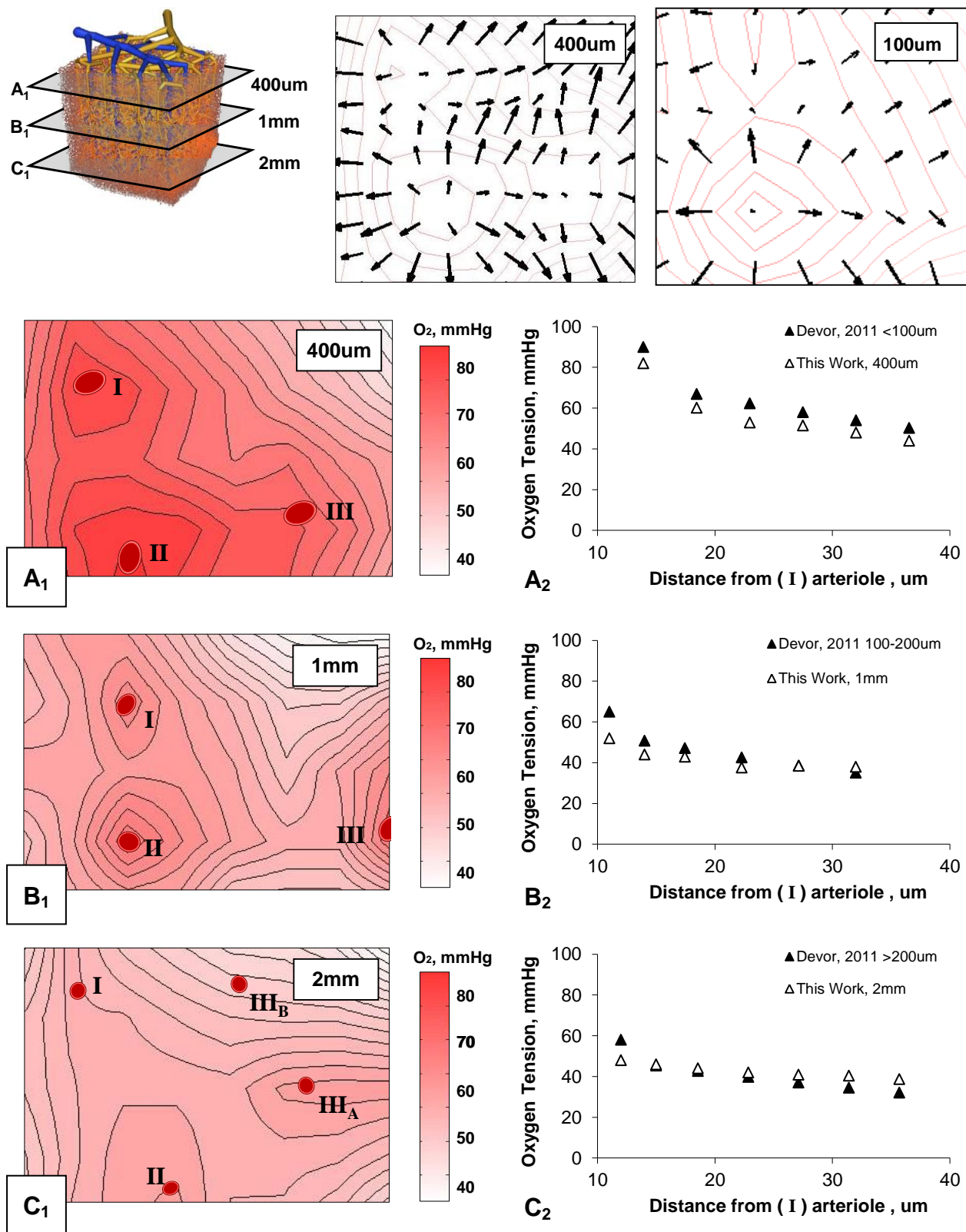


Figure 7 Radial oxygen gradient as a function of cortical depth 400 μm (A), 1 mm (B), and 2 mm (C) below the cortical surface. Top row also shows the oxygen tension gradient in the molecular layer (a) as a vector field at 400 μm and 1 mm. In-plane radial oxygen gradients of three arterials (I–III) are displayed in the left hand column (Panels A1, B1, C1). The right hand column shows in-plane oxygen tension as a function of distance to arterioles. The simulated oxygen gradient agrees with trends observed *in vivo* in the rat cortex in panels A2 to C2.

Dynamic Contrast Agent Dilution

$$V \frac{dC_a}{dt} = \vec{u} \vec{\nabla} C_a + \vec{\nabla} \cdot D_a \vec{\nabla} C_a \quad 7$$

Axial Oxygen Gradients

Axial gradients across microcirculatory paths inside the territory of a single draining vein are depicted in Figure 7C. The computations show the gradual drop in arteriole oxygen tension from the penetrating arteriole of 80 mmHg to 40 mmHg in the draining vein. These numbers are similar to trends in oxygen tension found for the rodent cortex.⁷³ There is a wide spectrum of path lengths through the microcirculation. We also found that longer paths tend to leave the capillary bed with lower oxygen tension than shorter paths. The venous mixing effect resulting from capillary inflow with varying oxygen tension was predicted by the network model and has been well established experimentally.⁷⁴ In our model the arterioles contributed 20% of the total oxygen extraction, while the bulk occurred in the capillary bed. These fractions of oxygen extraction match the 20% reported by Vovenko and Popel.^{64, 73}

Radial Oxygen Perfusion Profiles

Radial oxygen perfusion profiles in the tissue were assessed as a function of radial distance to the nearest blood vessel. As shown in Figure 7, a single penetrating arteriole marked (I) as was selected as a vessel of interest. Its perivascular oxygen tension field was traced as it descended through the cortical layers. Radial oxygen gradients were captured for this penetrating arteriole in the molecular, external pyramidal and internal pyramidal layers. To better assess the evolution of oxygen tension profiles, laminar tissue slices of the microvascular subsection were created and contour maps of the oxygen tension field were generated. We also produced a display of the tissue oxygen gradient fields (vector field depicted by arrows) for the 400 μm and 1 mm laminae of the cortical tissue shown in the top row of Figure 7. The radial

oxygen gradients around the penetrating arteriole were higher near the cortical surface than in deeper regions.

Radial oxygen tension in the molecular layer ranged from 80 mmHg at a distance of 10 μm , to 45 mmHg at 50 μm distance. The oxygen tensions in the external and internal pyramidal layers were \sim 50 mmHg at 10 μm , to 40 mmHg at 50 μm of distance as shown in panels A, B, and C of Figure 7. The computed profiles agreed with the trends of laminar oxygen gradients obtained in the rodent cortex.^{9,14} These oxygen gradients seem to be a result of the capillary-depleted regions adjacent to larger arterioles. The high oxygen tension in the perivascular space make it plausible why there is no need for capillaries close to arterioles.

We also simulated oxygen tension in regions embedded in the dense capillary mesh, but situated further away from larger blood vessels. Our simulations for regions without larger vessels show shallow oxygen profiles, completely flattening about 30 μm away from the nearest capillary. We also investigated whether intracapillary gradients became steeper with higher oxygen demand. To emulate this effect, we adjusted the parameters CMRO within physiologic ranges. The parameter sensitivity studies as a function of CMRO revealed that the level of oxygen tension dropped with increasing metabolic demand (Results not shown).

Discussion

We presented a computer model to predict oxygen exchange between the microvasculature and brain cells in a relatively large cortical subsection. We developed a novel dual mesh technique to overcome problem size limitations that would be required in simulations with a single computational mesh smoothly connecting microvessels and brain cells at the length scale of individual capillaries. The use of two distinct coarse overlapping meshes avoided the need for a contiguous mesh sharply separating both compartments. The numerical quality of the method was established with mesh independence studies and validation against the analytical approaches.

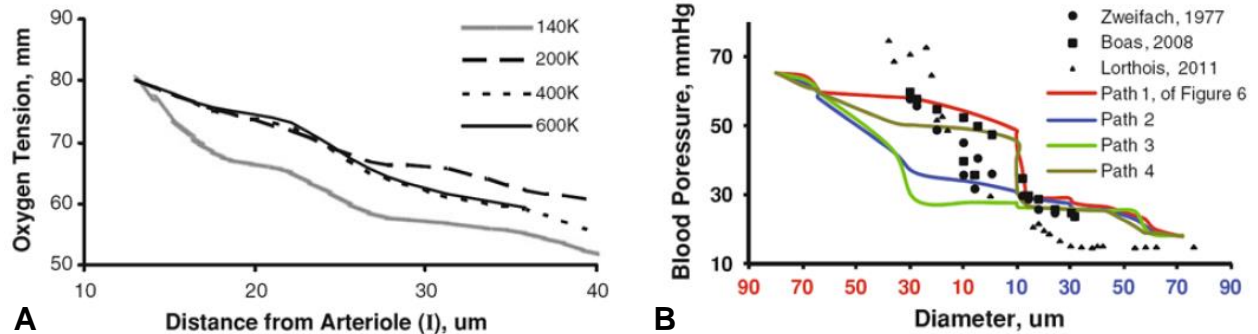


Figure 8 Mesh independence study and blood pressure validation. (A) Model prediction of extravascular oxygen gradient in the capillary-depleted cylinder surrounding a descending arteriole (I)—discussed in detail in Figure 6—as a function of mesh density. Predicted oxygen tension stabilized after increasing the number of tetrahedral elements from 400,000 to 600,000. All results are reported for the 400,000 element mesh. (B) Microvasculature pressure gradients of multiple paths (paths 1–4 introduced in Figure 6) from a penetrating arteriole to its corresponding draining venule of our subsection of the secondary cortex, compared to point measurements made to animal and computational models. The chosen pressure boundary conditions or pial arterioles ($P_{\text{arterial}} = 65 \text{ mmHg}$) to the draining venule ($P_{\text{venous}} = 18 \text{ mmHg}$) govern the pressure drop of the model. Trends compares well against empirical results⁸² and models4 with similar boundary conditions.

Our novel method applied to a relatively large cortical subsection captured every single blood vessel including all capillaries, yet kept the problem size for steady blood flow as well as oxygen exchange between blood and tissue tractable. We also introduced a novel method to build pial and cortical arterial as well as venous trees by combining real image data with a modified CCO technique to synthesize blood vessels below the image resolution.

We further presented a new method to create an anastomosed capillary bed based on Voronoi tessellation. We described the step-by-step construction mechanism as well as the mathematical operations to attain desirable properties such as segment length, degree of tortuosity and smooth diameter transitions from pre-capillaries to post-capillary venules. The capillary bed algorithm offers consistent closure to microcirculation models with a physiological basis significantly advancing prior models limited to arterial trees, or merely using mathematical arguments to “close” the system equations without anatomically consistent representation of the capillary bed.

Our morphologically accurate, physiologically consistent, multi-scale computer network model of the cortical microcirculation encompasses the spatial arrangement of all cerebral vessels ranging from the pial arterioles and venules down to the level of individual capillaries as well as the surrounding extravascular space. Distribution of vessel blood pressure, flow, velocity and oxygen tension in both vessels and cerebral tissue were predicted in three dimensional spatial coordinates. A detailed comparison with prior experiments as well as the extensive compilation of earlier models demonstrates that our large models matched known literature values for blood flow, blood flow velocities, cerebral blood flow per volume and trends of pressure distribution. The large portion of blood flow resistance predicted for the microvascular bed implicate capillaries as an effective location for blood flow control, and in effect also an ideal actuator site to regulate oxygen supply. Small changes in capillary lumen or boundary layer resistance⁴¹ would very sensitively impact flow distribution and indirectly control oxygen exchange.

Perivascular oxygen gradients were found to be flatter in deeper pyramidal layers compared to the molecular layer closer to the cortical surface. Our model also quantified the gradual oxygen extraction along penetrating arterioles; a trend observed previously in the cortex of animals. The predicted three-dimensional oxygen distribution also showed larger oxygen gradients around arterioles, whereas areas distant of larger blood vessels exhibited flatter oxygen gradients. Also, the oxygen tension around capillaries appears to be almost uniform. It seems plausible that the random arrangement of the cortical microvasculature is capable of ensuring adequate oxygen levels for neurons irrespective of their location in the cortex.

The flatter profiles in deeper cortical layers should not be mistaken for lacking oxygen gradients between the extra- and intracellular compartments. The current tissue model does not distinguish between the extra and intracellular spaces. Consequently, the mass transfer from the extracellular compartment through the cell membrane to the site of mitochondrial metabolism of oxygen is currently not resolved in our computations. Instead, a simplified first order cellular metabolism rate has been assigned to the lumped extravascular compartment. Intracellular oxygen gradients and oxygen tension in the mitochondria have not been addressed in this study.

Our simulations are carried on such a large computational domain without cutting large vessels so that the resolution of the boundary interface for the capillary vessels and the tissue elements does not impact the results in the interior. Our large scale approach also addresses the call for a new methodological framework to reduce the number of boundary nodes. Our *in silico* subsection of the brain has a very small number of boundary nodes, roughly 3.0% for the vascular network and only 2.2% for the tissue mesh. A large model with only a small fraction of boundary nodes frees the analysis from the burden of engineering specific boundary conditions for each vessel group; a process which runs the risk of importing undue boundary effects into the computational domain.

Future work should include more complete cellular metabolic mechanisms involving ATP production, glucose, CO₂ transport, and pH calculation. A two phase model for the bound and free oxygen could be incorporated by considering the relationship between oxygen concentration and oxygen tension as described by the Hill equation.²³ Moreover, the formation and dissociation of carboxylic acid is a major factor in controlling pH levels, which affects the oxygen binding kinetics of hemoglobin. Future models should also easily incorporate variable hematocrit. Pulsatile blood flow through compliant blood vessels would allow for open and closed loop control of cerebral blood flow, and more interestingly oxygen dynamics to better elucidate BOLD signals in functional MRI. Detailed dynamics of vasodilation and vasoconstriction in cerebral autoregulation have also not yet been addressed in this work. Regional activation of specific cortical layers requires closed loop dynamics of autoregulatory control, possibly through oxygen-chemoreceptive neurons which release biochemical signaling agents such as nitric oxide or catecholamine.⁴⁶

Our model elucidates the role of the three-dimensional spatial arrangement of the microcirculation on cortical oxygen supply. Extensive literature validation confirmed the model's ability to match hemodynamic and oxygen tension trends within experimental tolerances and uncertainty. Using the proposed dual mesh techniques, it is conceivable that a biological simulation encompassing each brain cell will become tractable in the near future.

Supplemental 1

Generation of mesh-like capillary bed

We invented a novel computational method to synthesize mesh-like capillary networks. A mesh-like capillary bed connected to the arterial and venous trees is essential for the anatomically consistent closure of hemodynamic simulations with the following key properties: (i) even random spacing of desired average segment length (ii) connection to arteriole and venule terminals (iii) adjustable degree of tortuosity, and (iv) smooth diameter transitions from the pre-capillaries to post-capillary venules. To the best of our knowledge, this algorithm for capillary synthesis has never been proposed in the literature.

The methodology encompasses a six step procedure illustrated Figure 9A-E. In the first step, the computational domain between the terminal nodes of the arterial (a_1 , a_2) and venous (v_1) trees is evenly divided by Delaunay triangulation.⁸ The Delaunay mesh creates an even partition of the intravascular space. This partition is shown in Figure 9A by triangles for clarity. The new Delaunay nodes are more densely spaced than the arterial and venous terminals (a_1 , a_2 , v_1). The number of Delaunay nodes controls the desired average capillary segment length in the emerging capillary bed. It is tempting to use the Delaunay edges directly as capillary segments. However, the branching factor of three-dimensional Delaunay meshes is not physiological, easily exceeding 50 edges per node in complex brain geometries, while real capillary meshes have only bifurcations (branching factor of two).

Therefore, we construct the dual mesh, known as a Voronoi tessellation,⁷² as depicted in Figure 9B. The Voronoi cells have branching factors of two in two dimensions, and three in for three dimensions. To provide closure, each arterial terminal is connected to the closest capillary node. Similarly, each terminal node of the venous tree is linked to the Voronoi mesh without allowing a venous and an arterial terminal to connect to the same capillary node. In effect, the arterial and the venous trees are linked through the capillary bed creating a closed network

structure without dangling segments. The crude Voronoi capillary mesh depicted in Figure 9C requires three more refinement steps for better physiological match with real capillary beds.

In every capillary node with more than three segment connections, one superfluous segment can be deleted. This process we term pruning is required only three dimensional Voronoi meshes (not shown). We choose to eliminate the shortest edge, whose removal does not leave another node connected to the deleted edge dangling. We refrained from pruning Voronoi trifurcations in which no edge can be removed without causing dangling capillary nodes.

Several researchers have pointed out the significance of the tortuosity in hemodynamic simulations.¹⁸ Optionally, we can control tortuosity of capillary segments by Bezier curve interpolation, as depicted in Figure 9D with detailed mathematical description given in Supplemental 2. The pruned, tortuous capillary bed still requires the reasonable diameters for each segment. A simple choice is constant diameters for all segments, but has the disadvantage of sharp transitions from the arteriole tree to the capillary bed, and from the capillary bed to the venous tree. We propose to enforce smooth diameter transitions with slight tapering coming from the arteriole side and slow diameter increases towards the venous side as follows: We perform blood flow simulations as in eq. 2-3 through the network as a function of segment length and diameter. The mean pressure, P , is defined as the arithmetic mean of all capillary node pressures; σ_F is its standard deviation. All segments within the pressure range, $P \pm 2\sigma_F$, were assigned the minimum diameter, $D_{min} = 3$ mm. Pre- and post-capillary segments connecting to arteriole and venule terminals were assigned a diameter commensurate with their parent terminal. For all segments between the terminals and the minimum diameter group, we computed their diameters by iteratively executing the averaging scheme given in eq. 8. This method for ensuring smooth diameter transitions is similar to physiological regularization techniques. Our level-set type approach gives rise to smooth diameter transitions, which

monotonically decreases from inlet pre-capillary vessels to the smallest capillaries, then increase to the post-capillary veins.

Capillary diameter smoothing

$$d = \sum_{j=1}^N \frac{d_{i,j}}{N} \quad 8$$

where $d_{i,j}$ is the diameter of segment j connected to segment i

If needed to further reduce sharp diameter transitions, the flow computations can be repeated with the adjusted diameters. Additional passes of diameter averaging can be performed until a sufficiently smooth diameter transition and spectrum is achieved.

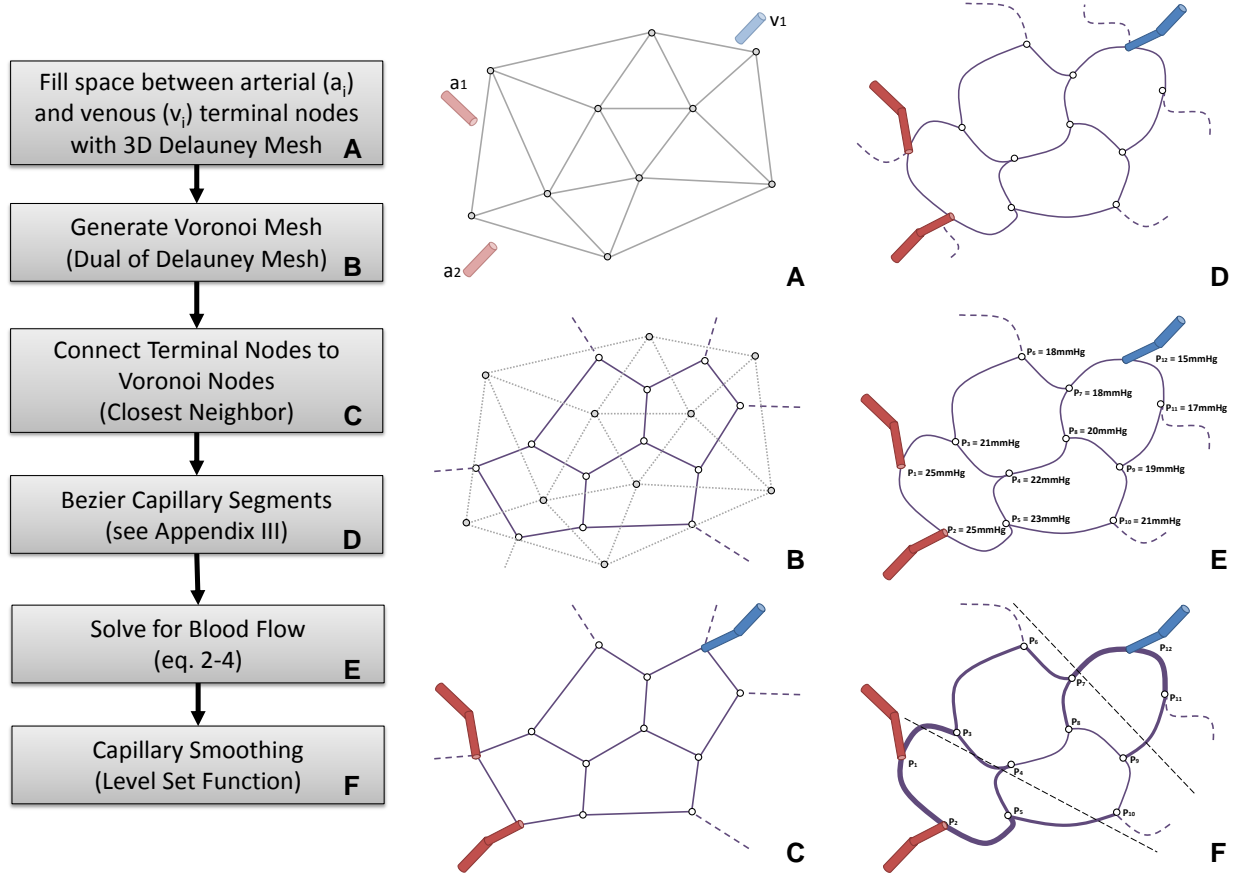


Figure 9 Stepwise construction of capillary beds. (A) Delaunay triangulation of the space between the terminal nodes of the arteriole tree (a_1 , and a_2) and the venous tree (v_1). Mesh density (shown as triangles for clarity) controls the segment length of the desired capillary bed. (B) Construction of Voronoi tessellation, which is the dual of the Delaunay mesh. (C) Connection of arterial and venous terminal to the closest neighbor capillary node. (D) Bezier curve approximation of capillary segments to adjust desired degree of tortuosity. (E) Network flow simulation yields a pressure field to determine the mean capillary pressure, P . Segments within a desired pressure range, $P \pm 2\sigma_F$, are assigned the smallest capillary diameter, $D_{\min} = 3 \mu\text{m}$. (F) Diameters of capillary segments are according to an iterative averaging scheme, producing smooth transitions from the pre-capillary arterioles to the post-capillary venules. Steps E to F can be repeated to eliminate sharp diameter transitions at the inlets and outlets of the capillary bed.

Supplemental 2

Cubic Bezier curves

A cubic Bezier curve is a vector function in terms of the scalar parameter t as defined in eq. 9. It is defined by two end points, \vec{P}_0 and \vec{P}_1 and two control points, \vec{C}_0 and \vec{C}_1 as shown in Figure 13A. The endpoints delineate the curve; the control points dictate the shape of the curve.

$$\vec{B}(t) = (1-t)^3 \cdot \vec{P}_0 + 3t(1-t)^2 \cdot \vec{C}_0 + 3t^2(1-t) \cdot \vec{C}_1 + t^3 \cdot \vec{P}_1 \quad t \in [0,1] \quad 9$$

For each capillary segment between points \vec{P}_0 and \vec{P}_1 , a 3D Bezier curve with desired degree of tortuosity can be constructed. To ensure reasonable transitions between different segments, we derive the control points for a given segment as a function of its neighboring segments. The first step is to find the auxiliary point \vec{A}_0 , defined as the average of the set of points, $\vec{P}_{0,1}$ connected to \vec{P}_0 exclusive of \vec{P}_1 as given in eq. 10. Similarly, auxiliary point \vec{A}_1 , is found from the set of points, $\vec{P}_{1,1}$ connected to \vec{P}_1 except for \vec{P}_0 :

$$\vec{A}_0 = \frac{\sum_{i=1}^N \vec{P}_{0,i}}{N}$$

$\forall \vec{P}_{0,i}$ connect to \vec{P}_0 , except for \vec{P}_1

$$\vec{A}_1 = \frac{\sum_{i=1}^N \vec{P}_{1,i}}{N} \quad 10$$

$\forall \vec{P}_{1,i}$ connect to \vec{P}_1 , except for \vec{P}_0

Finally, the desired control \vec{C}_0 and \vec{C}_1 are calculated with eq. 11, where the scalar α controls the degree of tortuosity: $\alpha = 0$ produces a straight line, $\alpha = 1.0$ gives in the most tortuous curve. We recommend a value of $\alpha = 0.25$ for natural capillary mesh appearance. Sample meshes with and without Bezier vessels are depicted in Figure 10C-D. Note that arc lengths of Bezier curves given in eq. 12 are always greater than the straight line counterpart.

$$\vec{C}_0 = \vec{P}_0 + \alpha \cdot (\vec{P}_0 - \vec{A}_0) \quad \alpha \in [0,1]$$

$$\vec{C}_1 = \vec{P}_1 + \alpha \cdot (\vec{P}_1 - \vec{A}_1) \quad \alpha \in [0,1]$$

11

Analytical arc length:

$$\int_0^1 |\dot{B}(t)| dt = \int_0^1 \sqrt{\sum_{i=x,y,z} \left[\frac{dB_i(t)}{dt} \right]^2} dt$$

Where $B_i(t)$ are the components of $B(t)$

Numerically

$$\int_0^1 \sqrt{\sum_{i=x,y,z} \left[\frac{dB_i(t)}{dt} \right]^2} dt \approx \sum_{t_j}^M \left\{ \sqrt{\sum_{i=x,y,z} \left[\frac{\Delta B_i(t)}{\Delta t_j} \right]^2} \Delta t_j \right\} \quad 12$$

where $\frac{\Delta B_i(t)}{\Delta t_j}$ are the numerical derivatives of the components of $B(t)$ along the arc t

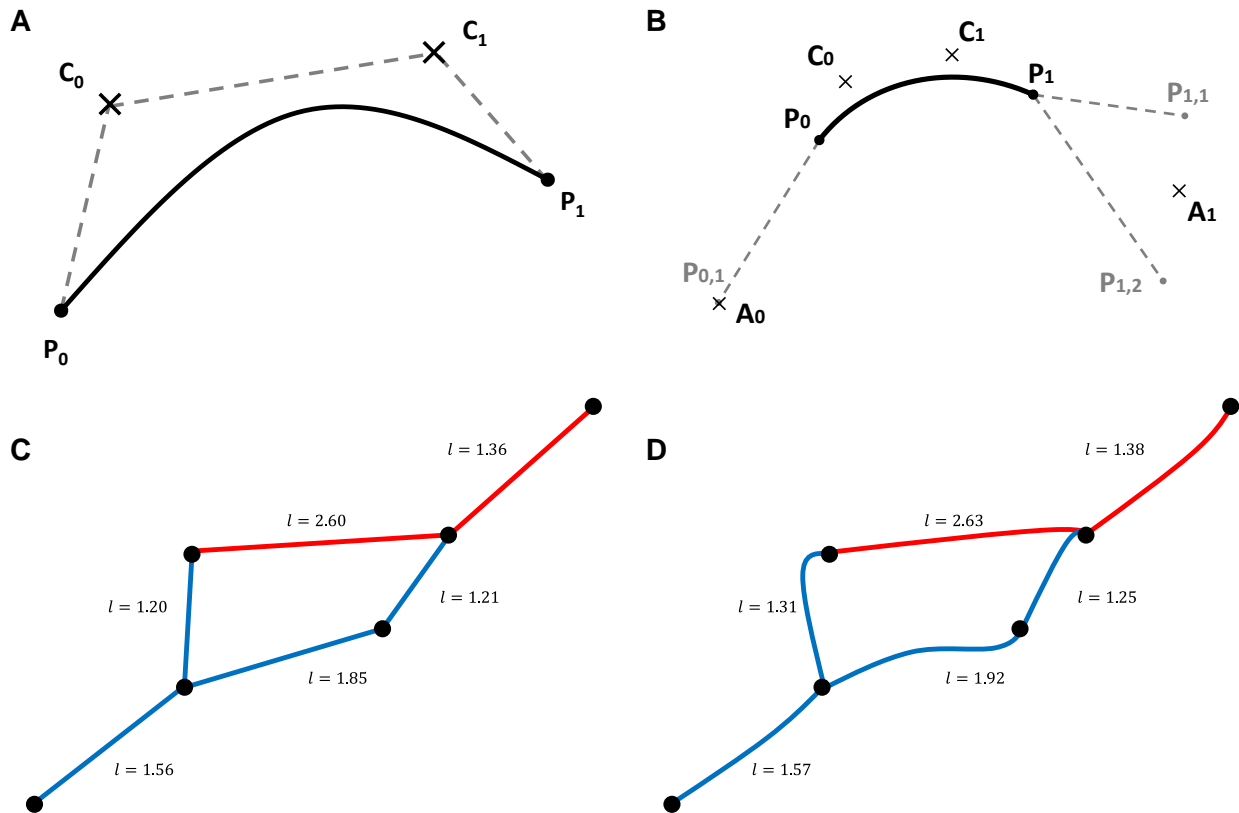


Figure 10 Bezier Curve adjustment of capillary tortuosity. (A) Depiction of a Bezier curve between endpoints, \vec{P}_0 , \vec{P}_1 and control points, \vec{C}_0 , \vec{C}_1 . (B) Automatic generation of control points based on segments connected to the current Bezier segment. (C) Straight line segments. (D) Tortuous capillary segment with Bezier curve parameter, $\alpha = 0.25$.

Supplemental 3

Krogh Cylinder: Discrete and analytical solutions

At the request of one reviewer, we also included a comparison of our dual mesh technique with an analytical Krogh model. Even though the Krogh cylinder offers an analytical solution to the oxygen diffusion with 0th order reaction, it has several limitations including the lack of axial dispersion which makes it imperfect for numerical validation studies.³⁶ Several extension of the Krogh model have been proposed by Secomb,²⁵ but approaches like Green's function are beyond the intended scope of numerical validation of our network.

We plotted the results for a cylindrical domain with a single blood vessel in its center as described in Krogh's original work.³⁷ The analytical radial concentration profiles, $C(r, z)$ at different levels of the axial coordinate are given eq. 13 and 14 as a function of the product of the inlet concentration, C_0 , and the bulk velocity, V , the radius of the vessel, r_C , the thickness of the wall t_m , the radius of the tissue cylinder, r_T , and the zero order rate of solute destruction in the tissue, R_0 , and the diffusion of the solute in tissue, D . The concentration of solute in the tissue at the wall boundary, $C_{r_C+t_m}$ equal to the flux of transport through the vessel governed by the mass transport coefficient, K_0 , as shown in eq. 14. Finally, eq. 14 includes the axial concentration profile inside the blood vessel, $C(z)$, at the axial coordinate, z . The radial and axial solute gradients were computed for the analytic solution as shown in Figure 11.

$$C(z, r) = \bar{C}_{r_C+t_m} + \frac{R_0}{4D_T} [r^2 - (r_C + t_m)^2] - \frac{R_0 r_T^2}{2D_T} \ln \frac{r}{r_C + t_m} \quad 13$$

$$\text{with } \bar{C}_{r_C+t_m} = C(z) - \frac{R_0}{2r_C K_0} r_*^2$$

$$C(z) = C_0 - \frac{R_0}{V r_C^2} r_*^2 z, \quad r_*^2 = [r_T^2 - (r_C + t_m)^2] \quad 14$$

We compare oxygen extraction numerically computer with our model to the analytical Krogh model.¹⁵ The central blood vessel was discretized with cylindrical segments of $\Delta z = 8$ mm in length. A relatively coarse tetrahedral mesh to represent the extravascular space was constructed with the same dimensions, a mesh edge length of 34 μm , which is the same resolution as used in Chapter II. Flow, oxygen inlet concentration, mass transfer and 0th order oxygen consumption were implemented with the same parameters as in the Krogh model listed compactly in Table IV. Figure 11 summarize the results for the analytical and the numerical methods described in this work. Radial oxygen profiles of all tetrahedral cells falling with an axial range of $z = 570 \pm 1$ mm were plotted as dots in Figure 11. For the analytical solution, two profiles were drawn for $z = 569$ mm and $z = 571$ mm, corresponding to the extreme axial positions of the tetrahedral elements in that zone. The analytical and our numerical results are in excellent agreement as expected.

For completeness, we also checked total oxygen exchange and plotted the radial oxygen profiles. Although the total oxygen exchange matches exactly within numerical tolerances, the extraction profile along the axis cannot be identical as expected. This result is valid, as the Krogh model neglects axial dispersion, while our model does not. Therefore the slight mismatch is actually a confirmation of the quality of the proposed technique. Additionally, a molar balance was constructed to determine the soundness of the discrete method and enforcement of mass conservation.

The rate of $5 \mu\text{mole}/\text{cm}^3$ entering the cylinder at a velocity of $500 \mu\text{m}/\text{s}$ with a cross sectional area of $78.5 \mu\text{m}^2$ gives an inlet flux of $19.63 \times 10^{28} \mu\text{mole}/\text{s}$. The outlet concentration from cylinder was determined as $3.74 \mu\text{mole}/\text{cm}^3$ in the analytical, and $3.72 \mu\text{mole}/\text{cm}^3$ in the discrete model. These outlet concentrations give rise to an outlet flux of $14.69 \times 10^{28} \mu\text{mole}/\text{s}$ in the analytical solution and $14.61 \times 10^{28} \mu\text{mole}/\text{s}$ in the discrete model. The volume of the tissue cylinder (total tissue cylinder volume minus the vessel volume) is $4.93 \times 10^6 \mu\text{m}^3$ in the analytical domain and

$4.98 \times 10^6 \mu\text{m}^3$ in the discrete domain, giving a volumetric 0th order reaction rate of $4.93 \times 10^6 \mu\text{mole/s}$ and $4.98 \times 10^6 \mu\text{mole/s}$, respectively. This compares to the 0th destruction rate computed by the analytical and discrete methods with a reported numeric error <0.002 . This error scales accordingly for the large microvessel subsection model presented in this paper.

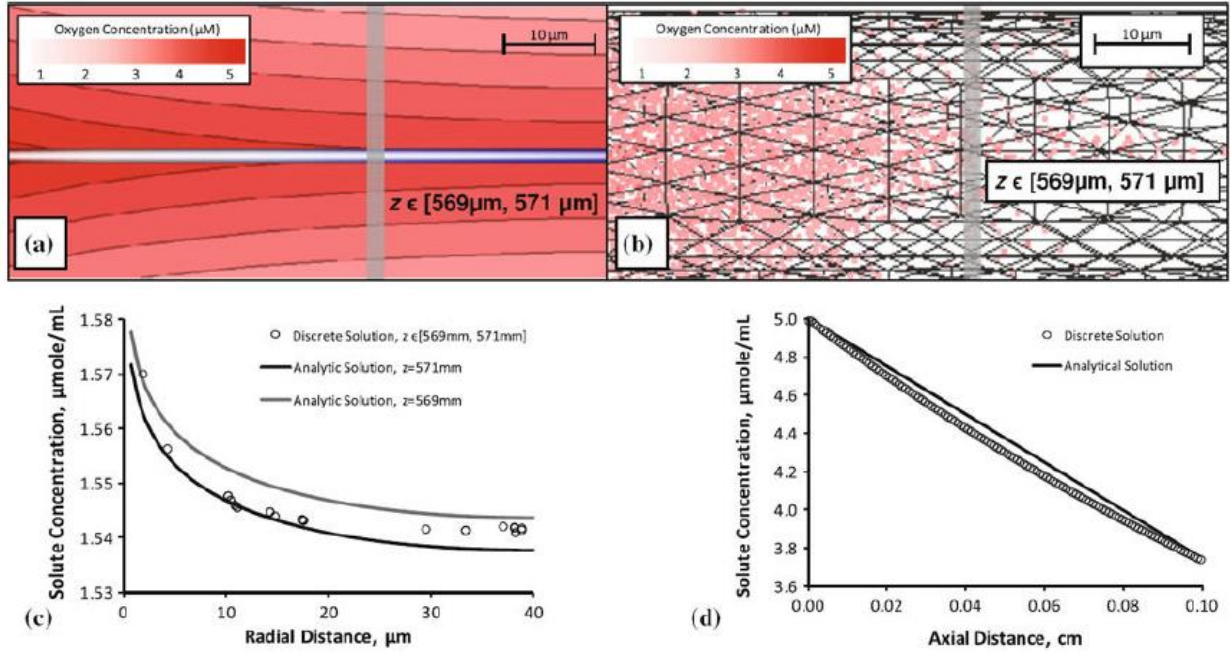


Figure 11 Krogh cylinder solution of tissue oxygen perfusion from a single vessel, comparison of analytical and discrete methods. (a) Analytical solution of a Krogh cylinder with capillary radius ($r_c = 5 \mu\text{m}$) and capillary length ($L = 1000 \mu\text{m}$) and surrounding tissue radius ($r_T = 40 \mu\text{m}$) and a constant injection of solute ($C_0 = 5 \mu\text{mole/mL}$). This radial distribution was determined at $z = 570 \mu\text{m}$. (b) Solution of the same system using the discrete approach described in this paper. (c) Discrete radial concentration of solute compared to realizations of the analytical solution for $z = 569 \text{mm}$ and $z = 571 \text{mm}$ (d) axial distribution of oxygen between the analytical and the discrete solution.

Table IV Parameters of distribution using the Krogh model

Variable	C_0	V	r_c	L	t_m	r_T	D	R_0	K_0
Value	5	500	5	1000	0.5	40	800	0.01	0.575
Unit	$\mu\text{mole}/\text{cm}^3$	$\mu\text{m}/\text{s}$	μm	μm	μm	μm	$\mu\text{m}^2/\text{s}$	$\mu\text{mole}/\text{cm}^3/\text{s}$	$\mu\text{m}/\text{s}$

Cited Literature

1. Aroesty, J., and J. F. Gross. The mathematics of pulsatile flow in small vessels. I. Casson theory. *Microvasc. Res.* 4:1–12, 1972.
2. Behera, D. Textbook of Pulmonary Medicine. Jaypee Brothers Medical Pub, 2010.
3. Blinder, P., A. Y. Shih, C. Rafie, and D. Kleinfeld. Topological basis for the robust distribution of blood to rodent neocortex. *Proc. Natl Acad. Sci. USA.* 107:12670–12675, 2010.
4. Boas, D. A., S. R. Jones, A. Devor, T. J. Huppert, and A. M. Dale. A vascular anatomical network model of the spatio-temporal response to brain activation. *NeuroImage* 40:1116–1129, 2008.
5. Cassot, F., F. Lauwers, C. Fouard, S. Prohaska, and V. Lauwers-Cances. A novel three-dimensional computer-assisted method for a quantitative study of microvascular networks of the human cerebral cortex. *Microcirculation* 13:1–18, 2006.
6. Cassot, F., F. Lauwers, S. Lorthois, P. Puwanarajah, V. Cances-Lauwers, and H. Duvernoy. Branching patterns for arterioles and venules of the human cerebral cortex. *Brain Res.* 1313:62–78, 2010.
7. Cassot, F., F. Lauwers, S. Lorthois, P. Puwanarajah, and H. Duvernoy. Scaling laws for branching vessels of human cerebral cortex. *Microcirculation* 16:331–344, 2 p following 344, May 2009.
8. Delaunay, B. Sur la sphere vide. *Bull. Acad. Science USSR VII: Class Sci. Mat.*, pp. 793–800, 1934.
9. Devor, A., S. Sakadzic, P. A. Saisan, M. A. Yaseen, E. Roussakis, V. J. Srinivasan, S. A. Vinogradov, B. R. Rosen, R. B. Buxton, A. M. Dale, and D. A. Boas. “Overshoot” of $O(2)$ is required to maintain baseline tissue oxygenation at locations distal to blood vessels. *J. Neurosci.* 31:13676–13681, 2011.

10. Duff, I. S., and J. K. Reid. The design of MA48: A code for the direct solution of sparse unsymmetric linear systems of equations. *ACM Trans. Math. Softw.* 22:187–226, 1996.
11. Duong, T. Q., and S. G. Kim. In vivo MR measurements of regional arterial and venous blood volume fractions in intact rat brain. *Magnetic Resonance in Medicine* 43:393–402, 2000.
12. Duvernoy, H. M., S. Delon, and J. L. Vannson. Cortical blood vessels of the human brain. *Brain Research Bulletin* 7:519–579, 1981.
13. Espagno, J., L. Arbus, A. Bes, R. Billet, A. Gouaze, Ph. Frerebeau, Y. Lazorthes, G. Salamon, J. Seylaz, and B. Vlahovitch. La circulation cerebrale. *Neuro-Chirurgie*, 15, 1969.
14. Fang, Q., S. Sakadzic, L. Ruvinskaya, A. Devor, A. M. Dale, and D. A. Boas. Oxygen advection and diffusion in a three-dimensional vascular anatomical network. *Optics Express* 16:17530–17541, 2008.
15. Fletcher, J. Mathematical modeling of the microcirculation. *Mathematical Biosciences* 38:159–202, 1978.
16. Fung, Y. C., and B. W. Zweifach. Microcirculation—mechanics of blood flow in capillaries. *Annu. Rev. Fluid Mech.* 3:189–&, 1971.
17. Gjedde, A., H. Kuwabara, and A. M. Hakim. Reduction of functional capillary density in human brain after stroke. *Journal of Cerebral Blood Flow and Metabolism* 10:317–326, 1990.
18. Goldman, D., and A. S. Popel. A computational study of the effect of capillary network anastomoses and tortuosity on oxygen transport. *Journal of Theoretical Biology* 206:181–194, 2000.
19. Gould, I. G., T. Marinnan, C. Maurice, M. Qader, B. Henry, M. Pervais, N. Vaicaitis, Y. Zhu, A. Rogers, and A. A. Linninger. Hemodynamics of cerebral vasculature. Presented at the Proceedings of the 11th International Symposium on Process Systems Engineering, Singapore, 2012.

20. Guibert, R., C. Fonta, and F. Plouraboue. Cerebral blood flow modeling in primate cortex. *Journal of Cerebral Blood Flow and Metabolism* 30:1860–1873, 2010.
21. Guibert, R., C. Fonta, and F. Plouraboue. A new approach to model confined suspensions flows in complex networks: application to blood flow. *Transport in Porous Media* 83:171–194, 2010.
22. Guibert, R., C. Fonta, L. Risser, and F. Plouraboue. Coupling and robustness of intra-cortical vascular territories. *NeuroImage* 62:408–417, 2012.
23. Hill, A. V. The combinations of haemoglobin with oxygen and with carbon monoxide. I. *Biochem J* 7:471–480, 1913.
24. Hirsch, S., J. Reichold, M. Schneider, G. Szekely, and B. Weber. Topology and hemodynamics of the cortical cerebrovascular system. *Journal of Cerebral Blood Flow and Metabolism* 32:952–967, 2012.
25. Hsu, R., and T. W. Secomb. A Green's function method for analysis of oxygen delivery to tissue by microvascular networks. *Mathematical Biosciences* 96:61–78, 1989.
26. Hunziker, O., H. Frey, and U. Schulz. Morphometric investigations of capillaries in the brain cortex of the cat. *Brain Research* 65:1–11, 1974.
27. Huppert, T. J., M. S. Allen, H. Benav, P. B. Jones, and D. A. Boas. A multicompartement vascular model for inferring baseline and functional changes in cerebral oxygen metabolism and arterial dilation. *Journal of Cerebral Blood Flow and Metabolism* 27:1262–1279, 2007.
28. Ito, H., I. Kanno, H. Iida, J. Hatazawa, E. Shimosegawa, H. Tamura, and T. Okudera. Arterial fraction of cerebral blood volume in humans measured by positron emission tomography. *Annals of Nuclear Medicine* 15:111–116, 2001.
29. James, K. R., and W. Riha. Convergence criteria for successive overrelaxation. *Siam Journal on Numerical Analysis* 12:137–143, 1975.
30. Jensen, F. B. Red blood cell pH, the Bohr effect, and other oxygenation-linked phenomena in blood O₂ and CO₂ transport. *Acta Physiologica Scandinavica* 182:215–227, 2004.

31. Karch, R., F. Neumann, M. Neumann, and W. Schreiner. A three-dimensional model for arterial tree representation, generated by constrained constructive optimization. *Computers in Biology and Medicine* 29:19–38, 1999.
32. Karch, R., F. Neumann, M. Neumann, and W. Schreiner. Staged growth of optimized arterial model trees. *Annals of Biomedical Engineering* 28:495–511, 2000.
33. Karch, R., F. Neumann, B. K. Podesser, M. Neumann, P. Szawlowski, and W. Schreiner. Fractal properties of perfusion heterogeneity in optimized arterial trees: a model study. *Journal of General Physiology* 122:307–321, 2003.
34. Kasischke, K. A., E. M. Lambert, B. Panepento, A. Sun, H. A. Gelbard, R. W. Burgess, T. H. Foster, and M. Nedergaard. Two-photon NADH imaging exposes boundaries of oxygen diffusion in cortical vascular supply regions. *Journal of Cerebral Blood Flow and Metabolism* 31:68–81, 2011.
35. Keller, A. L., A. Schuz, N. K. Logothetis, and B. Weber. Vascularization of cytochrome oxidase-rich blobs in the primary visual cortex of squirrel and macaque monkeys. *Journal of Neuroscience* 31:1246–1253, 2011.
36. Kreuzer, F. Oxygen supply to tissues: the Krogh model and its assumptions. *Experientia* 38:1415–1426, 1982.
37. Krogh, A. The number and distribution of capillaries in muscles with calculations of the oxygen pressure head necessary for supplying the tissue. *Journal of Physiology* 52:409–415, 1919.
38. Lauwers, F., F. Cassot, V. Lauwers-Cances, P. Puwanarajah, and H. Duvernoy. Morphometry of the human cerebral cortex microcirculation: general characteristics and space-related profiles. *NeuroImage* 39:936–948, 2008.
39. Linninger, A. A. Biomedical systems research—New perspectives opened by quantitative medical imaging. *Computers & Chemical Engineering* 36:1–9, 2012.

40. Linninger, A. A., M. R. Somayaji, T. Erickson, X. Guo, and R. D. Penn. Computational methods for predicting drug transport in anisotropic and heterogeneous brain tissue. *Journal of Biomechanics* 41:2176–2187, 2008.
41. Lipowsky, H. H. Microvascular rheology and hemodynamics. *Microcirculation*, 12:5–15, 2005.
42. Lorthois, S., and F. Cassot. Fractal analysis of vascular networks: insights from morphogenesis. *Journal of Theoretical Biology* 262:614–633, 2010.
43. Lorthois, S., F. Cassot, and F. Lauwers. Simulation study of brain blood flow regulation by intra-cortical arterioles in an anatomically accurate large human vascular network. Part II: flow variations induced by global or localized modifications of arteriolar diameters. *NeuroImage* 54:2840–2853, 2011.
44. Lorthois, S., F. Cassot, and F. Lauwers. Simulation study of brain blood flow regulation by intra-cortical arterioles in an anatomically accurate large human vascular network: part I: methodology and baseline flow. *NeuroImage* 54:1031–1042, 2011.
45. Mintun, M. A., B. N. Lundstrom, A. Z. Snyder, A. G. Vlassenko, G. L. Shulman, and M. E. Raichle. Blood flow and oxygen delivery to human brain during functional activity: theoretical modeling and experimental data. *Proc Natl Acad Sci U S A* 98:6859–6864, 2001.
46. Neubauer, J. A., and J. Sunderram. Oxygen-sensing neurons in the central nervous system. *Journal of Applied Physiology* 96:367–374, 2004.
47. Niimi, H., Y. Komai, S. Yamaguchi, and J. Seki. Microembolic flow disturbances in the cerebral microvasculature with an arcadal network: a numerical simulation. *Clin Hemorheol Microcirc* 34:247–255, 2006.
48. Nishimura, N., C. B. Schaffer, B. Friedman, P. D. Lyden, and D. Kleinfeld. Penetrating arterioles are a bottleneck in the perfusion of neocortex. *Proc Natl Acad Sci U S A* 104:365–370, 2007.

49. Nolte, J., and J. W. Sundsten. The human brain: an introduction to its functional anatomy (5th ed.). St. Louis: Mosby, 2002.
50. Pawlik, G., A. Rackl, and R. J. Bing. Quantitative capillary topography and blood flow in the cerebral cortex of cats: an in vivo microscopic study. *Brain Research* 208:35–58, 1981.
51. Pries, A. Biophysical aspects of blood flow in the microvasculature. *Cardiovascular Research* 32:657–667, 1995.
52. Pries, A. R., T. W. Secomb, P. Gaehtgens, and J. F. Gross. Blood flow in microvascular networks. Experiments and simulation. *Circulation Research* 67:826–834, 1990.
53. Rakusan, K., and P. Wicker. Morphometry of the small arteries and arterioles in the rat heart: effects of chronic hypertension and exercise. *Cardiovascular Research* 24:278–284, 1990.
54. Reichold, J., M. Stampanoni, A. Lena Keller, A. Buck, P. Jenny, and B. Weber. Vascular graph model to simulate the cerebral blood flow in realistic vascular networks. *J. Cereb. Blood Flow Metab.* 29:1429–1443, 2009.
55. Rhodin, J. A. Ultrastructure of mammalian venous capillaries, venules, and small collecting veins. *Journal of Ultrastructure Research* 25:452–500, 1968.
56. Risser, L., F. Plouraboue, P. Cloetens, and C. Fonta. A 3D-investigation shows that angiogenesis in primate cerebral cortex mainly occurs at capillary level. *International Journal of Developmental Neuroscience* 27:185–196, 2009.
57. Risser, L., F. Plouraboue, A. Steyer, P. Cloetens, G. Le Duc, and C. Fonta. From homogeneous to fractal normal and tumorous microvascular networks in the brain. *Journal of Cerebral Blood Flow and Metabolism* 27:293–303, 2007.
58. Rostrup, E., I. Law, M. Blinkenberg, H. B. W. Larsson, A. P. Born, S. Holm, and O. B. Paulson. Regional differences in the CBF and BOLD responses to hypercapnia: a combined PET and fMRI study. *NeuroImage* 11:87–97, 2000.

59. Safaeian, N., M. Sellier, and T. David. A computational model of hemodynamic parameters in cortical capillary networks. *J. Theor. Biol.* Dec 2 2010.
60. Sakadzic, S., E. Roussakis, M. A. Yaseen, E. T. Mandeville, V. J. Srinivasan, K. Arai, S. Ruvinskaya, A. Devor, E. H. Lo, S. A. Vinogradov, and D. A. Boas. Two-photon high-resolution measurement of partial pressure of oxygen in cerebral vasculature and tissue. *Nature Methods* 7:755–759, 2010.
61. Schneider, M., S. Hirsch, B. Weber, and G. Szekely. Physiologically based construction of optimized 3-D arterial tree models. *Med Image Comput Comput Assist Interv* 14:404–411, 2011.
62. Schneider, M., J. Reichold, B. Weber, G. Szekely, and S. Hirsch. Tissue metabolism driven arterial tree generation. *Medical Image Analysis* 16:1397–1414, 2012.
63. Schreiner, W., R. Karch, M. Neumann, F. Neumann, P. Szawlowski, and S. Roedler. Optimized arterial trees supplying hollow organs. *Medical Engineering & Physics* 28:416–429, 2006.
64. Sharan, M., E. P. Vovenko, A. Vadapalli, A. S. Popel, and R. N. Pittman. Experimental and theoretical studies of oxygen gradients in rat pial microvessels. *Journal of Cerebral Blood Flow and Metabolism* 28:1597–1604, 2008.
65. Si, H. TetGen, A Quality Tetrahedral Mesh Generator and Three-Dimensional Delaunay Triangulator, 1.4 ed. Berlin, 2006.
66. Sorenson, A., G., W. A. Copen, L. Ostergaard, F. S. Buonanno, R. G. Gonzalez, G. Rordorf, B. R. Rosen, L. H. Schwamm, R. M. Weisskoff, and W. J. Koroshetz. Hyperacute stroke: simultaneous measurement of relative cerebral blood volume, relative cerebral blood flow, and mean tissue transit time. *Neuroradiology*, 210, 519–527, 1999.
67. Su, S. W., M. Catherall, and S. Payne. The influence of network structure on the transport of blood in the human cerebral microvasculature. *Microcirculation* 19:175–187, 2012.

68. Takahashi, T., T. Nagaoka, H. Yanagida, T. Saitoh, A. Kamiya, T. Hein, L. Kuo, and A. Yoshida. A mathematical model for the distribution of hemodynamic parameters in the human retinal microvasculature network. *J Biorheol* 23:77–86, 2009.
69. Tang, W., L. Zhang, A. Linninger, R. S. Tranter, and K. Brezinsky. Solving kinetic inversion problems via a physical trust region gauss-newton method. *Industrial and Engineering Chemistry Research* 44:3626–3637, 2005.
70. Tsai, P. S., J. P. Kaufhold, P. Blinder, B. Friedman, P. J. Drew, H. J. Karten, P. D. Lyden, and D. Kleinfeld. Correlations of neuronal and microvascular densities in murine cortex revealed by direct counting and colocalization of nuclei and vessels. *Journal of Neuroscience* 29:14553–14570, 2009.
71. Vaicaitis, N. M., B. J. Sweetman, and A. A. Linninger. A computational model of cerebral vasculature, brain tissue, and cerebrospinal fluid. Presented at the 21st European Symposium on Computer-Aided Process Engineering, Greece, 2011.
72. Voronoi, G. Nouvelles applications des parametres continus a la theorie des formes quadratiques. Deuxie`me me´moire. Recherches sur les paralle´lloè`dres primitifs. *Journal fur die reine und angewandte Mathematik* 134:198–287, 1908.
73. Vovenko, E. Distribution of oxygen tension on the surface of arterioles, capillaries and venules of brain cortex and in tissue in normoxia: an experimental study on rats. *Pflugers Archiv. European Journal of Physiology* 437:617–623, 1999.
74. Vovenko, E. P., and A. E. Chuikin. Oxygen tension in rat cerebral cortex microvessels in acute anemia. *Neuroscience and Behavioral Physiology* 38:493–500, 2008.
75. Vovenko, E. P., and A. E. Chuikin. Tissue oxygen tension profiles close to brain arterioles and venules in the rat cerebral cortex during the development of acute anemia. *Neuroscience and Behavioral Physiology* 40:723–731, 2010.
76. Weber, B., A. L. Keller, J. Reichold, and N. K. Logothetis. The microvascular system of the striate and extrastriate visual cortex of the macaque. *Cerebral Cortex* 18:2318–2330, 2008.

77. Yang, Y., W. Engelen, S. Xu, H. Gu, D. A. Silbersweig, and E. Stern. Transit time, trailing time, and cerebral blood flow during brain activation: measurement using multislice, pulsed spin-labeling perfusion imaging. *Magnetic Resonance in Medicine* 44:680–685, 2000.
78. Zagzoule, M., and J. P. Marc-Vergnes. A global mathematical model of the cerebral circulation in man. *Journal of Biomechanics* 19:1015–1022, 1986.
79. Zhang, L. B., K. Kulkarni, M. R. Somayaji, M. Xenos, and A. A. Linninger. Discovery of transport and reaction properties in distributed systems. *AIChE Journal* 53:381–396, 2007.
80. Zhang, L. B., C. Xue, A. Malcolm, K. Kulkarni, and A. A. Linninger. Distributed system design under uncertainty. *Industrial and Engineering Chemistry Research* 45:8352–8360, 2006.
81. Zweifach, B. W. Quantitative studies of microcirculatory structure and function. I. Analysis of pressure distribution in the terminal vascular bed in cat mesentery. *Circulation Research* 34:843–857, 1974.
82. Zweifach, B. W., and H. H. Lipowsky. Quantitative studies of microcirculatory structure and function. III. Microvascular hemodynamics of cat mesentery and rabbit omentum. *Circulation Research* 41:380–390, 1977.

III. HEMATOCRIT DISTRIBUTION AND TISSUE OXYGENATION IN LARGE MICROCIRCULATORY NETWORKS

(Based on a previously published article titled as Gould, Ian G., and Andreas A. Linninger. "Hematocrit distribution and tissue oxygenation in large microcirculatory networks." *Microcirculation* 22, no. 1 (2015): 1-18.)

Abstract

Objective Oxygen tension in the brain is controlled by the microcirculatory supply of red blood cells, but the effect of non-Newtonian blood flow rheology on tissue oxygenation is not well characterized. This paper assesses different biphasic blood flow models for predicting tissue oxygen tension as a function of microcirculatory hemodynamics.

Methods Two existing plasma skimming laws are compared against measured RBC distributions in rat and hamster microcirculatory networks. A novel biphasic blood flow model is introduced. The computational models predict tissue oxygenation in the mesentery, cremaster muscle, and the human secondary cortex.

Results This investigation shows deficiencies in prior models, including inconsistent plasma skimming trends and insufficient oxygen perfusion due to the high prevalence (33%) of RBC-free microvessels. Our novel method yields physiologically sound RBC distributions and tissue oxygen tensions within one standard deviation of experimental measurements.

Conclusions A simple, novel biphasic blood flow model is introduced with equal or better predictive power when applied to historic raw data sets. It can overcome limitations of prior models pertaining to trifurcations, anastomoses, and loops. This new plasma skimming law eases the computations of bulk blood flow and hematocrit fields in large microcirculatory networks and converges faster than prior procedures.

Introduction

Brain activity-induced changes in vascular tone and oxygen consumption modulate blood flow and tissue oxygenation. The effects of changing cerebral blood flow, oxyhemoglobin dissociation and tissue oxygenation can be measured by functional imaging techniques such as optical imaging¹, or magnetic resonance imaging (fMRI)². For interpreting the spatiotemporal relationship between *in vivo* measurements, computational methods can play an important role. Several imaging studies³⁻⁶ recognize the significance of computational models for investigating the functional relationship between cerebral angioarchitecture⁷⁻¹⁰, blood flow¹¹⁻¹², and oxygen exchange¹³⁻¹⁷. Computational models for microcirculatory hemodynamics need to account for the nonideal flow behavior of erythrocyte-bound oxygen, which in turn is necessary to predict tissue oxygenation. Blood flow in the microcirculation is highly non-Newtonian because of the biphasic nature of red blood cells and plasma. We will show that improperly formulated phase separation laws drastically impact predicted oxygen distribution to the tissue, especially how the prediction of RBC-free capillaries leads to drastically low oxygen tension. Before presenting a novel methodology for microcirculatory oxygen exchange between blood and tissue, a brief introduction of non-linear biphasic blood flow is given.

Microscopic forces cause biphasic flow and the creation of the endothelial surface layer

The nonideal microcirculatory flow behavior is caused by the biphasic cell suspension in blood plasma. In microvessels ($d < 100\mu\text{m}$) small platelets and white blood cells migrate towards the endothelial wall¹⁸, while red blood cells (RBC) preferentially travel near the center¹⁹. Neglecting white blood cells and platelets, RBC and plasma are the two essential components of the biphasic microcirculation theory. *Margination*²⁰ is the rheological segregation of RBC from plasma due to two governing forces, particle pair collisions and wall induced particle migration²⁰. RBC-RBC collisions cause erythrocytes to disperse radially. RBC interactions with the vessel wall drives them towards the center^{19,21}.

The microscopic force balance between the radial and the wall-induced dispersion leads to the formation of the *cell free layer* (CFL), a thin annular region adjacent to the vessel wall and the endothelial surface layer (ESL)^{20,22}. The CFL contains mainly plasma and no RBCs²³⁻²⁴. The CFL also restricts the space available for erythrocytes, thus altering their velocity relative to the plasma. This relative velocity difference between the RBC and plasma phase determines their volumetric and flux based concentrations known as *hematocrit*.

Macroscopic behavior of tube and discharge hematocrit in a single channel

The volumetric concentration of the RBC phase is known as the *tube hematocrit*, H_t , which is often determined optically as the volume fraction occupied by RBCs. Because narrowing vessels or bifurcations alter the speed of the RBC phase, u , relative to the plasma phase, v , the tube hematocrit changes along the flow path. Due to phase velocity differences, the tube hematocrit is not the same as the *discharge* or *cup hematocrit*, H_d . It is helpful to consider a single narrowing blood vessel shown in Figure 12 to distinguish between tube and discharge hematocrit, H_t and H_d .

The *discharge hematocrit* is the ratio of the volumetric flux of the RBCs divided by the bulk volumetric flow, Q . The relations between the bulk, V , and phase velocities, u and v , are illustrated in Figure 12 and defined in eqs. 15-17. The RBC phase velocity, u , is equal to the volumetric flux of the RBC phase, Q_{RBC} , divided by the core area occupied by the RBC phase, A_e . In a single channel at steady state, the discharge hematocrit remains constant due to conservation of RBCs.

$$Q = VA \quad 15$$

$$u = \frac{Q_{RBC}/A}{H_t} \text{ or } Q_{RBC} = uA_e \quad 16$$

$$v = \frac{Q_P/A}{1 - H_t} \text{ or } Q_P = vA_p \quad 17$$

The *tube hematocrit* is defined as the ratio of the area occupied by the RBCs over the total cross sectional area, shown in Supplemental 1. The relationship between discharge and tube hematocrit H_d and H_t is equal to the ratio of the RBC phase velocity over the bulk velocity as in eq. 18. This correlation was empirically established by Fahraeus²⁵, and has subsequently been validated experimentally²⁵⁻²⁷. This relationship can also be derived analytically for axisymmetric idealized flows²⁸, more details can be found in Supplemental 1.

$$\frac{H_d}{H_t} = \frac{u}{V} \quad 18$$

As the blood vessel diameter narrows, the RBC phase flux remains constant, while the core area containing the RBCs, A_c , shrinks. As the vessel narrows in diameter, the CFL occupies an increasingly larger portion of the cross sectional area. Therefore, the RBC velocity, u , accelerates faster than the plasma phase velocity, v . This leads to a relative velocity difference, or *drift velocity*, v_{Drift} , between the RBC phase and the plasma phase. The CFL is also responsible for the uneven distribution of RBCs in bifurcations, which is discussed in the following section.

Plasma skimming at bifurcations

Single Bifurcations. Krogh first observed the uneven RBC distribution at capillary bifurcations²⁹. This phenomenon, later termed plasma skimming, causes hemodilution in the thinner daughter branch while increasing hematocrit in the thicker branch. The prediction of phase separation, hemodilution and hemoconcentration has been the object of numerous modeling efforts summarized in Table V. Fahraeus showed that the thinner daughter branch tends to siphon a large proportion of its flow from the CFL of the parent vessel²⁵. Accordingly, the thin branch receives more plasma than corresponds to its bulk blood flux. The thicker daughter branch carries a large fraction of the RBCs from the parent vessel.

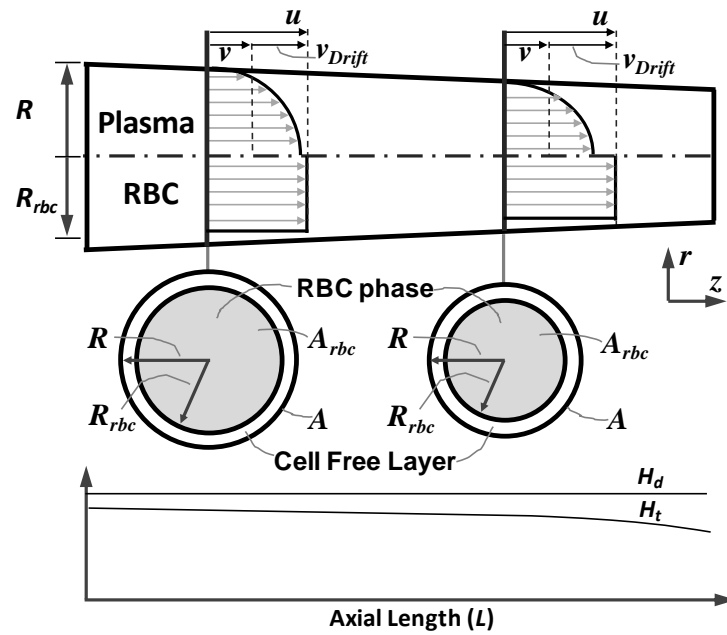


Figure 12 Tube and discharge hematocrit along a narrowing vessel. As the channel narrows, the CFL occupies an increasingly larger fraction of the cross sectional area, causing the RBC phase velocity u to increase relative to the plasma velocity v . Also, the drift velocity between the phases, v_{Drift} , becomes large. In effect, the tube hematocrit, H_t , decreases along the flow direction, while the discharge hematocrit, H_d , stays constant. The radius of the blood vessel occupied by RBCs, R_e , is defined by the difference between the radius of the vessel lumen, R_p , and the thickness of the CFL.

Analytical studies by Perkkiö revealed that the RBC split fraction is only weakly influenced by the parent discharge hematocrit³⁰. Fenton²⁷ proposed a plasma skimming law relating the kinematics of the daughter branch to the RBC distribution. However, his model does not converge for bifurcations with daughter branches of large diameter differences.³¹

Using dissipative particle dynamics, Karniadakis³² identified branch volumetric bulk flow rate, blood viscosity, and vessel geometry as key parameters for solving the plasma skimming problem. Even though models such as Zhang's or Karniadakis' can explain complex phenomena without the need for adjustable parameters³²⁻³³, the computational effort is substantial for a single bifurcation. Applying these methods to entire microcirculatory networks with tissue oxygen exchange is currently prohibitive. Due to this limitation, particle dynamics models were not considered in this comparative study.

Networks. Thin side branches siphon plasma from their tributary, thus gradually decreasing in discharge hematocrit. Simultaneously, the same phenomenon augments the hematocrit in the main arterial trunk. This network effect produces an uneven spatial RBCs distribution in the microcirculation. An extensive review by Pittman¹⁷ makes clear that microvascular hemodynamic data is needed to understand the delivery of oxygen to tissue. Using both continuous and flash illuminated monochromatic light measurements, Pries³⁴ measured the discharge and tube hematocrit within a 31mm^2 large section of the rodent mesentery using a light absorbance method calibrated using *in vitro* methods. He correlated the RBC flux in the daughter branches to the splitting ratio of the bulk blood flow^{22,35}, and carefully fitted the plasma skimming effect to parent vessel discharge hematocrit, bulk flow fractions, and the dimensions of the daughter branches.

Table V List of biphasic mathematical models for phase separation and plasma skimming

Author	Year	Vessels	Trifurcations	Plasma Skimming	Network	Oxy.
This Work	2014	3128	•	•	•	•
Safaeian ¹³	2013	492		•	•	•
Zhang ³³	2013	3		•		
Karniadakis ³²	2012	3		•		
Fry ³⁶	2012	383-547		•	•	
Plouraboue ³¹	2010	28	•		•	
Pozrikidis ³⁷	2009	511		•	•	
Boas ³⁸	2008	190		•	•	•
Tsoukias ¹⁵	2007	12		•	•	•
Pries ²²	2005	546		•	•	
Popel ³⁹	2000	12		•	•	•
Pries ³⁵	1996	65		•	•	
Audet ⁴⁰	1987	3		•		
Pries ³⁴	1986	1,303		•		
Fenton ^{27,41}	1985	3		•		
Perkkiö ³⁰	1985	3		•		
Dellimore ⁴²	1983	3		•		
Schmid-Schoenbein ⁴³	1980	3		•		

The most recent version has been used by other groups to predict oxygen transport in small networks. Popel demonstrated in a biphasic plasma and hematocrit computational study that geometrical factors of the microcirculation and capillary tortuosity enhance oxygen transport^{15,39}. Boas *et al.* investigated the spatio-temporal response of vascular network models but with a lumped extracellular space³⁸. Safaeian and David used a generic network model to predicted oxygen tension in the extravascular space of an artificially generated capillary bed¹³. Few other models exist for predicting the uneven distribution of RBCs in networks. Recently, Plouraboue proposed a RBC split computations assuming the existence of a hematocrit potential³¹.

In spite of these previous computational studies summarized in Table V, critical questions remain. Which spatial distribution patterns occur along main arterioles and in the capillary bed due to plasma skimming? How does the two-phase flow behavior impact oxygen delivery to tissue? To test the predictive quality of plasma skimming models for tissue oxygen exchange in large microcirculatory networks, we performed a comparative study between experimental data from animal models and three model predictions.

In this paper, the sensitivity of oxygen extraction from the capillary bed to different plasma skimming laws was investigated. To address this task, a well-known empirically fitted model²², Model 1, was implemented and critically assessed. For the first time, we will point out several inadequacies as will be shown in the results section. In addition, a recent hematocrit potential method³¹, Model 2, was implemented and evaluated as it has not yet been independently discussed in the literature. Physiologic insufficiencies limiting these existing models prompted the creation of a simple, yet accurate phase separation law, which will be presented here for the first time. The novel *kinetic plasma skimming model* (KPSM), denominated as Model 3, incorporates the vessel Fahraeus effect and plasma skimming. Benefits and shortcomings are compared for single bifurcations, microcirculatory networks and with respect to tissue oxygen exchange predictions.

Materials and Methods

Bulk Blood Flow

The three-biphasic blood flow models follow the formulation in eq. 2 of bulk blood flow, Q , through each vascular network junction in steady state. To compute the blood pressure drop in a vessel segment we first assume the viscosity adjusted Hagen-Poiseuille law given in eq. 20. Here, α is the hydraulic resistance, L , is the segment length, μ is the dynamic viscosity of blood plasma, R is the vessel radius, and H_d is the discharge hematocrit. In these simulations, the plasma viscosity is set to 1.0cP. The empirical viscosity adjustment η_{vivo} accounts for the nonideal blood rheology⁴⁴, and is a function of vessel radius and the discharge hematocrit, which needs to be determined using a suitable plasma-skimming method (Model 1-3).

$$\vec{\nabla} \cdot Q = 0 \quad 19$$

$$\Delta P = Q\alpha = Q \cdot \frac{8\mu L}{\pi R^4} \cdot \eta_{vivo}(R, H_d) \quad 20$$

Phase separation involves tracking the motion of the two separate phases, RBC and plasma. The sum of the RBC flux, Q_{RBC} , and the plasma flux, Q_P , is equal to the bulk blood flow, Q . The RBC flux balance can be written in terms of the discharge hematocrit, $Q_{RBC}=Q \cdot H_d$, is given in eq. 21.

$$\nabla \cdot Q_{RBC} = \nabla \cdot (QH_d) = 0 \quad 21$$

Model 1

Model 1 is an empirical phase skimming law proposed by Pries²². We chose it for evaluation, because it has been used in several network studies^{13,31,38,45}. To compute the RBC split at each bifurcation, this model uses the ratio of bulk flow rates of daughter over parent vessel the diameter of the parent and both daughter branches, and the discharge hematocrit of the parent

vessel. Because Model 1 requires the upstream hematocrit to be known before the RBC flux into downstream vessels can be computed, the resulting system of equations is non-linear.

Model 2

Model 2, developed by Plouraboue³¹, postulates the existence of hematocrit potential, \hat{H} . This hypothesis leads to an elegant elliptical problem which requires only elementary conservation laws with no adjustable parameters. Eq. 22 enforces conservation of the RBC flux at each vessel junction. The hematocrit potential approach renders a diffusion type problem, for which closure is achieved by setting Neumann boundary conditions equal to the inlet hematocrit and an arbitrary zero hematocrit potential at the outlet, $\hat{H}=0$. The discharge hematocrit, H_d , for each blood vessel segment is easily computed as the potential difference, $\Delta\hat{H}$, between nodes.

$$\nabla \cdot Q_{RBC} = \sum_{i=1}^N (\Delta\hat{H} \cdot Q) = \sum_{i=1}^N \Delta\hat{H} \frac{\pi R^4}{8\mu \cdot \eta_{vivo} L} \Delta P = 0 \quad 22$$

Model 3

The proposed *kinematic plasma skimming model* (KPSM) correlates the hematocrit distribution to geometry and kinematic properties of the bifurcation. The RBC split at each bifurcation depends on branch diameter ratios, the bulk flow fraction, and a single adjustable drift parameter, M , to account for the extent of plasma skimming.

A template bifurcation is depicted in Figure 13, where the parent vessel 1 feeds into the thinner branch 2 and the thicker daughter branch 3, or $A_2 < A_3$. Continuity in eq. 19 ensures that parent bulk flow is equal to the sum of the daughter branches, $Q_1 = Q_2 + Q_3$. RBC flux balances for all branches obey eq. 21. To compute the desired RBC split, an ideally mixed tracer is first considered. In biphasic blood flow erythrocytes preferentially travel inside the thicker branch. The RBC concentrations in the two daughter branches are different; discharge hematocrit H_2 and H_3 are therefore not identical.

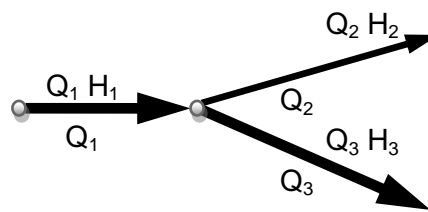


Figure 13 Schematic of a bifurcating vessel carrying biphasic blood flow composed of RBC and plasma phase. Branch 3 receives more bulk blood, Q_3 , and disproportionately more RBCs, $Q_3 \cdot H_3$, than the weaker branch 2.

Daughter branches that are fed with equal volumetric bulk flow rates receive unequal RBC fluxes if they have different diameters³¹⁻³². Empirical observations of the plasma skimming phenomenon^{22,27,34} have documented that daughter vessels with smaller diameters receive more plasma and less RBCs than their sister branches. The thin daughter branch hematocrit is equal to the concentration of the feeding branch, H_1 , minus the hematocrit depletion, ΔH . However, this unknown hematocrit depletion term cannot be used to reduce the degrees of freedom to solve split of hematocrit. By rewriting the hematocrit depletion in terms of an adjusted discharge hematocrit, H^* , and the known plasma skimming coefficient, θ , as shown in eq. 23, plasma skimming can be solved. The kinematic plasma skimming coefficient, θ , is defined in eq. 24 as a function of the diameter ratio of the daughter branch relative to the parent branch and the drift parameter M . By using these terms to express the hematocrit depletion, the discharge hematocrit into the daughter branches is computed by solving the RBC split balance in eq. 25. The volumetric flow rates, Q , are already known, and the parent vessel hematocrit is either the solution of a separate bifurcation equation in the interior of the domain, or a known value at its boundary. This leaves eq. 25 with exactly one unknown, the adjusted discharge hematocrit, H^* for any number of branches. This novel RBC split method correctly enforces RBC conservation for any number of daughter branches.

$$H_2 = H_1 - \Delta H = \theta_2 \cdot H^* \qquad H_3 = \theta_3 \cdot H^* \qquad 23$$

$$\theta_2 = \left(\frac{A_2}{A_1}\right)^{\frac{1}{M}} \qquad \theta_3 = \left(\frac{A_3}{A_1}\right)^{\frac{1}{M}} \qquad 24$$

$$Q_1 H_1 = Q_2 H_2 + Q_3 H_3 = Q_2 \theta_2 H^* + Q_3 \theta_3 H^* \qquad 25$$

Given that both daughter branches in real vascular bifurcations are typically leaner than the feeding parent vessel, the cross sectional ratio of daughter to parent branch is less than unity, $\theta_2 < 1$, $\theta_3 < 1$, and also $\theta_2 < \theta_3$. The functional relationship of the skimming coefficient θ and the drift parameter M are shown in Supplemental 2. A commented example with implementation

details is given in Supplemental 3. The proposed phase splitting law can easily be extended to trifurcations, anastomoses, as well as loops with multiple inlet and outlets. These geometries are essential for modeling capillary beds. The tube hematocrit is determined using the steady state rheological drift-flux theory, described in more detail in Supplemental 1.

Model 3 Parameterization of the Drift Parameter M

Figure 14 shows the functional relationship of the skimming coefficient θ and the drift parameter M . Large M values diminish the degree of phase separation for a given diameter ratio as expected. Also, θ tending to unity weakens the plasma skimming effect, leading to a RBC split equal to that of an ideally mixed tracer. The drift term M reflects the balance of RBC collision forces and wall induced forces. When collision forces dominate ($M \gg 1$), the CFL shrinks, causing the RBC phase to behave like a well-mixed solute. Conversely, $M=1$ marks a shift towards wall induced forces, widening the CFL and increases the effect of plasma skimming. For the parameter ranges of $M < 1$, such as $M=0.5$ shown in Figure 14, the plasma skimming coefficient θ would be smaller than the cross sectional ratio. Very small θ values produce unrealistically low hematocrit in the thin branch. Therefore the range of $M < 1$ was considered inadmissible in our hematocrit phase splitting law.

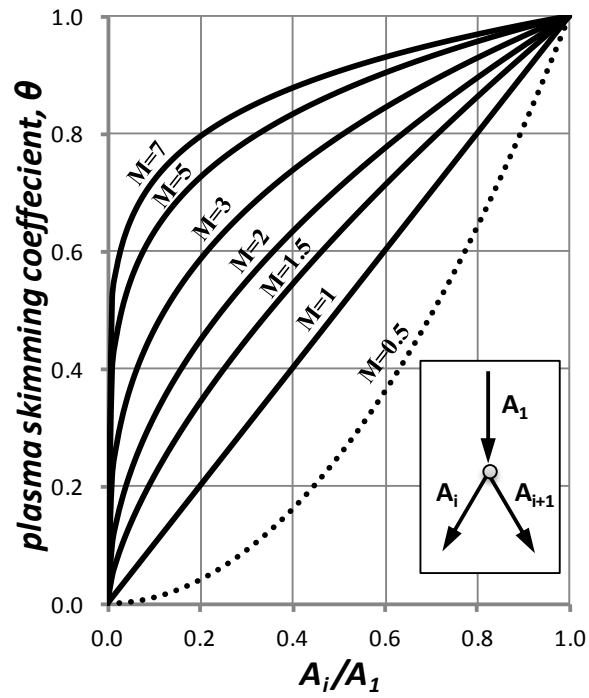


Figure 14 Correlation of the plasma skimming coefficient θ for each daughter branch diameter as a function of different drift parameters M . As M increases, θ tends towards unity for all diameter ratios. $M < 1$ are inadmissible

The parametric value M was determined by data fitting the RBC flux ratio of the two daughter branches with bifurcation data. In the individual bifurcation data, $M=1.13$ gave a mismatch error of 3.2% in the thin branch and 2.5% in the thick branch, which is less than spontaneous velocity variations reported⁴⁶ in the measured data of 5%. Optimization of the M parameter was re-performed on a larger mesentery network with the ratio of individual vessel discharge hematocrit over systemic hematocrit used as the control variable. Compared against intravital microscopy measurements of the rat mesentery³⁴, $M=5.25$ gave the best fit. This value of M was used in all subsequent network simulations.

In theory, the drift parameter might be a function of the vessel caliber that would be adjusted to the CFL thickness. Mechanistic models to compute the CFL thickness are available in the literature^{24,47}. However, data fitting for a diameter dependent parameter would require more data sets containing microvascular bifurcations with exact measurements of branch diameters and discharge hematocrit. Such data sets are unavailable at this time.

Iterative solution method for the plasma skimming models

A flowchart of the iterative methods for all models is summarized in Figure 15. Because flow and hematocrit computations are coupled, a fixed point iteration approach was adopted. Initially, the discharge hematocrit, H_d , is set to the systemic hematocrit, H_{sys} . Then, the bulk blood flow is solved by computing the vascular resistance, α , for every vessel using eq. 20. The volumetric blood flow rate, Q , follows from mass conservation in eq. 19. The updated discharge hematocrit H_d' is then computed using one of the three different plasma skimming models. Once the discharge hematocrit is computed, it is reinserted into the bulk flow computation as an adjustment of the vascular resistance using eq. 20. The bulk flow vector, Q , is then utilized to recompute the discharge hematocrit. This iterative bulk flow procedure constitutes the *outer loop*, and continues until the infinity norm of the difference between the old H_d and the H_d' update has reached a tolerance level of $r < 10^{-5}$.

For the *inner* loop, each model has a different procedure for the discharge hematocrit update, H_d' . Since Model 1 requires knowledge of the upstream parent vessel discharge hematocrit, H_1 , to compute the RBC split in the bifurcation, a nested iteration is required. Figure 15A shows the additional nesting level of the inner loop due to the implicit dependence of the hematocrit computations. Successive underrelaxation is used for the non-linear hematocrit field updates. For every pass of the outer loop, the non-linear inner loop must be fully converged. The convergence criterion of the inner loop is also set for the infinity norm of updates to be smaller than a tolerance level of $\varepsilon=10^{-5}$. An indirect iterative solution is adopted due to the large number of vessels and resulting equations for the *inner loop*. It should be noted that this iterative procedure is used to compute the discharge hematocrit only. Because the discharge hematocrit is solved in the inner loop by enforcing mass conservation, an additional step is not required in the outer loop to ensure that mass is conserved throughout the system. The tube hematocrit is determined as function the discharge hematocrit and vessel geometry described in Supplemental 1 using eq. 31.

Model 2 solves the hematocrit potential, \hat{H} , at every vessel junction using elliptical equations described in eq. 22, and shown in Figure 15B. The diffusion type problem can readily be solved with a Poisson solver. In Model 3, the discharge hematocrit can be solved for every bifurcation using the linear equations 23-25 with the blood bulk flow field, Q , coming from the outer loop computations. In contrast to Model 1, the inner loop of Model 3 is linear.

Network Effects may lead to Hemoconcentration more than unity

At each bifurcation, plasma skimming causes a daughter branch to become more hemoconcentrated. Over a large network, this concentration effect may lead to H_d' values greater than or equal to unity. To ensure that H_d' remains less than unity, hematocrit transport from parent to daughter branch in highly hemoconcentrated vessels may be treated as a simple convection problem by adjusting the plasma skimming coefficient, θ , to one. A hematocrit

threshold parameter t is introduced, which is initially set to 0.9. During the inner loop computation shown in Figure 15, H_d' at each vessel is compared to t . If H_d' is less than t , θ for that vessel is set to one. After each pass of the inner loop, if H_d' in any vessel is greater than unity than t is decremented by 0.05 and a sub-loop is introduced. This sub-loop sets θ to one when H_d' is more than t , re-computes H_d' as a function of θ and decrements t . This sub-loop is repeated until H_d' is less than unity everywhere.

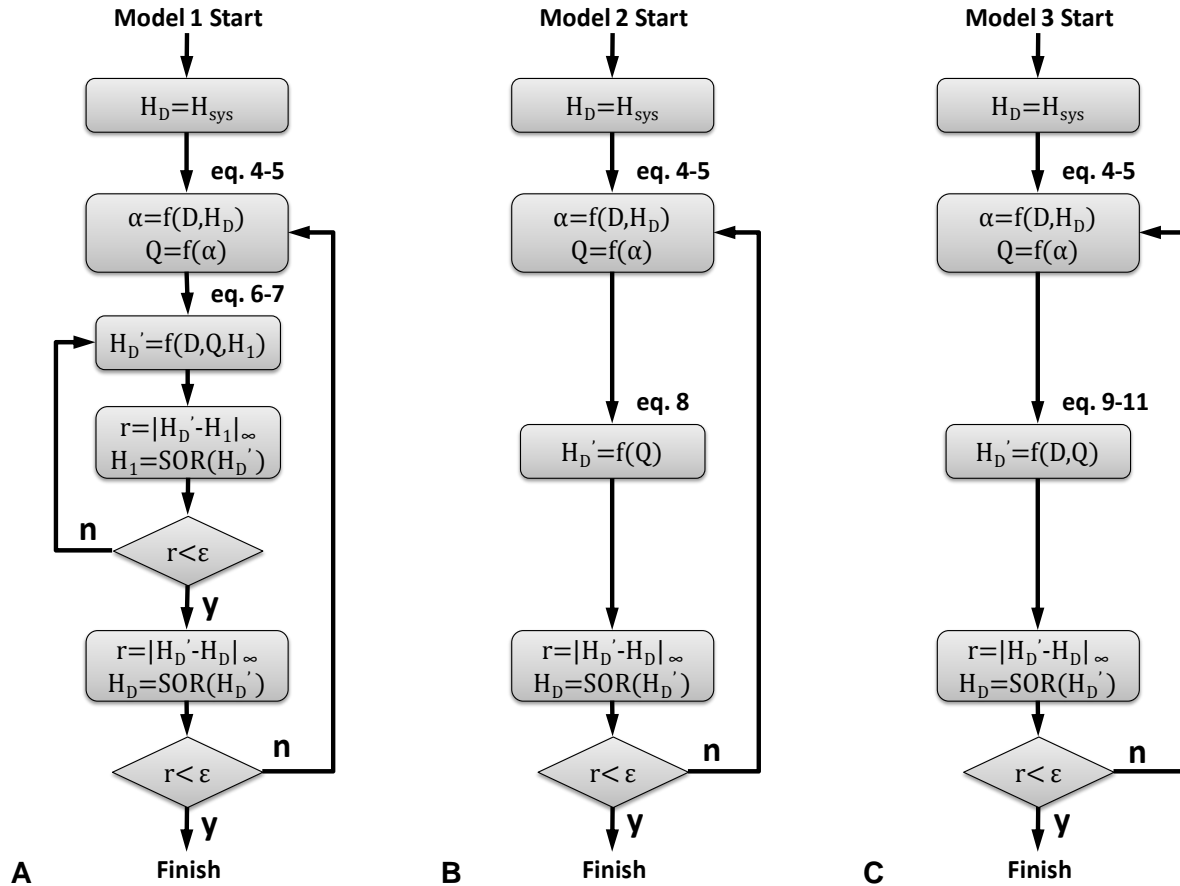


Figure 15 Flowchart describing the implementation for each of the models to solve for the bulk blood flow, Q , and discharge hematocrit, H_d ; **A.** Model 1, **B.** Model 2, and **C.** Model 3. Since Model 1 requires knowledge of the upstream hematocrit to compute the RBC split at a bifurcation, the inner loop is non-linear. In contrast, Model 2 and 3 have a linear inner loop. D is the vessel diameter, α is the flow resistance, and the tolerance is $\epsilon=10^{-5}$.

Tissue Oxygenation

Oxygen transfer from blood to tissue was computed using a previously developed dual-mesh technique⁸. The impact of RBC distribution on tissue oxygenation was quantified via the oxygen transfer model given in Supplemental 2. This model has two main compartments, blood flowing in the microcirculation and tissue in the extravascular spaces. Hemoglobin-bound oxygen is transported by convection with the RBC phase, and transfers through the endothelial cell layer into the extravascular space where tissue oxygen is moving by hindered diffusion⁴⁸ and consumed according to the metabolic rate. The physiologically accurate microvascular network was embedded into an extravascular volumetric mesh composed of 77,500 square tissue cells with 20 μ m side length. Each vessel segment is assigned to a unique tissue cell; each tissue cell may contain multiple blood vessels. The arterial inlet oxygen partial pressure was set to $pO_2=65.4\text{mmHg}$ ⁴⁹. Oxygen tensions in all blood vessels of the physiologically accurate microvessel networks and inside the spatially distributed tissue spaces were computed at steady state.

Results

Predictions of the three models were compared with experimental plasma skimming data acquired from rodent microcirculatory networks^{34,46}. Discharge hematocrit distributions were computed using each model. The effect of RBC phase separation on spatial distribution of oxygen was also quantified and judged against measured data⁴⁹⁻⁵⁰.

Hematocrit distribution in single bifurcations

Pries⁴⁶ performed experiments on a single bifurcation in the rat mesentery using a multidetection intravital microscope. Tube hematocrit was determined using an *in vitro* calibrated optical density method, from which discharge hematocrit was determined. The relative bulk flow through the branches was controlled by gradually increasing the downstream

resistance for daughter branch 1 with a clamp. Discharge hematocrit and bulk blood flow through each branch was measured and raw experimental data is plotted in Figure 16.

The RBC flux ratio of both daughter branches was predicted with each of the three biphasic models for the experimental range of fractional blood flow γ , as shown Figure 16. Model 1 predictions shown as a solid line in panel A show that for lower fractional blood flows, the thin daughter branch receives fewer RBC than an ideally mixed tracer. In the thick branch, the model predictions agree with the experimentally observed hemoconcentration. Overall, Model 1 matches the trend with a residual sum of squares, $RSS=0.017$. We also computed the RSS for the empirically fitted *in vitro* model presented in the original study⁴⁶ ($RSS=0.01$). This data is not shown, as this *in vitro* model was a data fitting effort for this single case and does not scale to the generic bifurcation. The authors of this *in vitro* model do not recommend applying it to networks.

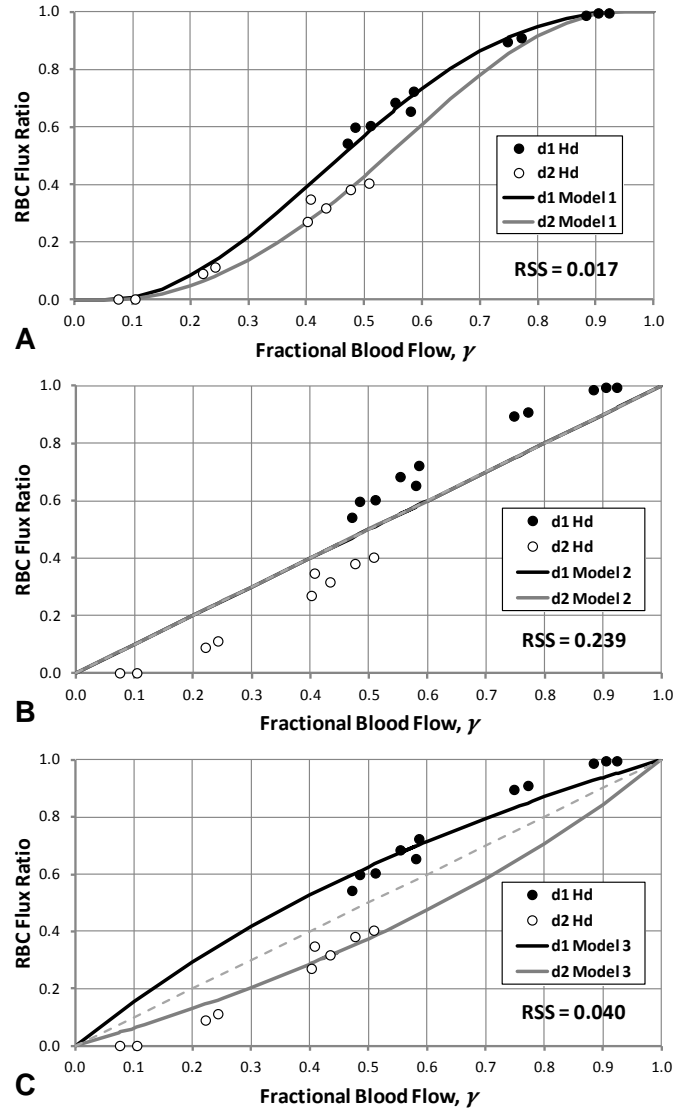


Figure 16 The RBC flux split fraction as a function of the fractional bulk blood flow, γ , on the ordinate in a single bifurcation in the rat mesentery⁴⁶. Circles show observed RBC split for varying flow rates forced by gradually constricting the thinner branch shown with open circles ($d_1=6\mu\text{m}$). Closed circles are used for the thicker branch ($d_2=8\mu\text{m}$). Solid lines show numerical results for the thin (black) and thick (gray) branches as predicted by **A.** Model 1, **B.** Model 2, and **C.** Model 3 ($M=1.13$). The residual sum of squares, RSS , is reported. Model 1 shows the best match to empirical data. Plasma-skimming pattern is observed both in Model 1 and the Model 3. The grey dashed line represents a well-mixed contrast agent dividing equally between the two daughter branches.

Model 2 shows a linear trend of hematocrit splitting in a single bifurcation, predicting RBC fluxes equal to that of an ideally mixed tracer for all flow ranges. The residual values for this single bifurcation study are large with $RSS=0.239$. This proportional splitting of RBC fluxes is due to the equal outlet hematocrit potentials at both outlets. However, Model 2 is capable of predicting unequal RBC splitting when several bifurcations are arranged in series, as shown in the original paper³¹.

Model 3 captures the non-linear relation between fractional blood flow and the RBC flux ratio. For all ranges of γ , the RBC split ratio agrees reasonably with the experimental trends. The statistical correlation between the measurements and the predictions gives a fit with $RSS=0.040$. It is worth noting that despite its simplicity, Model 3 has a similar match to the empirical single bifurcation data as the non-linear Model 1 plasma skimming law.

Hematocrit distribution in the rat mesentery network

Raw data was obtained from the literature of a 31mm^2 section of rodent mesentery, scanned with a multidiode silicon target camera using flash illumination³⁴. Approximately 100 microscopic monochromatic images were stitched together to map a sizable territory shown in Figure 17A. Diameter distribution histograms were reported on all 1,303 vessels in this section. Continuous recording and flash images were used to measure the discharge and tube hematocrit for all vessels; measurements were reported as scatter plots and histograms. Hemodilution was observed in thin branching vessels; hemoconcentration was observed in the main arteriole trunk. All vessels were reported to have a hematocrit of at least 10% of the systemic hematocrit³⁴.

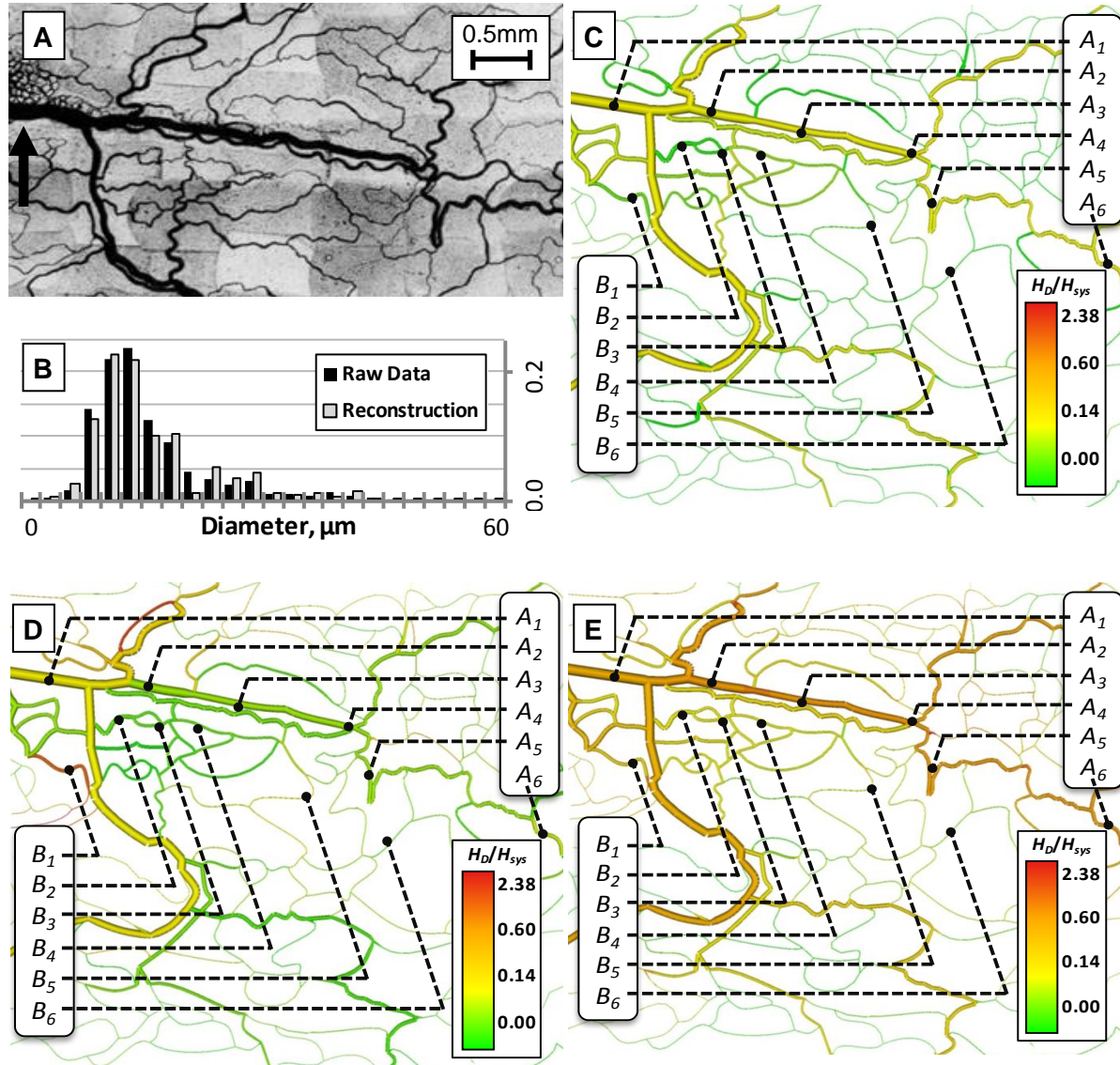


Figure 17 Spatial distribution of discharge hematocrit as predicted by three models. **A.** Image of the network shown in microscopic monochromatic images^{34,51}, with arrow indicating the arterial inlet. A large vessel trunk spans the microvessel image from right to left, bifurcating near the inlet to form a side branch that curves downwards. As the main trunk near advances towards the right portion of the image, it bifurcates into two smaller branches that follow a tortuous path toward the edge of the domain. **B.** Manual reconstruction of the image captured vessel morphology features and diameter distributions. Histogram shows matching diameter spectra between original image and reconstruction. Vessels of interest were identified at key side branches (B_1 - B_6) and along the main arterial trunk (A_1 - A_6). Spatial distribution of discharge hematocrit (H_D) as computed by **C.** Model 1, **D.** Model 2, and **E.** Model 3. Vessels empty of RBCs are shown in yellow. Model 1 predicts many capillaries without any RBCs. Both Model 1 and Model 3 show hemoconcentration in the arteriole trunk from left to right, Model 2 shows hemodilution in main vessels in direct opposition to the plasma skimming experiments. Numerical values are listed in Table VI. Frame A reproduced from original work³⁴ with publisher permission.

Network connectivity, topology and diameter distribution were reconstructed from the monochromatic images shown in Figure 17A using manual image reconstruction techniques⁵²⁻⁵³ to capture the vessel connectivity and match the diameter spectrum shown in the Figure 17B. The mesentery vascular morphology was captured in two parts. First, vessel tortuosity was captured by hand using a network reconstruction tool ImageJ⁵⁴. This tool allows users to carefully trace the vascular topology, obtaining vessel connectivity's and lengths. The vessel diameter spectra shown in Figure 16B depicts the reasonable match between the original data³⁴ and the reconstructed model.

Table VI Comparison of H_d and partial pressure (pO_2) to model predictions in rat mesentery

Side Branches	Experimental Data			Model 1		Model 2		Model 3	
	$D, \mu\text{m}$	$p\text{O}_2, \text{mmHg}^{49}$	H_d/H_{sys}^{34}	H_d/H_{sys}	$p\text{O}_2$	H_d/H_{sys}	$p\text{O}_2$	H_d/H_{sys}	$p\text{O}_2$
B_1	44.1	--	0.75- 0.55 range	0.74	50.72	2.35	65.89	0.74	66.09
B_2	27.0	65		0.74	66.06	0.38	67.63	0.67	67.14
B_3	20.4	61		0.71	63.02	0.29	68.30	0.58	67.50
B_4	16.1	66		0.45	57.41	0.43	49.56	0.55	49.67
B_5	7.5	62		0.40	17.31	0.64	00.00	0.53	51.23
B_6	7.3	62		0.00	0.00	0.52	00.00	0.53	49.56
Arterial Trunk	Experimental Data			Model 1		Model 2		Model 3	
	$D, \mu\text{m}$	$p\text{O}_2, \text{mmHg}^{49}$	H_d/H_{sys}^{34}	H_d/H_{sys}	$p\text{O}_2$	H_d/H_{sys}	$p\text{O}_2$	H_d/H_{sys}	$p\text{O}_2$
A_1	60.0	---	1.00- 1.50 Range	1.02	65.45	1.02	65.44	1.02	67.68
A_2	51.3	---		1.07	65.65	0.69	61.48	1.19	67.10
A_3	39.6	65		1.12	65.75	0.69	59.48	1.21	67.64
A_4	21.7	67		1.26	64.75	0.67	57.43	1.24	65.51
A_5	24.8	61		1.31	64.85	0.67	56.23	1.26	65.30
A_6	18.8	61		1.56	63.58	0.46	54.02	1.42	63.47

At the inlet artery marked with an arrow in Figure 17A, the systemic hematocrit was set equal to original⁵⁵ measurements, $H_{sys}=0.42$. To enhance segment tortuosity, we applied Bezier approximation with a scalar tortuosity value of $\alpha_B=0.25$ as described previously⁸. Inlet pressure was set to 85mmHg ($D=56\mu\text{m}$) and outlet pressures of vessels leaving the domain were set using a diameter-dependent pressure function⁵⁶⁻⁵⁸. The perfusion in the rat mesentery has been measured as $119.8\pm 5.7\text{mL/min/100g}$ using a continuous arteriovenous oxygen difference analyzer⁵⁹. The bulk flow computations in eq. 19-20 gave a total tissue blood perfusion of 113.2mL/100g/min (Model 3). The predicted tissue perfusion between each model differed by less than 1.5%.

Model 1 predicted hemodilution in side branches (B_1 - B_6 in Figure 17B) from $H_d/H_{sys}=0.74$ to 0.00. Hemodilution was experimentally observed as $H_d/H_{sys}=0.75$ in arterioles branching from the larger artery, down to $H_d/H_{sys}=0.55$ in more distal branches³⁴. Moreover, many capillaries receive little or no RBCs, such as vessel B_6 in Table VI and all green vessels in Figure 17B. For the vessels of the main trunk (A_1 - A_6), hemoconcentration is predicted with the range of $H_d/H_{sys}=1.02$ - 1.56 , this is in excellent agreement with experimental data of $H_d/H_{sys}=1.00$ - 1.50 .

Model 2 predicts hemoconcentration for small side branches (B_1 - B_6 in Figure 17C). Some vessels reach the unrealistically high value of $H_d/H_{sys}=2.35$, indicating that bulk flow through the vessel is entirely made of red blood cells. Hemoconcentration in the smaller side branches consequently cause hemodilution in the larger arterioles. In the main trunk (A_1 - A_6), the relative hematocrit drops from 1.02 to 0.46. Hemodilution of the main artery with simultaneous hemoconcentration in side braches is opposite to the trends observed *in vivo*. Because of its *unrealistic* phase separation predictions, we did not further consider Model 2 in subsequent analysis.

The hematocrit distribution predicted by Model 3 is displayed in Figure 17D. The results show a physiological hemodilution of $H_d/H_{sys}=0.74$ - 0.53 for small side-branching vessels (B_1 -

B_6). The computed range for the side branches is closer to experimental values than Model 1. In addition, Model 3 predicts that none of the capillaries are completely devoid of erythrocytes at steady state. In the main arterial trunk (A_1 - A_5), hematocrit is concentrated from $H_d/H_{sys}=1.02$ - 1.42 . The extent of hemoconcentration is slightly smaller, because more RBCs are discharged into the capillary bed.

Hierarchical distribution of hematocrit.

The hematocrit distribution in vessels of varying diameters was further investigated. The results are summarized in the histograms shown in Figure 18, where the blood vessels are grouped into different bins based on their discharge hematocrit and diameter. Darker colors indicate more concentrated discharge hematocrit values.

Model 1 predicts many capillaries with low hematocrit ($H_d/H_{sys}<0.13$, or $H_d<0.06$). Numerous capillaries have zero hematocrit; these vessels have been labeled as “zero RBC vessels.” Model 3 predicts that all capillaries have $H_d/H_{sys}>0.10$, matching the lower hematocrit threshold recorded experimentally^{34,60}. This phenomenon and its consequences for predicting oxygen transfer to tissue are discussed in more detail in the next section.

Tissue oxygen supply in the rat mesentery network

To study the impact of hematocrit distribution on tissue oxygenation, we collected experimental oxygen data in the microcirculation and in the extravascular tissue. The oxygen partial pressure measured with phosphorescence quenching microscopy (PQM)⁴⁹ was $pO_2=65.7\pm 2.4$ mmHg for arterioles with $D=28.4\pm 0.6$ μ m. Average tissue oxygen tension measured with PQM⁵⁰ were $pO_2=34.1\pm 7.8$ mmHg. The total oxygen consumption measured in the rodent mesentery using a dual-beam spectrophotometric method⁵⁹ was 3.40 ± 0.21 mL/min/100g.

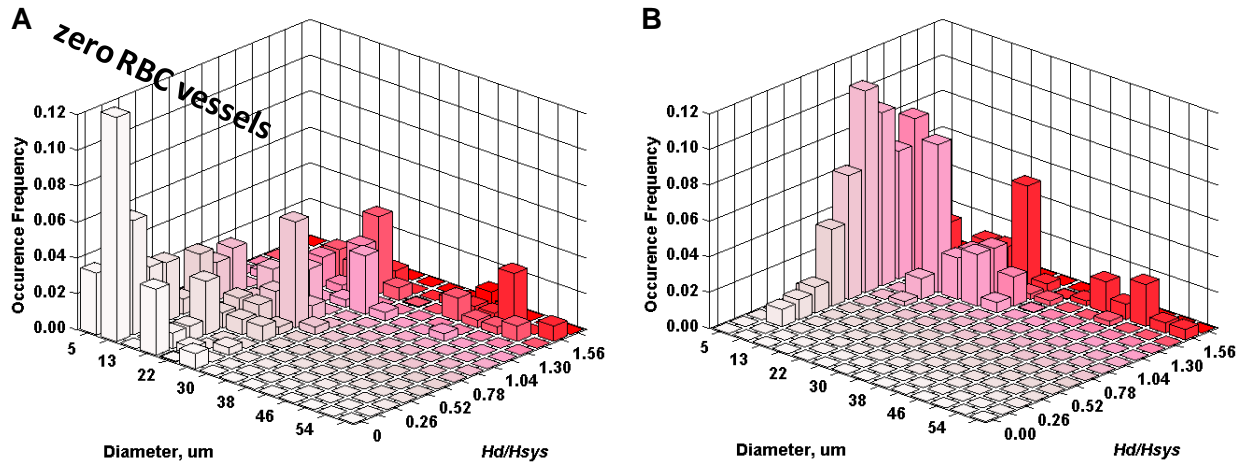


Figure 18 Distribution of discharge hematocrit in small vessels as predicted by **A.** Model 1 and **B.** Model 3. Bars shown in white indicate vessels with no RBCs. Model 1 has a high incidence of zero RBC vessels, which are mostly capillaries. Model 3 predicts no RBC-free vessels.

Figure 19A depicts the oxygen in the blood and tissue predicted by Model 1. The computed tissue oxygenation is relatively low in comparison to the experimental values. Also, oxygen tension for smaller branching arterioles ($D < 10\mu\text{m}$) was below 18mmHg in B_5 - B_6 . This prediction is well below PQM measurements⁵⁰ of $62.6 \pm 2.9\text{mmHg}$, as shown in Table VI. Additionally, the average mesentery tissue partial oxygen pressure predicted by Model 1 of $24.4 \pm 5.2\text{mmHg}$ is about 28% lower than the measured level of $pO_2 = 34.1 \pm 7.8\text{mmHg}$. The low tissue oxygen tension leads to a predicted *oxygen consumption* of 2.56mL/min/100g , roughly more than two thirds of the experimental level.

The oxygen tension in arterioles (A_1 - A_6) for Model 3 was 63-65mmHg as shown in Figure 19B and Table VI; this is comparable to measurements obtained by PQM. The average tissue oxygen partial pressure predicted by Model 3 was $pO_2 = 29.1 \pm 3.1\text{mmHg}$, which is a similar range as the measured value of $34.1 \pm 7.8\text{mmHg}$. In Model 3, more oxygen is distributed to the tissue than in Model 1. Model 3 gives oxygen consumption of 3.35mL/min/100g ; this is closer to the experimental values than Model 1.

The effect of low-hematocrit capillaries on oxygen tension

An investigation was conducted to uncover the possible causes of low tissue oxygen tension predicted by Model 1. Oxygen exchange from vessel to tissue was determined by mass conservation for every single blood vessel, reported as mmol/s. Blood vessels were segregated into groups by diameter, and the mean oxygen exchange for each group was reported, as shown in Figure 20A. Oxygen exchange for each group is reported in bold and the percentage of oxygen exchange compared to the whole network is also reported. This figure illustrates that tissue oxygenation is very sensitive to small vessels with diameters less than $20\mu\text{m}$, which accounted for more than 95% of the total network oxygen exchange.

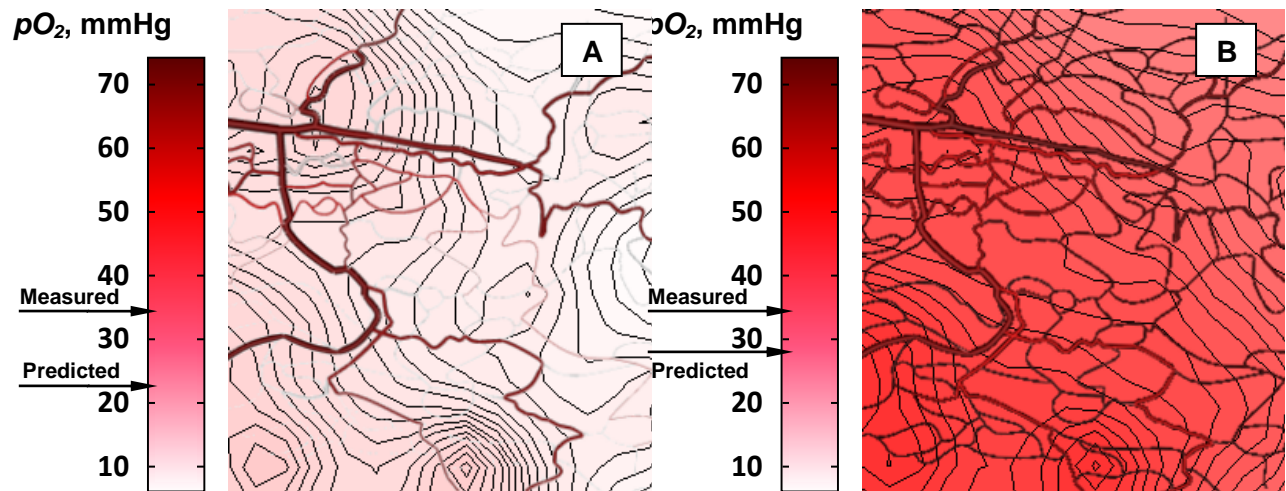


Figure 19 Tissue oxygen distribution to the mesentery tissue. Contour maps of oxygen tension in the mesentery tissue computed using 77,500 square mesh cells with 20 μ m side length. **A.** Model 1, and **B.** Model 3, with respective vessel oxygen tension. Arrows indicate *measured* physiologic tissue oxygen tension of $34.1 \pm 7.8 \text{ mmHg}^{50}$ and *predicted* average tissue oxygen tension for Model 1 ($pO_2 = 24.4 \pm 5.2 \text{ mmHg}$) and Model 3 ($pO_2 = 29.1 \pm 3.1 \text{ mmHg}$).

The hematocrit content of these small vessels was then investigated. The predictions of Model1 and Model 3 for the H_d/H_{sys} value for each vessel in the mesentery network was compared against raw data³⁴. Again, vessels were separated into groups by their diameter, and the mean value for each group was determined as shown in Figure 20B. The mesentery raw data is shown as dark grey bars, the predictions of Model 3 as light grey speckled bars, and the predictions of Model 1 as white bars. Analysis of the original rat mesentery³⁴ data shows that every diameter group has an average H_d/H_{sys} greater than 0.70. Additionally, not one vessel in the original data was reported with $H_d/H_{sys}=0$. For each group, Model 3 predictions matched the measured data set within one standard deviation. The comparison of Model 1 predictions against measured data has a statistically significant p -value ($p<0.01$) for diameters less than 30 μ m. This undersupply of RBCs to small capillaries also denies adjacent extravascular cells to oxygen supply, because these small vessels are the site of oxygen exchange with the tissue, as shown in Figure 20A.

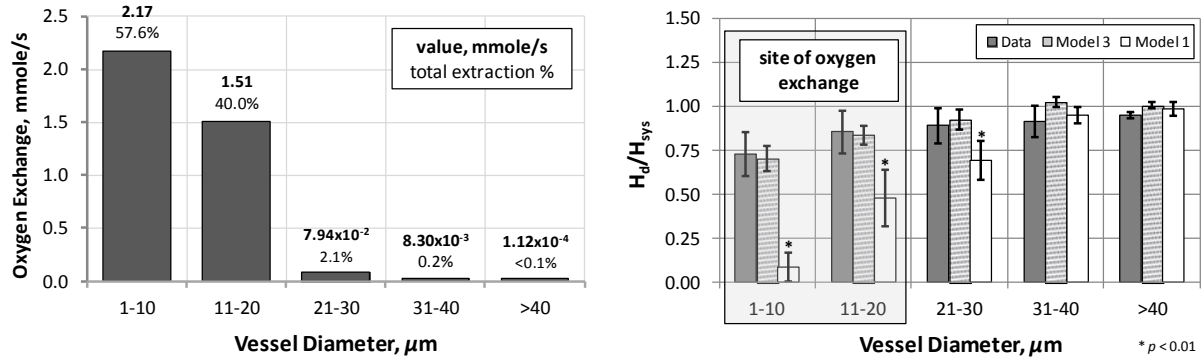


Figure 20 The sensitivity of effect of oxygen exchange on small vessel hematocrit. **A.** The percent of oxygen exchange duty by vessels grouped by diameter. Mean oxygen exchange values in mmol/s are reported in bold, and their corresponding percent are shown underneath. Vessels with diameter less than $20\mu\text{m}$ accounted for more than 95% of the total network oxygen exchange. **B.** A comparison of Model 1 and 3 predictions of H_d/H_{sys} against rat mesentery measurements³⁴, as grouped by diameter. The collected mesentery data is shown as dark grey bars, the predictions of Model 3 as light grey speckled bars, and the predictions of Model 1 as white bars. For vessels with diameter less than $30\mu\text{m}$, the large error between Model 1 predictions and measured mesentery data has a statistically significant p -value ($p < 0.01$), denoted by an asterisk.

Hematocrit distribution in the cremaster muscle

As an additional model validation, plasma skimming model predictions were compared against raw measurements of the hamster cremaster muscle. The discharge hematocrit measurements⁶¹ were acquired with an intravital microscope connected to a television system. The relationship between fractional blood flow, γ , and the *RBC flux ratio* in each daughter branch at every bifurcation is shown as open circles in Figure 21. A set of hamster cremaster bifurcations were designed using the microcirculatory sample trees given in the original paper⁶¹ in the size range of 3.6 to 6 μm . The fractional flow ratios between the parent and daughter branches were aligned with the original study for the analysis. The predictions of Model 1 and Model 3, shown as filled circles in Figure 21, reasonably correlate with the sigmoidal trend observed by Klitzmann⁶¹, also shown. Model 1 predicts that 33% of vessels are empty of RBCs, which are marked as filled gray circles and labeled as non-physiologic RBC free vessels in Figure 21A. Model 3 in Figure 21B shows no vessels with zero hematocrit over the entire bulk flow range in agreement the cremaster data.

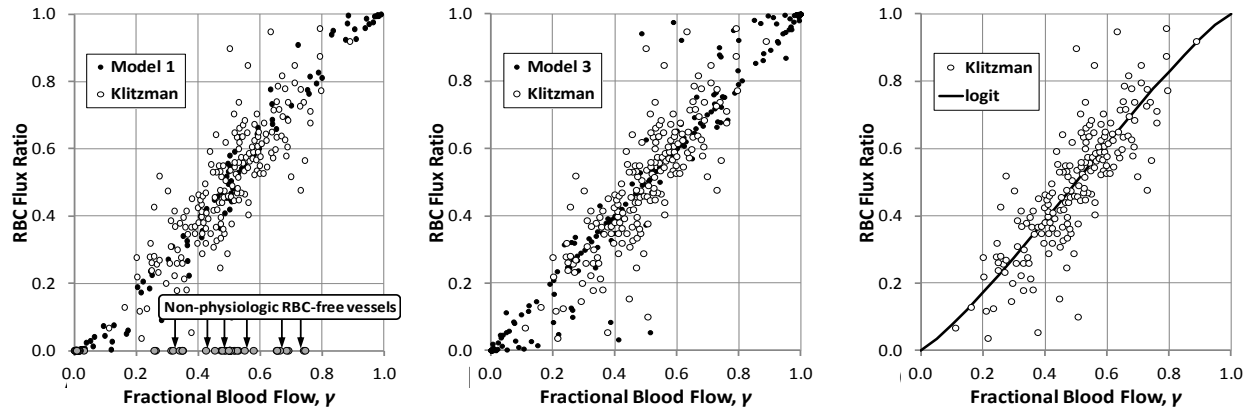


Figure 21 Measured and computed RBC flux split as a function of volumetric blood flow. Empty circles showing measurements from the hamster cremaster muscle⁶¹ are compared against numerical predictions shown as filled circles from, **A.** Model 1, and **B.** Model 3. The *logit* function proposed by Klitzman⁶¹ is shown as a solid black line in **C.** While the experiments show no RBC free vessels, Model 1 includes many vessels carrying no RBCs marked as gray circles. Model 3 predicts no vessels with zero hematocrit in agreement with the experiment, as does the *logit* function.

Discussion

Computer predictions for the RBC distribution in large microvascular networks using a novel phase skimming law were presented and compared with predictions from two prior models in the literature. *Plasma skimming in a single bifurcation* was predicted correctly by Model 1. For bifurcations with almost even flow, Model 1 showed some deviations from the experimental data. Model 2 does not capture non-linear phase splitting phenomena in a single bifurcation. The inability of predicting phase separation in single bifurcation was also reported in the original description of this method³¹. The robust prediction of Model 3 is continuous for all blood flow ranges, and closely matches measured data whether the daughter branches receive equal or disparate blood flows. This single bifurcation study shows that the comparison of measured physiologic data to model predictions is comparable between Model 3 and the more complex non-linear Model 1. It also shows that for a single bifurcation, Model 2 is incapable of producing physiologically meaningful results. In order to fully comprehend the physiological impact of the plasma skimming law however, these models must be compared using a microcirculatory network.

For *mesentery networks*, Model 2 concentrates RBC in side branches, in direct opposition to the plasma skimming phenomenon observed *in vivo*. This result does not support its main hypothesis for the *existence of a hematocrit potential*. Both Model 1 and Model 3 correctly predict plasma skimming in side branches that gradually become more concentrated in plasma in qualitative and quantitative agreement with measured data^{34,55}. The main difference concerns the capillary bed for which Model 1 predicts sections with no RBCs at all, while all capillaries in Model 3 have at least 10% of the systemic hematocrit. This minimum threshold of capillary hematocrit has been observed in both rodent and feline measurements^{34,60}, and is reflected in the mesentery study presented in Figure 21.

The prediction of RBC-free vessels by Model 1 results in hemoglobin-bound oxygen perfusion calculations that deviate significantly from measured tissue oxygen tension. Model 3 matched the experimental PQM results within 10%, while Model 1 deviated more than 70% from the measured data (PQM: $3.40 \pm 0.21 \text{ mL/min/100g}$, Model 1: 2.56 mL/min/100g , Model 3: 3.35 mL/min/100g). The error in Model 1 cannot be attributed to model uncertainty, because all parameters for mass transfer, metabolism and hindered oxygen diffusion⁶² were held at the same values in both computations. This error is due to the differences in capillary hematocrit.

Further investigation of the capillary bed hematocrit reveals the effects of problematically low hematocrit predictions by Model 1. The study of diameter-based oxygen exchange in Figure 20A using Model 3 reveals that microvessels with diameters less than $20 \mu\text{m}$ are the major site of oxygen exchange. These capillaries contribute the most, due to their high surface area to volume ratio as well as their low resistance to oxygen mass transfer through the endothelium. Therefore, physiological hematocrit in the capillary bed is critical for accurate oxygen exchange predictions. Model 1 fails to adequately supply the capillary bed with the oxygen-enriched hematocrit it needs to properly supply the surrounding tissue. As shown in Figure 20B, Model 1 grossly undersupplies vessels with $d < 20 \mu\text{m}$ when compared against measured rat mesentery H_d/H_{sys} values.

The frequency of RBC-devoid vessels predicted by Model 1 directly depends on the level of a model-specific cutoff parameter, X_0 . This parameter determines the minimum volumetric bulk flow of a daughter branch to receive any RBC flux. As the definition of this threshold value has changed in previous version of Model 1, so has the prediction of RBC-devoid vessels. All versions of Model 1 predict some fraction of blood vessels to be devoid of RBCs, leading to RBC-free vessels. Even though at any part in time, a fraction of microvessels may contain low or zero hematocrit, a sustained lack of RBC perfusion would lead to tissue death and is not realistic for steady state simulations.

The large fraction of RBC-free vessels in Model 1 steady state raises concerns with its consistency of oxygen predictions. Steady state perfusion should be distinguished from dynamic snapshot observations of RBC distributions. Physiological studies⁶³⁻⁶⁴ have established that fluctuating bifurcation kinematics and RBC rouleaux formation render the RBC distribution in a vascular network a constantly changing spatiotemporal phenomenon. Branches with low hematocrit experience reduced effective viscosity and therefore a decrease in vascular resistance. This augments blood flow, which in turn elevates RBCs in that branch again, raising the effective viscosity⁶³. The ebb and flow of RBC splitting at a bifurcation is a dynamic phenomenon. This spatiotemporal patchiness must be approached dynamically; a microvessel observed as having zero hematocrit at one time point will contain RBCs in another⁶⁴. Since blood plasma is a poor oxygen carrier, capillaries cannot be permanently free of RBC without consequent tissue damage¹⁷. Yet, temporal fluctuations are not reflected in the steady state predictions such as Model 1-3. Figures 5-8 show that Model 1 predicts large sections of the mesentery microcirculation are drastically low in RBC flux, leading to insufficient oxygen supply to surrounding tissue. Even as a temporal snapshot, Model 1 predicts a fraction of RBC-free vessels (33%) which greatly exceeds confocal microscopy⁶⁴ dynamic hematocrit measurements (3.6%). In summary, steady state plasma skimming models should not yield physiologically unrealistic cases of vessels permanently free of RBCs. Temporal dynamics cannot be addressed with steady state model predictions, but can be studied with particle dynamics models^{33,65}.

Finally, the convergence times for Model 1 in the mesentery network (2198ms) were 2.3 times slower than Model 3 (968ms), as shown in Table VII. The predictive quality and computational complexity of the three models is summarized in Table VII.

Large-scale cerebral microcirculation. Model 1 requires the most expensive convergence time due to the non-linear plasma skimming law. CPU time difference was observed for the mesentery simulations shown in Table VII. To better illustrate the need for robust plasma

skimming computations in blood vessel networks, an application to predict tissue oxygenation of a three-dimensional model of the human microcirculation in the brain was implemented. This physiologically accurate morphology of a $3 \times 3 \times 3$ mm subsection of the microcirculatory blood supply to the human secondary cortex has been established in previous work⁸. This microcirculatory network has 36 penetrating arterioles and 12 draining veins connected via a contiguous capillary bed⁷⁻⁹. The microcirculatory network of over 256,000 vessels was embedded into an extravascular volumetric mesh composed of 600,000 cubic tissue cells of $34\mu\text{m}$ face length. Predicted partial pressure drop from arterioles to capillaries was 18.12mmHg, which is close to experimental data⁶⁶ of 19.7mmHg. Figure 22B shows the predicted microcirculatory hematocrit distribution between $H_d/H_{\text{sys}}=0.25-1.50$. Figure 22C shows oxygen tension with contours in three cortical layers at $z=0.30\text{mm}$, 1.35mm , and 2.40mm below the pial surface.

Table VII Drawbacks to models predicting the spatial distribution of discharge hematocrit

Issue	Model 1	Model 2	Model 3
Plasma Skimming in side braches	Y	N, opposite trend	Y
Hemocontration of main arterial tributaries	Y	N, opposite trend	Y
Physiologically range of capillary hematocrit H_d	N	N	Y
Avoidance of RBC free vessels, $H_d \neq 0$	N	Y	Y
Linear plasma skimming equations	N	Y	Y
Convergence time, mesentery (ms)	2198	756	968
Convergence time, larger network (ms)	N	1256	1527
Oxygen Extraction (PQM: 3.40mL/min/100g)	2.56	n/a	3.35
Average Tissue Oxygen (PQM: 34.1 \pm 7.8mmHg)	24.4 \pm 5.2	n/a	29.1 \pm 3.1

Moreover, the biphasic hemodynamic Model 3 transferred more oxygen deeper into the tissues $pO_2=40.84\pm0.06\text{mmHg}$ ($z=2.40\text{mm}$) compared to simulations performed at constant hematocrit, in which the deep layers only has $pO_2=30.25\pm1.93\text{mmHg}$ (computations not shown). It is important to note that the biphasic hemodynamics produces more even tissue oxygenation; the three layers had almost the same oxygen tension ($41.76\pm0.07\text{mmHg}$ at $z=0.30\text{mm}$, $41.76\pm0.06\text{mmHg}$ at 1.35mm , and $40.84\pm0.06\text{mmHg}$ at 2.40mm) despite the partial pressure drop in the penetrating arterioles. This uniformity cannot be realized using constant hematocrit, in which the deep layer had lower oxygen tension than the surface layer ($46.97\pm0.59\text{mmHg}$ at $z=0.30\text{mm}$, $42.66\pm0.12\text{mmHg}$ at 1.35mm , and $30.25\pm1.93\text{mmHg}$ at 2.40mm). Therefore, biphasic blood rheology seems to play a role in ensuring *even* tissue oxygenation throughout the cortex.

The cortical tissue section could not be computed with Model 1, as the plasma skimming formula cannot address trifurcations occurring in the cerebral capillary bed. As on the smaller mesentery model, Model 2 inaccurately predicts hemodilution in the large arterial trunks and hemoconcentration in the smaller side branches. For the cerebral topology, the result is hemodiluted penetrating arterioles and nearly RBC-devoid capillaries near the white-gray matter interface.

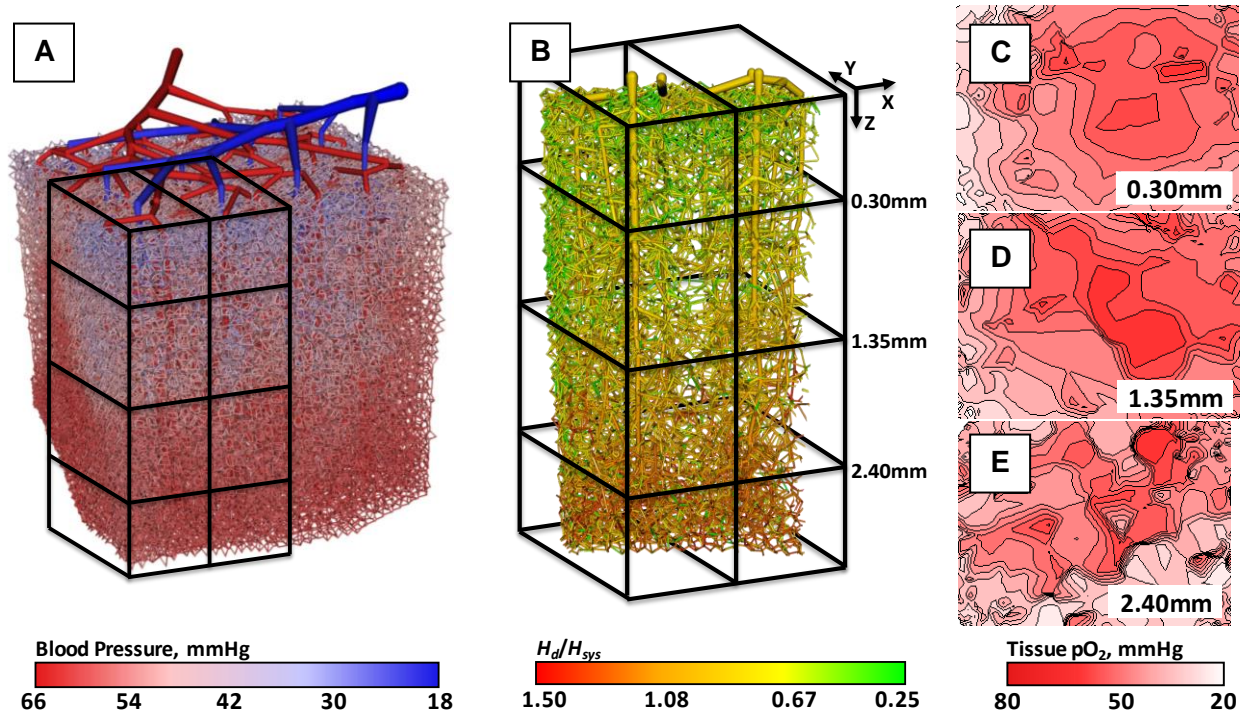


Figure 22 Computed tissue oxygenation in a 3x3x3mm section of the secondary human cortex predicted by Model 3. **A.** Predicted blood pressures, red marks high arterial, blue lower venous pressure regions. **B.** Hematocrit distribution in a small subsection supplied by six penetrating arterioles and three draining veins. Oxygen perfusion to tissue in three layers of the cerebral cortex **C.** 0.30mm, **D.** 1.35mm, and **E.** 2.40mm. Average oxygen tension in the three layers was 41.76 ± 0.07 mmHg (0.30mm), 41.76 ± 0.06 mmHg (1.35mm), and 40.84 ± 0.06 mmHg (2.40mm). Cerebral tissue near the surface of the cortex is well supplied. Model 3 predicts physiologic oxygenation in deeper layers (2.40mm) due to hemoconcentration in the penetrating arterioles. In contrast, constant hematocrit computations gave lower oxygen tension in deep tissue (30.25 ± 1.93 mmHg, computations not shown).

Limitations. This study outlines a new method for predicting the spatial distribution of RBCs in microvascular networks. One limitation of this study is that predictions for all three methods were compared against data obtained from literature instead of novel microcirculatory measurements. Additionally, the oxygen unbinding was simplified in this study by assuming equilibrium saturation according to the Hill equation for a constant pH value. Furthermore, the plasma skimming coefficient may be organ or species specific. Because we only had access to rodent mesentery and hamster cremaster muscle data, future studies may be required to assert the drift parameter (M) for other organs or other species including humans. Plasma viscosity was assumed to be 1.0cP, whereas measured plasma viscosity is closer to 1.3cP. Finally, the study was conducted at steady state, while dynamic simulations would be needed for reproducing the time dependent fMRI signals.

Conclusions and Future directions. This article discussed the effect of nonideal microcirculatory hemodynamics on oxygen exchange in large microcirculatory networks. Two existing hematocrit distribution models were evaluated and found to be incomplete. Model 1 predictions of RBC-devoid capillaries led to a severe undersupply of oxygen to brain tissue, while Model 2 failed to capture the correct trends in the microcirculatory plasma skimming. A new kinetic plasma skimming model (KPSM) was introduced which can predict biphasic blood flow, and tissue oxygen transfer at the cellular level. Comparison with experimental data from the rat mesentery and the hamster cremaster muscle showed it to be at least as accurate than previous models. Moreover blood flow and hematocrit field computations with KPSM converge faster, because the plasma skimming law is linear. The novel, two phase model is easy to implement, because it only requires bifurcation geometry and kinematic parameters. It is readily applicable to trifurcations, anastomoses, and loops occurring in the capillary bed. The better match of oxygen tension in blood and tissue is further evidence for the suitability of Model 3 for large scale microcirculatory blood flow simulations. The application of Model 3 to the three-

dimensional cerebral microcirculation in the secondary cortex lays the groundwork for future dynamic tissue oxygenation during simulated functional hyperemia.

Possible future works may include investigating the sensitivity of Model 1 on the feed hematocrit to better match tissue oxygen tension gradients. It may be possible to reduce this model's dependence on feed hematocrit, eliminating the need for the inner loop and greatly enhance simulation times. However, Model 1 describing steady state would still be unable to predict the RBC redistribution dynamics at a bifurcation.

Conversely, the novel kinematic phase splitting computations proposed in Model 3 can be extended for dynamic simulations and 3D computational fluid dynamic blood flow predictions. Dynamics could be accounted for with relative ease by simply incorporating a node hematocrit accumulation in eq. 25. Three dimensional spatial resolution would require force balances that explicitly quantify the effects of the RBC-RBC collisions and wall-induced forces. Ideas such as the diffusive collision term and a convective wall dispersion effect as proposed by Graham²⁰ would be a reasonable starting point. These driving forces, when simultaneously solved with the biphasic Navier-Stokes momentum balances, would result in the direct computation of the CFL layer thickness.

A robust method for determining plasma skimming is a milestone towards the larger goal of coupling of hemodynamic response to neural depolarization and metabolism. The logical next step would lead to a full coupling of cerebral blood flow and oxygen exchange. As stated by Hudetz⁶⁷, "...The principle mediators, their cellular sources and the molecular targets of flow-dependent cerebrovascular regulatory mechanisms must be coordinated with the roles of various microvascular components." A systemic model of vascular response to neuronal firing, such as the multimodal control approach proposed by Kleinfeld⁴, requires a holistic understanding of the spatial distribution of RBCs. This work is the first step in this direction.

Supplemental 1

Phase and bulk velocity as a function of phase flow regime

The ratio between the discharge and tube hematocrit can be computed analytically by integrating the volumetric flow of the RBC phase and the blood bulk over the cylindrical cross sectional area using RBC flow profile assumptions. In Figure 23A the flow profile of the RBC phase is assumed to have a plug flow profile with a constant cell concentration of H_{core} . The cylindrical radius r_0 , the CFL thickness, δ , and the radius of the cylindrical vessel, r_0 , are shown in eq. 26. The variable thickness of the CFL is dependent on vessel discharge hematocrit, H_d , and vessel lumen diameter³². As a first approximation, a constant CFL thickness was assumed to determine the tube hematocrit. The discharge hematocrit, not the tube hematocrit, is used to compute blood viscosity and the extent of plasma skimming and is not affected by this assumption. The high packing density of erythrocytes within the RBC phase leaves little room for plasma. The core concentration of erythrocytes, H_{core} , has been observed to be constant⁶⁸⁻⁶⁹.

The tube hematocrit, H_t , in eq. 27 integrates the hematocrit plug profile over the cross sectional area. The tube hematocrit is also related to the cross sectional area of the blood vessel, A_p , and the cross sectional area core of the RBC phase, A_e , which is equal to $\pi(r_0 - \delta)^2$. To compute the tube hematocrit, H_t , a flat velocity profile pertaining to a single file flow regime is assumed. For the determination of H_t , this flat profile is numerically indistinguishable from the slightly curved plug profile that has been empirically observed in microvessels.

$$H_t(r) = \begin{cases} H_{core} & 0 \leq r \leq r_0 - \delta \\ 0 & r_0 - \delta \leq r \leq r_0 \end{cases} \quad 26$$

$$H_t = \int_0^{r_0} \frac{2\pi r H_t(r)}{\pi r_0^2} dr = H_{core} \left(1 - \frac{\delta}{r_0}\right)^2 = H_{core} \frac{A_e}{A_p} \quad 27$$

The discharge hematocrit is defined as the ratio of the volumetric RBC cell flux, \dot{q}_{RBC} , divided by the bulk flux, Q , as in eq. 29. The bulk velocity profile, $v_z(r)$, is parabolic for laminar flow as given in eq. 28, where v_{max} is the maximum velocity.

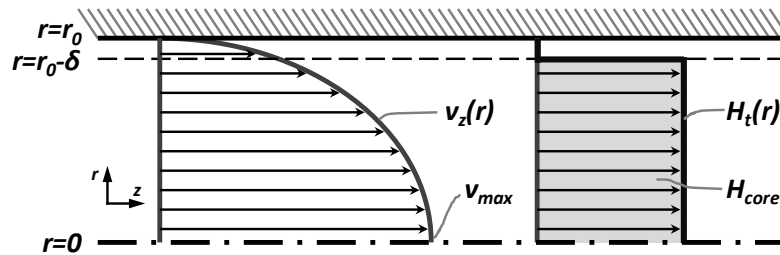


Figure 23 Flow profile integration of the bulk and hematocrit phase. Established laminar flow profile for the blood bulk, $v_z(r)$, and the plug flow profile $H_t(r)$ for the RBC phase with a local volume concentration of H_{core} . The RBC phase radially exists from $r=0$ to $r=r_0-\delta$, where δ is the thickness of the CFL and r_0 is the radius of the cylindrical vessel lumen. CFL thickness evaluated as $0.8\mu\text{m}$.

$$v_z(r) = v_{max} \left[1 - \left(\frac{r}{r_0} \right)^2 \right] \quad 28$$

$$H_d = \frac{\dot{q}_{RBC}}{Q} = \frac{\int_0^{r_0} 2\pi r H_t(r) v_z(r) dr}{\int_0^{r_0} 2\pi r v_z(r) dr} = H_{core} \left(1 - \frac{\delta}{r_0} \right)^2 \left[2 - \left(1 - \frac{\delta}{r_0} \right)^2 \right] = H_t \cdot \frac{u}{V} \quad 29$$

Using eqs. 27 and 29, the discharge to tube hematocrit ratio can be correlated as a function of CFL thickness, δ , and the vessel radius, r_0 , as shown in eq. 30, or in terms of the velocity ratio between the RBC phase, u , over the bulk, V .

$$\frac{H_t}{H_d} = \left[2 - \left(1 - \frac{\delta}{r_0} \right)^2 \right]^{-1} = \frac{V}{u} \quad 30$$

This equation can be rearranged to solve for the tube hematocrit, H_t , as a function of the discharge hematocrit, H_d , the outer radius of the vessel, r_0 , and the thickness of the vessel wall, δ as shown in eq. 31. This equation translates the tube hematocrit from the discharge hematocrit. This computation of tube hematocrit occurs after the completion of the iterative *outer loop* which is used to solve the nonlinear discharge hematocrit distribution problem.

$$H_t = H_d \cdot \left[2 - \left(1 - \frac{\delta}{r_0} \right)^2 \right]^{-1} \quad 31$$

Supplemental 2

Computation of tissue oxygenation

For tissue oxygenation, hemoglobin-bound, O_b , and unbound oxygen, O_u , must be distinguished. The concentration of unbound oxygen can be computed from the oxygen dissociation curves^{15,39}. While bound oxygen is convected with the RBC phase; only the unbound oxygen is free to diffuse from the plasma into the tissue. At equilibrium, the ratio between O_b and total oxygen, O_{tot} , can be described by the Hill equation given in eq. 32. The saturation of oxyhemoglobin, σ , depends on the oxygen tension at pH=7.4 and 50% saturation³⁹ (P_{50} =29.3mmHg), and the Hill constant³⁹ (n =2.2). Computed tissue and blood oxygen concentrations were converted to partial pressures as described elsewhere⁷⁰.

Hill equation for oxygen saturation

$$\sigma(O_b) = \frac{O_b}{O_{tot}} = \frac{P_c^n}{P_c^n + P_{50}^n} \quad 32$$

A dynamic tissue oxygenation model was presented previously by Boas³⁸. Popel derived a similar curvilinear capillary oxygen extraction model^{15,39}. These models have been expanded in this work to include a completely discretized extravascular space using a dual mesh technique described in detail previously⁸. In brief, the tissue mesh is registered to the same domain as the vasculature network, where every vessel is assigned to a single tissue element, and each tissue element may contain multiple vessels. Oxygen is convected through the vessels using the simple transfer model of eq. 18, in which only the RBC-bound oxygen is balanced by accounting for convection and oxygen exchange with the tissue. Blood vessels are represented as line segments, and balance equations are applied at the nodes. Bound oxygen accumulates in a blood vessel with RBC volume, V_b . Oxygen transport is explicitly dependent on the discharge hematocrit, entering and exiting from vessels according to the convective flux term with RBC phase velocity, u . Mass transfer to the tissue is driven by the concentration difference between unbound oxygen, O_u , and tissue oxygen, O_t . According to the saturation equilibrium, only the

unbound oxygen is available for tissue transport, $O_u = \sigma(O_b)$, as in eq. 32. Also S_b , is the surface area of the endothelium and U , the endothelial wall transport coefficient which is a function of wall thickness^{8,38}.

blood oxygen

$$V_b \frac{dO_b}{dt} = u\vec{\nabla}O_b - S_b U(O_u - O_t) = u\vec{\nabla}O_b - S_b U(\sigma(O_b) - O_t) \quad 33$$

Blood oxygen is coupled to the tissue oxygen transport in eq. 34. For every element in the extravascular tissue mesh, oxygen accumulation is equal to extravascular oxygen diffusion, oxygen transfer across the endothelium and cellular metabolism. The adjusted tissue volume, V_t^* , is the total tissue volume reduced by the volumina of all blood vessel segments contained in the tissue cell. The simulation parameter $k=8.2 \times 10^{-6} \text{cm}^3 \text{O}_2 / \text{cm}^3 / \text{s}$ is the metabolic rate of oxygen consumption⁷¹, and $D=1.04 \times 10^{-5} \text{cm}^2 / \text{s}$ is the effective extravascular diffusion coefficient of oxygen⁷¹.

tissue oxygen

$$V_t^* \frac{dC_t}{dt} = \vec{\nabla} \cdot D\vec{\nabla}O_t + \sum_{i=1}^N [S_{b,i} U \Delta(\sigma(O_{b,i}) - O_t)] - kV_t^* O_t \quad 34$$

For the steady state simulations, accumulation in eqs.33 and 34 is equal to zero.

Supplemental 3

Implementation details of Model 3

The generic formulae of Model 3 can be used to construct RBC flux conservation envelopes around vessel junctions of any connectivity. Figure 24 shows two separate cases to better illustrate the implementation of the novel kinematic plasma skimming law.

The bifurcation described in Figure 24A has a known inlet hematocrit H_i and volumetric flow rates Q . The plasma skimming coefficients θ_2 and θ_3 are determined from the diameter ratio between the respective daughter branch and the parent vessel, described in eq. 24. The conservation of RBC flux is shown in Figure 24A, with only the adjusted hematocrit H^* as the unknown. The daughter branch discharge hematocrit is the product of the adjusted hematocrit H^* and the plasma skimming coefficient for that branch.

The mass conservation of RBC flux through a trifurcation is constructed with exactly the same procedure, as shown in Figure 24B. A plasma skimming coefficient is determined for each branch, and the adjusted hematocrit H^* is solved by mass conservation. Daughter branch discharge hematocrit values are determined exactly the same as in the case of a single bifurcation.

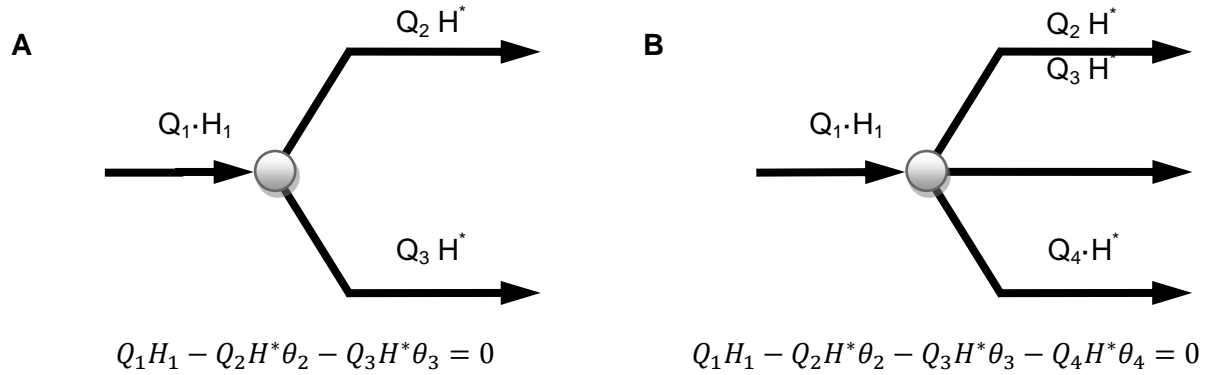


Figure 24 Construction of mass conservation equations using Model 3. The discharge hematocrit of the upstream vessel is H_1 , and the volumetric bulk flow for each vessel, Q , is known. The plasma skimming coefficient, θ , for each daughter branch is computed using eq. 24, for **A**, a bifurcation, and **B**, a trifurcation. The adjusted hematocrit, H^* , for both case studies is computed by mass conservation. The daughter branch discharge hematocrit is the product of its plasma skimming coefficient θ for each branch and the adjusted hematocrit, H^* .

Cited Literature

1. M. A. Yaseen, V. J. Srinivasan, S. Sakadzic, H. Radhakrishnan, I. Gorczynska, W. Wu, J. G. Fujimoto and D. A. Boas. "Microvascular oxygen tension and flow measurements in rodent cerebral cortex during baseline conditions and functional activation" J Cereb Blood Flow Metab 31: 1051-63, 2011.
2. T. J. Huppert, M. S. Allen, S. G. Diamond and D. A. Boas. 2. "Estimating Cerebral Oxygen Metabolism From fMRI With a Dynamic Multicompartment Windkessel Model" Human Brain Mapping 30: 1548-1567, 009
3. P. S. Tsai, J. P. Kaufhold, P. Blinder, B. Friedman, P. J. Drew, H. J. Karten, P. D. Lyden and D. Kleinfeld. "Correlations of neuronal and microvascular densities in murine cortex revealed by direct counting and colocalization of nuclei and vessels" J Neurosci 29: 14553-70, 2009.
4. D. Kleinfeld, P. Blinder, P. J. Drew, J. D. Driscoll, A. Muller, P. S. Tsai and A. Y. Shih. "A guide to delineate the logic of neurovascular signaling in the brain" Front Neuroenergetics 3: 1-9, 2011.
5. Q. Fang, S. Sakadzic, L. Ruvinskaya, A. Devor, A. M. Dale and D. A. Boas. "Oxygen advection and diffusion in a three- dimensional vascular anatomical network" Opt Express 16: 17530-41, 2008.
6. J. Reichold, M. Stampanoni, A. Lena Keller, A. Buck, P. Jenny and B. Weber. "Vascular graph model to simulate the cerebral blood flow in realistic vascular networks" J Cereb Blood Flow Metab 29: 1429-43, 2009.
7. N. M. Vaičaitis, B. J. Sweetman and A. A. Linninger. 2011. A computational model of cerebral vasculature, brain tissue, and cerebrospinal fluid. In 21st European Symposium on Computer-Aided Process Engineering. Greece

8. A. A. Linninger, I. G. Gould, T. Marinnan, C. Y. Hsu, M. Chojecki and A. Alaraj. "Cerebral microcirculation and oxygen tension in the human secondary cortex" *Ann Biomed Eng* 41: 2264-84, 2013.
9. I. G. Gould, T. Marinnan, C. Maurice, M. Qader, B. Henry, M. Pervais, N. Vaicaitis, Y. Zhu, A. Rogers and A. A. Linninger. Hemodynamics of cerebral vasculature. In *Proceedings of the 11th International Symposium on Process Systems Engineering*. Singapore, 2012.
10. R. Karch, F. Neumann, M. Neumann and W. Schreiner. "Staged growth of optimized arterial model trees" *Ann Biomed Eng* 28: 495-511, 2000.
11. B. Weber, A. L. Keller, J. Reichold and N. K. Logothetis. "The microvascular system of the striate and extrastriate visual cortex of the macaque" *Cereb Cortex* 18: 2318-30, 2008.
12. S. Lorthois, F. Cassot and F. Lauwers. "Simulation study of brain blood flow regulation by intra-cortical arterioles in an anatomically accurate large human vascular network: Part I: methodology and baseline flow" *NeuroImage* 54: 1031-42, 2011.
13. N. Safaeian and T. David. "A computational model of oxygen transport in the cerebrocapillary levels for normal and pathologic brain function" *J Cereb Blood Flow Metab* 33: 1633-41, 2013.
14. M. A. Mintun, B. N. Lundstrom, A. Z. Snyder, A. G. Vlassenko, G. L. Shulman and M. E. Raichle. "Blood flow and oxygen delivery to human brain during functional activity: theoretical modeling and experimental data" *Proc Natl Acad Sci U S A* 98: 6859-64, 2001.
15. N. M. Tsoukias, D. Goldman, A. Vadapalli, R. N. Pittman and A. S. Popel. "A computational model of oxygen delivery by hemoglobin-based oxygen carriers in three-dimensional microvascular networks" *J Theor Biol* 248: 657-74, 2007.
16. M. W. Dewhirst, B. Klitzman, R. D. Braun, D. M. Brizel, Z. A. Haroon and T. W. Secomb. "Review of methods used to study oxygen transport at the microcirculatory level" *International Journal of Cancer* 90: 237-255, 2000.

17. R. N. Pittman. "Oxygen transport in the microcirculation and its regulation" *Microcirculation* 20: 117-37, 2013.
18. G. J. Tangelder, H. C. Teirlinck, D. W. Slaaf and R. S. Reneman. "Distribution of blood platelets flowing in arterioles" *Am J Physiol* 248: H318-23, 1985.
19. A. Kumar and M. D. Graham. "Mechanism of Margination in Confined Flows of Blood and Other Multicomponent Suspensions" *Phys. Rev. Lett.* 109: 108102, 2012.
20. A. Kumar and M. D. Graham. "Margination and segregation in confined flows of blood and other multicomponent suspensions" *Soft Matter* 8: 10536-10548, 2012.
21. A. Kumar and M. D. Graham. "Segregation by membrane rigidity in flowing binary suspensions of elastic capsules" *Physical Review E* 84, 2011.
22. A. R. Pries and T. W. Secomb. "Microvascular blood viscosity in vivo and the endothelial surface layer" *Am J Physiol Heart Circ Physiol* 289: H2657-64, 2005.
23. A. S. Popel and P. C. Johnson. "Microcirculation and Hemorheology" *Annu Rev Fluid Mech* 37: 43-69, 2005.
24. D. A. Fedosov, B. Caswell, A. S. Popel and G. E. Karniadakis. "Blood flow and cell-free layer in microvessels" *Microcirculation* 17: 615-28, 2010.
25. R. Fahraeus. "The Suspension Stability of the Blood" *Physiological Reviews* 9: 241-274, 1929.
26. J. H. Barbee and G. R. Cokelet. "The Fahraeus effect" *Microvasc Res* 3: 6-16, 1971.
27. B. M. Fenton, T. C. Russel and G. R. Cokelet. "Nonuniform Red Cell Distribution in 20 to 100 μ m Bifurcations" *Microvasculature Research* 29: 103-126, 1985.
28. T. W. Secomb, R. Skalak, N. Oezkaya and J. F. Gross. "Flow of axisymmetric red blood cells in narrow capillaries" *J. Fluid Mech.* 163: 405-23, 1986.
29. A. Krogh, G. A. Harrop and P. B. Rehberg. "Studies on the physiology of capillaries: III. The innervation of the blood vessels in the hind legs of the frog" *Journal of Physiology* 56: 179-89, 1922.

30. J. Perkkio, J. Hokkanen and R. Keskinen. "Theoretical model of phase separation of erythrocytes, platelets, and plasma at branches" *Med Phys* 13: 882-6, 1986.
31. R. Guibert, C. Fonta and F. Plouraboue. "A New Approach to Model Confined Suspensions Flows in Complex Networks: Application to Blood Flow" *Transport in Porous Media* 83: 171-194, 2010.
32. X. Li, A. S. Popel and G. E. Karniadakis. "Blood-plasma separation in Y-shaped bifurcating microfluidic channels: a dissipative particle dynamics simulation study" *Phys Biol* 9: 026010, 2012.
33. X. W. Yin, T. Thomas and J. F. Zhang. "Multiple red blood cell flows through microvascular bifurcations: Cell free layer, cell trajectory, and hematocrit separation" *Microvascular Research* 89: 47-56, 2013.
34. A. R. Pries, K. Ley and P. Gaehtgens. "Generalization of the Fahraeus Principle for Microvessel Networks" *American Journal of Physiology* 251: H1324-H1332, 1986.
35. A. Pries. "Biophysical aspects of blood flow in the microvasculature" *Cardiovasc Res* 32: 657-667, 1995.
36. B. C. Fry, J. Lee, N. P. Smith and T. W. Secomb. "Estimation of blood flow rates in large microvascular networks" *Microcirculation* 19: 530-8, 2012.
37. C. Pozrikidis. "Numerical Simulation of Blood Flow Through Microvascular Capillary Networks" *Bulletin of Mathematical Biology* 71: 1520-1541, 2009.
38. D. A. Boas, S. R. Jones, A. Devor, T. J. Huppert and A. M. Dale. "A vascular anatomical network model of the spatio-temporal response to brain activation" *NeuroImage* 40: 1116-29, 2008.
39. D. Goldman and A. S. Popel. "A computational study of the effect of capillary network anastomoses and tortuosity on oxygen transport" *Journal of Theoretical Biology* 206: 181-194, 2000.

40. D. M. Audet and W. L. Olbricht. "The Motion of Model Cells at Capillary Bifurcations" *Microvascular Research* 33: 377-396, 1987.
41. B. M. Fenton, D. W. Wilson and G. R. Cokelet. "Analysis of the effects of measured white blood cell entrance times on hemodynamics in a computer model of a microvascular bed" *Pflugers Arch* 403: 396-401, 1985.
42. J. W. Dellimore, M. J. Dunlop and P. B. Canham. "Ratio of cells and plasma in blood flowign past branches in small plastic channels" *American Journal of Physiology* 244: H635-H643, 1983.
43. G. W. Schmid-Schonbein, R. Skalak, S. Usami and S. Chien. "Cell Distribution in Capillary Networks" *Microvascular Research* 19: 18-44, 1980.
44. A. R. Pries, B. Reglin and T. W. Secomb. "Remodeling of blood vessels: responses of diameter and wall thickness to hemodynamic and metabolic stimuli" *Hypertension* 46: 725-31, 2005.
45. S. Lorthois, F. Cassot and F. Lauwers. "Simulation study of brain blood flow regulation by intra-cortical arterioles in an anatomically accurate large human vascular network. Part II: flow variations induced by global or localized modifications of arteriolar diameters" *NeuroImage* 54: 2840-53, 2011.
46. A. R. Pries, K. Ley, M. Claassen and P. Gaehtgens. "Red-Cell Distribution at Microvascular Bifurcations" *Microvascular Research* 38: 81-101, 1989.
47. W. Pan, D. A. Fedosov, B. Caswell and G. E. Karniadakis. "Predicting dynamics and rheology of blood flow: A comparative study of multiscale and low-dimensional models of red blood cells" *Microvasc Res* 82: 163-70, 2011.
48. E. Sykova and C. Nicholson. "Diffusion in brain extracellular space" *Physiol Rev* 88: 1277-340, 2008.
49. A. S. Golub, M. C. Barker and R. N. Pittman. "Microvascular oxygen tension in the rat mesentery" *Am J Physiol Heart Circ Physiol* 294: H21-8, 2008.

50. N. Hangai-Hoger, P. Cabrales, J. C. Briceno, A. G. Tsai and M. Intaglietta. "Microlymphatic and tissue oxygen tension in the rat mesentery" *Am J Physiol Heart Circ Physiol* 286: H878-83, 2004.
51. A. R. Pries, A. Fritzsche, K. Ley and P. Gaehtgens. "Redistribution of red blood cell flow in microcirculatory networks by hemodilution" *Circ Res* 70: 1113-21, 1992.
52. M. R. Somayaji, M. Xenos, L. Zhang, M. Mekarski and A. A. Linninger. "Systematic design of drug delivery therapies" *Computers & Chemical Engineering* 32: 89-98, 2008.
53. A. A. Linninger, M. R. Somayaji, T. Erickson, X. Guo and R. D. Penn. "Computational methods for predicting drug transport in anisotropic and heterogeneous brain tissue" *J Biomech* 41: 2176-87, 2008.
54. J. Alam, A. Shaheen and M. S. Anwar. "Accessing select properties of the electron with ImageJ: an open-source image-processing paradigm" *European Journal of Physics* 35, 2014.
55. G. Kanzow, A. R. Pries and P. Gaehtgens. "Analysis of the hematocrit distribution in the mesenteric microcirculation" *Int J Microcirc Clin Exp* 1: 67-79, 1982.
56. B. W. Zweifach. 1. "Quantitative studies of microcirculatory structure and function. I. Analysis of pressure distribution in the terminal vascular bed in cat mesentery" *Circ Res* 34: 843-57, 1974.
57. B. W. Zweifach. "Quantitative studies of microcirculatory structure and function. II. Direct measurement of capillary pressure in splanchnic mesenteric vessels" *Circ Res* 34: 858-66, 1974.
58. B. W. Zweifach and H. H. Lipowsky. "Quantitative studies of microcirculatory structure and function. III. Microvascular hemodynamics of cat mesentery and rabbit omentum" *Circ Res* 41: 380-90, 1977.
59. C. L. Mesh and B. L. Gewertz. "The effect of hemodilution on blood flow regulation in normal and postischemic intestine" *J Surg Res* 48: 183-9, 1990.

60. H. H. Lipowsky, S. Usami and S. Chien. "In vivo measurements of "apparent viscosity" and microvessel hematocrit in the mesentery of the cat" *Microvasc Res* 19: 297-319, 1980.
61. B. Klitzman and P. C. Johnson. "Capillary network geometry and red cell distribution in hamster cremaster muscle" *Am J Physiol* 242: H211-9, 1982.
62. C. Nicholson, K. C. Chen, S. Hrabetova and L. Tao. "Diffusion of molecules in brain extracellular space: theory and experiment" *Prog Brain Res* 125: 129-54, 2000.
63. Y. C. Fung. "Stochastic flow in capillary blood vessels" *Microvasc Res* 5: 34-48, 1973.
64. A. Villringer, A. Them, U. Lindauer, K. Einhaupl and U. Dirnagl. "Capillary perfusion of the rat brain cortex. An in vivo confocal microscopy study" *Circ Res* 75: 55-62, 1994.
65. X. J. Li, P. M. Vlahovska and G. E. Karniadakis. "Continuum- and particle-based modeling of shapes and dynamics of red blood cells in health and disease" *Soft Matter* 9: 28-37, 2013.
66. E. Vovenko. "Distribution of oxygen tension on the surface of arterioles, capillaries and venules of brain cortex and in tissue in normoxia: an experimental study on rats" *Pflugers Arch* 437: 617-23, 1999.
67. A. G. Hudetz. "Blood flow in the cerebral capillary network: a review emphasizing observations with intravital microscopy" *Microcirculation* 4: 233-52, 1997.
68. S. Chien and K. Jan. "Ultrastructural basis of the mechanism of rouleaux formation" *Microvasc Res* 5: 155-66, 1973.
69. J. J. Bishop, A. S. Popel, M. Intaglietta and P. C. Johnson. "Rheological effects of red blood cell aggregation in the venous network: A review of recent studies" *Biorheology* 38: 263-274, 2001.
70. D. Goldman and A. S. Popel. "Computational modeling of oxygen transport from complex capillary networks. Relation to the microcirculation physiome" *Adv Exp Med Biol* 471: 555-63, 1999.

71. K. Yaegashi, T. Itoh, T. Kosaka, H. Fukushima and T. Morimoto. "Diffusivity of oxygen in microvascular beds as determined from PO₂ distribution maps" AJP - Heart 270: H1390-H1397, 1996.

IV. THE CAPILLARY BED OFFERS THE LARGEST HEMODYNAMIC RESISTANCE TO THE CORTICAL BLOOD SUPPLY

(Previously published as Gould, Ian Gopal, Philbert Tsai, David Kleinfeld, and Andreas Linninger. "The capillary bed offers the largest hemodynamic resistance to the cortical blood supply." *Journal of Cerebral Blood Flow & Metabolism* 37, no. 1 (2017): 52-68.)

Abstract

The cortical angioarchitecture is a key factor in controlling cerebral blood flow and oxygen metabolism. Difficulties in imaging the complex microanatomy of the cortex have so far restricted insight about blood flow distribution in the microcirculation. A new methodology combining advanced microscopy data with large scale hemodynamic simulations enabled us to quantify the effect of the angioarchitecture on the cerebral microcirculation. High-resolution images of the mouse primary somatosensory cortex were input into with a comprehensive computational model of cerebral perfusion and oxygen supply ranging from the pial vessels to individual brain cells. Simulations of blood flow, hematocrit and oxygen tension show that the wide variation of hemodynamic states in the tortuous, randomly organized capillary bed is responsible for relatively uniform cortical tissue perfusion and oxygenation. Computational analysis of microcirculatory blood flow and pressure drops further indicates that the capillary bed, including capillaries adjacent to feeding arterioles ($d < 10\mu\text{m}$), are the largest contributors to hydraulic resistance.

Introduction

Biochemical signaling between cerebral microcirculatory blood flow and the supply of oxygen to the brain is critical for normal brain function as well as disease states including ischemia¹⁻⁵, micro-infarcts⁶⁻⁸, and functional hyperemia⁹⁻¹¹. The functional interaction of cerebral hemodynamics, angioarchitecture and brain cell metabolism is known as the neurovascular unit (NVU). It has been hypothesized that control of the NVU depends on the orientation and arrangement of the microvessels¹²⁻¹³. Moreover, non-Newtonian hemodynamic effects such as plasma skimming or the Fahraeus-Lindqvist effect may contribute to homogeneous oxygen supply in the cerebral cortex¹⁴⁻¹⁶. Experimental inaccessibility and microdimensions of the cortical tissue have so far limited the ability to verify these hypotheses. In this work, we combine an almost complete inventory of brain cells and blood vessels obtained from sizable sections of the mouse cortex with a first principles computational model to better elucidate microcirculatory blood and oxygen perfusion patterns.

The functional relationship between microcirculation, tissue topology, and oxygen supply has been the object of experimental and computational studies for over thirty years¹⁷⁻²¹. The supply of oxygen from the blood to the surrounding tissue has been quantified in empirical²²⁻²³ and theoretical²⁴⁻²⁵ studies, but have typically been limited to a single blood vessel. However, single vessel studies fail to describe network effects. Recent attempts to explore networks employ hierarchal tree-like structures to model small sections of the microcirculation^{3,26-30}. However, experimental evidence has been unable to identify a hierarchal order to blood pressure³¹, hematocrit³², red blood cell velocity³³ or oxygen saturation. Other studies employed random geometric space filling methods;³⁴⁻³⁵ unfortunately these structures did not conform to the vessel topology seen in microscopy. However, topology significantly affects oxygen exchange^{12,36}. Another study³⁷ reconstructed a microcirculatory network from a thin section of the human cortex; yet in the resulting shallow computational domain most microvessels are

intersected by boundaries, thus failing to achieve three-dimensional network connectivity. This model is also subject to delicate boundary condition choices which weakened its predictive power. Another study³⁸ combined human image data with a modified constructive geometric optimization algorithm³⁹ to synthesize a physiologically realistic, randomized model of the NVU. The topology of artificially generated NVUs is statistically equivalent to the topology of real networks obtained by laser microscopy²⁰. However, that study concerns the human cortex but not the mouse.

This paper presents simulation results of blood supply and oxygen delivery in a large section of the mouse brain covering the pial network, penetrating vessels, the complete capillary bed and almost all neuronal and glial brain cells. Two-photon microscopy imaging data of the murine somatosensory cortex⁴⁰ was used to create a physiologically accurate multi-scale computational model of the cortical microcirculation. Simulations predicted realistic values for red blood cell velocity, hematocrit and oxygen tension in blood vessels, extracellular space as well as intracellular compartments.

Materials and Methods

The methods section describes data acquisition of the four somatosensory cortex specimens in the mouse. The mathematical background for modeling non-Newtonian hemodynamics, oxygen transport across the blood brain barrier and metabolism in the extravascular space is given.

Data acquisition

In four specimens, homologous sections of the somatosensory cortex were extracted and imaged with two photon microscopy⁴⁰⁻⁴³. Each section, with volumes $V_1=1.14$, $V_2=1.94$, $V_3=2.85$, and $V_4=2.71\text{mm}^3$ respectively, extends the full depth of the cortex down to the white matter, covering about 1-2% of the gray matter of the entire mouse brain⁴⁴. Brain cell nuclei were labeled with a DNA stain and their locations vectorized⁴¹; neuronal nuclei were further labeled

with a pan-neuronal marker. Neuronal cell density ranged from 120,727-208,509cells/mm³. Glial cell distribution was sparser with a range of 42,976-141,319cells/mm³.

All blood vessels were labeled with a fluorescent gel under conditions that preserved lumen interior diameter. The spatial arrangement and connectivity of blood vessels, including all capillaries, were recorded. Every vessel in the four data sets was assigned one of five labels: (i) pial artery, (ii) penetrating arteriole, (iii) capillary, (iv) penetrating venule, or (v) pial vein. Pial arteries and penetrating arterioles were separated into different groups according to the diameter and location within the section. Vessel segments close to the cortical surface (within 100µm) with a diameter larger than 10µm were considered pial arteries. Vessels branching from surface arterioles were labeled descending arterioles. The tree-like descending arterioles were traced until the capillary bed was reached. The capillary bed was separated from the penetrating arterioles assessing the branching order from the arterioles as well as a 6µm diameter cutoff. Vessels that were within 3 branching orders of a large arteriole in the direction of blood flow were considered to be penetrating arterioles. No effort was made to differentiate pre-capillary arterioles from post-arteriole capillaries.

This was not performed in the parent study⁴⁰ and requires differential labeling of smooth muscle versus pericytes^{84,85}. For example, the molecular marker for smooth muscle actin, or proteoglycan *NG2*, would be needed to label both smooth muscle and *actin*, while the marker for intermediate filament *desmin* would be needed to label arteriolar smooth muscle⁸⁶ only. A similar segregation based on size and branching order was applied in reverse to label penetrating venules and surface pial veins; specifically, a capillary-penetrating venules cutoff for diameters less than 6µm and a penetrating venules-pial veins cutoff for diameters less than 12µm within a depth of 100µm below the pia.

Biphasic blood flow computations

Microcirculation was modeled as a biphasic suspension consisting of red blood cells and plasma flowing through a network of interconnected cylindrical segments¹⁶. Non-Newtonian blood viscosity was calculated as a function of the local hematocrit and vessel diameter¹⁵. More theoretical background for bulk blood flow computations is given in Supplemental Information, and all boundary conditions are described in Table VIII. Hematocrit distribution is computed using a drift-flux model described previously¹⁶. Red blood cells (RBC) and plasma distributions were computed using a kinetic plasma skimming model (KPSM)¹⁶ to determine the discharge hematocrit, H_d , and the RBC velocity in each segment. In the mass conservation for red blood cells in eq. 35, the flux of RBCs through a vessel, Q_{RBC} , is equal to the product of the bulk blood flow, Q , and the discharge hematocrit. An uneven distribution of RBCs in each bifurcation results from the velocity difference between RBCs and plasma, known as *plasma skimming*. Red blood cell mass conservation is written for a single bifurcation in eq. 36. The difference in discharge hematocrit for two daughter branches, H_2 and H_3 , and the parent vessel, H_1 , was determined by solving for the *adjusted hematocrit*, H^* . The adjusted hematocrit depends on kinematic plasma skimming coefficients, θ_i , which are geometric functions of the cross-sectional area fraction of daughter to parent vessels, A_i/A_1 , and the drift parameter, $M=5.25$, given in Table IX.

$$\nabla \cdot (QH_d) = \nabla \cdot Q_{RBC} = 0 \quad 35$$

$$Q_1 H_1 - Q_2 H_2 - Q_3 H_3 = 0 \quad 36$$

$$H_2 = H_1 - \Delta H = \theta_2 \cdot H^*$$

$$H_3 = \theta_3 \cdot H^*$$

$$\theta_2 = \left(\frac{A_2}{A_1} \right)^{\frac{1}{M}}$$

$$\theta_3 = \left(\frac{A_3}{A_1} \right)^{\frac{1}{M}}$$

Blood pressure boundary conditions were assigned to all pial vessels entering and leaving the domain using the choices described in Table VIII. A discharge hematocrit of 0.35 was set for each inlet on the pial surface. The model further assumed a fully developed hematocrit field at the outlet (no change of hematocrit across the last segment).

Oxygen convection in erythrocytes and plasma

Oxygen convection in the blood stream and transport into the tissue was solved using a previously presented dual-mesh technique^{16,38}. Oxygen bound to hemoglobin, C_{HbO_2} , travels at the velocity of the RBC phase, u_{RBC} , as in eq. 37. Axial oxygen diffusion within the cylindrical vessel segment was neglected. Furthermore, non-linear oxygen-hemoglobin dissociation kinetics^{36,46} from the erythrocytes to plasma were implemented. The rate of oxygen desaturation from hemoglobin to plasma, $\dot{R}_{R \rightarrow P}$, in eq. 37 was given by a first order kinetic rate law, described in eq. 47-49 of Supplemental Information, where additional details on the full binding kinetics are provided. It is important to note that the proposed oxygen dissociation kinetics obeys to the well-known Hill equation when reaching equilibrium.

$$-u_{RBC} \cdot \nabla C_{HbO_2} - \dot{R}_{R \rightarrow P} = 0 \quad 37$$

Free plasma oxygen, C_{plO_2} , was convected with plasma phase velocity, u_{pl} , given in eq. 38. Oxygen transported from the capillary bed across the endothelial membrane of the blood brain barrier (BBB) was driven by the concentration difference between free oxygen in the plasma and in the extracellular space, C_{ECsO_2} .

Oxygen extraction across the BBB from the blood to the extravascular space in eq. 38 is a function of vessel surface area, S_b , oxygen permeability of the endothelial tissue, U , and endothelial wall thickness, w_b . Wall thickness was modeled as a linear function of the vessel lumen diameter, d , for arteries, capillaries and veins as annotated in Table IX.

Table VIII Summary of boundary conditions used in the microcirculatory perfusion computations

	Biphasic Blood Flow	
	Pressure ^{31,87, 88}	Hematocrit
Arterial Inlet	120mmHg	0.35
Venous Outlet	5mmHg	fully developed, $\nabla H = 0$
	Oxygen	
	RBC ⁶⁰	Plasma
Pial Arterial Inlet	68.4mmHg	68.4mmHg [*]
Pial Venous Outlet	fully developed, $\nabla C_{RBC} = 0$	fully developed [*] , $\nabla C_p = 0$
Tissue Surface	No Flux	
Tissue GW Interface	Cyclic	
Tissue Boundaries	Cyclic	

*In equilibrium with RBC oxygen tension according to the Hill Equation

$$-u_{pl} \cdot \nabla C_{plO_2} + \dot{R}_{R \rightarrow P} - S_b \frac{U}{w_b} (C_{plO_2} - C_{ECsO_2}) = 0 \quad 38$$

At the pial arterial inlets, the bound oxygen tension was set to $pO_2=68.4\text{mmHg}$, listed in Table VIII, as measured by two photon microscopy⁶⁰. This value corresponds to RBC saturation of 83%. The concentration of free plasma oxygen was set under the assumption of equilibrium between the RBC and plasma phases according to the Hill equation. At pial outlets, both free and bound oxygen fields were assumed to be fully developed.

Tissue oxygen diffusion and metabolism

Tissue oxygen leaving the vasculature across the BBB enters the extracellular space (ECS). The ECS was discretized into a uniform Cartesian grid of a fixed edge length. Blood flow, pressure and oxygen profiles were shown to be independent of the domain discretization. Results of a comprehensive mesh independence study can be found in Supplemental Information. Each cubic tissue element may contain multiple blood vessels; therefore its oxygen supply stems from multiple segments, N_v , as given in the summation term of eq. 39. Extravascular oxygen can diffuse through the tissue characterized by the diffusion coefficient, D_{ECsO_2} . The cortical surface was assumed to be impermeable to oxygen as shown in Table VIII. At the sides of the cortical section, cyclic boundary conditions were enforced by connecting faces on opposing sides of the specimen to emulate an infinite domain. A cyclic boundary condition was applied at the gray-white matter interface as well, connecting the left half to the right half. Because the specimens are thick, the boundary choices had a mild effect in the interior of the domain³⁸.

Table IX Cerebral oxygen transport parameters used in this work

Parameter	Description	Value	Units	Reference
α_{pl}	Plasma oxygen solubility	2.82×10^{-5}	$\text{mL O}_2 \cdot \text{mL}^{-1} \text{ mmHg}^{-1}$	Christoforides ⁴⁷
α_t	ECS oxygen solubility	2.80×10^{-5}	$\text{mL O}_2 \cdot \text{mL}^{-1} \text{ mmHg}^{-1}$	Liu ⁴⁶
β	Hb- O ₂ binding capacity	0.52	$\text{mL O}_2 \cdot (\text{mL RBC})^{-1}$	Goldman ³⁶
D_{ECS}	ECS oxygen diffusivity	1.8×10^3	$\mu\text{m}^2 \cdot \text{s}^{-1}$	Mintun ⁴⁸
k_f	Rate of Hb-O ₂ dissociation	50.0	s^{-1}	This Work
M	Plasma skimming coefficient	5.25	--	Gould ¹⁶
n	Hb saturation Hill coefficient	2.7	--	Ellis ⁵⁰
P_{50}	pO ₂ for 50% Hb saturation	37	mmHg	Ellis ⁵⁰
k_m	Mito. O ₂ metabolism	3.5	s^{-1}	This Work
R_{CMRO}	O ₂ metabolic rate (0 th order)	2.6	$\mu\text{mol} \cdot \text{g}^{-1} \cdot \text{minute}^{-1}$	Cui ⁵²
k_{CMRO}	O ₂ metabolic rate (1 st order)	1.0	s^{-1}	This Work
S_g	Glia cell surface area	1,780	μm^2	Rodríguez ⁵³
S_m	Mito. surface area	3.75	μm^2	Hoppler ⁵⁴
S_n	Neur. cell surface area	23,430	μm^2	Howard ⁵⁵
U^{**}	O ₂ mass transfer coefficient	1.77×10^3	$\mu\text{m}^2 \cdot \text{s}^{-1}$	Popel ⁵⁶
w_b	Endothelial Wall Thickness [*]	1-5	μm	Linninger ³⁸
w_n	Neur. membrane thickness	40	nm	Schmitt ⁵⁷
w_g	Glial membrane thickness	20	nm	Schmitt ⁵⁷
w_m	Mito. membrane thickness	10	nm	Sjostrand ⁵⁸
V_m	Mito. volume	1.83	μm^3	Hoppler ⁵⁴
V_n	Neur. cell volume	5,694	μm^3	Howard ⁵⁵
V_g	Glial cell volume	869	μm^3	Williams ⁵⁹

* Formula for wall thickness: $w_b = \theta \cdot d + \delta$; arteries ($\theta=0.2$, $\delta=0.4$), capillaries ($\theta=0$, $\delta=1$), and veins ($\theta=0.021$, $\delta=0.94$)

**Pial vessels were assigned a mass transfer coefficient of zero

It has been shown previously³⁸ that the dual mesh technique used here produces the same results as the analytical Krogh cylinder for a single capillary. However, Krogh's model cannot predict oxygen transfer in microcirculatory networks. Oxygen exchange in the cortex depends on two critical factors outside the scope of the Krogh model: (i) three-dimensional angioarchitecture as well as (ii) axial diffusion through the ECS.

Oxygen metabolism in the extravascular tissue was computed with two distinct versions described in the next section. The first assumed a first order rate law of oxygen consumption. The second approach also predicted subcellular oxygen gradients.

First order rate law for tissue oxygen consumption. The first approach assumed first order reaction kinetics. Accordingly, oxygen metabolism was equal to the product of the extracellular oxygen concentration, C_{ECSO_2} , the volume of each tissue cell, V_{ECS} , and the first-order cerebral metabolic rate of oxygen consumption, k_{CMRO} , as in eq. 39.

$$\sum_{i=1}^{N_v} S_{b,i} \frac{U_i}{w_{b,i}} (C_{pIO_2,i} - C_{ECSO_2}) + \vec{\nabla} \cdot D_{ECSO_2} \vec{\nabla} C_{ECSO_2} - V_{ECS} k_{CMRO} C_{ECSO_2} = 0 \quad 39$$

Intracellular oxygen tension approach. The second, more detailed approach aimed at computing intracellular oxygen tension gradients between the extracellular space, the cell cytoplasm and the mitochondria. This subcellular metabolism is anisotropic because it incorporates the spatial distribution of neuronal and glial nuclei. Oxygen consumption in each tissue cell depended on the number of neurons, N_n , and glial cells, N_g . Oxygen transport into the interior of each neuron was driven by the concentration gradient between the ECS and the neuronal cytoplasm, C_{nO_2} , as described in eq. 40. Transport across the neuronal cell membrane was limited by its surface area, S_n , and the membrane thickness, w_n . Oxygen supplied into each glial cell was likewise determined by the concentration gradient between the ECS and the glial cytoplasm, C_{gO_2} , and was regulated by the glial membrane surface area, S_g , and its thickness, w_g .

$$\sum_{i=1}^{N_v} S_{b,i} \frac{U_i}{w_{b,i}} (C_{plO_2,i} - C_{ECSO_2}) + \vec{\nabla} \cdot D_{ECSO_2} \vec{\nabla} C_{ECSO_2} - \sum_{j=1}^{N_n} S_n \frac{U}{w_n} (C_{ECSO_2} - C_{nO_2,j}) - \sum_{k=1}^{N_g} S_g \frac{U}{w_g} (C_{ECSO_2} - C_{gO_2,k}) = 0 \quad 40$$

Oxygen metabolism in neurons. The oxygen conservation balance for each neuron is given in eq. 41. Oxygen reaching the cytoplasm was transported into its mitochondria, C_{mnO_2} , the actual site of oxygen metabolism. The flux from the cytoplasm into the mitochondria was governed by the mass transport coefficient, U , the mitochondrial surface area, S_m , and its membrane thickness, w_m . In this study, the inner and outer membranes of the mitochondria were assumed to form a single layer.

$$S_n \frac{U}{w_n} (C_{ECSO_2} - C_{nO_2}) - \sum_{i=1}^{M_n} S_m \frac{U}{w_m} (C_{nO_2} - C_{mnO_2,i}) = 0 \quad 41$$

Since mitochondria could not be imaged directly, their spatial distribution within the neuronal cell body was set as follows. Each neuron was assigned an average number of mitochondria⁶¹⁻⁶², $M_n=839$, whose locations were spatially distributed according to a probability distribution function⁶² along the efferent dendrites and axon fiber using the cell nuclei coordinate as reference, shown in Figure 30A. Axons were assumed to be oriented perpendicular to the cortical surface. This process of random mitochondria distribution was repeated for every neuron. The spatial allocation of mitochondria enabled us to approximate anisotropic reaction rates as a function of the known position of nuclei.

Oxygen transported across the mitochondrial membrane was consumed by the electron transport chain. The reaction rate was assumed to be of first order with a rate constant k_m . In eq. 42, C_{mnO_2} is the concentration of oxygen within neuronal mitochondria, V_m , is the mitochondrial volume. Oxygen tension in the ECS, cells and mitochondria was converted from molar concentrations using Henry's solubility, α_t , given in Table IX.

$$S_m \frac{U}{w_m} (C_{no_2} - C_{mno_2}) - V_m k_m C_{mno_2} = 0 \quad 42$$

Oxygen metabolism in glial cells. Oxygen concentration in the glial cytoplasm, C_{mno_2} , and mitochondria, C_{mgo_2} , was computed using a similar approach as described for neurons according to eq. 43-44. The number of mitochondria, $M_g=283$, for each glial cell was taken from fractional density data⁶³⁻⁶⁵. The spatial distribution of the glial mitochondria was assumed to lie within a sphere around the nucleus as shown in Figure 30B. The total rate of metabolized oxygen in each tissue cube depended on the number of mitochondria, which in turn is a function of the anisotropic spatial distribution of neurons and glial cells.

$$S_g \frac{U}{w_g} (C_{ECSO_2} - C_{go_2}) - \sum_{i=1}^{M_g} S_m \frac{U}{w_m} (C_{go_2} - C_{mgo_2,i}) = 0 \quad 43$$

$$S_m \frac{U}{w_m} (C_{go_2} - C_{mgo_2}) - V_m k_m C_{mgo_2} = 0 \quad 44$$

Results

First, the topology of the microcirculation in the four primary somatosensory cortical sections was statistically examined. Next, blood flow and oxygen transport predictions are presented. Finally, trajectories of blood pressures, hematocrit and RBC oxygen saturation along paths from the arterial inlets to venous outlets were analyzed.

Morphological statistical analysis

The multi-scale dimensions of the cortical sections are displayed in Figure 25A-B. Blood vessels embedded in the cellular matrix are displayed at multiple length scales, from pial vessels at the cortical surface down to the capillary bed. Probability density functions (PDF) describing the distribution of vessel diameter, length, volume, and surface area, as well as vessel and neuronal density, are shown in Figure 26.

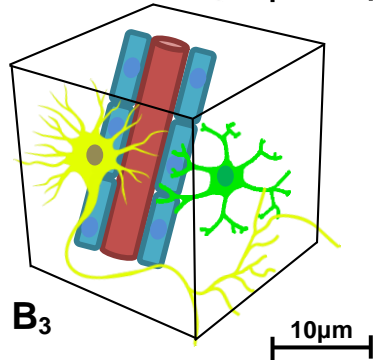
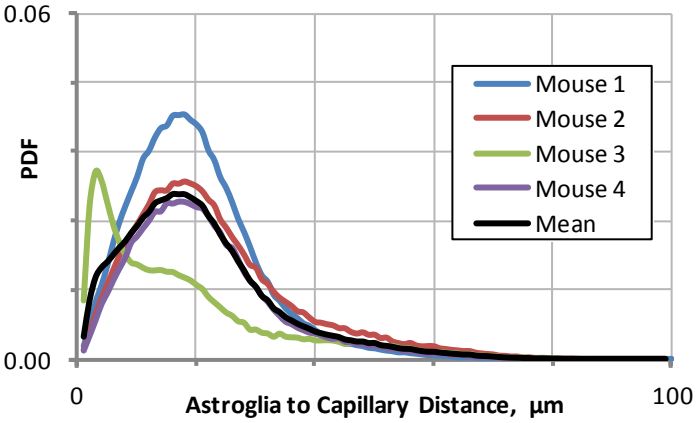
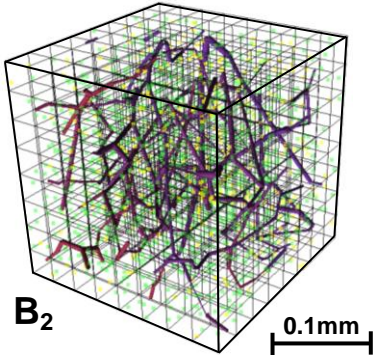
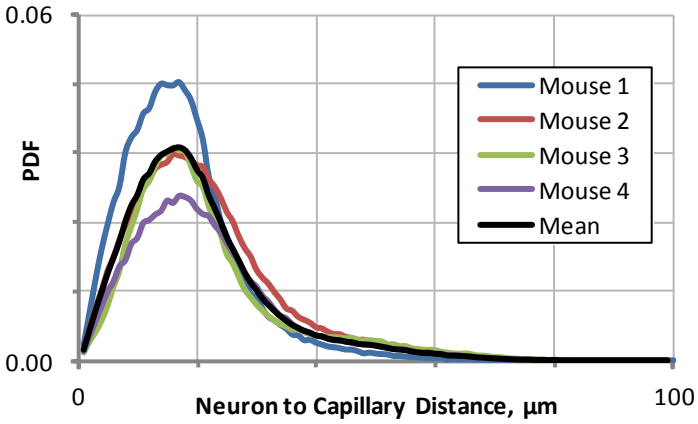
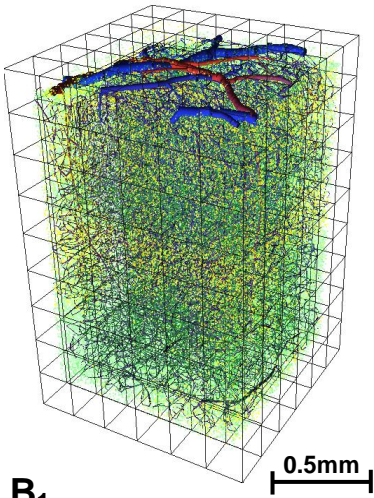
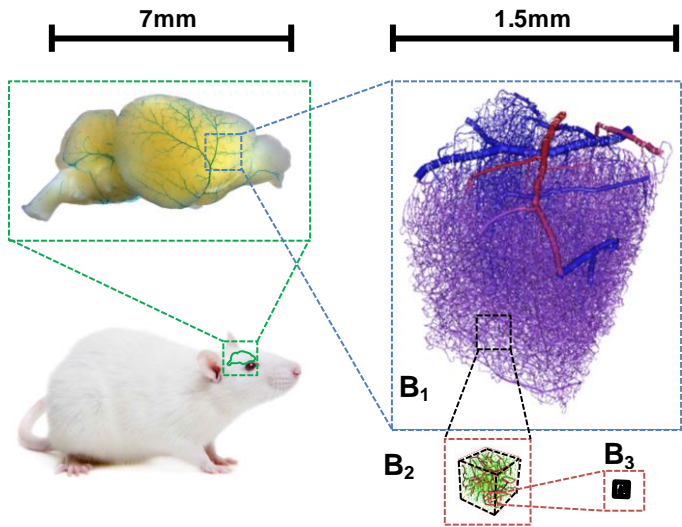


Figure 25 Vectorized data of the multi-scale vascular and cellular morphology of the mouse cerebral cortex. **A.** Illustration of the multiscale resolution of the murine cerebral vasculature from the cortical surface vessels down to the cellular level. (Whole brain snapshot taken from the NIH supported KOMP Phenotyping Pilot project⁴⁵). **B.** Full view of the microvascular network with cerebral arterioles in red, draining veins in blue, and capillaries in purple. Neuronal cells are displayed in yellow and glial cells in green at the 0.5mm resolution. (Frames **B₁** to **B₃** show data in increasing magnification **B₁**. 1.0mmx1.0mmx1.2mm, **B₂**. 200µmx200µmx200µm, and **B₃**. 25µmx25µmx25µm. At the finest resolution in **B₃**, cell bodies of neurons and glial cells were added for clarity). Histogram of cell to capillary distance for **C.** neurons and **D.** glial cells.

Distances of glial cells and neurons to the nearest capillaries were computed and reported as a PDF, shown in Figure 25C-D. The mean distance between the neurons to the closest microvessel was $17.8\mu\text{m}$. The mean glial-capillary distance was $18.2\mu\text{m}$. The glial spacing in the third mouse specimen was shorter than the other three, as shown in Figure 25D.

For all metrics, the variance within each data set was compared to the average of all four mouse cortical sections. Overall, the distribution of vessel length, diameter and vessel density per volume were found to be statistically similar in all four data sets ($RSS < 0.04$). However, the surface area occupied by penetrating arterioles and venules was significantly smaller in the second data set; see Supplemental Information for additional details.

A PDF for vessel diameters was constructed in Figure 26A showing an average diameter of $3.8 \pm 0.3\mu\text{m}$. The diameter distribution of the capillary bed has a mean of $3.5 \pm 0.2\mu\text{m}$. Vessel length distribution ranged from 1-200 μm as shown in Figure 26B. The number of capillaries as a function of cortical depth is given in Figure 26C. Capillary density was lowest near the cortical surface and at the gray-white matter interface at an approximate depth of 0.8-0.9mm. The volumetric ratio of blood vessels to tissue amounts to 0.8-1.5%, this result compares well to previous measurements^{20,40,66}. Vessel surface area is plotted in Figure 26D showing that the capillary bed occupies over 85% of surface area in all cortical samples. Figure 26E shows the distribution of volume fractions for each of the four data sets and Figure 26F plots the distribution of neurons as a function of depth.

The volume distributed as follows; pial arteries ($18.8 \pm 8.5\%$), penetrating arterioles ($2.9 \pm 1.3\%$), capillaries ($56.6 \pm 4.7\%$), penetrating venules ($3.1 \pm 1.5\%$), and pial veins ($18.7 \pm 6.2\%$). The total lumen of non-capillary vessels accounts for less than 45% of the entire microcirculatory blood volume. Data Set 2 was an outlier in this distribution, with a sparse distribution of penetrating arterioles (1.4%) and penetrating venules (0.8%). Over 92% of all junctions in the capillary bed are bifurcations, only 7% are trifurcations, and 1% exhibit higher order connectivity.

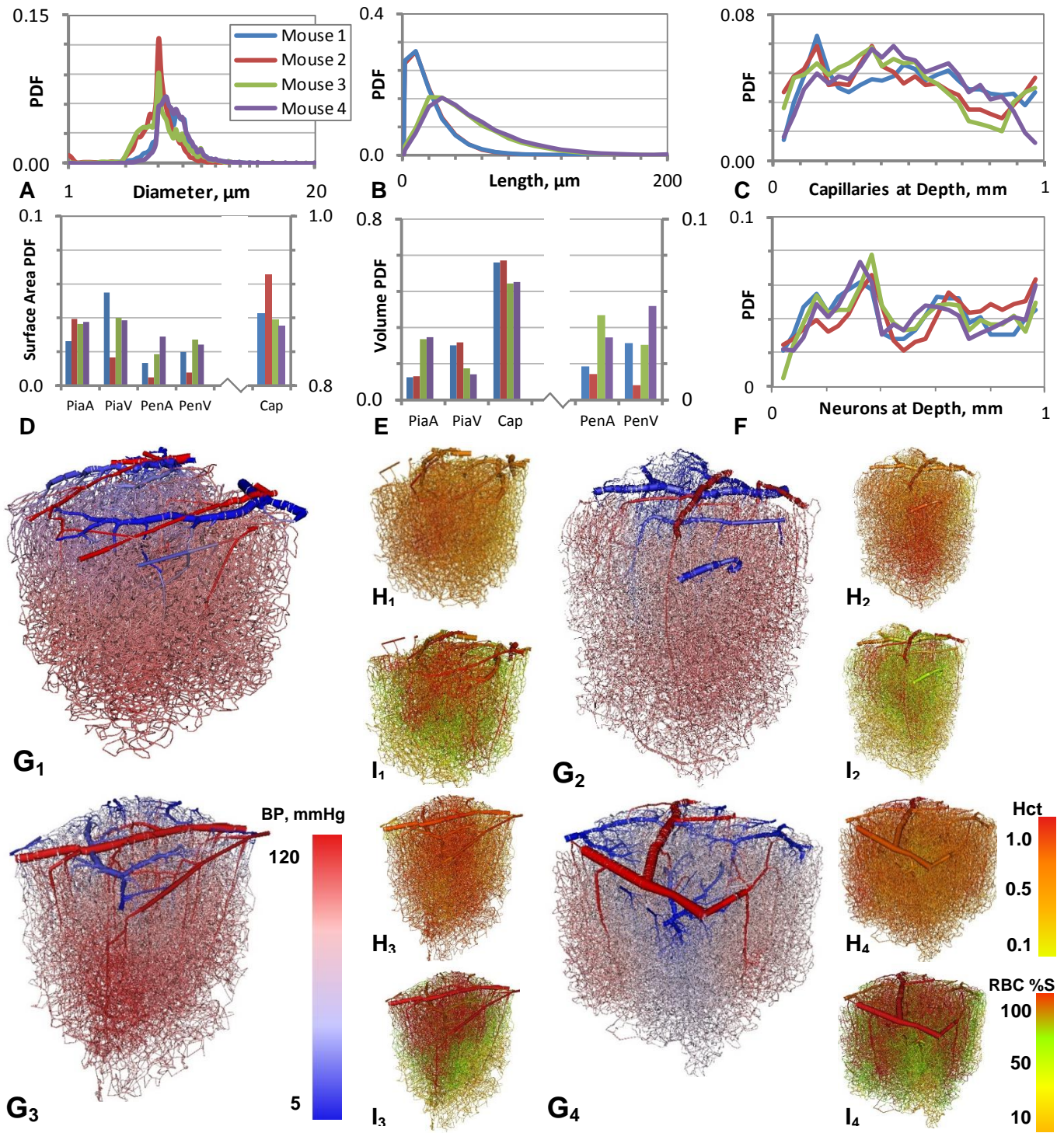


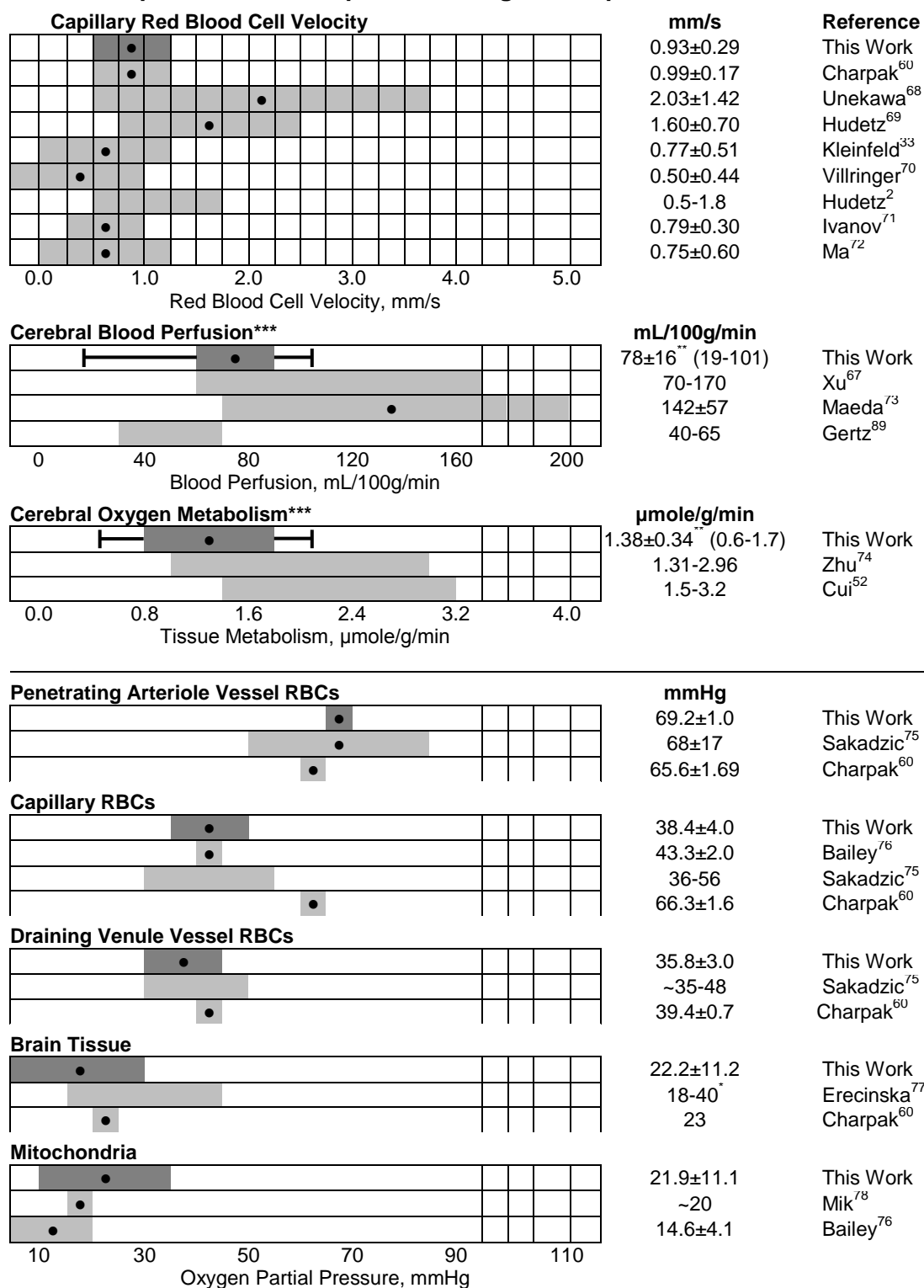
Figure 26 Statistical analysis of the four primary somatosensory cortical mouse data sets with superimposed hemodynamic simulation results. Probability density functions of anatomical parameters: **A.** vessel diameter, **B.** vessel length, and **C.** the number of capillaries located at a given depth. Distributions for pial arteries (PiaA), pial veins (PiaV), penetrating arterioles (PenA), penetrating venules (PenV) and capillaries (Cap) with respect to **D.** surface area, and **E.** lumen volume fraction. **F.** Probability density function of neuronal density at a given depth. **G-I.** Computational results for blood pressure, hematocrit, and RBC saturation. Color-coding for **G.** blood pressure from red (120mmHg) to blue (5mmHg), **H.** hematocrit from orange (0.99) to green (0.11), and **I.** RBC saturation from red (90%) to orange (2%).

Microcirculatory angioarchitecture. Figure 27 illustrates the anatomical hierarchy of the cortical angioarchitecture. The pial arteries form a network on the cortical surface. Long range pial arteries convey blood to more distal regions horizontally along the cortical surface. Penetrating arterioles siphon blood flow from the surface pials into the gray matter. These penetrating vessels carry blood perpendicular from the surface down to all six cortical layers. The distribution of microvessels in the capillary bed is isotropic with no apparent orientational preference. Finally, venules drain the capillary bed and penetrating venules bring blood back to the cortical surface where the pial veins discharge the blood into the venous sinuses.

Hemodynamics

Figure 26G-I also depicts computed blood pressures, hematocrit, and RBC oxygen tension for all four mouse data sets. The main computational results are summarized in Table X, which also shows comparisons to prior experimental studies. The distribution of RBC velocities matches previous measurements⁶⁸ as can be seen in Figure 28A. The average capillary RBC velocity was $0.93 \pm 0.29 \text{ mm/s}$, which falls within the range of measurements shown in Table X. Red blood cells in the penetrating arterioles travel at a speed of $14.18 \pm 2.02 \text{ mm/s}$, and draining venules at $7.83 \pm 1.11 \text{ mm/s}$. These speeds exceed RBC velocity in the capillary bed. Bulk blood velocity (RBCs and plasma together) through penetrating arterioles and veins was compared to recent ultrafast ultrasound localization microscopy measurements⁸³. Reported blood velocity acquired by ultrasound in descending vessels ranged between 1 to 14 mm/s, comparable to computational predictions in both penetrating arteries, $9.51 \pm 1.32 \text{ mm/s}$, and penetrating venules, $5.26 \pm 0.74 \text{ mm/s}$. The discharge hematocrit in the capillary bed agrees with two-photon microscopy studies⁶⁰ from $H_d = 0.1$ -0.9 as shown in Figure 28B.

Table X Comparison of model predictions against experimental measurements



* Rat Measurement

** Omitting Data Set 2

*** The entire range of computed values from data set 1 - 4 is indicated with a horizontal bar

Oxygen exchange

Vascular Oxygen Tension. Oxygen tension predictions in the blood vessels were compared to recent *in vivo* two-photon PO_2 microscopy mouse experiments⁶⁰ which measured arterial and venous RBC oxygen at different cortical depths. Figure 28C and Table X show that the predicted penetrating arteriole RBC oxygen content is fairly uniform between cortical layers, with an average of 69.2 ± 1.0 mmHg. The difference between the predicted arterial oxygen tension and measurements was less than 10%, which falls within the range of experimental error. The *predicted* venous RBC oxygen tension was between 34.2-41.3 mmHg. These results agree with the venous RBC oxygen tension of 39.4 ± 0.7 mmHg recently measured by the Charpak⁶⁰ lab.

Tissue oxygen tension. Figure 29 illustrates the simulated oxygen tension for the extravascular space. Figure 29A shows that the tissue oxygen tension is everywhere lower than the arteriole and venule oxygen tension. The mean tissue oxygen tension was found to be 22.2 ± 11.2 mmHg, which is 45.1 mmHg lower than the mean arterial tension, 67.3 ± 3.6 mmHg, and 16.0 mmHg lower than the average venule, 38.2 ± 9.0 mmHg. Total oxygen consumption in different compartments is summarized in Figure 29B. Accordingly, tissues near arterioles (within a distance $< 10 \mu\text{m}$) were predicted to have higher oxygen metabolism, followed by tissues in the vicinity of venules. The average CMRO in the more distant tissues (distance $> 10 \mu\text{m}$) amounted to $1.15 \pm 0.93 \mu\text{mole/g/min}$.

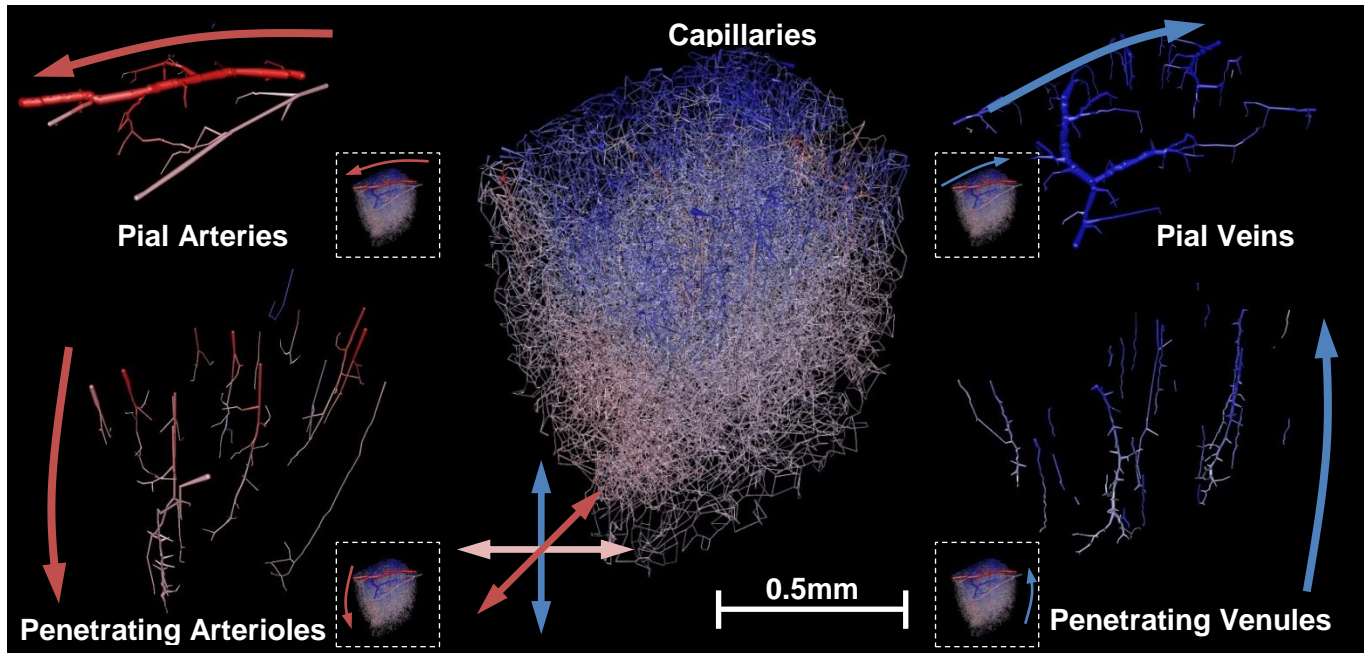


Figure 27 Depiction of the anatomical hierarchy of arterial, venous and capillary microvessels in the primary somatosensory cortex for the first data set. Vessels are painted in colors corresponding to the blood pressure depicting arteries in red and veins in blue. Large surface pial vessels distribute blood along the surface of the cortex, and feed penetrating arterioles. Penetrating arterioles divert blood into deeper cortical layers. The capillary bed distributes blood uniformly in all directions. Venules collect the blood from the capillary bed and return it to the cortical surface. Pial veins convey the venous blood from the surface to the sinuses.

Figure 29C-F reports characteristic oxygen concentration profiles in the tissue for all four data sets. The high resolution of extravascular oxygen tension was calculated using fine mesh discretization discussed in the Supplemental Information. Three-dimensional oxygen tension patterns in blood vessels are depicted in Figure 26I. Here, tissue oxygen tension is plotted along three rays collinear with the x, y and z axes penetrating the domain center as depicted in the inlay of Figure 29C. Along all directions, the profiles shows tissue oxygen tension spikes in the vicinity penetrating arterioles, whose locations are marked with red dotted lines. Oxygen tension is also elevated around draining venules marked with dotted blue lines. Between vessels, the tissue oxygen tension is relatively uniform with a mean of 22.2 ± 11.2 mmHg. This fairly even oxygen tension falls within the physiological range of 18-40 mmHg, which is highlighted as a gray shaded box for clarity. Although the boundary zones follow similar trends, they are omitted in Figure 29 to limit the analysis to the core. Reported profiles were invariant to finer mesh resolutions with edge lengths of $6.6 \mu\text{m}$, thus demonstrating mesh independence (see Supplemental Information).

Prediction of intracellular oxygen gradients

Subcellular oxygen tensions in the ECS, neuronal cytoplasm and neuronal mitochondria were predicted using the vectorized neuronal and glial data in combination with the spatial distribution procedure illustrated in Figure 30A for the glial mitochondria and Figure 30A B for neuronal mitochondria. For cortical layers I-IV oxygen tension differences between the ECS, neuronal cytoplasm and neuronal mitochondria are displayed in Figure 30A C. The schematic in Figure 30A D illustrates the differences between the ECS, neuronal cell cytoplasm (N), glial cell cytoplasm (G) and mitochondrial oxygen tension. The mean oxygen tension in the cytoplasm of the neurons in the four layers is 25.90 ± 11.15 mmHg, slightly lower than the oxygen tension in the extracellular space (25.91 ± 11.16 mmHg). The oxygen gradient across the neuronal cell membrane was 134×10^{-6} mmHg.

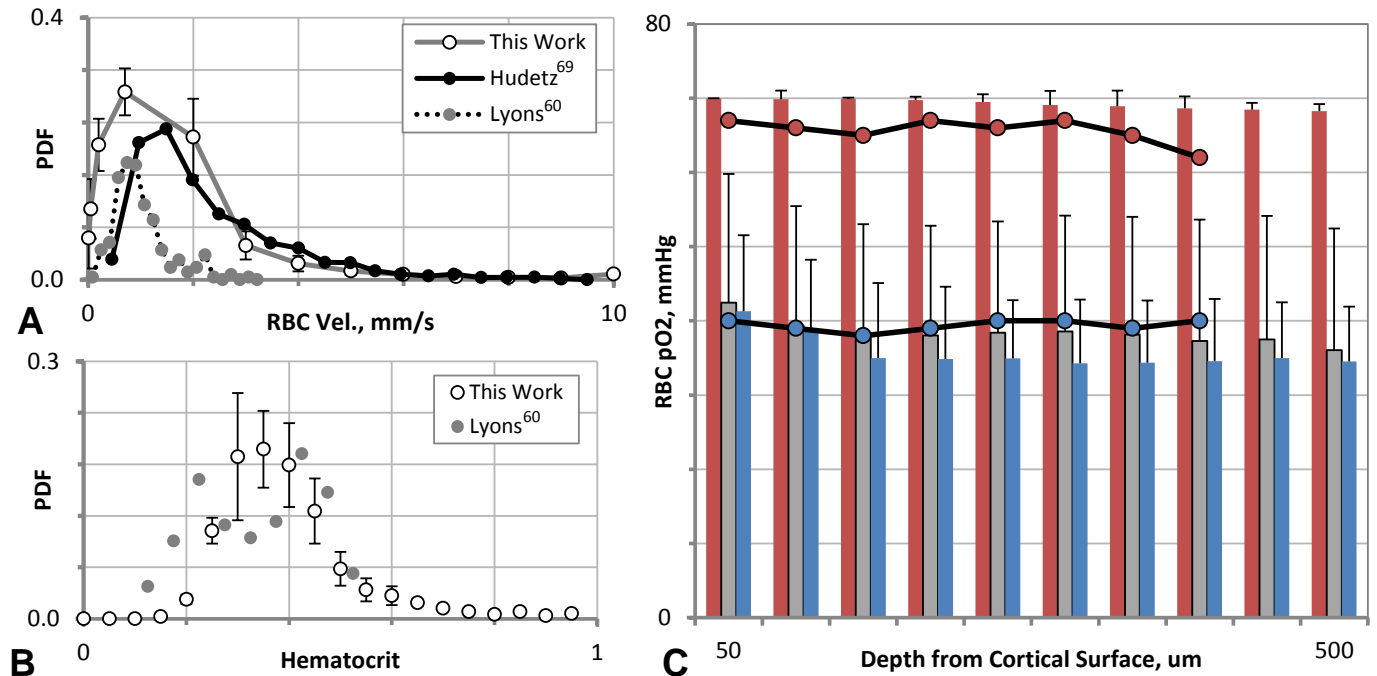


Figure 28 Comparison of predicted hematocrit distribution, RBC velocity and RBC oxygen tension to measured data. **A.** The predicted capillary RBC velocity matches measurements acquired with high-speed camera laser-scanning confocal microscopy⁶⁸. Both simulation and experiment show that more than 88% of RBCs travel at speeds below 2mm/s. **B.** The PDF for capillary hematocrit shows that the majority of capillaries have a hematocrit between 0.25-0.50 comparing well to two-photon measurements.⁶⁰ **C.** Mean RBC oxygen tension at different depths from the cortical surface (50-500 μ m). Bars indicate arterial (red), capillary (gray) and venous (blue) RBC oxygen tension compared to measured data⁶⁰ drawn as lines with connected dots in red for arteries and veins in blue.

The oxygen tension in the neuronal cytoplasm was 250×10^{-6} mmHg above the mitochondria as shown in Figure 30C. Intracellular oxygen tension was simultaneously predicted for glial cells. The oxygen tension in the glial cytoplasm is 25.90 ± 11.16 mmHg, which is 134×10^{-6} mmHg below the surrounding ECS. It should be noted that both kinetic models of oxygen consumption yield comparable oxygen metabolism rates. However, only the mitochondrial model allows predicting oxygen gradients between the ECS, the cytoplasm and the mitochondria. The first order oxygen metabolism model does not resolve individual intracellular oxygen differences because the three compartments are lumped.

Path analysis

To better understand spatial variations of hemodynamic states, path analysis from all arterial inlets to venous outlets was performed. Blood pressure, hematocrit, RBC saturation and plasma oxygen tension trajectories along several representative paths for mouse one were analyzed and plotted as a function of diameter in Figure 31. Each path begins at an arterial inlet and follows the direction of blood flow, making random choices at each bifurcation, thus traversing the capillary bed and returning to the surface through a draining pial vein. All possible paths were enumerated and the maximum and minimum pressures are painted as shaded regions in Figure 31B-F. The average trajectory of each hemodynamic state was plotted as a black solid line.

The pressure was recorded for all paths for each of the four data sets, and the average pressure drop is shown in Figure 31B. Minimum and maximum pressure along all paths (data not shown) are depicted as a shaded region. Blood pressure decreases monotonically in each path displayed in Figure 31C, which is consistent with the flow direction of the blood supply. The pressure drop is steepest in capillaries ($d < 10 \mu\text{m}$) including small vessels fed by adjacent penetrating arterioles. The locations of these steep pressure drops suggest that the capillary bed is the major site of blood flow resistance.

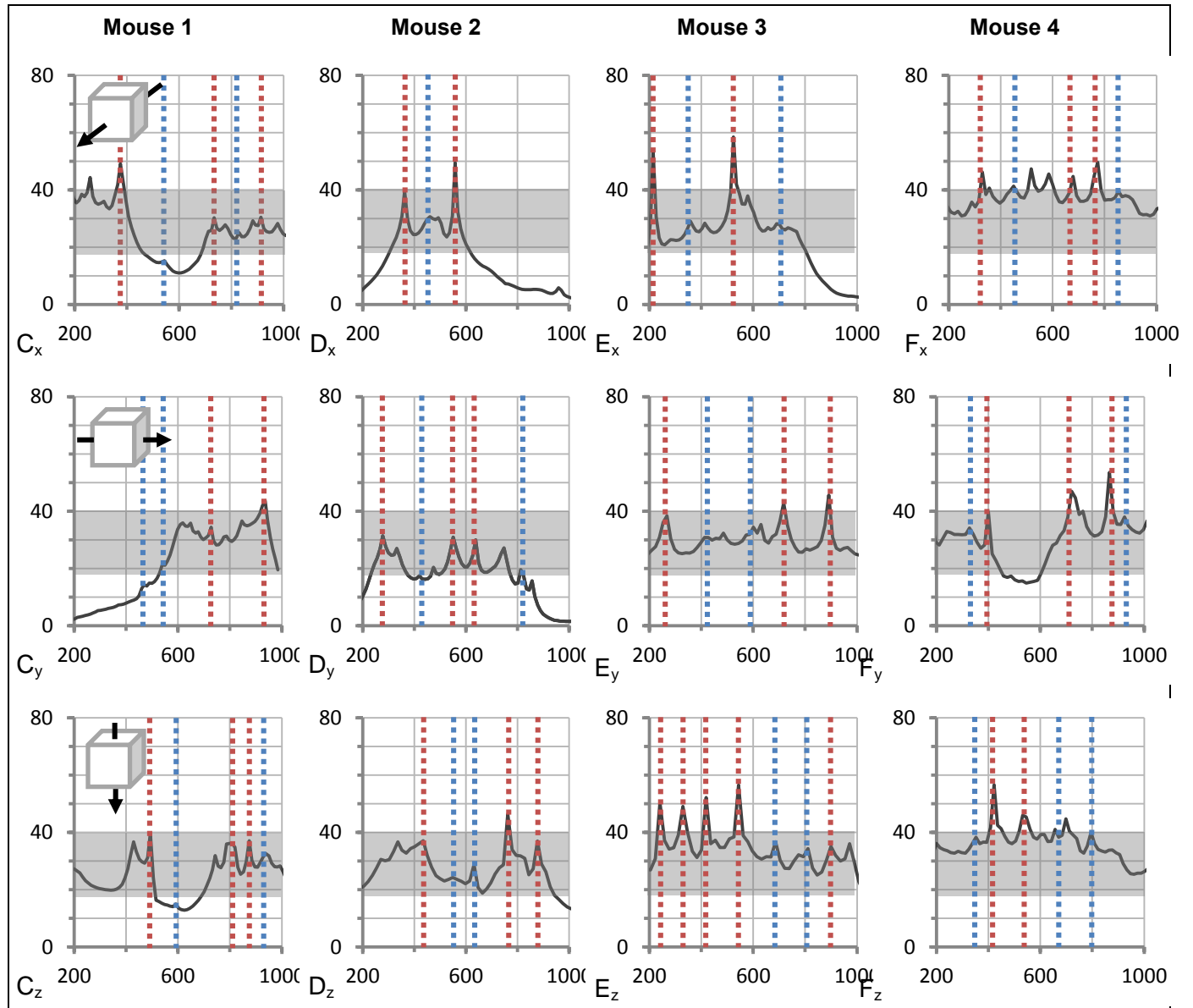
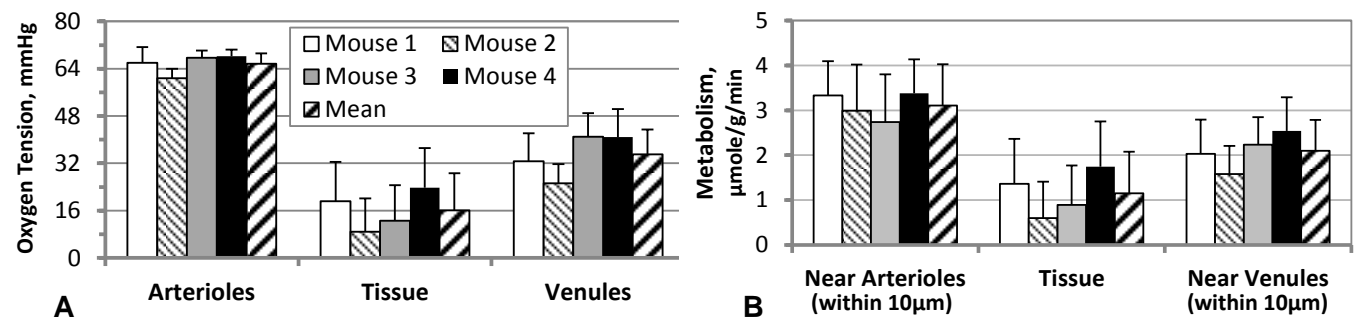


Figure 29 Oxygen tension in the murine cortical tissue. **A.** Average oxygen tension in the arterioles, tissue and venules in all four data sets, standard deviation as capped lines. The tissue is an oxygen sink and therefore lower than both arteries and veins. **B.** Oxygen metabolism as a function of proximity to penetrating vessel. Oxygen tension along a ray passing through the center of each of the four data sets (**C-F**) in the x-direction, y-direction, and z-direction. Dotted vertical lines illustrate the position of penetrating arterioles (red) and penetrating venules (blue), gray box indicates experimentally measured oxygen tension in the murine cortex (18-40mmHg).

In addition, five representative paths were traced individually in the first data set and are drawn as solid lines of different colors as illustrated in Figure 31A. The hemodynamic states of blood pressure, hematocrit, RBC saturation and plasma oxygen tension were taken along each of these paths. Hematocrit tends to concentrate in deep reaching penetrating arterioles due to *plasma skimming* as shown in Figure 31D. For example, in some paths (green path), the hematocrit of penetrating arterioles rises to $H_d=0.60$ which is higher than its pial supply vessel of $H_d=0.35$. Paths connecting to the capillary bed closer to the surface (orange path), tend to have lower hematocrit than paths traveling deeper into the cortex. The RBC content in the capillary bed is highly variable depending on the location and hematocrit of its feeders. Some segments are more concentrated, $H_d=0.60$, or more dilute, $H_d=0.11$, than the systemic hematocrit. In venules, the highly variable red blood cell concentration in the capillaries is remixed. Therefore, the discharge hematocrit in draining veins returns to $H_d=0.35$.

The RBC oxygen saturation remains fairly constant at 83% in the thick-walled surface arteries and penetrating arterioles as depicted in Figure 31E. Oxygen saturation then drops dramatically where the penetrating arterioles feed the thin-walled capillary bed. Depending on the path, RBC saturation decreased anywhere to 10% (purple and blue path) to very low values (green and orange path) in the capillary bed. This variability in oxygen saturation in the capillary bed depends on the path length and orientation. All paths eventually feed into the draining venules, from highly concentrated (58%, blue path) to low saturation (45%, orange path). This variability in RBC saturation is reflected in the plasma oxygen tension depicted in Figure 31F.

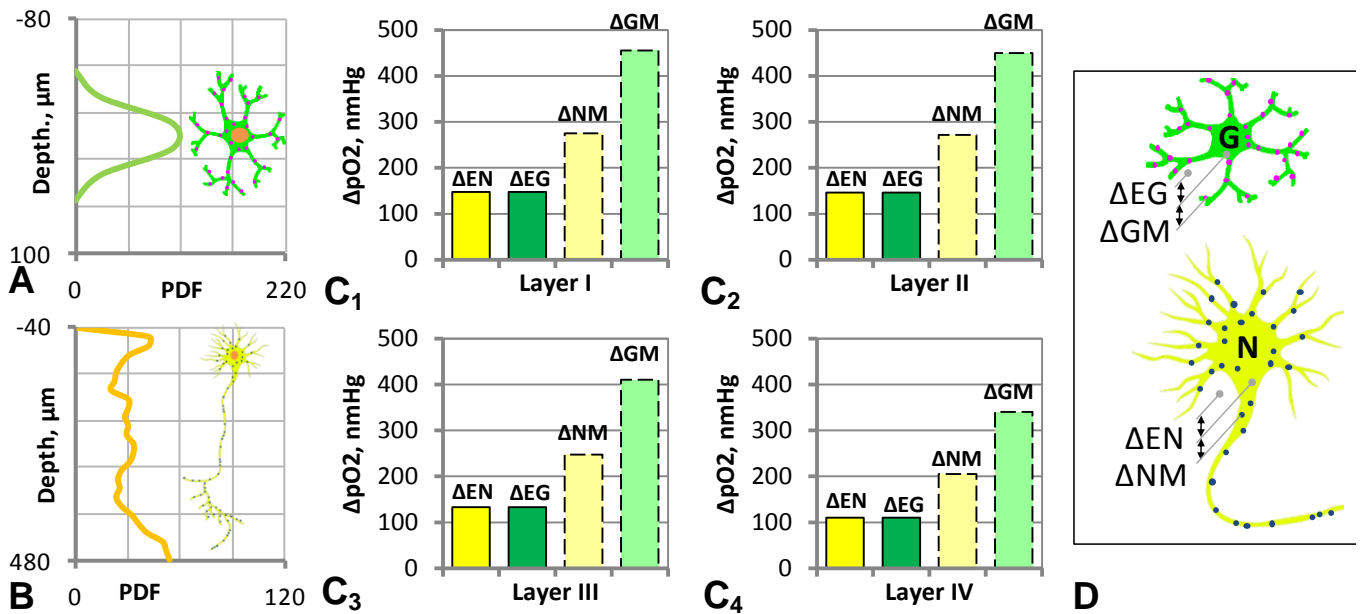


Figure 30 Predicted tissue, cellular, and intercellular oxygen gradients. Mitochondria were spatially distributed to different location with the respect to the cell nucleus according to a cell-specific PDF: **A**. PDF for mitochondria location around glial nucleus (x=0mm) **B**. PDF of mitochondria in neurons. **C₁-C₄**. Oxygen tension gradient between ECS and neuronal cytoplasm (ΔEN), neuronal cytoplasm and mitochondria (ΔNM), ECS and glial cell cytoplasm (ΔEG), and glial cell cytoplasm to glial mitochondria (ΔGM) are reported for cortical layers I-IV. **D**. Illustration of the differences between the ECS, neuronal cell cytoplasm (N), glial cell cytoplasm (G) and mitochondrial oxygen tension.

Discussion

The complex interaction of microcirculatory network topology, oxygen metabolism and hemodynamics was quantified by detailed simulations reaching down to the cellular level. Microvessels were labeled by size, cortical depth and hierarchy. Non-Newtonian biphasic hemodynamics, RBC velocity, RBC saturation and oxygen turnover were predicted throughout the primary somatosensory cortex of four animals. Intracellular oxygen gradients between the cytoplasm and mitochondrial oxygen tension inside neurons and glial cells were also computed. Through the interrogation of every path through the cortical blood supply, a quantitative picture of all *hemodynamic state transitions* inside the microcirculation emerges. The computational results identify capillaries adjacent to feeding arterioles and the capillary bed ($d < 10\mu\text{m}$) as the major site of hemodynamic resistance.

Hemodynamics and variability along microcirculatory paths

Simulations show that even capillaries with identical blood flow, caliber and path length may convey red blood cells at different velocities. Though capillary diameter and path length contribute to blood flow resistance, the variability of RBC velocity within the capillary bed depends on hematocrit fluctuations. Plasma skimming concentrate RBCs in deeper reaching penetrating arterioles, while paths near the surface tend to be more dilute. Concentration of red blood cells in the penetrating arterioles ensures that deep tissue near the gray-white matter interface is well-supplied with oxygen and nutrients. The kinematic plasma skimming method (KPSM) was chosen over prior models because it can compute RBC splitting at trifurcations and higher order vessel junctions. Table X offers a comprehensive comparison of all predications against known experimental results. It shows that our model agrees reasonably with most known experimental values at the macroscopical blood flow level as well as subcellular properties such as mitochondrial oxygen tension.

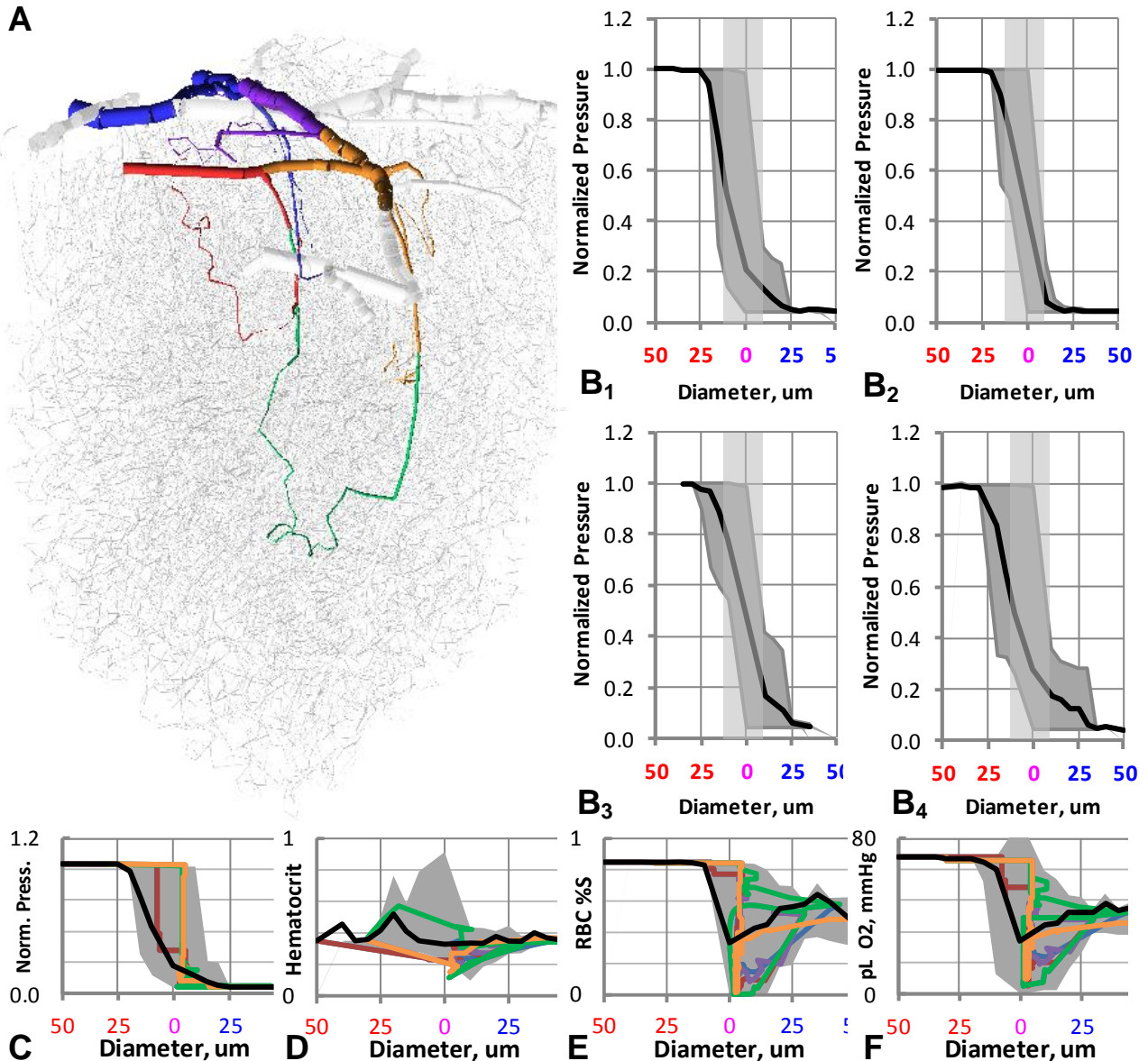


Figure 31 Path analysis in a representative data set (mouse one). **A.** Anatomy of the cortical microcirculation with five typical flow paths. Each path follows the blood flow from an inlet pial artery through the capillary bed returning to the surface via draining venules. **B₁-B₄.** Mean pressure paths and range of microcirculatory blood pressure shown for all four data sets. Light gray shaded box indicates the capillary bed (vessels with diameter < 10 μm), where the main pressure drop occurs. This shaded region includes pre-capillary arterioles, capillaries and post-capillary venules. **C-F.** The computed hemodynamic trajectory of each flow path is reported for **C.** blood pressure, **D.** discharge hematocrit, **E.** RBC saturation, and **F.** plasma pO₂. Upper and lower ranges of all paths (only five individual paths are shown) are drawn as a gray shaded region, illustrating the heterogeneity of the capillary bed. Averages of all paths are drawn as a black line. Note that averages do not well characterize the wide variety of hemodynamic state transitions that occur in the capillary bed.

Like hematocrit, RBC oxygen tension varies little in the surface pial arteries. Below the cortical surface in the microcirculation, the random arrangement of the blood vessels creates a multiplicity of paths producing a wide spectrum of blood pressures, hematocrit and RBC tensions. The path analysis further shows that blood pressures, hematocrit and oxygen tension cannot be attributed to blood vessels by diameter or membership within an ordered hierarchy. Moreover, there is no “standard” trajectory of hemodynamic state transitions; this finding has important implications for experiments.

Individual experimental point measurements only describe a single path, which in general do not coincide with other paths in the same cortical section or those acquired in a different animal. Discrepancies reported in the literature may not indicate experimental error, but merely reflect the wide variability of the natural hemodynamic states in the microcirculation. In order to confirm our predictions of the variance in the capillary bed, numerous measurements in three dimensional tissue samples instead of point measurements are needed.

Microcirculatory resistance distribution

The path analysis reported in Figure 31B clearly indicated that the largest pressure drops occur in the smallest vessels ($d < 10\mu\text{m}$). Accordingly, it appears that these small vessels contribute the bulk of the hemodynamic resistance. While this model does not differentiate between pre-capillary arterioles or post-arteriole capillaries, it is clear that the majority of hydraulic resistance lies near and around the capillary bed, and not in the penetrating arterioles. Tracing individual paths through the microcirculation, as indicated by the colored lines in Figure 31C, show that the steepest pressure drops occur in the capillary bed.

Limitations

The comparison to experimental data shows that cerebral blood perfusion as well as cerebral oxygen metabolism is at the lower end of the experimental trends indicating a reduced inflow of blood and oxygen. We believe that some microvessels may not have been recognized

by the image reconstruction software so that the current model, although anatomically fairly complete, may still miss vessels present in the real cortex. Overall microcirculatory resistance may have been artificially increased by a systematic underestimation of microvessel inner diameter in the original reconstruction from two-photon images of the murine cortex. This issue was partially compensated for by our choice of a relatively high inlet pressure.

This overestimation of microcirculatory resistance in the original data set was overcome using an alternate method in Schmid et al.⁹¹. By “right-shifting” the entire diameter spectrum of the same microcirculatory networks, the mean inner microvessel diameter increased to 4.5 μ m, decreasing overall microcirculatory resistance. Additionally, this separate study computed the hematocrit distribution (and hence hemodynamic resistance) using a discrete RBC-tracking plasma skimming method. It is unclear how this approach of computing microcirculatory hematocrit distribution compares to the plasma skimming method employed in this study. Due to these fundamental changes in the structure of the microcirculatory angioarchitecture and the biophysics of the hemodynamic simulation, this alternative simulation which utilizes the same vessel structure data set cannot be compared to or validated against this study.

The criterion for differentiating between small arterioles and capillaries relied on branching order and vessel diameter; *actin* and *desmin* labeling of the parent data set to differentiate between pre-capillary arterioles and post-arteriole capillaries is not available at this time. The original data sets contained arteriolar loops that did not connect to the capillary bed. These non-physiologic “dead-end loops” were corrected by connecting them to the capillary bed to ensure flow through every vessel. None of the four cortical samples had more than 30 dead-end-loops, which is equivalent to less than 0.1% of all blood vessel segments- a minimal change to the original data.

Not all smooth muscle and endothelial cells were detected; therefore the metabolic demands of these cell types could not be incorporated in this study which may underestimate oxygen extraction by muscle cells in the wall of larger arterial vessels. Furthermore, because

the position of mitochondria was not determined, a spatial distribution of mitochondria inside the neurons and glial cells was merely assumed according to a probabilistic density function. Extracellular and mitochondrial oxygen tensions between simulations and experiments matched well, but cytoplasmic oxygen tension is experimentally inaccessible at this time. Because glucose transport, carboxylic acid production, and pH calculation were not addressed in this work, oxygen binding kinetics were computed using a set $\text{pH}=7.4$. A pH sensitive computation of oxygen binding kinetics using the Adair⁴⁹ model may be an appropriate step forward. A more complex model⁵¹ of oxygen and glucose metabolism could also shed insight into the controlling factors for CMRO.

Future work

The predicted wide range of hemodynamic values in the capillary bed underscores the difficulty in comparing point measurements between different experiments, animal specimens, laboratories or computer simulations. This work suggests that the variation of blood pressure, flow and oxygen tension may be wider than previously expected. Recent experimental studies of oxygen distribution in the cerebral microcirculation^{60,75} confirm the patchiness of hemodynamic states within the capillary bed. Accordingly, multiple measurements tracing numerous paths from the surface pials down to the capillary bed are needed for meaningful characterization of microcirculatory flow patterns and validation.

The capillary bed, specifically capillaries adjacent to feeding arterioles, was identified as the primary site of flow resistance. While dilation of a single capillary hardly changes global blood flow, a concerted dilation of capillaries in a sizeable cortical subsection would drastically reduce the hemodynamic resistance thus increasing blood perfusion to that region. Accordingly, adjustments of capillary bed resistance may serve to regulate tissue perfusion in response to brain injury. On the other hand, the smooth muscles of arteries and arterioles enable control over blood supply from the cortical surface to the deep layers. This second potentially fast

activation of the arterial blood supply via vasodilation and constriction may be activated during functional hyperemia. Detailed models of cerebral microcirculation such as the system presented here may in the future aide in determining the role of vasoconstriction of arterioles or pericytes in regulating cortical blood perfusion.

Supplemental 1

Blood flow computations

Microcirculatory blood flow is modeled as a biphasic suspension composed of a plasma phase and a red blood cell phase. The bulk flow estimations are given in this section; the drift flux computation for the uneven distribution of red blood cells in bifurcations has been described in section Biphasic blood flow computations of this chapter.

Due to the low Womersley numbers ($Wo < 0.1$) in the microvessels, pulsatile motion of blood can be ignored. Additionally, low Reynolds numbers in the microcirculation ($Re < 1$) permit neglecting inertia so that steady conditions may be assumed for bulk flow. The microcirculation is represented as a network of interconnected cylindrical vessel segments. Mass conservation is enforced by the continuity eq. 45. The hydrostatic blood pressure drop across a vessel, ΔP is the product of the bulk flow, Q , through the vessel and its vascular resistance, α . Each cylindrical vessel segment is assigned a hydraulic resistance approximated by the viscosity modified Poiseuille Law, described in eq. 46 which is a function of the dynamic viscosity of blood plasma, μ , and the vessel's length, L , radius, R , and the *in vivo* viscosity adjustment, η_{vivo} . The viscosity adjustment depends on vessel radius and discharge hematocrit⁷⁹⁻⁸⁰. The drift flux velocity between the plasma and RBCs is given in eq. 35-36 in the methods section. The bulk and hematocrit fields are solved iteratively until simultaneous convergence. Plasma viscosity was assumed to be 1.0cP; plasma viscosity has been measured to be 1.3cP

$$\vec{\nabla} \cdot Q = 0 \quad 45$$

$$\Delta P = Q\alpha = Q \cdot \frac{8\mu L}{\pi R^4} \cdot \eta_{vivo}(R, H_d) \quad 46$$

Supplemental 2

Nonlinear biphasic oxygen dissociation

Oxygen dissociation kinetics from oxygen bound on erythrocytes to the plasma was approximated as a first-order reversible reaction, shown in eq. 47. The oxygen dissociation reaction rate from the red blood cells to the plasma, $\dot{R}_{R \rightarrow P}$, is governed by the first Adair forward reaction rate constant, k_f , the backward dissociation reaction rate constant, k_b , the hematocrit, H_t , and the volume of the cylindrical blood vessel segment, V_b .

$$\dot{R}_{R \rightarrow P} = H_t V_b (k_f C_{HbO_2} - k_b C_{pO_2}) \quad 47$$

By introducing the equilibrium constant, $K_{eq} = k_b/k_f$, the backward reaction rate constant can be eliminated as shown in eq. 48. The introduction of the equilibrium constant into the dissociation kinetics guarantees the reaction rates obey the Hill equation at equilibrium.

$$\dot{R}_{R \rightarrow P} = H_t V_b k_f (C_{HbO_2} - K_{eq} C_{pO_2}) \quad 48$$

The equilibrium constant is equal to the ratio of the freely dissolved plasma oxygen concentration, C_{pO_2} , over the bound oxygen concentration shown in eq. 49. The bound oxygen concentration is the product of the total oxygen carrying capacity of RBC, β , and the hemoglobin saturation, S . Hemoglobin saturation is a function of plasma oxygen tension, pO_2 , defined as the product of the plasma free oxygen concentration and the Henry's solubility of oxygen in plasma, α_{pl} .

$$K_{eq} = \frac{\beta \cdot S(C_{pO_2} \cdot \alpha_{pl})}{C_{pO_2}} \quad S(pO_2) = \frac{1}{1 + (P_{50}/pO_2)^n} \quad 49$$

The physiological equilibrium saturation of RBC is determined by the Hill equation⁸¹⁻⁸², which describes hemoglobin saturation in terms of the oxygen tension at 50% oxygen saturation, P_{50} , and the Hill coefficient, n , defined in Table IX. A constant value of pH=7.4 was assumed.

Supplemental 3

Distribution of surface area for each data set

The distribution of vessel surface area between pial arteries, penetrating arterioles, capillaries, penetrating venules and pial veins was determined for each data set as shown in Table XI. The distribution of surface area to capillaries was over-represented in data set 2, and penetrating arterioles and venules were below standard deviation when compared to the average of all four data sets. Low blood flow and tissue perfusion were computed this second data set, indicating that these statistical morphological variations affect the microcirculatory hydraulic resistance.

Table XI Percent surface area fraction

Data Set	Mouse 1	Mouse 2	Mouse 3	Mouse 4	Mean
Pial Arteries	2.6%	3.9%	3.6%	3.8%	3.5±0.5%
Penetrating Arterioles	1.3%	0.5%	1.9%	2.9%	1.6±0.9%
Capillaries	88.5%	93.1%	87.8%	87.1%	89.1±2.4%
Penetrating Venules	2.0%	0.8%	2.7%	2.4%	2.0±0.7%
Pial Veins	5.5%	1.7%	4.0%	3.9%	3.8±1.4%

Supplemental 4

Mesh Independence Investigation

This section demonstrates that computer predictions of the coupled hemodynamics and oxygen transport models were independent of mesh discretization. The edge length for the extravascular domain was gradually refined for each data set. The cylindrical vessel segments in the network were also refined so that the arc length of each vessel was commensurate with the edge length of the mesh. Predictions stabilized when edge length was in the order of 5-10 μ m as exemplified for total oxygen extraction shown in Figure 32. For the finest mesh resolution (6.6 μ m), more than 3 million equations had to be solved iteratively with an over-relaxed Gauss Seidel method requiring 14-24 CPU hours.

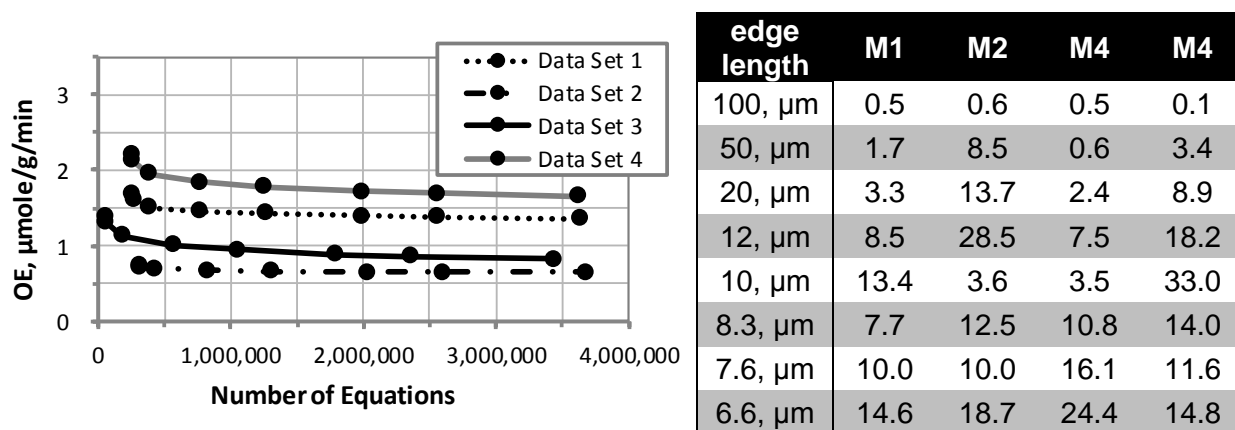


Figure 32 Mesh Independence Study. Oxygen extraction and profiles (data not shown) was computed for different edge lengths for each data set. In coarse meshes (50-100 μm), oxygen extraction was sensitive to edge length. As the computational domain for solving the reaction-diffusion equations was gradually refined, oxygen transport was no longer affected. For all four data sets mesh independence was achieved between 2.5-3.0 million equations corresponding to an approximate mesh edge length of 6.6 μm .

Supplemental 5

Hierarchy of Hydraulic Resistance

The hydraulic conductivity as a function of branch order from the penetrating arteriole may be of interest in further determining the spatial distribution of resistance in the microcirculation. Each vessel within the capillary bed was assigned a minimum branch order based on the number of vessels traversed from its corresponding feeding penetrating arteriole. Should a vessel be connected by multiple paths to one or more penetrating arterioles (as is the case in the naturally anastomosed and highly interconnected capillary bed), the minimum order of branches to a penetrating arteriole was recorded. This categorization was limited as higher order capillaries could not be reliably categorized due to the multitude of feeding penetrators. As such, capillaries with branch order 7 or higher were excluded from the investigation.

Mean capillary diameter was plotted against branch order as shown in Figure 33A. Capillaries narrowed slightly as they increase in branching order, from 5 μ m at the first order branch to 4.1 μ m at the 4th through 7th order branches. This led to a corresponding increase in capillary hydraulic resistance as shown in Figure 33B. The average hydraulic resistance of capillaries connected to the feeding arteriole is nearly an order of magnitude lower than vessels with a branch order of 4th or higher. Simultaneously, higher branch order capillaries also display a higher variance for both diameter and resistance. This analysis demonstrates that the capillary bed cannot be modeled as a collection of resistors arranged in series. The contributions of high order branches to overall capillary bed resistance are both significant and highly variable.

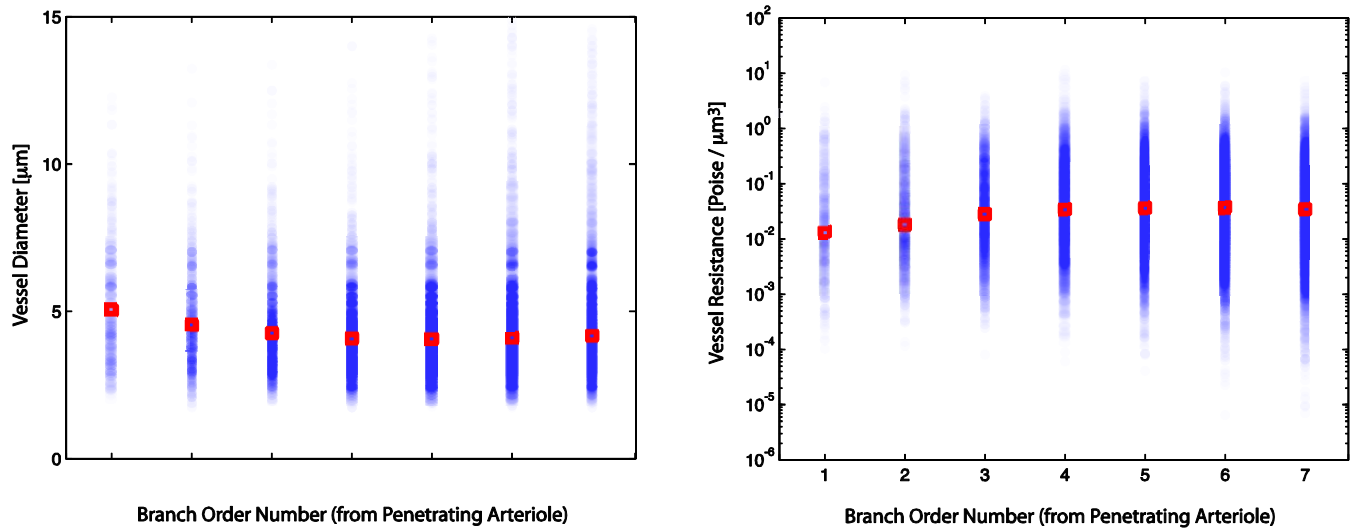


Figure 33 Morphological and hydraulic characteristics of the capillary bed as a function of branch order. Average values shown as a red box, distribution of values at each branch order shown in blue. **A.** Diameter of arterioles and capillaries as a function of branch order from the penetrating arteriole. The mean capillary diameter of 5μm decreases slightly with increasing branching order. **B.** Hydraulic resistance of individual vessels as a function of branch order. Mean capillary hydraulic resistance near the feeding arteriole is an order of magnitude lower than vessels with a branch order of 4th or higher.

Cited Literature

1. Devor A, Sakadzic S, Saisan PA, Yaseen MA, Roussakis E, Srinivasan VJ, et al. "Overshoot" of O_2 is required to maintain baseline tissue oxygenation at locations distal to blood vessels. *J Neurosci* 31: 13676-81, 2011.
2. Hudetz AG. Blood flow in the cerebral capillary network: a review emphasizing observations with intravital microscopy. *Microcirculation* 4: 233-52, 1997.
3. Boas DA, Jones SR, Devor A, Huppert TJ, Dale AM. A vascular anatomical network model of the spatio-temporal response to brain activation. *NeuroImage* 40: 1116-29, 2008.
4. Kaufmann AM, Firlik AD, Fukui MB, Wechsler LR, Jungreis CA, Yonas H. Ischemic core and penumbra in human stroke. *Stroke* 30: 93-9, 1999.
5. Nishimura N, Schaffer CB, Friedman B, Lyden PD, Kleinfeld D. Penetrating arterioles are a bottleneck in the perfusion of neocortex. *Proc Natl Acad Sci U S A* 104: 365-70, 2007.
6. Shih AY, Friedman B, Drew PJ, Tsai PS, Lyden PD, Kleinfeld D. Active dilation of penetrating arterioles restores red blood cell flux to penumbral neocortex after focal stroke. *J Cereb Blood Flow Metab* 29: 738-51, 2009.
7. Helmchen F, Kleinfeld D. In Vivo Measurements of Blood Flow and Glial Cell Function with Two-Photon Laser-Scanning Microscopy. *Angiogenesis: In Vivo Systems, Pt A* 444: 231-54, 2008.
8. del Zoppo GJ, Mabuchi T. Cerebral microvessel responses to focal ischemia. *J Cereb Blood Flow Metab* 23: 879-94, 2003.
9. Reglin B, Pries AR. Metabolic control of microvascular networks: oxygen sensing and beyond. *J Vasc Res* 51: 376-92, 2014.
10. Lecoq J, Parpaleix A, Roussakis E, Ducros M, Houssen YG, Vinogradov SA, et al. Simultaneous two-photon imaging of oxygen and blood flow in deep cerebral vessels. *Nature Medicine* 17: 893-U262, 2011.

11. Zonta M, Angulo MC, Gobbo S, Rosengarten B, Hossmann KA, Pozzan T, et al. Neuron-to-astrocyte signaling is central to the dynamic control of brain microcirculation. *Nat Neurosci* 6: 43-50, 2003.
12. Pittman RN. Oxygen transport in the microcirculation and its regulation. *Microcirculation* 20: 117-37, 2013.
13. Goldman D, Popel AS. Computational modeling of oxygen transport from complex capillary networks. Relation to the microcirculation physiome. *Adv Exp Med Biol* 471: 555-63, 1999.
14. Tsoukias NM, Goldman D, Vadapalli A, Pittman RN, Popel AS. A computational model of oxygen delivery by hemoglobin-based oxygen carriers in three-dimensional microvascular networks. *Journal of Theoretical Biology* 248: 657-74, 2007.
15. Secomb TW, Pries AR. Blood viscosity in microvessels: Experiment and theory. *Comptes Rendus Physique* 14: 470-8, 2013.
16. Gould IG, Linninger AA. Hematocrit distribution and tissue oxygenation in large microcirculatory networks. *Microcirculation* 22: 1-18, 2015.
17. Duvernoy H, Delon S, Vannson JL. The vascularization of the cerebellar cortex. *Brain Res Bull* 11, 1983.
18. Cassot F, Lauwers F, Lorthois S, Puwanarajah P, Cances-Lauwers V, Duvernoy H. Branching patterns for arterioles and venules of the human cerebral cortex. *Brain Res* 1313: 62-78, 2010.
19. Duvernoy HM, Delon S, Vannson JL. Cortical blood vessels of the human brain. *Brain Res Bull* 7: 519-79, 1981.
20. Lauwers F, Cassot F, Lauwers-Cances V, Puwanarajah P, Duvernoy H. Morphometry of the human cerebral cortex microcirculation: general characteristics and space-related profiles. *NeuroImage* 39: 936-48, 2008.
21. Intaglietta M, Johnson PC, Winslow RM. Microvascular and tissue oxygen distribution. *Cardiovasc Res* 32: 632-43, 1996.

22. Vovenko EP, Chuikin AE. Tissue oxygen tension profiles close to brain arterioles and venules in the rat cerebral cortex during the development of acute anemia. *Neurosci Behav Physiol* 40: 723-31, 2010.
23. Vovenko EP, Chuikin AE. Oxygen tension in rat cerebral cortex microvessels in acute anemia. *Neurosci Behav Physiol* 38: 493-500, 2008.
24. Krogh A. The supply of oxygen to the tissues and the regulation of the capillary circulation. *Journal of Physiology* 52: 457-74, 1919.
25. Kirkpatrick JP, Dewhirst MW. Analytic solution to steady-state radial diffusion of a substrate with first-order reaction kinetics in the tissue of a Krogh's cylinder. *Radiation Research* 169: 350-4, 2008.
26. Huppert TJ, Allen MS, Benav H, Jones PB, Boas DA. A multicompartiment vascular model for inferring baseline and functional changes in cerebral oxygen metabolism and arterial dilation. *J Cereb Blood Flow Metab* 27: 1262-79, 2007.
27. Smith AF, Secomb TW, Pries AR, Smith NP, Shipley RJ. Structure-based algorithms for microvessel classification. *Microcirculation* 22: 99-108, 2015.
28. Fang Q, Sakadzic S, Ruvinskaya L, Devor A, Dale AM, Boas DA. Oxygen advection and diffusion in a three- dimensional vascular anatomical network. *Opt Express* 16: 17530-41, 2008.
29. Hellums JD, Nair PK, Huang NS, Ohshima N. Simulation of intraluminal gas transport processes in the microcirculation. *Ann Biomed Eng* 24: 1-24, 1996.
30. Goldman D. Theoretical models of microvascular oxygen transport to tissue. *Microcirculation* 15: 795-811, 2008.
31. Zweifach BW, Lipowsky HH. Quantitative studies of microcirculatory structure and function. III. Microvascular hemodynamics of cat mesentery and rabbit omentum. *Circ Res* 41: 380-90, 1977.

32. Pries AR, Ley K, Gaehtgens P. Generalization of the Fahraeus Principle for Microvessel Networks. *American Journal of Physiology* 251: H1324-H32, 1986.
33. Kleinfeld D, Mitra PP, Helmchen F, Denk W. Fluctuations and stimulus-induced changes in blood flow observed in individual capillaries in layers 2 through 4 of rat neocortex. *Proc Natl Acad Sci U S A* 95: 15741-6, 1998.
34. Safaeian N, David T. A computational model of oxygen transport in the cerebrocapillary levels for normal and pathologic brain function. *J Cereb Blood Flow Metab* 33: 1633-41, 2013.
35. Schneider M, Hirsch S, Weber B, Szekely G. Physiologically based construction of optimized 3-D arterial tree models. *Med Image Comput Comput Assist Interv* 14: 404-11, 2011.
36. Goldman D, Popel AS. A computational study of the effect of capillary network anastomoses and tortuosity on oxygen transport. *Journal of Theoretical Biology* 206: 181-94, 2000.
37. Lorthois S, Cassot F, Lauwers F. Simulation study of brain blood flow regulation by intra-cortical arterioles in an anatomically accurate large human vascular network: Part I: methodology and baseline flow. *NeuroImage* 54: 1031-42, 2011.
38. Linninger AA, Gould IG, Marinnan T, Hsu CY, Chojecki M, Alaraj A. Cerebral microcirculation and oxygen tension in the human secondary cortex. *Ann Biomed Eng* 41: 2264-84, 2013.
39. Karch R, Neumann F, Neumann M, Schreiner W. Staged growth of optimized arterial model trees. *Ann Biomed Eng* 28: 495-511, 2000.
40. Blinder P, Tsai PS, Kaufhold JP, Knutsen PM, Suhl H, Kleinfeld D. The cortical angiome: an interconnected vascular network with noncolumnar patterns of blood flow. *Nat Neurosci* 16: 889-97, 2013.

41. Tsai PS, Kaufhold JP, Blinder P, Friedman B, Drew PJ, Karten HJ, et al. Correlations of Neuronal and Microvascular Densities in Murine Cortex Revealed by Direct Counting and Colocalization of Nuclei and Vessels. *Journal of Neuroscience* 29: 14553-70, 2009.
42. Kaufhold JP, Tsai PS, Blinder P, Kleinfeld D. Vectorization of optically sectioned brain microvasculature: learning aids completion of vascular graphs by connecting gaps and deleting open-ended segments. *Medical Image Analysis* 16: 1241-58. 2012.
43. Shih AY, Driscoll JD, Drew PJ, Nishimura N, Schaffer CB, Kleinfeld D. Two-photon microscopy as a tool to study blood flow and neurovascular coupling in the rodent brain. *J Cereb Blood Flow Metab* 32: 1277-309, 2012.
44. Zhang K, Sejnowski TJ. A universal scaling law between gray matter and white matter of cerebral cortex. *Proceedings of the National Academy of Sciences of the United States of America* 97: 5621-6, 2000.
45. Trans-NIH Knock-Out Mouse Project (KOMP) U01HG004080-04S1 supplemental Recovery Act funds: KOMP Repository at UC Davis and CHORI (U42RR024244)
46. Liu G, Mac Gabhann F, Popel AS. Effects of fiber type and size on the heterogeneity of oxygen distribution in exercising skeletal muscle. *PLoS One* 7: e44375, 2012.
47. Christoforides C, Laasberg LH, Hedley-Whyte J. Effect of temperature on solubility of O₂ in human plasma. *J Appl Physiol* 26: 56-60, 1969.
48. Mintun MA, Lundstrom BN, Snyder AZ, Vlassenko AG, Shulman GL, Raichle ME. Blood flow and oxygen delivery to human brain during functional activity: theoretical modeling and experimental data. *Proc Natl Acad Sci U S A* 98: 6859-64, 2001.
49. Adair GS, Bock AV, Field HJ. The Hemoglobin System: VI. The Oxygen Dissociation Curve of Hemoglobin. *J. Biol. Chem.* 63, 1925.
50. Ellis CG, Bateman RM, Sharpe MD, Sibbald WJ, Gill R. Effect of a maldistribution of microvascular blood flow on capillary O₂ extraction in sepsis. *Am J Physiol Heart Circ Physiol* 282: H156-64, 2002.

51. Kembro JM, Aon MA, Winslow RL, O'Rourke B, Cortassa S. Integrating Mitochondrial Energetics, Redox and Ros Metabolic Networks: A Two-Compartment Model. *Biophysical Journal* 104: 657a-a, 2013.
52. Cui WN, Zhu XH, Vollmers ML, Colonna ET, Adriany G, Tramm B, et al. Non-invasive measurement of cerebral oxygen metabolism in the mouse brain by ultra-high field O-17 MR spectroscopy. *Journal of Cerebral Blood Flow and Metabolism* 33: 1846-9, 2013.
53. Rodriguez JJ, Yeh CY, Terzieva S, Olabarria M, Kulijewicz-Nawrot M, Verkhatsky A. Complex and region-specific changes in astroglial markers in the aging brain. *Neurobiol Aging* 35: 15-23, 2014.
54. Hoppeler H, Hudlicka O, Uhlmann E. Relationship between Mitochondria and Oxygen-Consumption in Isolated Cat Muscles. *Journal of Physiology-London* 385: 661-75, 1987.
55. Howard CV, Jolleys G, Stacey D, Fowler A, Wallen P, Browne MA. Measurement of total neuronal volume, surface area, and dendritic length following intracellular physiological recording. *Neuroprotocols* 2: 113-20, 1993.
56. Popel AS, Pittman RN, Ellsworth ML. Rate of Oxygen Loss from Arterioles Is an Order of Magnitude Higher Than Expected. *American Journal of Physiology* 256: H921-H4, 1989.
57. Schmitt FO. *Fibrous Proteins-Neuronal Organelles*. Presented at Proc. N. A. S., 1968.
58. Sjostrand FS, Cassell RZ. Structure of inner membranes in rat heart muscle mitochondria as revealed by means of freeze-fracturing. *J Ultrastruct Res* 63: 111-37, 1978.
59. Williams V, Grossman RG, Edmunds SM. Volume and surface area estimates of astrocytes in the sensorimotor cortex of the cat. *Neuroscience* 5: 1151-9, 1980.
60. Lyons D, Boido D, Paprpaleix A, Charpak S. Imaging local neuronal activity by monitoring pO₂ transients in capillaries. In *Jacques Monod*. Roscoff, France, 2014.
61. Miller KE, Sheetz MP. Axonal mitochondrial transport and potential are correlated. *Journal of Cell Science* 117: 2791-804, 2004.

62. Nafstad PH, Blackstad TW. Distribution of mitochondria in pyramidal cells and boutons in hippocampal cortex. *Z Zellforsch Mikrosk Anat* 73: 234-45, 1966.
63. Holash JA, Noden DM, Stewart PA. Re-evaluating the role of astrocytes in blood-brain barrier induction. *Dev Dyn* 197: 14-25, 1993.
64. Schnitzer J. Immunocytochemical studies on the development of astrocytes, Muller (glial) cells, and oligodendrocytes in the rabbit retina. *Brain Res Dev Brain Res* 44: 59-72, 1988.
65. Jou MJ, Peng TI, Sheu SS. Histamine induces oscillations of mitochondrial free Ca^{2+} concentration in single cultured rat brain astrocytes. *Journal of Physiology* 497 (Pt 2): 299-308, 1996.
66. Reichold J, Stampanoni M, Lena Keller A, Buck A, Jenny P, Weber B. Vascular graph model to simulate the cerebral blood flow in realistic vascular networks. *J Cereb Blood Flow Metab* 29: 1429-43, 2009.
67. Xu K, Radhakrishnan K, A.Serhal, Allen F, LaManna JC, Puchowicz MA. In *Oxygen Transport to Tissue XXXII*, ed. JCLe al.: Springer Science+Business Media, 2011.
68. Unekawa M, Tomita M, Tomita Y, Toriumi H, Miyaki K, Suzuki N. RBC velocities in single capillaries of mouse and rat brains are the same, despite 10-fold difference in body size. *Brain Research* 1320: 69-73, 2010.
69. Hudetz AG, Feher G, Kampine JP. Heterogeneous autoregulation of cerebrocortical capillary flow: Evidence for functional thoroughfare channels? *Microvascular Research* 51: 131-6, 1996.
70. Villringer A, Them A, Lindauer U, Einhaupl K, Dirnagl U. Capillary perfusion of the rat brain cortex. An in vivo confocal microscopy study. *Circ Res* 75: 55-62, 1994.
71. Ivanov KP, Kalinina MK, Levkovich Yu I. Blood flow velocity in capillaries of brain and muscles and its physiological significance. *Microvasc Res* 22: 143-55, 1981.
72. Ma YP, Koo A, Kwan HC, Cheng KK. On-line measurement of the dynamic velocity of erythrocytes in the cerebral microvessels in the rat. *Microvasc Res* 8: 1-13, 1974.

73. Maeda K, Mies G, Olah L, Hossmann KA. Quantitative measurement of local cerebral blood flow in the anesthetized mouse using intraperitoneal [C-14]iodoantipyrine injection and final arterial heart blood sampling. *Journal of Cerebral Blood Flow and Metabolism* 20: 10-4, 2000.
74. Zhu XH, Zhang Y, Tian RX, Lei H, Zhang NY, Zhang XL, et al. Development of O-17 NMR approach for fast imaging of cerebral metabolic rate of oxygen in rat brain at high field. *Proceedings of the National Academy of Sciences of the United States of America* 99: 13194-9, 2002.
75. Sakadzic S, Mandeville ET, Gagnon L, Musacchia JJ, Yaseen MA, Yucel MA, et al. Large arteriolar component of oxygen delivery implies a safe margin of oxygen supply to cerebral tissue. *Nature Communications* 5, 2014.
76. Bailey DM, Taudorf S, Berg RMG, Lundby C, Pedersen BK, Rasmussen P, et al. Cerebral formation of free radicals during hypoxia does not cause structural damage and is associated with a reduction in mitochondrial PO₂; evidence of O-2-sensing in humans? *Journal of Cerebral Blood Flow and Metabolism* 31: 1020-6, 2011.
77. Erecinska M, Silver IA. Tissue oxygen tension and brain sensitivity to hypoxia. *Respiration Physiology* 128: 263-76, 2001.
78. Mik EG, Johannes T, Zuurbier CJ, Heinen A, Houben-Weerts JH, Balestra GM, et al. In vivo mitochondrial oxygen tension measured by a delayed fluorescence lifetime technique. *Biophys J* 95: 3977-90, 2008.
79. Fahraeus R. The Suspension Stability of the Blood. *Physiological Reviews* 1929; 9: 241-74
80. Pries AR, Secomb TW. Microvascular blood viscosity in vivo and the endothelial surface layer. *Am J Physiol Heart Circ Physiol* 289: H2657-64, 2005.
81. Hill AV. The Combinations of Haemoglobin with Oxygen and with Carbon Monoxide. I. *Biochem J* 7: 471-80, 1913.

82. Hill AV. The Combinations of Haemoglobin with Oxygen and Carbon Monoxide, and the effects of Acid and Carbon Dioxide. *Biochem J* 15: 577-86, 1921.
83. Errico C, Pierre J, Pezet S, Desailly Y, Lenkei Z, Couture O, et al. Ultrafast ultrasound localization microscopy for deep super-resolution vascular imaging. *Nature* 527: 499-502, 2015.
84. Hall CN, Reynell C, Gesslein B, Hamilton NB, Mishra A, Sutherland BA, et al. Capillary pericytes regulate cerebral blood flow in health and disease. *Nature* 508:55-60, 2014.
85. Hill RA, Tong L, Yuan P, Murikinati S, Gupta S, Grutzendler J. Regional blood flow in the normal and ischemic brain is controlled by arteriolar smooth muscle cell contractility and not by capillary pericytes. *Neuron* 87: 95-110, 2015.
86. Shih AY, Rühlmann C, Blinder P, Devor A, Drew PJ, Friedman B, et al. Robust and fragile aspects of cortical blood flow in relation to the underlying angioarchitecture. *Microcirculation* 22: 204-18, 2015.
87. Morimoto S, Cassell MD, Beltz TG, Johnson AK, Davisson RL, Sigmund CD. Elevated blood pressure in transgenic mice with brain-specific expression of human angiotensinogen driven by the glial fibrillary acidic protein promoter. *Circulation research* 89: 365-72, 2001.
88. Oshio K, Watanabe H, Song Y, Verkman AS, Manley GT. Reduced cerebrospinal fluid production and intracranial pressure in mice lacking choroid plexus water channel Aquaporin-1. *The FASEB journal* 19: 76-8, 2005.
89. Gertz K, Priller J, Kronenberg G, Fink KB, Winter B, Schröck H, et al. Physical activity improves long-term stroke outcome via endothelial nitric oxide synthase–dependent augmentation of neovascularization and cerebral blood flow. *Circulation research* 99: 1132-40, 2006.
90. Gertz K, Priller J, Kronenberg G, Fink KB, Winter B, Schröck H, et al. Physical activity improves long-term stroke outcome via endothelial nitric oxide synthase–dependent

augmentation of neovascularization and cerebral blood flow. *Circulation research* 99: 1132-40, 2006.

91. Schmid, F., P. S. Tsai, D. Kleinfeld, P. Jenny, and B. Weber. Depth-dependent flow and pressure characteristics in cortical microvascular networks. *PLOS Computational Biology* 13:e1005392, 2017.

V. MORPHOLOGICALLY CONSISTENT MODEL REDUCTION OF BRAIN MICROCIRCULATION ACCURATELY COMPUTES CEREBRAL BLOOD FLOW RESPONSE

Abstract

Treatment of cerebrovascular diseases is often hampered by inaccurate diagnosis of the severity and distribution of underperfused cortical regions. A holistic, whole organ, model of the cortical vasculature would provide key insight into which regions of the cortex are critically low in blood supply and the impact of different intervention options. However, such a model would require complete closure of the arterial and venous cerebral vasculature through the microcirculation – a complex, interconnected microcirculatory structure that encompasses billions of vessels.

In this chapter two model reduction strategies are proposed to close the cerebral circulation, a *serial resistance configuration* and a *conductive plate network*.

Construction details are described for each model, and their performance is compared on four cortical murine data sets. The *serial* model demonstrates a wide variation of estimated fractional capillary resistance between the four data sets, $43.20 \pm 23.16\%$, whereas the *plate* model consistently attributes the majority of the vascular resistance to the capillary bed, $89.14 \pm 6.37\%$. The serial model is unable to accurately predict the changing response to cortical perfusion following variation in arterial blood pressure when compared to the full microcirculation network whereas the *plate network* performance closely matches the simulated blood flow response.

Introduction

The metabolic demand of the human brain is so great that it demands 20% of the systemic volumetric blood flow. This extraordinary demand of cerebral blood flow is necessary to supply nutrients to neurons during functional activation. Blood flow is continuously shunted and redistributed between different territories of the brain in response to changing neuronal activity. Blood flow is tightly controlled by vasodilation and vasoconstriction of cerebral microvessels. This highly localized control of blood flow to different subsections of the human brain is not well understood, despite decades of study dedicated to the morphology and function of the cerebral microcirculation.

Architecture of the cerebral microcirculation has been studied extensively in humans^{1,2} macaque³ and mice^{4,5}. The relationship between blood flow and metabolic oxygen supply in small subsections of the cerebral cortex⁶⁻⁸ have been investigated with computational models. These *in silico* models characterize every single blood vessel as cylinders with an assigned length and radii. This faithful representation of the cerebral microcirculatory architecture is computationally expensive. Recent models⁹, which model <3% of the murine cortex, consist of more than 150,000 microvessels.

This modeling approach cannot be scaled to simulate the entire human brain without a massive increase in computational cost. With a density of 10,000 microvessels per cubic millimeter¹ and a total volume near 1,500cm³, such a model of the human brain would consist of over 150 *billion vessels*. Mathematical methods that do not use matrix inversion or highly parallelizable linear algebra solvers may be deployed to make such a computation possible. However, a model reduction strategy could be deployed to decrease the number of equations needed to simulate the cerebral microcirculation.

Development of a successful model reduction approach requires a detailed investigation of cerebral hemodynamics. As few human data sets are available at this time, a study of the mouse cortex is presented which can be scaled to fit the human cerebrovasculature. The relationship between blood flow, blood pressure and hydraulic resistance has been studied extensively in four different 3D murine cortical subsections⁹. The angioarchitecture of each subsection is divided into five vascular compartments; pial arteries, penetrating arterioles, capillaries, ascending venules and pial veins as shown in Figure 34. A detailed hemodynamic investigation of these five compartments across the four data sets is presented in Table XII. These microvascular compartments are the target of the model reduction presented in this Chapter.

This work presents two model reduction strategies, the *serial resistance configuration* and the *conductive plate model*. The *serial resistance configuration* presents the cerebral microcirculation as a series of resistors, each representing a single microvascular compartment. This approach is typical of whole body circulatory model where individual organs are represented as a single resistor. The *conductive plate model* retains the morphology of pial surface while simplifying the other vascular compartments. This is achieved by reducing the penetrating arterioles (PA) and ascending venules (AV) to single vessels and simplifying the interconnected capillary bed to a 2D plate.

An analysis of the model reduction strategies is presented, aimed at answering two important physiological questions: What are the relative contributions of arteries, capillaries and veins to the microvascular resistance? Which of the two simple resistance configuration best characterizes microvascular perfusion patterns?

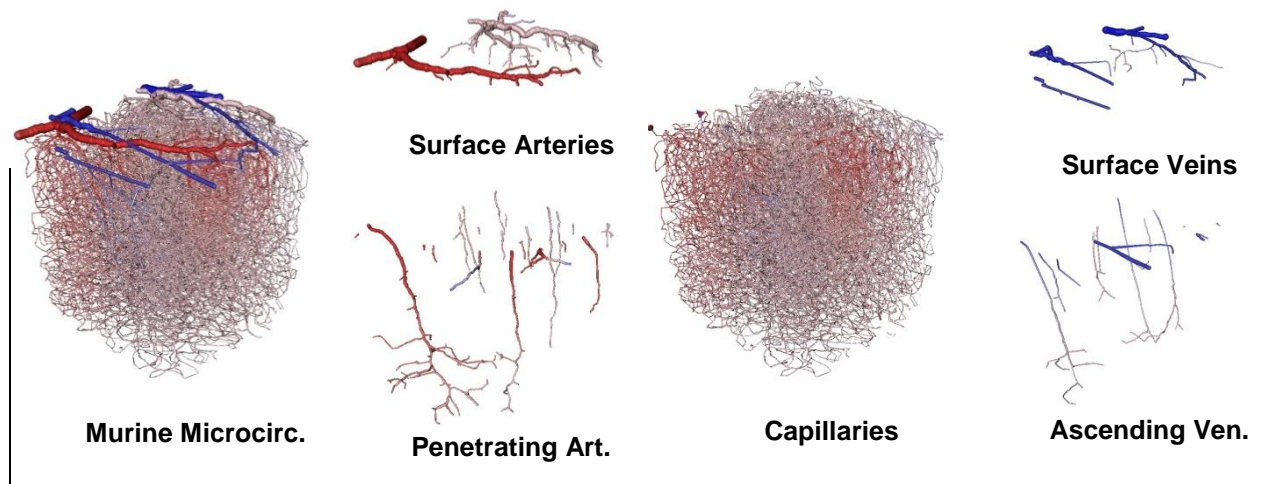


Figure 34. The angioarchitecture and hierarchy of cortical microcirculation; the surface pial arteries, penetrating arterioles (PA), capillaries, ascending venules (AV), and pial surface veins in one of the murine data sets. Vessel color corresponds with blood pressure from arterial inlets (red) to venous outlets (blue). Surface pial arteries travel along the cortical surface, narrowing until they descend into the parenchyma as penetrating arterioles. These PA feed the capillary bed, which is in turn drained by ascending venules. The AV journey back to the cortical surface where they empty into the cortical surface veins.

Table XII Morphological and Hemodynamic Parameters of each mouse

	Mouse 1	Mouse 2	Mouse 3	Mouse 4
No. Surface Arteries	897	347	180	812
No. Surface Veins	1740	524	484	1573
No. PA vessels	1369	930	403	1613
No. AV vessels	934	384	476	2011
No. Capillaries	129251	157483	38004	132698
No. Total Vessels	134191	159668	39547	138707
No. PA Trees	20	10	24	38
No. AV Trees	66	39	81	139
Ratio AV/PA	3.30	3.90	3.38	3.66
Total No. PA + AV	86	49	105	177
Cortical Volume, mm³	1.14	1.93	2.84	2.71
Cortical SA, mm²	1.05	1.18	1.60	1.96
Perfusion, mL/100g/min	60.61	17.72	62.30	95.01

Methods

In this section the structure of the cerebral microcirculatory angioarchitecture is described, and network blood flow simulations are briefly outlined. Additional details on the network blood flow simulations are presented in previous work⁹. The process of estimating blood flow resistance across each of the five vascular structures is also described. Finally, the construction of both the *serial resistance configuration* and the *conductive plate network* is shown. Four murine microcirculatory data sets are utilized during the construction of both the *serial* and *plate* models.

Cerebral microcirculatory angioarchitecture

Each data set consists of bifurcating pial arteries traveling along the cortical surface that dive into the cortex as penetrating arterioles as shown in Figure 34. These arteriole trees travel deep into the murine cortex until they feed into the capillary bed, a highly-interconnected network of narrow vessels. This cyclic graph is drained by ascending venules which rise to the top of the cortical surface where they are collected by pial veins. These five microvascular compartments are the target of the model reduction. The pressure drop and blood flow through these five vascular compartments in each of the four data sets is used as training data for the construction of both reduced order models.

Network blood flow simulations

Bulk blood flow is computed throughout the network by enforcing continuity across blood vessel junctions as shown in eq. 50. Each blood vessel is described as a cylindrical element with diameter, D , and length, L . Hydraulic resistance across each vessel is determined with the Hagen-Poiseuille equation described in eq. 51, where the

blood pressure drop across each vessel, ΔP , is equal to the product of the hydraulic resistance, α , and the bulk blood flow rate, Q . The hydraulic resistance for each blood vessel is a function of vessel length, L , diameter, D , and blood viscosity, μ . Blood viscosity is a function of vessel diameter and hematocrit¹⁰; hematocrit was set to 0.35 for every vessel.

$$\nabla \cdot Q = 0 \quad 50$$

$$\Delta P = Q \cdot \alpha \quad \alpha = \frac{128\mu L}{\pi D^4} \quad 51$$

Boundary conditions are assigned as known pressure values at the arterial inlet and venous outlet of the network, $P_{in}=120\text{mmHg}$ and $P_{out}=5\text{mmHg}$. Bulk blood flow simulation performed on each of the four complete data sets before model reduction are referred to in this chapter as “full simulation” results.

Resistance computation for each vascular group

Blood vessels in each data set are labeled as described in the previous Chapter, forming delineated vessel groups, g , as shown in Figure 34. The feeding vessels for each group are identified and their diameter, D_i , and pressure, P_i , are taken from the full simulations for all inlet vessels, N_{in}^g . The mean inlet pressure, \bar{P}_{in}^g , is computed using a fourth power diameter weighted average as described in eq. 52. The mean outlet pressure, \bar{P}_{out}^g , is computed in a similar fashion for all outlet vessels, N_{out}^g .

$$\bar{P}_{in}^g = \frac{\sum_{i=1}^{N_{in}^g} P_i D_i^4}{\sum_{i=1}^{N_{in}^g} D_i^4} \quad \bar{P}_{out}^g = \frac{\sum_{i=1}^{N_{out}^g} P_i D_i^4}{\sum_{i=1}^{N_{out}^g} D_i^4} \quad g = \begin{cases} \text{pial arteries} \\ \text{penetrating arterioles} \\ \text{capillaries} \\ \text{ascending venules} \\ \text{pial veins} \end{cases} \quad 52$$

The arrangement of vessels in the penetrating arteriole vascular group requires a different approach to determine mean inlet and outlet pressure. Each of these groups is composed of several structurally independent trees, each with one inlet and multiple outlets. The mean inlet and outlet pressure for each tree is determined using the same approach described above. The mean inlet and outlet pressure for the entire vascular group is reported as the tree inlet diameter weighted average. The same process was repeated for ascending venules. If the mean outlet pressure of an upstream group (i.e. pial arteries) did not match the mean inlet pressure of a downstream group (i.e. PA), then the higher of the values was assigned as the pressure for both.

The hydraulic vascular resistance, α^g , for each group is determined as shown in eq. 53, from the average pressure drops across the group and the bulk blood flow through the group, Q^g , taken from the full simulation results. The hydraulic resistance for each vessel group, g , is determined from the blood flow and pressure drop.

$$\alpha^g = \frac{\bar{P}_{in}^g - \bar{P}_{out}^g}{Q^g} \quad 53$$

Serial resistance configuration

The *serial resistance configuration* is constructed as a set of five resistors, one for each vascular group, connected in series as shown in Figure 35A. The resistance of each vascular group is determined in two steps.

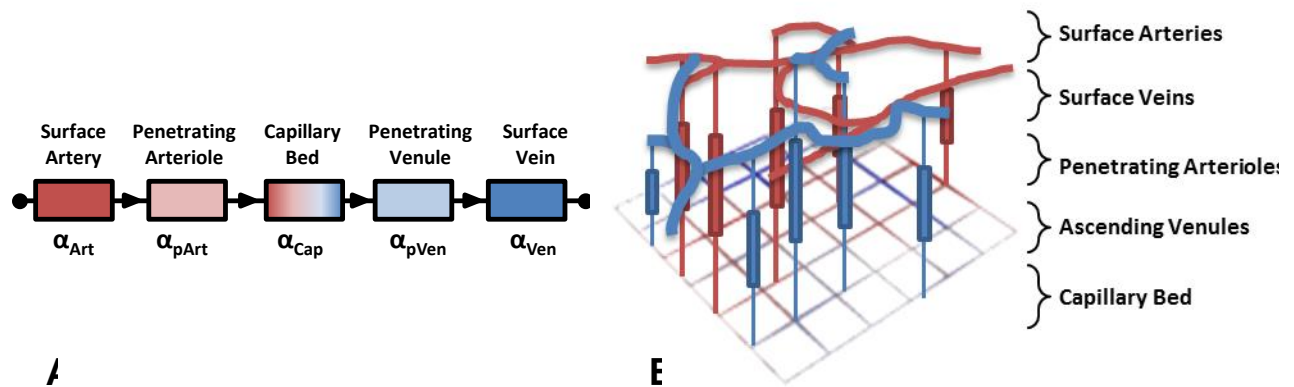


Figure 35. Generation of simplified blood flow models. **A.** Schematic of the *serial resistor configuration* and **B.** the *conductive plate network*. Resistances were fitted at nominal conditions of arterial inlet pressure of 120mmHg and venous outlet pressure of 5mmHg for all groups; surface pial arteries, penetrating arterioles, capillaries, ascending venules and surface pial veins.

In the first step, the resistance of each vascular group in each of the microcirculatory mouse networks is determined using the resistance computation described above. The results of these computations are described in detail in Table . In the second step, the vascular resistance of each group is averaged across all four data sets to determine the final vascular resistances of each group as shown in Table . The total hydraulic resistance across the entire structure was computed as the sum of the *serial resistors*.

Conductive plate network

The *conductive plate network* is an improved version of an earlier concept separately propositioned by Duvernoy² and Kleinfeld¹¹. As shown in Figure 35B, surface pial arteries are not modified from the original data set. Individual penetrating arterioles are reduced from a branching tree to a single vessel connecting the surface pial arteries to the capillary bed.

The resistance for each PA in each data set is determined using eq. 52 and 53 which is then plotted as a function of the feeding penetrating arteriole diameter (92 total). Using data collected from all four data sets, a fourth order linear regression is performed. The resulting diameter-resistance relationship, given in Figure 36A, is used to estimate the hydraulic resistance of each penetrating arteriole, $R^2=0.4404$. Penetrating arteriole tree resistance is modeled as a function of the reciprocal diameter to the fourth power mirroring the form of the Hagen-Poiseuille equation.

Table XIII Hemodynamic parameters of each vessel structure

		Surf. Art.	PA	Cap.	AV	Surf. Ven.
Mouse 1	Blood Flow, nL/min	12.42	12.42	12.42	12.42	12.42
	<i>P_{in}</i> , mmHg	120.00	87.35	45.41	19.89	7.82
	<i>P_{out}</i> , mmHg	87.35	45.41	19.89	7.82	5.00
	ΔP , mmHg	32.65	41.94	25.52	12.07	2.82
	Resistance, mmHg·s/nL	2.63	3.38	2.05	0.97	0.23
Mouse 2	Blood Flow, nL/min	6.17	6.17	6.17	6.17	6.17
	<i>P_{in}</i> , mmHg	120.00	118.39	101.50	11.31	7.26
	<i>P_{out}</i> , mmHg	118.39	101.50	11.31	7.26	5.00
	ΔP , mmHg	1.61	16.89	90.19	4.05	2.26
	Resistance, mmHg·s/nL	0.26	2.74	14.62	0.66	0.37
Mouse 3	Blood Flow, nL/min	31.89	31.89	31.89	31.89	31.89
	<i>P_{in}</i> , mmHg	120.00	118.45	89.51	32.53	16.38
	<i>P_{out}</i> , mmHg	118.45	89.51	32.53	16.38	5.00
	ΔP , mmHg	1.55	28.94	56.98	16.15	11.38
	Resistance, mmHg·s/nL	0.05	0.91	1.79	0.51	0.36
Mouse 4	Blood Flow, nL/min	46.32	46.32	46.32	46.32	46.32
	<i>P_{in}</i> , mmHg	120.00	92.27	48.45	22.42	8.92
	<i>P_{out}</i> , mmHg	92.27	48.45	22.42	8.92	5.00
	ΔP , mmHg	27.73	43.81	26.03	13.50	3.92
	Resistance, mmHg·s/nL	0.60	0.95	0.56	0.29	0.08

Table XIV Fractional vascular resistance of the *Serial Resistance Configuration*

	Surface Arteries	Penetrating Arterioles	Capillaries	Ascending Venules	Surface Veins
Mouse 1	28.39	36.47	22.19	10.49	2.45
Mouse 2	1.40	14.68	78.43	3.52	1.96
Mouse 3	1.35	25.17	49.55	14.04	9.90
Mouse 4	24.12	38.10	22.64	11.74	3.41
Average	13.82±12.53	28.60±9.45	43.20±23.16	9.95±3.92	4.43±3.20

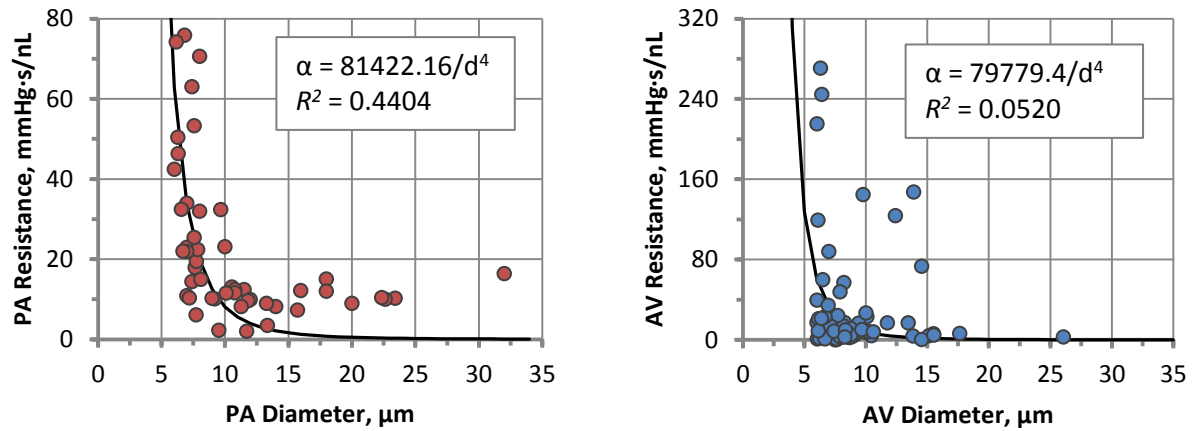


Figure 36. Linear regression of vascular resistance of penetrating vessels as a function of root diameter: **A.** penetrating arterioles ($N=92$) **B.** penetrating venules ($N=325$). Regression formula and R^2 shown in boxed insets. The regression formula was used to assign penetrating arteriole and venule resistances in the *conductive plate network*.

Surface veins and ascending venules were treated similarly to their arterial counterparts; surface pial veins are unmodified while ascending venules are reduced to a single vessel linking the capillary bed to the surface pial veins. Estimation of ascending venule resistance as a fourth order function of draining venule diameter ($R^2=0.0520$) is described in Figure 36B which utilizes all 325 ascending venules across the four data sets.

Penetrating arterioles and venules are connected to a two-dimensional conductive plate representing the capillary bed. This conductive plate was constructed as a 2D evenly spaced square lattice with dimensions of 1.5mm×1.5mm with grid spaces every 50μm resulting in a 30×30 framework. Venules are connected to the closest grid point on the 2D capillary conductive plate. These grid points are excluded when connecting the penetrating arterioles to the capillary bed. This exclusion prevented penetrating arterioles from connecting directly to ascending venules which would create an arteriovenous malformation and bypass the resistance of the capillary bed.

Each arc of the grid is treated as a cylindrical vessel with a diameter and hydraulic resistance as computed by eq. 51. The diameter of all capillaries is kept consistent for the entire plate, which is determined by a linear fitting function from the number of PA and AV. This function was constructed in two steps.

In the first step, the optimal conductance, c (the reciprocal of resistance), of the capillary bed for each data set was computed as the outcome of a minimization problem. Blood flow through the *conductive plate network*, \hat{Q} , is a function of the plate conductance. The optimal plate conductance is obtained by minimizing the residual, R , between the *conductive plate network* blood flow, \hat{Q} , and the full model blood flow, Q , as given in

system 54. This is repeated across all four data sets as shown in Figure 37, and is reported as the length independent conductance for Mouse 1 (165.79), Mouse 2 (99.69), Mouse 3 (296.85), and Mouse 4 (597.33nL/mmHg/s/ μ m).

$$\min_c R = (Q - \hat{Q}(c))/Q \quad 54$$

In the second step, the optimal plate conductance is determined as a linear function of the number of PA and AV as show in Figure 38A, $R^2=0.9738$. Linear functions of cortical surface area ($R^2=0.8875$), cortical volume ($R^2=0.4319$), and for the number of PA alone ($R^2=0.9434$) were also considered as shown in Figure 38B-D. However, the linear function of plate conductance dependent on the combined count of PA and AV is selected because this method demonstrated the tightest fit. This computed plate conductance is then transformed into an assigned capillary diameter by inverting the Hagen-Poiseuille equation. For this inversion a capillary viscosity of 1.191×10^{-5} mmHg·s is assigned, the computed *in vitro* viscosity of a capillary with a diameter of 4.5 μ m and a discharge hematocrit of 0.35.

The resistance for each group is then determined using the group resistance procedure described previously. The resistance of each vascular group in each data set, including averages across all groups, is described in detail in Table .

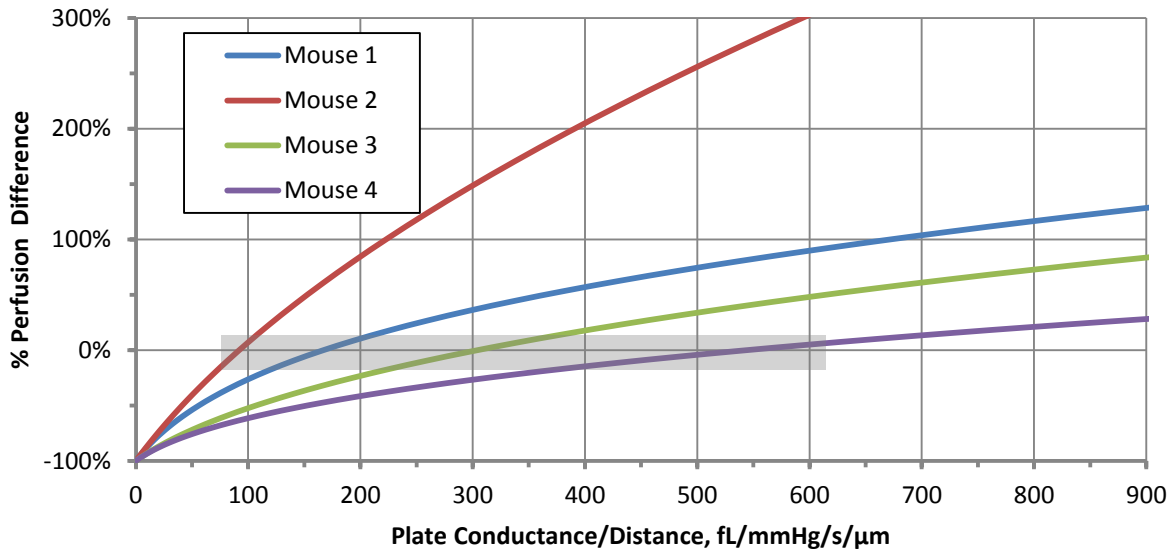


Figure 37. Capillary plate conductance optimized to match the inlet arterial blood flow between the conductive plate model, \hat{Q} , and the full microcirculation network, Q . Plate conduction was varied by adjusting the uniform capillary diameter of the plate network until $|R| < 0.10$. Final optimized capillary plate conduction was 165.79 (Mouse 1), 99.69 (Mouse 2), 296.85 (Mouse 3), and 597.33.14 fL/mmHg/s/μm (Mouse 4). The dependent control variable of the optimization routine is reported independent of cylinder length, i.e. conduction / arc length.

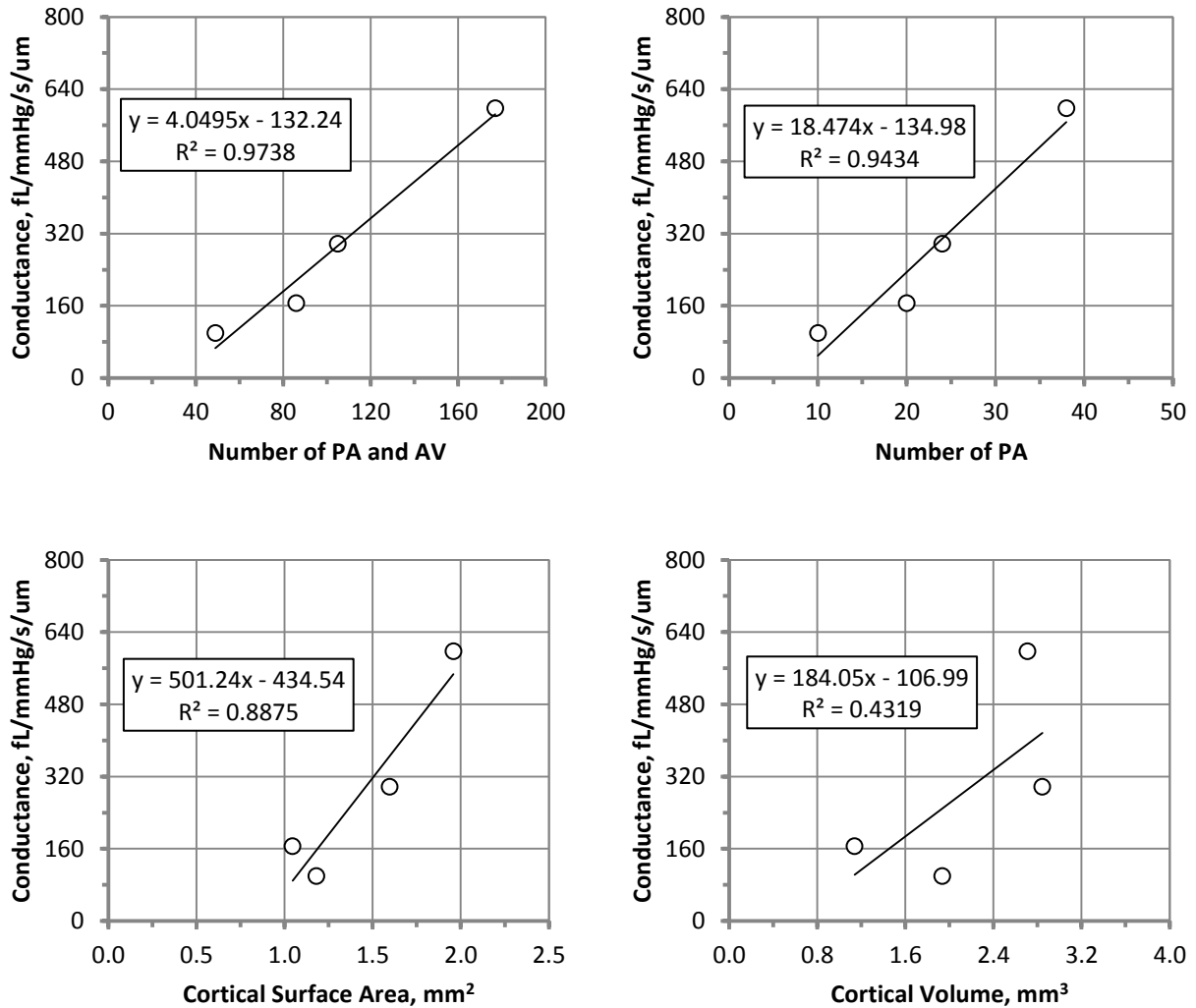


Figure 38. Optimized length independent capillary plate conductance as a function of **A.** number of PA and AV, **B.** number of PA, **C.** cortical surface area, and **D.** the cortical volume of each data set. The linear fit of number of PA and AV to capillary plate conductance is the tightest fit ($R^2=0.9738$).

Results

Resistance distributions across each vessel group were compared between all four data sets for both the *serial resistance configuration* and the *conductive plate network*. The blood flow response of each model reduction strategies is compared to the performance of the full network model.

Resistance distribution

Resistances are compared for each vessel group in each data set for the *serial resistance configuration* as shown in Figure 39 and in Table . The *serial* model describes the vascular resistance as being evenly distributed between surface arteries, PA and the capillary bed for both Mouse 1 and 4. Mouse 2 and 3 have the majority of their vascular resistance residing within the capillary bed. In all four data sets, the *serial* model assigns little resistance to the AV or surface pial veins. The average fractional resistance distribution for the surface pial arteries ($13.82 \pm 12.53\%$), PA ($28.60 \pm 9.45\%$), capillaries ($43.20 \pm 23.16\%$), AV ($9.95 \pm 3.92\%$), and surface pial veins ($4.43 \pm 3.20\%$) demonstrates a high variation between data sets.

Hydraulic resistances for each vessel group in the *conductive plate network* were determined using eq. 52 and 53. This computation was performed for each data set. Results are reported as a fractional resistance distribution in Figure 40 and in Table . The capillary bed is the major site of the microvascular resistance for Mouse 1 (89.73%), Mouse 2 (99.25%), Mouse 3 (84.98%) and Mouse 4 (82.61%) with an average of $89.14 \pm 6.37\%$. The fractional resistance attributed to the surface arteries ($3.07 \pm 2.41\%$), the PA ($1.81 \pm 1.11\%$), the AV ($3.20 \pm 3.04\%$), and the surface veins ($2.78 \pm 2.55\%$) is consistently low in all four data sets.

Blood flow response

Cortical perfusion was predicted for a wide range of physiological pressure drops using the *serial resistance configuration* and the *conductive plate network* in Figure 41A-D for all data sets. Inlet arterial pressure was varied from 100-140mmHg while the venous pressure was kept fixed at 5mmHg. Performance of the *serial* model, shown as a red line, and *plate* model, shown as a blue line, are compared against the performance of the full network model which is shown as a green line. In all four data sets, the *conductive plate model* more reliably predicts the blood flow response of the full microcirculatory network than the *serial resistance configuration*. Comparison of the computed perfusion of each model at an arterial inlet pressure of 120mmHg demonstrates that the *conductive plate* predictions ($M_1=1.67\%$, $M_2=70.40\%$, $M_3=6.15\%$, $M_4=13.36\%$) are much closer to the full network results than the serial resistance configuration ($M_1=8.90\%$, $M_2=119.25\%$, $M_3=57.59\%$, $M_4=70.79\%$).

Table XV Fractional vascular resistance of the *Conductive Plate Model*

	Surface Arteries	Penetrating Arterioles	Capillaries	Ascending Venules	Surface Veins
Mouse 1	6.96	2.68	89.73	0.26	0.36
Mouse 2	0.52	0.06	99.25	0.06	0.11
Mouse 3	1.81	1.65	84.98	6.23	5.33
Mouse 4	2.99	2.84	82.61	6.23	5.33
Average	3.07±2.41	1.81±1.11	89.14±6.37	3.20±3.04	2.78±2.55

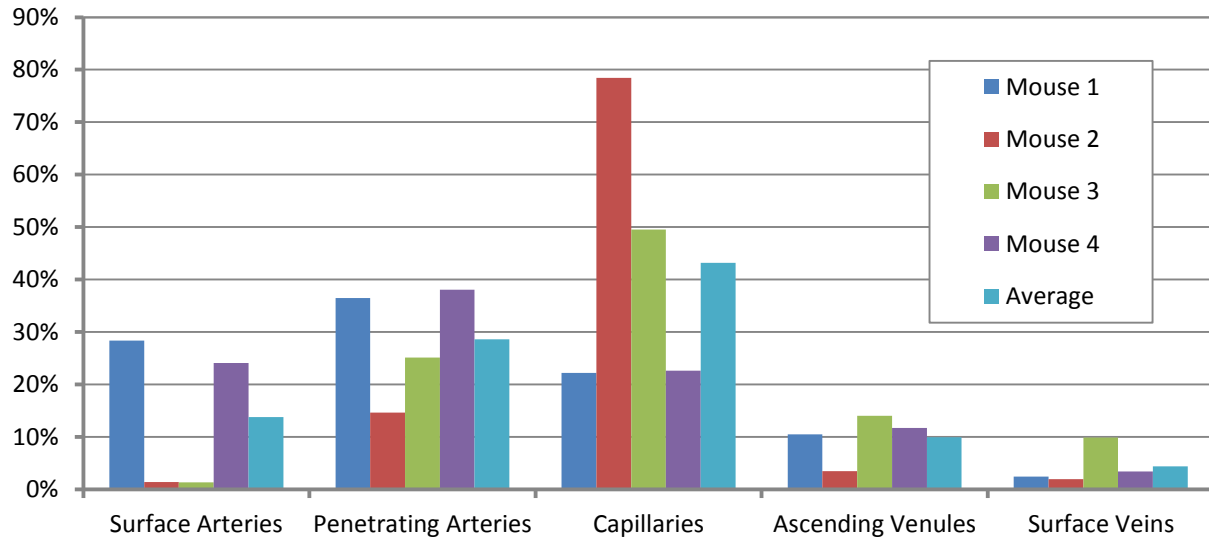


Figure 39. Fractional resistance distribution between the five microcirculatory vascular compartments determined by the *serial resistor configuration*. The *serial* model gives different values for each group including the capillary resistance in the four data sets. The average resistance of each vascular compartment does not adequately represent any of the four data sets.

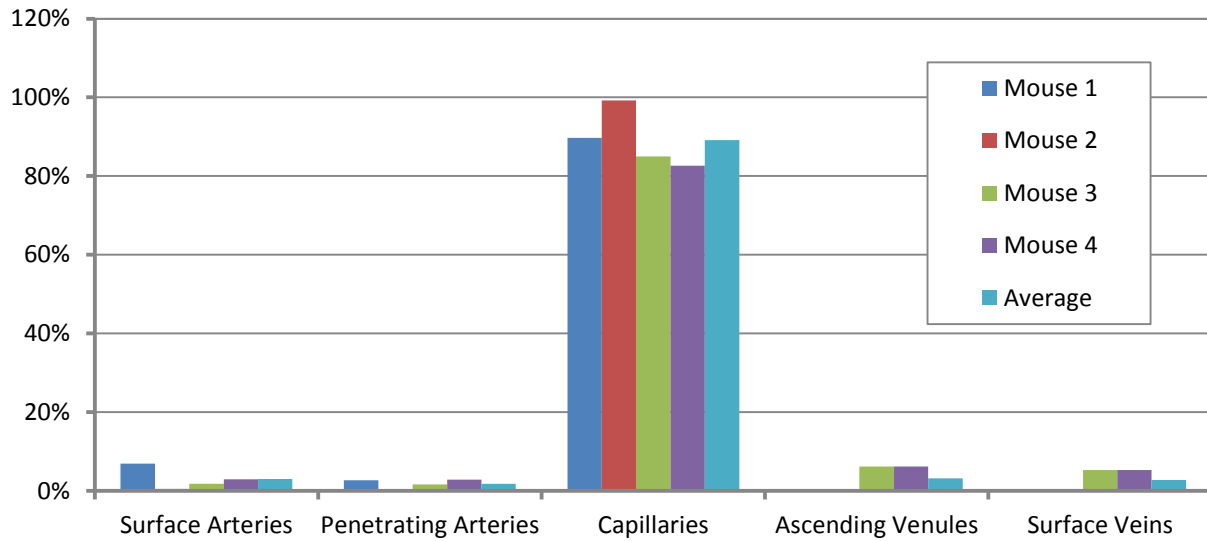


Figure 40. The distribution of fractional resistance as determined by the *conductive plate* network. The *plate* model gives similar values for each group with most of the vascular resistance residing in the capillary bed for all four data sets. The average resistance value of each vascular compartment accurately characterizes all four of the mouse data sets.

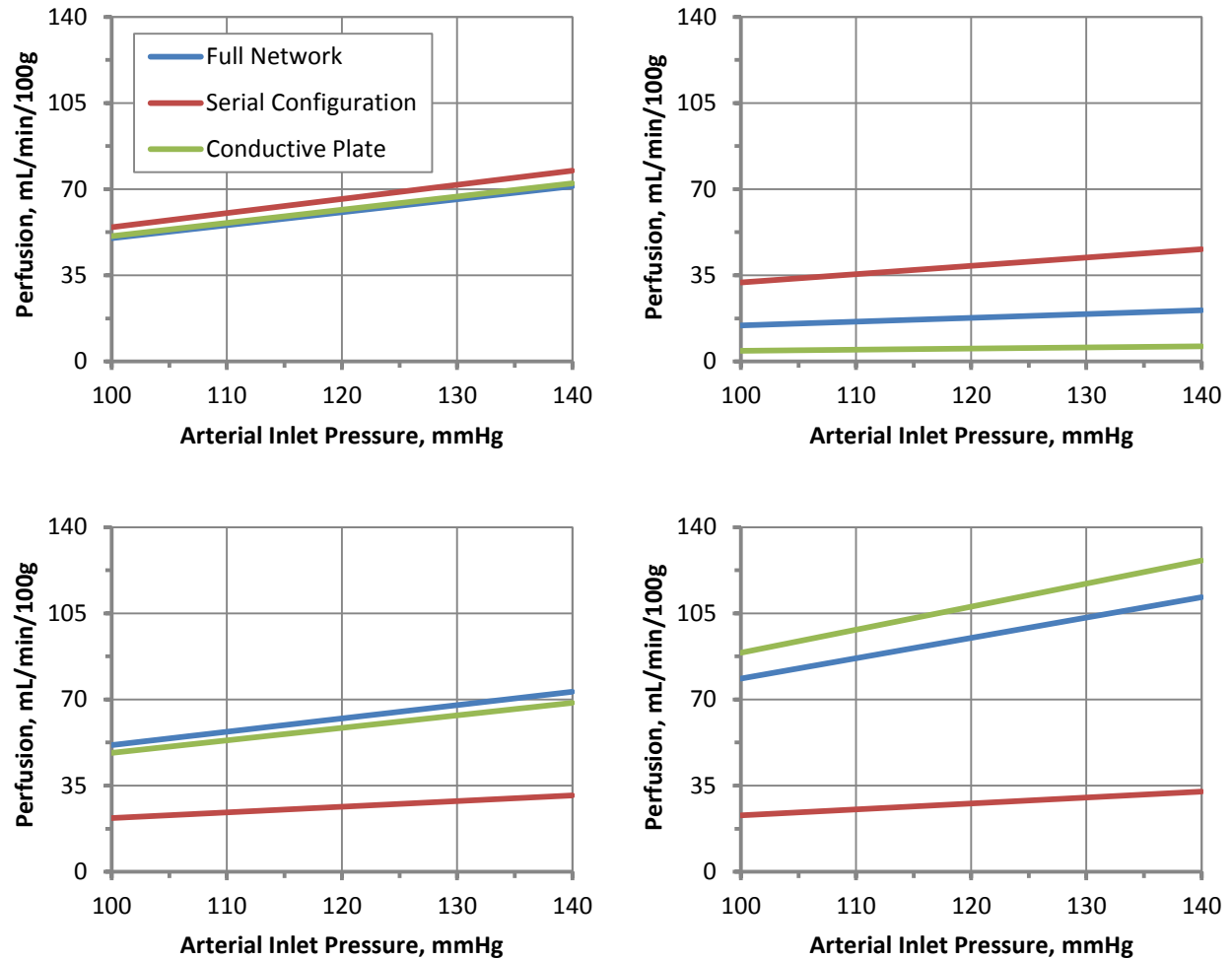


Figure 41. Cortical perfusion as a function of arterial inlet blood pressure for the full network (blue), *serial resistor configuration* (red) and *conductive plate network* (green). Changing blood flow response for the full network model and both model reduction approaches are shown for **A.** Mouse 1, **B.** Mouse 2, **C.** Mouse 3, and **D.** Mouse 4. The perfusion predictions of the *plate model* are consistently closer to the results of the full network than the blood perfusion computed by the *serial configuration*.

Discussion

Model Construction

In this chapter, the construction of both the *serial resistance configuration* and the *conductive plate network* are presented in detail. These methods are proposed as possible approaches to connect the feeding arteries to the draining veins along the pial surface of the brain, creating closure for a full cerebral circulatory model. The approach presented here in the mouse cortex model is constructed in a manner that can be scaled and applied to the human brain.

The proposed *serial resistance configuration*, while simple, neglects structural differences between each data set and attempts to represent the cerebral microcirculation as a lumped model. This *serial* model cannot account for connecting multiple feeding arterioles to multiple draining venules.

The *conductive plate network* retains the structure of the pial surface arteries and veins as well as the number of penetrating arterioles and ascending venules. The vascular resistance of both PA and AV was determined using a reciprocal fourth power function. While these methods provide a good fit approximating resistance in arteriole and venule trees with a base diameter less than 12 μm , this approach underestimates vascular resistance in trees with wider base vessels. However, only 13.33% of PA and AV trees have a base diameter greater than 12 μm .

As the majority of the microcirculatory resistance resides in the capillaries and vascular resistance is inconsistent between data sets do, it is necessary to scale the capillary bed conductance for each individual mouse cortex. The total count of PA and AV is more

closely correlated with the blood flow perfusion of each set than cortical surface area, cortical volume or the number of PA alone.

Resistance variation lower in the *plat network*

The fractional capillary resistances computed using the *serial resistance configuration* for the four data sets differed substantially ($43.20 \pm 23.16\%$). This high degree of variation indicates that the *serial configuration* fails to consistently delineate the relative resistance contributions of arterioles, capillaries and veins.

However, the fractional capillary resistance computed by the *conductive plate network* is relatively even between data sets ($89.14 \pm 6.37\%$). The plate model also characterizes the capillary bed as the site of the major microcirculatory resistance in all four data sets. The *plate* model clearly identifies the capillary bed as the major site of vascular resistance distribution in the cerebral microcirculation.

Conductive plate blood flow response matches full simulation

An investigation of the blood flow response to changing arterial pressure demonstrates the difference between the two models. The *serial resistance configuration* is unable to accurately predict blood flow in response to changing arterial inlet pressure. Figure 41 shows that blood flow is estimated nearly one-to-one for the first data set, while it severely underestimates data set 3 and 4, and slightly overestimates data set 2. The *plate network* however closely matches the predictions of the full network for all four data sets. Since the *serial resistance configuration* has only one aggregate resistance, it is unable to match the variation of microcirculatory resistances between each data set.

Comparison of model reduction strategies

Taken together, these results suggest that the *serial resistance configuration* is not well-suited for predicting microcirculatory blood flow reliably. The construction of the *serial configuration* neglects the changing architecture between each data set.

Moreover, this approach is unable to accurately predict changing blood flow in response to changes in arterial inlet pressure. Any reduced order model of the cerebral microcirculation must be able to accurately predict this change in perfusion. Larger full organ cerebral models that implement a model reduction may be dynamic with pulsatile inlet pressures or may predict a decreased blood flow in a disease state.

The *plate network* captures the overall changes in microcirculatory resistance by parametrically constructing the PA, AV and the capillary plate to be hemodynamically equivalent to the full network. The *plate network* is able to match the full model blood flow predictions for wide range of physiological pressures. These properties demonstrate that the *conductive plate network* is a suitable surrogate for the microcirculation in a full cerebrovascular model.

The reduced order model drastically diminishes the computational burden for computing blood flow. The *conductive plate network* computes reasonable flow rates for entire cortical sections at only 2.10% of the computational cost of the detailed simulation (80.7 CPU milliseconds for the *conductive plate network* with 2,345 equations versus the 3,832.6ms required to compute blood flow in the rigorous full model with 153,112 equations on Mouse 2, the largest data set).

These observations offer three important conclusions; (i) The *serial resistance configuration* is not apt to describe microcirculatory resistance, (ii) The *conductive plate network* can serve as a cost-effective surrogate for predicting blood flow in the cortical microcirculation, and (iii) The microcirculatory resistance resides mainly in the capillary bed, including capillaries adjacent to feeding arterioles.

Future Work

The construction of the *serial resistance configuration* may be improved by scaling the overall network resistance to the volume or surface area of the original data set, which may partially account for the variations in hemodynamic resistance between data sets.

The influence of the capillary bed grid resolution on the performance of the *conductive plate network* is unknown. A mesh independence study would establish at what grid resolution the capillary resistance is not affected by changes in network density of the conductive plate. This would be accomplished by optimizing the capillary conductance at each grid resolution until a finer resolution would no longer affect the optimal plate conductance.

Currently, the connection of the penetrating arterioles and descending venules to the capillary bed demand a minimum path length (and therefore resistance) through the capillary bed. Increasing the resolution of the capillary bed conductive plate would affect this minimum resistance. This minimum capillary resistance could be controlled by adding a set length pre-capillary vessel between the penetrating arterioles and the capillary bed, as well as a post-capillary connecting the capillary bed to the ascending venules.

Cited Literature

1. Lauwers, F., Cassot, F., Lauwers-Cances, V., Puwanarajah, P. & Duvernoy, H. Morphometry of the human cerebral cortex microcirculation: General characteristics and space-related profiles. *NeuroImage* **39**, 936–948 (2008).
2. Duvernoy, H. M., Delon, S. & Vannson, J. L. Cortical blood vessels of the human brain. *Brain Res. Bull.* **7**, 519–579 (1981).
3. Weber, B., Keller, A. L., Reichold, J. & Logothetis, N. K. The Microvascular System of the Striate and Extrastriate Visual Cortex of the Macaque. *Cereb. Cortex* **18**, 2318–2330 (2008).
4. Tsai, P. S. *et al.* Correlations of neuronal and microvascular densities in murine cortex revealed by direct counting and colocalization of nuclei and vessels. *J. Neurosci. Off. J. Soc. Neurosci.* **29**, 14553–14570 (2009).
5. Boas, D. A., Jones, S. R., Devor, A., Huppert, T. J. & Dale, A. M. A vascular anatomical network model of the spatio-temporal response to brain activation. *NeuroImage* **40**, 1116–1129 (2008).
6. Fang, Q. *et al.* Oxygen Advection and Diffusion in a Three Dimensional Vascular Anatomical Network. *Opt. Express* **16**, 17530–17541 (2008).
7. Lorthois, S., Cassot, F. & Lauwers, F. Simulation study of brain blood flow regulation by intra-cortical arterioles in an anatomically accurate large human vascular network. Part II: Flow variations induced by global or localized modifications of arteriolar diameters. *NeuroImage* **54**, 2840–2853 (2011).

8. Lorthois, S., Cassot, F. & Lauwers, F. A Simulation Study of Brain Blood Flow Regulation by Intra-cortical Arterioles in an Anatomically Accurate Large Human Vascular Network. *NeuroImage* **47**, S77 (2009).
9. Gould, I. G., Tsai, P., Kleinfeld, D. & Linninger, A. The capillary bed offers the largest hemodynamic resistance to the cortical blood supply. *J. Cereb. Blood Flow Metab.* **37**, 52–68 (2017).
10. Pries, A. R. & Secomb, T. W. Microvascular blood viscosity in vivo and the endothelial surface layer. *Am. J. Physiol. - Heart Circ. Physiol.* **289**, H2657–H2664 (2005).
11. Blinder, P. *et al.* The cortical angiome: an interconnected vascular network with noncolumnar patterns of blood flow. *Nat. Neurosci.* **16**, 889–897 (2013).

VI. LARGE SCALE ONE-DIMENSIONAL FLUID STRUCTURE INTERACTION

MODELS OF THE CEREBRAL VASCULATURE

Introduction

In the investigation of brain function, the functional magnetic resonance imaging (fMRI) measurement of the blood oxygen level dependent (BOLD) signal has become a widely used tool. However, the biophysical relationship that links blood oxygen content, blood flow and neuronal function is still not well understood³²⁻³³. In the past decade, several finite element models have been established to better understand the relationship between neuronal activity and the dynamic functional map provided by the BOLD signal³⁴⁻³⁵. These fMRI simulations of the BOLD signal are based off of closed network simulations oxygen convection, extraction and metabolism of the blood vessels and the surrounding tissue^{31,36-37}. However, these previous models assume rigid non-deforming vessels neglecting the distensibility of blood vessels. The effect of vessel deformation on hemodynamics during a functional control event and subsequent interpretation of the BOLD signal are unknown.

This investigation of auto regulatory and functional control of cerebral blood flow requires a robust computational method for solving the fluid-structure interaction (FSI) of passive compliance of distensible blood vessels. While previous research in the field has focused on the effects of changing vascular wall material properties¹⁻² these methods are typically limited to single vessel analysis. The dynamic distribution of blood flow throughout a cerebral microvessel network following a vasodilatory or constricting event requires a computational method that can solve this compliant vessel FSI problem for thousands of vessels, a computational cost that can be reduced by constructing the problem in 1D. Some methodology studies have been presented comparing the similarities between 1D and 3D approaches³⁻⁴ as well as the effects of enforcing different outlet boundary conditions⁵⁻⁶ and choices of flow profile⁷.

By comparing the performance of existing numerical integrators and validating their results against measured data, the most accurate and efficient computational method can be selected to investigate regulatory control of cerebral blood flow in microcirculatory blood vessel networks. An investigation is presented comparing the results of four numerical integrators; a linear and a nonlinear one-step implicit finite difference method, the two-step Richtmeyer -Morton explicit Lax-Wendroff method and an implicit integration of a Method of Weighted Residuals known as the Collocation Method.

In the first part, the 1D governing equations of mass conservation and momentum balance are derived, as well as the mechanical tube law that describes the wall movement arising from a transluminal pressure differences. An extended discussion is included detailing the terms of the constitutive wall movement equation. Each of the numerical integrators is introduced, including the details of their discretization and details of their implementation. A detailed discussion of the boundary equations is included.

Three case studies are presented, a canine aortic branch, a human pulmonary artery bifurcation, and a simplified microvessel network including both bifurcations and unions. Numerical results for the first two case studies are validated against dynamic *in vivo* measurements. Following the case studies the merits of each numerical integrator and obstacles of each are presented, including a report on computational cost and accuracy. Finally, a discussion on the effects of signal reflections at bifurcations is included, as well as an investigation into open loop control.

Methods

The 1D dynamic, distensible tube problem simultaneously solves for the hydrostatic pressure, fluid velocity and the vessel diameter across a single vessel. In order to solve all three variables, three equations are needed. Mass conservation is rigorously enforced within the vessel and at each vessel junction, and the fluid momentum is conserved in both the radial and

axial direction. The dynamic hydrostatic pressure difference between the blood and the extravascular space drives wall deformations as governed by an elastic tube law.

For both the mass and momentum conservations equations, the 3D radial equations are proposed and reduced to a 1D nonlinear partial differential equation. A linear elastic tube law is introduced and discussed in three forms; as an algebraic, ordinary, and partial differential equation.

Derivation of 1D Mass Conservation Balance

The differential form of the law of conservation of mass⁸ requires that the sum of the density, ρ , accumulation and the divergence of the product of the velocity vector, \vec{u} , and fluid density is equal to zero as described in eq. 55.

$$\frac{\partial \rho}{\partial t} + \nabla \cdot (\rho \vec{u}) = 0 \quad 55$$

Assuming that blood is incompressible and that the blood flow profile is symmetrical around the radial axis, mass continuity can be rewritten in terms of the axial, u_x , and radial, u_r , direction⁶. This equation is rewritten in a more recognizable form by application of the product rule as shown in eq. 57.

$$\nabla \cdot (\vec{u}) = 0 \quad 56$$

$$\frac{\partial u_x}{\partial x} + \frac{1}{r} \frac{\partial (r u_r)}{\partial r} = 0 \quad 57$$

Integration of eq. 57 over the cross sectional area of the vessel from the center to the vessel radius, R , gives rise to the following form of the mass continuity shown in eq. 58.

$$2\pi \int_0^R \left[\frac{\partial u_x}{\partial x} + \frac{1}{r} \frac{\partial (r u_r)}{\partial r} \right] r dr = 0 \quad 58$$

$$2\pi \int_0^R \frac{\partial u_x}{\partial x} r dr + 2\pi \int_0^R \frac{\partial (r u_r)}{\partial r} dr = 0 \quad 59$$

Substituting the first term in eq. 59 using the product rule we now achieve the form shown in eq. 60.

$$2\pi \int_0^R \frac{\partial(u_x r)}{\partial x} dr - 2\pi \int_0^R u_x \frac{\partial r}{\partial x} dr + 2\pi \int_0^R \frac{\partial(r u_r)}{\partial r} dr = 0 \quad 60$$

The integral for the third term is evaluated, and the second term is eliminated by employing a no-slip boundary condition at the wall, $[u_x]_R = 0$.

$$2\pi \frac{\partial}{\partial x} \int_0^R u_x r dr + 2\pi R [u_r]_R = 0 \quad 61$$

Enforcing that wall deformations occur in the radial direction only, the velocity in the radial direction, u_r , at the vessel radius, R , is evaluated as dynamic change in radius, $[u_r]_R = \partial R / \partial t$.

$$2\pi \frac{\partial}{\partial x} \int_0^R u_x r dr + 2\pi R \frac{\partial R}{\partial t} = 0 \quad 62$$

By the product rule, the second term can be transformed as shown in eq. 63, where the cross sectional area, A , is written using the term A . The integral of the first term is evaluated, using the definition of bulk fluid flow through a rigid cylinder given in eq. 64. Substituting eq. 64 into eq. 65, we obtain the 1D mass continuity in terms of volumetric flow and vessel cross sectional area.

$$2\pi R \frac{\partial R}{\partial t} = \pi \frac{\partial(R \cdot R)}{\partial t} = \frac{\partial A}{\partial t} \quad 63$$

$$Q = 2\pi \frac{\partial}{\partial x} \int_0^R u_x r dr \quad 64$$

$$\frac{\partial Q}{\partial x} + \frac{\partial A}{\partial t} = 0 \quad 65$$

Derivation of 1D Momentum Conservation

Two derivations of the 1D momentum conservation derivation are presented in the literature representing differences in assumptions made around the shape of the blood flow profile.

The first approach accounts for the second order velocity changes in the plug flow profile when computing axial velocity gradients, which has been presented in more recent works⁶ which focus on a single vessel. The second method is presented in earlier works⁹ which focus on discretizing larger vessel networks, and these second order terms are neglected.

Conservation of radial momentum is not computed, tube distensibility was determined using an instantaneous linear tube law. However, simplification of the conservation of radial momentum implies that blood pressure remains constant in the radial direction. The derivation of the simplified radial momentum conservation that leads to this assumption of the radial pressure profile can be found in Supplemental 3.

First Approach

The first approach to deriving the 1D momentum equations includes an approximation of the second order axial velocity terms in the blood flow profile. For symmetrical fluid flow around the radial axis, the x-momentum conservation equation states that the sum of the fluid acceleration, the axial and radial kinetic energy and the pressure gradient is equal to the viscous loss due to fluid friction, a function of the fluid kinematic viscosity, ν .

$$\frac{\partial u_x}{\partial t} + u_x \frac{\partial u_x}{\partial x} + u_r \frac{\partial u_x}{\partial r} + \frac{1}{\rho} \frac{\partial P}{\partial x} = \frac{\nu}{r} \frac{\partial}{\partial r} \left(r \frac{\partial u_x}{\partial r} \right) \quad 66$$

We can obtain the 1D transformation of axial momentum transport by integrating over the cross sectional area. The first term is substituted as described in eq. 64.

$$\frac{\partial Q}{\partial t} + 2\pi \int_0^R \left(u_x \frac{\partial u_x}{\partial x} + u_r \frac{\partial u_x}{\partial r} \right) r dr + \frac{1}{\rho} 2\pi \int_0^R \frac{\partial P}{\partial x} r dr = \nu \cdot 2\pi \int_0^R \frac{1}{r} \frac{\partial}{\partial r} \left(r \frac{\partial u_x}{\partial r} \right) r dr \quad 67$$

By the product rule, the first integral can be replaced as shown in eq. 68.

$$2\pi \int_0^R \left(ru_x \frac{\partial u_x}{\partial x} + ru_r \frac{\partial u_x}{\partial r} \right) dr = 2\pi \int_0^R \left(ru_x \frac{\partial u_x}{\partial x} + \frac{\partial(ru_r u_x)}{\partial r} - u_x \frac{\partial(ru_r)}{\partial r} \right) dr \quad 68$$

The second term in eq. 68 is eliminated by employing a no-slip boundary condition at the wall, $[u_x]_R = 0$. The third term can be replaced by substitution by rearranging the continuity in eq. 57 reducing the term in eq. 68 to the form presented in eq. 69.

$$2\pi \int_0^R \left(ru_x \frac{\partial u_x}{\partial x} + ru_x \frac{\partial u_x}{\partial x} \right) dr = 2\pi \int_0^R \frac{\partial(u_x \cdot u_x)}{\partial x} r dr = \frac{\partial}{\partial x} \left(\int_0^R u_x^2 \cdot 2\pi r dr \right) \quad 69$$

The velocity profile of blood in tapered vessels is flat⁶, as shown in eq. 70, except for the thin boundary layer near the vessel wall, δ , where the profile linearly transitions to zero following the no slip boundary condition, where \bar{u}_x is the plug-flow axial velocity outside the boundary layer.

$$u_x = \begin{cases} \bar{u}_x & \text{for } r \leq R - \delta \\ \bar{u}_x(R - r)/\delta & \text{for } R - \delta < r \leq R \end{cases} \quad 70$$

With this definition of the velocity profile, the integral in eq. 69 can be expressed as a power series. By dropping the later terms and retaining only the first and second order axial velocity terms, a simplified version of eq. 68 is found, shown in eq. 71. The integral in eq. 69 can then be shown as the derivative in eq. 72.

$$\int_0^R u_x^2 \cdot 2\pi r dr = A \bar{u}_x^2 = \frac{Q^2}{A} \quad 71$$

$$2\pi \int_0^R \left(ru_x \frac{\partial u_x}{\partial x} + ru_r \frac{\partial u_x}{\partial r} \right) dr = \frac{\partial}{\partial x} \left(\frac{Q^2}{A} \right) \quad 72$$

Returning to the third term on the left hand side in eq. 67, the pressure gradient term, can be simplified by evaluating the integral across the cross sectional area.

$$\frac{1}{\rho} 2\pi \int_0^R \frac{\partial P}{\partial x} r dr = \frac{1}{\rho} 2\pi \frac{\partial P}{\partial x} \frac{1}{2} r^2 = \frac{A}{\rho} \frac{\partial P}{\partial x} \quad 73$$

The viscous loss term on the right hand side of eq. 67 can be expressed by evaluating the integral and using the velocity profile definition given in eq. 70.

$$v \cdot 2\pi \int_0^R \frac{1}{r} \frac{\partial}{\partial r} \left(r \frac{\partial u_x}{\partial r} \right) r dr = v \cdot 2\pi \left[r \frac{\partial u_x}{\partial r} \right]_R = v 2\pi \left[r \frac{\partial u_x}{\partial r} \right]_R = -\frac{2\pi v R \bar{u}_x}{\delta} \quad 74$$

We can then substitute these definitions of the fluid acceleration, axial and radial kinetic energy, pressure gradient and the viscous loss due to fluid friction into eq. 66 to obtain a more recognizable form.

$$\frac{\partial Q}{\partial t} + \frac{\partial}{\partial x} \left(\frac{Q^2}{A} \right) + \frac{A}{\rho} \frac{\partial P}{\partial x} + \frac{2\pi v R \bar{u}_x}{\delta} = 0 \quad 75$$

Assuming that the ratio of the wall thickness is to the vessel radius is 1:4, the same viscous loss estimation is computed as estimated in whole brain studies⁹ as shown in eq. 76. The kinematic viscosity, ν , is replaced with the dynamic viscosity over the fluid density, μ/ρ

$$\frac{\partial Q}{\partial t} + \frac{\partial}{\partial x} \left(\frac{Q^2}{A} \right) + \frac{A}{\rho} \frac{\partial P}{\partial x} + \frac{8\mu}{\rho R^2} Q = 0 \quad 76$$

Introducing the fluid friction term $\gamma = 8\mu\pi/\rho$, the momentum equation can be rewritten in a more familiar form⁹.

$$\frac{\partial Q}{\partial t} + \frac{\partial}{\partial x} \left(\frac{Q^2}{A} \right) + \frac{A}{\rho} \frac{\partial P}{\partial x} + \gamma \frac{Q}{A} = 0 \quad 77$$

Second Approach

The second approach of obtaining the 1D transformation of axial momentum is obtained by integrating over the cross sectional as shown in eq. 78, similar to the first approach. The first term is integrated and expanded as show in eq. 79, and the axial velocity is substituted with the new term, U .

$$2\pi \int_0^R \left(\frac{\partial u_x}{\partial t} + u_x \frac{\partial u_x}{\partial x} + u_r \frac{\partial u_x}{\partial r} + \frac{1}{\rho} \frac{\partial P}{\partial x} \right) r dr = 2\pi \int_0^R \frac{\nu}{r} \frac{\partial}{\partial r} \left(r \frac{\partial u_x}{\partial r} \right) r dr \quad 78$$

$$2\pi \int_0^R \frac{\partial u_x}{\partial t} r dr = \frac{\partial}{\partial t} Q = A \frac{\partial U}{\partial t} + U \frac{\partial A}{\partial t} \quad 79$$

The second term in the integral on the left hand side is substituted using the product rule as shown in eq. 80. Approximating the second order derivative of the axial blood velocity in the x-direction as a flat profile, $\overline{u_x}$, the integral in eq. 80 is evaluated as shown in eq. 81. By dropping the second order axial velocity term, the axial velocity of the plug blood flow profile is assumed to be independent of the radius and can be factored out of the integral.

$$\pi \int_0^R 2u_x \frac{\partial u_x}{\partial x} r dr = \pi \int_0^R \frac{\partial u_x^2}{\partial x} r dr \quad 80$$

$$\pi \frac{\partial \overline{u_x}^2}{\partial x} \int_0^R r dr = \frac{1}{2} \frac{\partial \overline{u_x}^2}{\partial x} \pi R^2 = \frac{1}{2} \frac{\partial \overline{u_x}^2}{\partial x} A = A \frac{\partial}{\partial x} \left(\frac{U^2}{2} \right) \quad 81$$

By the product rule, the third term within on the left hand side of eq. 78 can be replaced as shown in eq. 82. Enforcing the no-slip boundary condition of $[u_x]_R = 0$ this reduces to the form shown in eq. 83.

$$2\pi \int_0^R \left(r u_r \frac{\partial u_x}{\partial r} \right) dr = 2\pi \int_0^R \left(\frac{\partial (r u_r u_x)}{\partial r} - u_x \frac{\partial (r u_r)}{\partial r} \right) dr \quad 82$$

$$2\pi \int_0^R \left(\frac{\partial (r u_r u_x)}{\partial r} - u_x \frac{\partial (r u_r)}{\partial r} \right) dr = 2\pi \int_0^R -u_x \frac{\partial (r u_r)}{\partial r} dr \quad 83$$

Approximating the axial blood flow profile as a flat value, $\overline{u_x}$, that is independent of the radius, r , the integral in eq. 83 is evaluated as shown in eq. 84. Enforcing that wall deformations occur in the radial direction only, the velocity in the radial direction, u_r , at the vessel radius, R , is evaluated as dynamic change in radius, $[u_r]_R = \partial R / \partial t$. Using the product rule as demonstrated in eq. 63, eq. 84 is rewritten as eq. 85.

$$2\pi \int_0^R -u_x \frac{\partial (r u_r)}{\partial r} dr = -\overline{u_x} 2\pi R [u_r]_R = -\overline{u_x} 2\pi R \frac{\partial R}{\partial t} \quad 84$$

$$-\overline{u_x} 2\pi R \frac{\partial R}{\partial t} = -\overline{u_x} \frac{\partial A}{\partial t} = -U \frac{\partial A}{\partial t} \quad 85$$

The pressure gradient and viscosity term are evaluated using the same method as described in the first approach which yields eq. 86 for the momentum equation, which reduces to a more familiar form shown in eq. 87.

$$A \frac{\partial U}{\partial t} + U \frac{\partial A}{\partial t} + A \frac{\partial}{\partial x} \left(\frac{U^2}{2} \right) - U \frac{\partial A}{\partial t} + \frac{A}{\rho} \frac{\partial P}{\partial x} + \gamma \cdot U = 0 \quad 86$$

$$\frac{\partial U}{\partial t} + \frac{\partial}{\partial x} \left(\frac{U^2}{2} + \frac{P}{\rho} \right) + \gamma \cdot \frac{U}{A} = 0 \quad 87$$

One limitation of this 1D formulation of the momentum equations is the oversimplification of viscous effects. The momentum conservation described in eq. 66 neglects the loss of momentum due to the second order viscous dissipation (viscous diffusion). Dropping this term simplifies the momentum equations to a hyperbolic system, unlike the original Navier-Stokes system. Implementation of these equations on bounded domains typically leads to reflections¹⁰ unless special care is taken at the boundaries, which are described in this report.

Linearized Momentum Equation

Not all solution methods can integrate partial differential equations. By presenting a linearized form of the momentum equation, multiple solution methods can be tested and applied side by side. A classical approach to solving the moving wall problem involves the spectral or normal mode analysis of the linearized Navier-Stokes equations at certain laminar flow conditions¹¹. By fixing the inlet pressure with an average value between systole and diastole, the nominal cross-sectional area, \bar{A} , and volumetric blood flow, \bar{Q} , can be determined for a single blood vessel. By use of the product rule, the nonlinear momentum equation can be rewritten using these nominal values as shown in eq. 88.

$$\frac{\partial Q}{\partial t} + \frac{2\bar{Q}}{\bar{A}} \frac{\partial Q}{\partial x} + \frac{\bar{A}}{\rho} \frac{\partial P}{\partial x} - \frac{\gamma}{\bar{A}} Q = 0 \quad 88$$

For systems with large fluctuations between in area and flow between systole and diastole, such as large blood vessel, the approximation of the nominal value may strongly affect the solution. Solving these systems with the linearized momentum equations may require a *fixed point iterative scheme* to match solutions found using the linearized version.

Tube Law

A final equation is needed to solve the distensible vessel problem, a mechanical law of the vessel wall displacement in response to a pressure difference across the luminal wall. Although the vessel wall is composed of a tunica intima and media layer (which are in turn made up of endothelial cells, smooth muscle, elastin and other connective material), these material properties become homogenous when a radial stress is introduced¹² by relating the circumferential stress of the wall to the pressure difference across the wall. By treating the elastic deformation of the vessel as a Hookian spring, a constitutive relationship between pressure and area is formed. The homogenous elastic material property is a product of the Young's Modulus, E , and the vessel wall thickness, h . The linear form of the elastic tube model can be determined, as shown in eq. 89. The difference between the vessel radius at rest, R^0 , and in response to a change in lumen pressure relative to a fixed extravascular pressure, P_{ex} , When $P = P_{ex}$, $R = R^0$.

$$\frac{Eh}{R^0} \left(1 - \frac{R^0}{R} \right) - (P - P_{ex}) = 0 \quad 89$$

This form of the tube deformation assumes that the lumen radius, or cross sectional area, responds instantaneously to a change in lumen pressure. To account for phase lag between lumen radius and pressure, a damping term is introduced. These terms have been developed in the standard viscoelastic model¹² shown in eq. 90, which described the vessel wall deformation as a function of the relaxation time for constant stress τ_1 and strain τ_2 .

$$\frac{Eh}{R^0} \left(1 - \frac{R^0}{R} \right) - \frac{Eh}{R^0} \tau_1 \frac{\partial}{\partial t} \left(\frac{R^0}{R} \right) - (P - P_{ex}) - \tau_2 \frac{\partial p}{\partial t} = 0 \quad 90$$

This equation differs slightly from the extended tube law proposed by Formaggia and Quarteroni¹³ which is derived from a generalized string model¹⁴. This mechanistic wall displacement model accounts for both viscoelastic and longitudinal stress along the surface of the vessel, neglecting inertial forces and axial viscoelastic force described in eq. 91.

$$\frac{Eh}{R^0} (R - R^0) - \kappa \frac{\partial R}{\partial t} - \beta \frac{\partial^2 R}{\partial x^2} - (P - P_{ex}) = 0 \quad 91$$

This generalized model of wall displacement lacks the strain term of the materialistic model proposed in eq. 90. It should be noted that both of these mechanistic wall deformation models neglect the mass of the tube wall, ignoring the effects of inertial forces¹⁵. Additionally, both of these models ignore the effects of historical loading and unloading strain of the vessel wall on the stress. To explore the effects of damping and enforcing longitudinal stress, the tube law presented in eq. 91 was used.

Inflow Boundary Conditions

At the input, the pressure is assigned as an input forcing function. The distensible tube law was enforced in eq. 91 was enforced to determine the wall movement in response to pressure changes across the lumen wall. At the inlet boundary, the tube law was modified by shifting the second order differential of the longitudinal stress term to the right, which is known as the uncentered approximation¹⁶.

The volumetric flow rate at the inlet is determined as a function of the pressure by applying the momentum equation at the first node. This allows for the inlet volumetric flow rate to initially develop as a function of the inlet pressure gradient and then in response to the flow gradient

Outflow Boundary Conditions

At the outlet, mass is conserved by assigning the steady-state mass conservation at the outlet, described in eq. 92.

$$\frac{\partial Q}{\partial x} = 0 \quad 92$$

Similarly to the inlet, the longitudinal stress term differential in the tube law was shifted to the left at the outlet, employing the uncentered approximation.

At the outlet, a fixed pressure was assigned, which led to wave reflections at the outlet as shown in Figure 42. A distensible virtual node was introduced connected to the outlet to ensure that waves could propagate through the outlet (a) without being reflected, and (b) maintaining a smooth pressure spatial profile from inlet to outlet. This non-reflective outlet boundary condition is described in the following section.

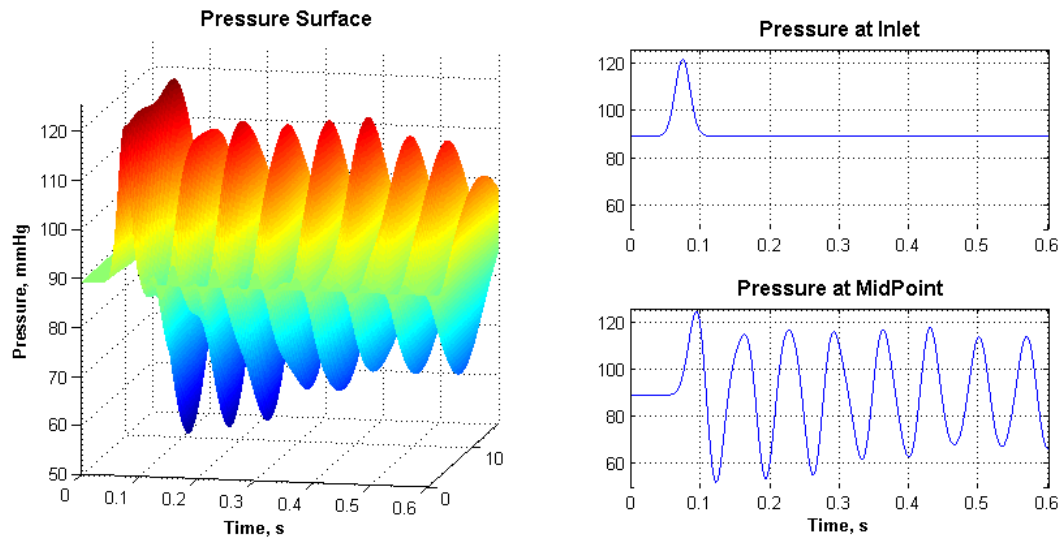


Figure 42 Effects of reflective outlet boundary condition on the pressure wave. Applying a single inlet pressure impulse through a short 16cm vessel causes reflections that bounce from inlet to outlet, lessening in intensity due to the loss of energy from viscous friction. These results were computed with the collocation method.

Non-Reflective RCR Outlet

When the outlet boundary values are not known from measured values, three outlet boundary conditions have been developed to estimate the peripheral flow rates¹⁷ fixed pressure outlet, resistance boundary condition, and the three-part Windkessel Model, also known as the *RCR*. Different choices in the outlet boundary conditions lead to changes in the outlet pressure gradients and, in the case of the fixed pressure outlet and resistance boundary condition, erroneous backflow in the form of a wave reflection. Wave reflection at the outlet are amplified by dropping the viscous diffusion terms in the 1D Navier-Stokes equations described in eq. 77 or eq. 87, which simplifies the problem to a hyperbolic system sensitive to boundary implementations¹⁰. To address this wave reflection, only the *RCR* model is discussed here.

The *RCR* model is a “circuit” which is attached to the outlet of the vessel which acts as an analog for the peripheral resistance and capacitance of the downstream vascular tree, as shown in Figure 43. In this circuit, the drop in voltage is analogous to the blood pressure drop and the current represents the blood flow.

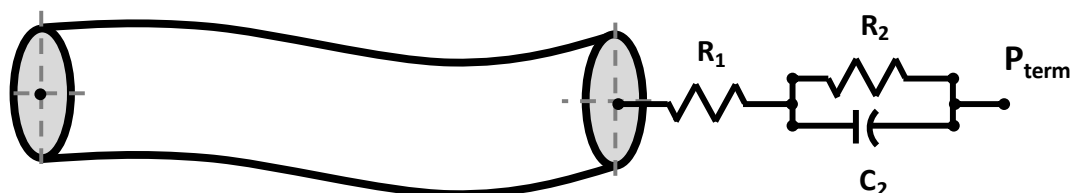


Figure 43 Schematic of the outlet non-reflective RCR circuit, also known as the Windkessel balloon model. The first resistor, R_1 , must be low enough to ensure that flow and pressure leave the vessel and enter the capacitor, C , which acts as a distensible balloon. The second resistor, R_2 , must be much lower than R_1 so that as the capacitor releases energy it leaves the system toward the terminal pressure, P_{term} , and not back into the blood vessel.

The outlet circuit is composed of an inlet resistor, R_1 , an outlet resistor, R_2 , and a virtual node with capacitance, C . By Kirchhoff's law, the pressure drop from the terminal node of the vessel, P_N , to the virtual node, P_V , through the R_1 resistor with a flow of Q_N , can be described by eq. 93. The pressure drop from the virtual node to “ground,” or the terminal pressure of the circuit, P_{term} , goes through either the R_2 resistor or is absorbed by the capacitor as described in eq. 94. Taking the derivative of eq. 93 with respect to time, substitution and rearrangement, the term P_V can be cancelled for an outlet pressure boundary condition for P_N as shown in eq. 95.

$$R_1 Q_N = P_N - P_V \quad 93$$

$$R_2 Q_N = P_V - P_{term} + R_2 C \frac{\partial P_V}{\partial t} \quad 94$$

$$P_N + R_2 C \frac{\partial P_N}{\partial t} = P_{term} + (R_1 + R_2) Q_N + R_1 R_2 C \frac{\partial Q_N}{\partial t} \quad 95$$

This virtual outlet node acts as a distensible “balloon” ensuring that the outlet pressure signal can leave the system. The resistance of R_1 must be low enough to ensure that the signal can leave the system, but high enough to limit the signal from traveling back into the vessel.

The parameters for the non-reflective outlet boundary conditions are not chosen physiologically, they are numerically selected to filter the outlet signal to match physiological observations. A manual optimization routine was undertaken to choose values of R_1 , R_2 and C to minimize wave reflections as evaluated by visual inspection. Terminal boundary conditions were deemed unacceptable if the amplitude of the reflected cross sectional area signal was greater than 25% the absolute amplitude of the incident signal in a test case of a single sigmoidal pulse.

Reflection Coefficient

The reflection coefficient, R_f , was computed at the terminal outlet of the network simulation using the approach²⁶ described in Sherwin et al. The reflection coefficient, R_f , is a ratio of the

change in pressure across the reflected wave, $\hat{\delta P}_N$, to the change in pressure in the incident wave, δP_N , of the target terminal outlet vessel, N . Assuming an instantaneous linear elastic tube law, the change in pressure is equivalent to the change in area, δA_N . The change in area in the reflected wave, $\hat{\delta A}_N$, is the difference between the change in area in the downstream vessel, δA_{N-1} , and the target vessel, δA_N , as shown in eq. 96.

$$R_f = \frac{\hat{\delta P}_N}{\delta P_N} = \frac{\hat{\delta A}_N}{\delta A_N} = \frac{\delta A_{N-1} - \delta A_N}{\delta A_N} = \frac{\delta A_{N-1}}{\delta A_N} - 1 \quad 96$$

An outlet R_f of -0.013 is reported for the network simulation, smaller than the reported range of outlet R_f of -0.4 to -0.5 in 1-D network simulation of the human body²⁶. It is assumed that this minimal reflection coefficient is acceptably small, as a literature search did not uncover reported R_f values in microvessel network studies.

Integration Methods

We present four different dynamic numerical integrators for solving the distensible vessel problem; a linear and nonlinear implicit finite difference method, the Richtmeyer-Morton two-step Lax-Wendroff method and a Method of Weighted Residuals known as the Collocation Method. Both explicit and implicit integrations are described for the Lax-Wendroff method including a brief discussion of the merits of each. The Collocation method is also described, dynamically integrated using an implicit Euler step.

Linear and Nonlinear Finite Difference with Euler Integrator

A finite difference discretization on a collocated grid was formulated using an implicit Euler time integration scheme. The problem was solved using both the nonlinear momentum conservation presented in eq. 77 and the linearized form presented in eq. 88. Using the blood flow form of the mass conservation balance presented in eq. 65 and the linearized form of the

momentum conservation, the entire system becomes a linear set of ordinary differential equations which can be transformed into algebraic equations using either the implicit or explicit Euler integration approach.

The resulting set of algebraic equations was solved using the solver suite available in MATLAB. The nonlinear set of algebraic equations was solved using (FSOLVE) which employed the Trust Region method. The linear set of algebraic equations was solved using the backslash operator, which employed LU decomposition. To maintain consistency, the equations here are presented here in residual form, including the linear and nonlinear form of the momentum balance.

Mass Conservation

$$\frac{A_i^{t+1} - A_i^t}{\Delta t} + \frac{1}{\Delta x} (Q_{i+1}^{t+1} - Q_i^{t+1}) = 0 \quad 97$$

Nonlinear Momentum Balance

$$\frac{Q_i^{t+1} - Q_i^t}{\Delta t} + \frac{1}{\Delta x} \left[\left(\frac{Q^2}{A} \right)_{i+1}^{t+1} - \left(\frac{Q^2}{A} \right)_i^{t+1} \right] + \frac{A_i^{t+1}}{\rho \Delta x} (P_{i+1}^{t+1} - P_i^{t+1}) - \gamma \left(\frac{Q}{A} \right)_i^{t+1} = 0 \quad 98$$

Linearized Momentum Balance

$$\frac{Q_i^{t+1} - Q_i^t}{\Delta t} + \frac{2\bar{Q}}{\bar{A}\Delta x} [Q_{i+1}^{t+1} - Q_i^{t+1}] + \frac{\bar{A}}{\rho \Delta x} (P_{i+1}^{t+1} - P_i^{t+1}) - \frac{\gamma}{\bar{A}} Q_i^{t+1} = 0 \quad 99$$

Tube Law

$$(P_i^{t+1} - P_{ex}) - E_L \left(\frac{A_i^{t+1}}{A_i^1} - 1 \right) - \kappa \left(\frac{A_i^{t+1} - A_i^t}{\Delta t} \right) - \beta \left(\frac{A_{i+1}^t - 2A_i^t + A_{i-1}^t}{\Delta x^2} \right) \quad 100$$

Lax-Wendroff

The three equations describing the distensible vessel problem, the mass conservation of eq. 65, the second approach to the momentum balance in eq. 87, and the tube law of eq. 89, describe a quasi-linear first order hyperbolic system. The first two equations of this system, the mass conservation and momentum balance, can be written in the general form of hyperbolic partial differential equations described in eq. 101.

$$\frac{\partial u(x, t)}{\partial t} + \frac{\partial f(u(x, t))}{\partial x} = 0 \quad 101$$

The dynamic update of these equations can be written in the form of the two-step Richtmeyer-Morton Lax-Wendroff scheme¹⁸. This finite difference based numerical method for solving hyperbolic partial differential equations is second-order accurate in both space and time. The implementation of the Lax-Wendroff integrator for the distensible tube problem (including bifurcations and unions) is based off an understanding of the implementation proposed in Zagzoule¹⁸.

The simplicity of implementation is an attractive feature of this simple finite difference scheme. Even more so when one considers the strategy offered by the explicit formulation, in which the solution of the hyperbolic wave problem is propagated forward from inlet to outlet without the need for simultaneously solving large sets of algebraic equations. However, this method exhibits a nearly-discontinuous dispersive response in response to shocks¹⁹, which limits its usefulness in modeling impulse response problem. The implicit formulation is useful for smoothing the numerical shock profile²⁰⁻²¹. Since the pulsatile pressure inlet for the distensible blood vessel problem is smooth and continuously differentiable, this formulation is not needed for this problem type. Details of the explicit discretization and notation on the two-step Richtmeyer-Morton Lax-Wendroff scheme are located in the Supplemental 1, including details on handling boundaries, bifurcations, unions and narrowing channels.

Parallel Computations

This two-step discretization in time and space explicitly solves blood pressure, velocity and vessel cross sectional area for each time step. This method relies exclusively on the values of each of these states in the previous time step at the node in question and the neighboring nodes. These values for the new time step can therefore be solved in any order and are not dependent on one another. Therefore, these computations can be easily solved in parallel, as the computation of each state for each time step can simply be distributed across multiple processors which compute the new time step independently. The ability of the two-step Lax-Wendroff integrator to independently compute the values of the new timeline extends to boundaries, bifurcations, and union as well as demonstrated in subsequent sections.

CFL Condition

At low magnitudes of the damping and longitudinal stress coefficients presented in the tube law, the system tends toward the behavior of a completely hyperbolic system. For the explicit formulation the stability of a hyperbolic system²³ is shown dependent on the Courant-Friedrichs-Lewy (CFL) condition, shown in eq. 102 where C is the speed of the pressure wave velocity through the tube.

$$\left(\left| \frac{Q}{A} \right| + C \right) \frac{\Delta t}{\Delta x} \leq 1 \quad 102$$

As the system is not completely hyperbolic due to the presence of the damping and longitudinal stress terms, the ratio of Δt to Δx shown here is the upper limit that must lead to a convergent solution; larger ratios of Δt to Δx may still converge. This criterion also assures the stability of the uncentered approximation²⁴ utilized at the boundary conditions. Application of the CFL convergence criterion

Collocation Method with Euler Integrator/Method of Weighted Residuals

The Method of Weighted Residuals (MWR) is an approximation technique for solving differential equations. The solution of these differential equations is considered to be well-approximated by a finite sum of a test function.

The value of this test function at selected grid points is assigned by a weighting function. Much like finite differences, MWR attempts to minimize the error at specific grid points. However, MWR minimizes the error between the sum of the test functions and the actual solution across all grid points simultaneously, enforcing a continuous solution based on the shape of the test function²⁵.

Presented is the MWR known as the Collocation Method, which uses a Dirac δ function as a weighting function. Specifically, Lagrangian polynomials are used to approximate the solution at selected grid points.

Lagrangian Polynomials

Lagrangian polynomials obey the same properties of the Dirac δ function at selected grid points as described in eq. 103, while providing a continuous surface appropriate for the physiological solution of the distensible vessel problem.

$$\delta(x - x_i) = \begin{cases} 1 & x = x_i \\ 0 & \text{otherwise} \end{cases} \quad 103$$

For a 3rd order polynomial as shown in Figure 44, three Lagrangian polynomials are constructed which obey the definition of the Dirac δ function, as shown in eq. 104.

$$L(x_1) = \frac{(x - x_2)(x - x_3)}{(x_1 - x_2)(x_1 - x_3)} \quad 104$$

$$L(x_2) = \frac{(x - x_1)(x - x_3)}{(x_2 - x_1)(x_2 - x_3)}$$

$$L(x_3) = \frac{(x - x_1)(x - x_2)}{(x_3 - x_1)(x_3 - x_2)}$$

With these definitions of the test function, we can now construct a definition of the weighting functions for the three variables that define our system, A , Q , and P , which are, respectively, a , q , and p as shown in eq. 105-107.

$$A(x) = \sum_{i=1}^3 a_i L_i(x) \quad 105$$

$$Q(x) = \sum_{i=1}^3 q_i L_i(x) \quad 106$$

$$P(x) = \sum_{i=1}^3 p_i L_i(x) \quad 107$$

These analytical definitions of A , Q , and P allow for a continuous solution to be calculated for the entire vessel. Additionally, due to the shape of the polynomial test function, the function is also continuously differentiable.

Euler Integration solved with Collocation

As the residual between the test function and the actual solution must be minimized at all points simultaneously, the linearized form of the momentum equation shown in eq. 88 is employed to construct a set of linear algebraic equations.

Since these equations must be solved simultaneously, there is no advantage to solving the dynamic advancement explicitly which only introduces convergence limitations and forces a small selection of dt as enforced by the CFL convergence criterion described in eq. 102.

For each of the formulations described below, the notation $L'_i(x_k)$ refers to the first order differentiation of the i^{th} Lagrangian polynomial evaluated at the grid point x_k , where $k = \{1,3\}$.

The values of \bar{Q} and \bar{A} are held constant for the entire vessel and do not need to be updated or indexed.

Mass Conservation

$$\frac{A_k^{t+1} - A_k^t}{\Delta t} + \sum_{i=1}^3 q_i L'_i(x_k) \quad k = \{1,5\} \quad 108$$

Momentum Balance

$$\frac{Q_k^{t+1} - Q_k^t}{\Delta t} + \frac{2\bar{Q}}{\bar{A}} \sum_{i=1}^3 q_i L'_i(x_k) + \frac{\bar{A}}{\rho} \sum_{i=1}^3 p_i L'_i(x_k) + \frac{\gamma}{\bar{A}} Q_k^{t+1} = 0 \quad k = \{1,5\} \quad 109$$

Tube Law

$$(P_i^{t+1} - P_{ex}) - E_L \left(\frac{A_i^{t+1}}{A_i^1} - 1 \right) - \kappa \left(\frac{A_i^{t+1} - A_i^t}{\Delta t} \right) - \beta \sum_{i=1}^3 p_i L''_i(x_k) \quad k = \{1,5\} \quad 110$$

MWR Splines: C0 and C1 continuity

For solving network models of the vasculature, it is necessary to ensure that *C0* (positional) and *C1* (first-order differential) continuity is enforced between the connecting polynomial equations shown in eq. 108-110. This is known as constructing a *spline*. By indexing the first and last grid points of adjacent polynomials as being defined identically, *C0* continuity was enforced by the definition of the Lagrangian test function, as shown in Figure 44.

To ensure that *C1* continuity was enforced for each *spline*, a new equation was introduced at each junction node for *A*, *Q*, and *P* as described in eq. 111-113, respectively.

$$\sum_{i=1}^5 a_{1,i} L'_{1,i}(x_4) - \sum_{i=1}^5 a_{2,i} L'_{2,i}(x_4) = 0 \quad 111$$

$$\sum_{i=1}^5 q_{1,i} L'_{1,i}(x_4) - \sum_{i=1}^5 q_{2,i} L'_{2,i}(x_4) = 0 \quad 112$$

$$\sum_{i=1}^5 p_{1,i} L'_{1,i}(x_4) - \sum_{i=1}^5 p_{2,i} L'_{2,i}(x_4) = 0 \quad 113$$

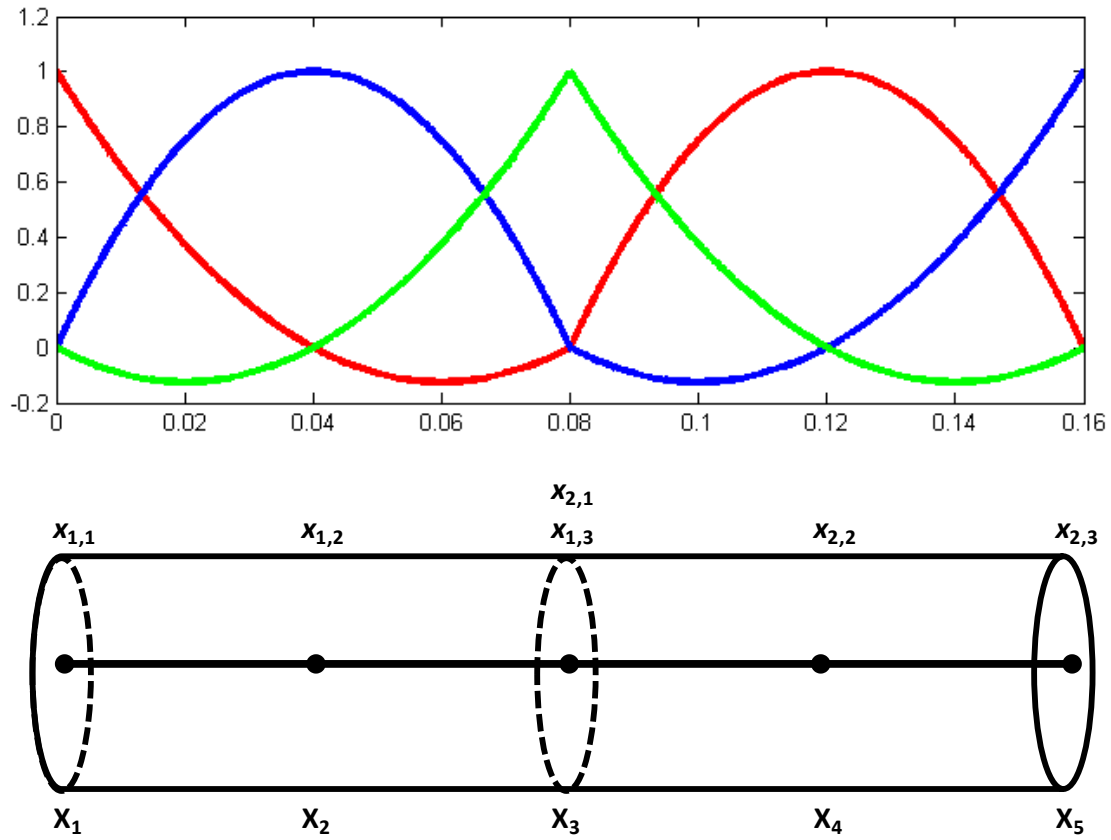


Figure 44 Lagrangian polynomials and indexing scheme for the calculation of continuous *splines*. Each vessel section is represented by a single 3rd order polynomial, and C0 continuity is enforced by the definition of Lagrangian polynomials as shown above. Each section is indexed locally, and a global index is shown beneath the cylinder schematic.

Results

To compare and validate these four methods, 2 case studies were conducted; a single vessel study of a canine aorta and the bifurcation of a sheep pulmonary artery. The canine study was compared against measured values¹⁰ and simulation results²⁷. Dynamic simulations of a simple cerebral microcirculation network were performed and harmonic steady-state, signal propagation and integration continuity are analyzed.

Canine Aorta Case Study

A case study was performed on a canine aorta, a large vessel measuring 8.0765mm in diameter. The physiological parameters of the vessel geometry and wall movement can be found in Table XVI, which were measured using sonomicrometer. The aortic input pressure was measured using a pressure microtransducer²⁸, and the wall displacement was measured using ultrasonic sonomicrometer aided by ultrasonic crystals.

Simulations were performed using the damping and longitudinal stress tube law described in eq. 91, using the coefficients and simulation parameters presented in Table XVI. The κ and β coefficients of the tube law were determined using an optimization routine (results not shown). At the inlet, pressure was approximated using a fifteen term Fourier Signal, flow was determined by the momentum balance and the area was computed using the tube law.

Table XVI Canine Aorta Case Study Parameters

	Parameter	Symbol	Value	Units	Reference
	Blood Viscosity	μ	3.5	g/m/s	¹⁰
	Blood Density	ρ	1050	kg/m ³	¹⁰
Canine Aorta	Vessel Wall Young's Modulus	E_L	22	kPa	²⁸
	Vessel Wall Thickness	w	1	mm	--
	Resting Radius	R^0	8.0765	mm	¹⁰
	Vessel Length	L	16	cm	¹⁰
	Time Step	Δt	0.15	ms	--
	Viscoelastic Damping Coefficient	κ	500	kg/m ³ /s	--
	Longitudinal Stress Coefficient	β	-100	kg/m/s ²	--
	Primary Outlet Resistance	R_1	20	MPa·s/m ³	--
	Secondary Outlet Resistance	R_2	1	kPa·s/m ³	--
	Outlet Compliance	C	1	cm ³ /Pa	--

The phase lag between the pressure wave and the area wave was computed at the vessel midpoint and compared against measurements from the canine model. The dynamic results of the pressure and area for each integrator are shown in Figure 45 as compared to the original measured data, with the residual sum of squares computed for each trajectory.

Note that the reported RSS value for both pressure and cross sectional area is dependent on the magnitude of range of recorded values; the RSS for pressure (80-130mmHg) is much higher than for the cross sectional area (15.5-18.0mm). Of the four compared methods, the nonlinear finite difference method gave the highest RSS value for cross sectional area (1.47) and pressure (781.87). Of the three remaining methods, the RSS value was comparatively low for the Lax-Wendroff method (RSS=54.21) and the Collocation method (RSS=51.52).

Note: Splines and the Collocation Method

The Collocation method required additional special attention to ensure proper application of this method weighted residuals. As shown in Figure 46, the number of splines used to approximate the signal had a significant effect on the reproduction of the propagated pressure and area signal. Too few segments, as shown in Figure 46C and Figure 46D resulted in an incorrect signal approximation, causing boundary reflections. Furthermore, no significant increase in signal fidelity was detected by increasing the spline from 5 to 10 segments.

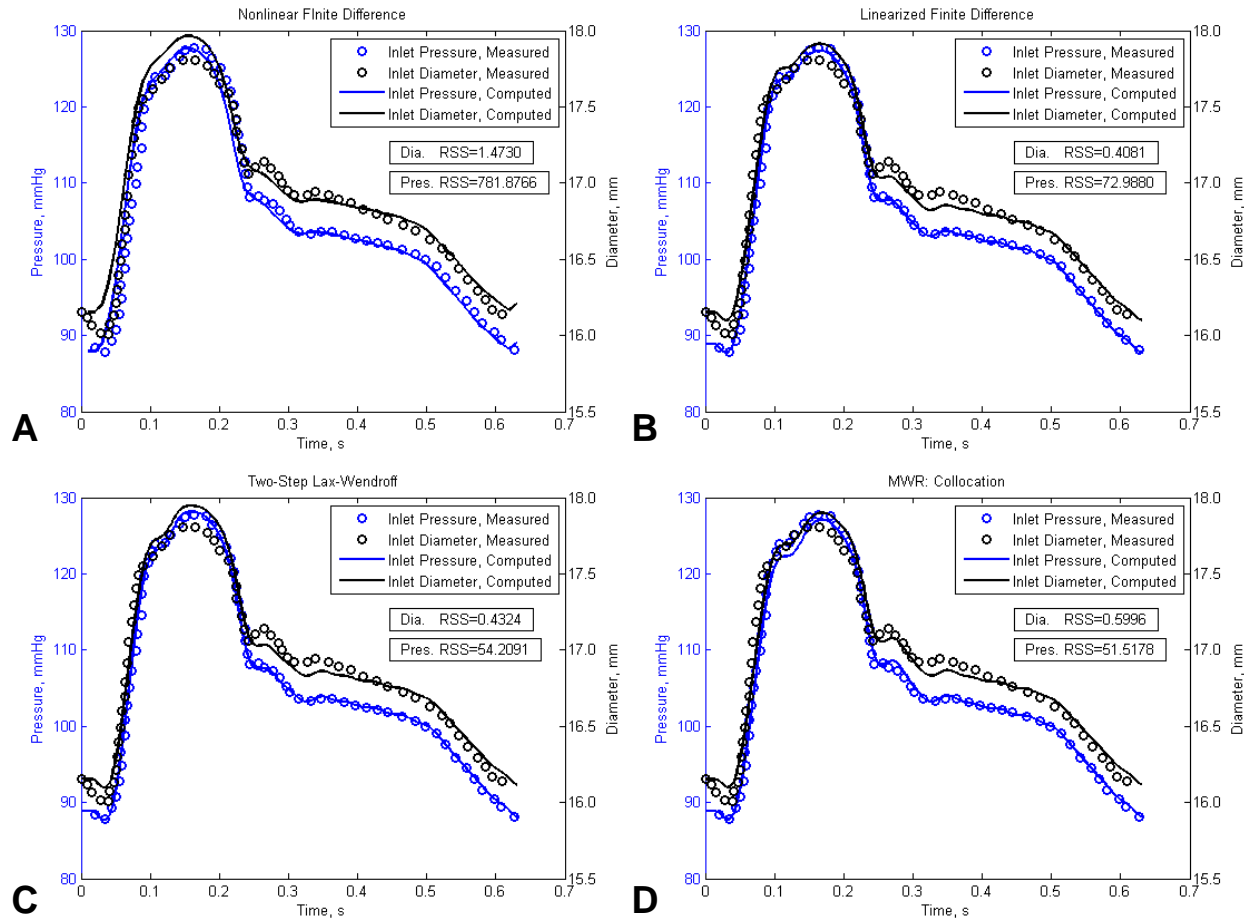


Figure 45 Validation of numerical methods against measurements from the canine aorta. An inlet pressure wave collected from *in vivo* measurements was applied to a single straight distensible vessel and wall displacement was computed using the **A.** nonlinear and **B.** linear finite difference method, **C.** the two-step Lax Wendroff method, and **D.** the implicitly integrated collocation method..

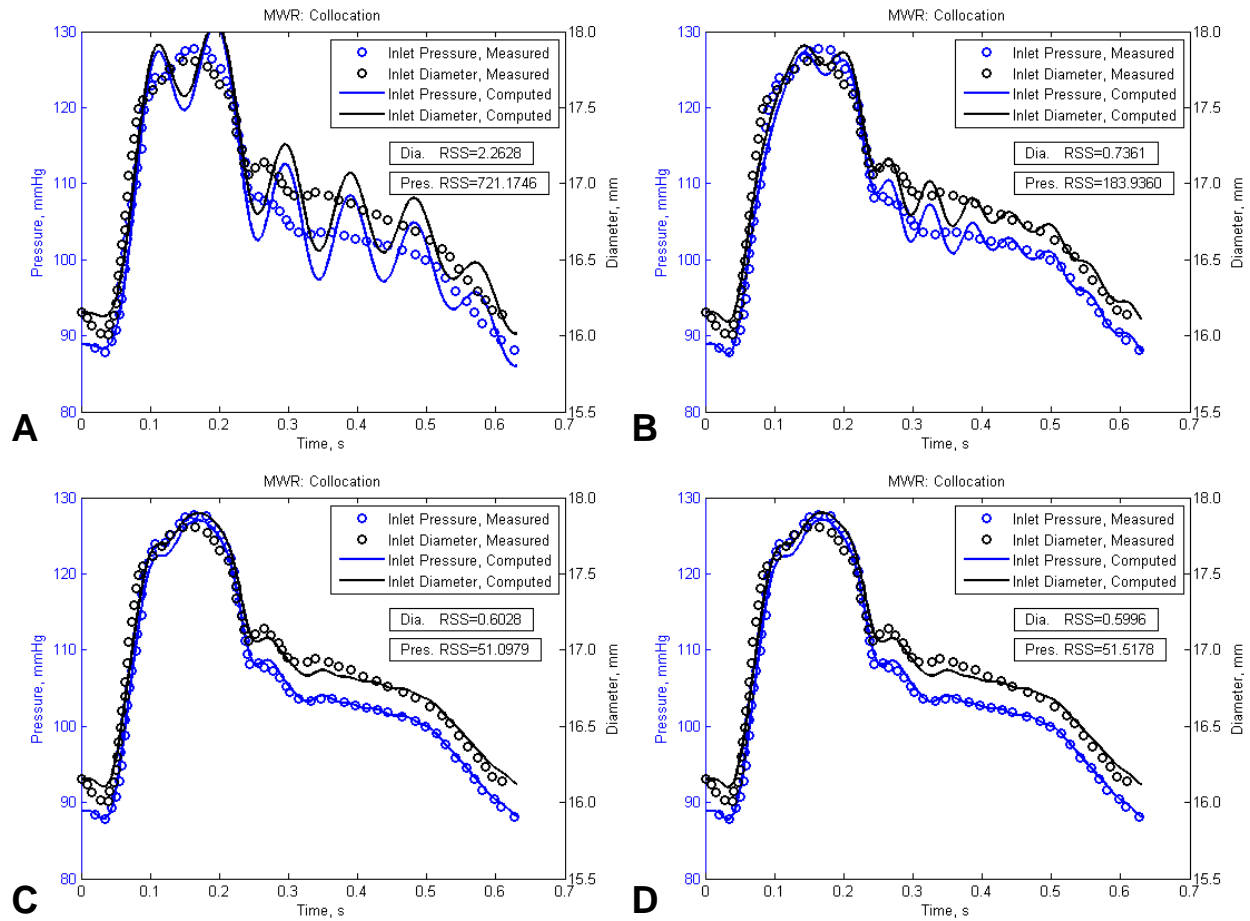


Figure 46 Effects of using consecutive splines with the collocation method using **A.** 1, **B.** 2, **C.** 5, and **D.** 10 segments. By increasing the number of 3rd order Lagrangian polynomials to represent the canine aorta, outlet boundary reflections were eliminated and the numerical simulation approached the measured values. No significant change in RSS was detected between 5 and 10 segments.

Integrator Comparison: Point Trajectories

In addition to comparing radius and pressure, flow matched well between the four different integrators described in Figure 47 which shows the comparison of the colored computed dynamic trajectories at the inlet (red), 5cm from the inlet (blue), 10cm from the inlet (green) and the outlet (black).

The collocation method, as shown in the third row, appears to have a slightly slower wave speed as shown by the slight increase in spread between trajectories. Conversely, the nonlinear one-step finite difference method, shown in the bottom row, shows a slightly faster wave speed as the trajectories are more closely packed together. However, this particular mode of result comparison does not allow for an in-depth realization of the differences between the methods.

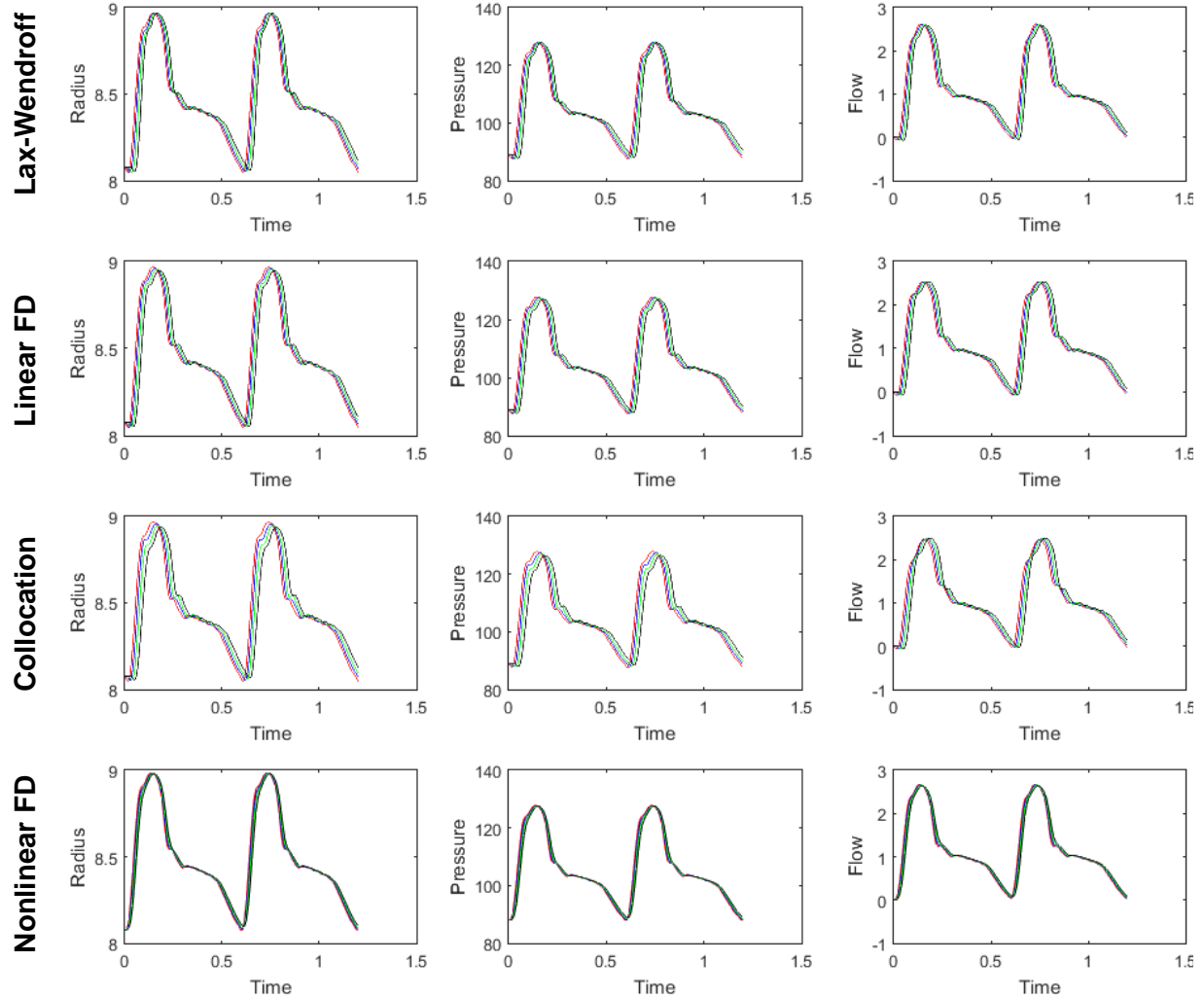


Figure 47 Dynamic oscillatory results of the four integrators at the proximal (red), 33% (blue), 66% (green), and distal segments (black) of a single vessel. Integrators are, from top row to bottom; Lax-Wendroff, Linear Finite Difference (FD), Collocation, Nonlinear FD. The spatial signal propagation is nearly immediate for the Nonlinear FD method as evidence by the lack of time lapse between the four colored lines. Similarly, the time lapse of signal propagation from inlet to outlet is longest when calculated by the Collocation method.

Integrator Comparison: Axial Profiles

The axial profile of the radius, pressure and flow across the entire vessel was determined at the inlet signal's peak base, $t=17.1\text{ms}$ (red), at the peak, $t=145.6\text{ms}$ (blue), at the secondary peak, $t=307.8\text{ms}$ (green), and at the valley at the end of the period, $t=614.0\text{ms}$ (black) as shown in Figure 48.

Small differences are detected between the profiles; at the vessel peak the collocation method predicts a lower outlet pressure than the other three methods, though it is unclear whether it is due to the signal not yet reaching the outlet or whether the vessel's axial profile is more rigid. Both the finite difference methods, linear and nonlinear, have a higher pressure and flow at the outlet node when the inlet signal reaches its peak.

Integrator Comparison: State Space Diagrams

The state-space diagram in Figure 49 clearly shows the phase lag between the three waves travelling through the vessel as predicted by each of the integrators. The collocation method predicts the largest pressure-flow state-space diagram while the nonlinear finite difference method describes the narrowest state-space diagram of the four integrators. Though the tube law contains both damping and longitudinal stress terms, the area-pressure state-space diagram is very narrow, to the point of almost being linear. A close-up as well as sensitivity study of the tube law is shown in Figure 50.

This sensitivity analysis shown in Figure 50 describes the relative effects that the longitudinal stress term, β , and the damping term, κ , have on the area-pressure state-space diagram. This analysis was performed on the Lax-Wendroff integrator only, and shows that the longitudinal stress term has little effect on the overall state-space diagram. The damping term has a more pronounced, though still small, effect on the phase lag between the area and pressure.

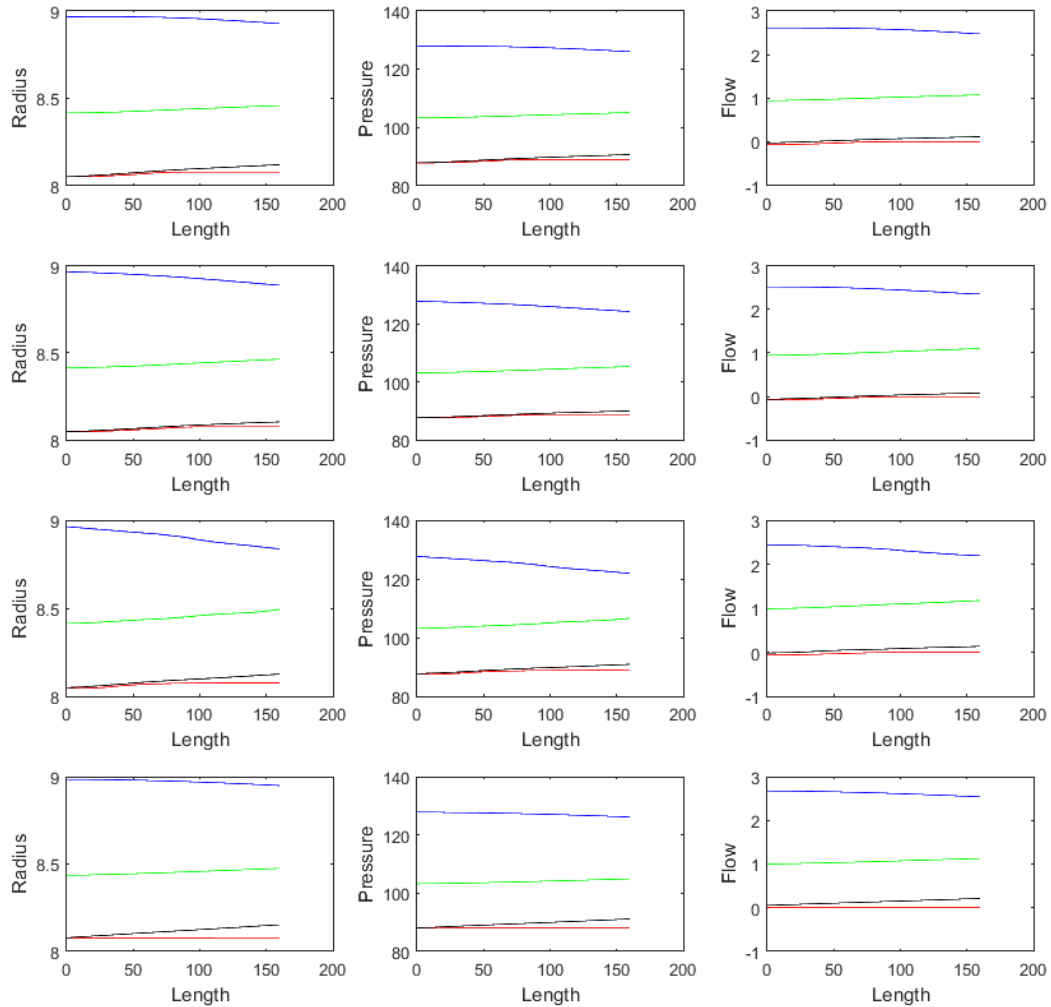


Figure 48 Dynamic oscillatory results of the four integrators at $t=17.1\text{ms}$ (red), $t=145.6\text{ms}$ (blue), $t=307.8\text{ms}$ (green), and $t=614.0\text{ms}$ (black) of a single vessel. Integrators are, from top row to bottom; Lax Wendroff, Linear Finite Difference, Collocation, Nonlinear Finite Difference. The axial profile of the Collocation method appears to be more rigid than the other three methods.

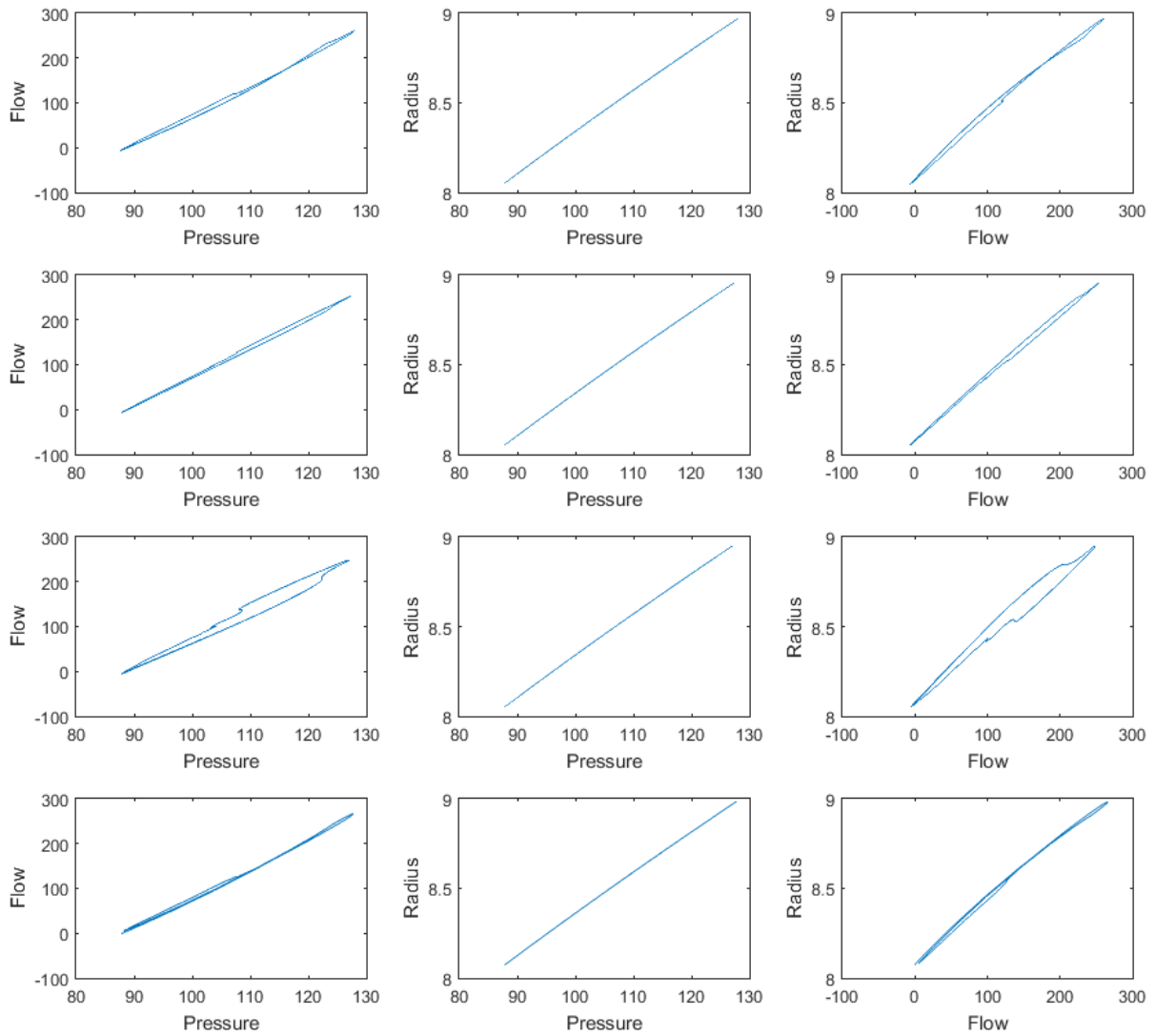


Figure 49 State space comparison of all four methods (Lax Wendroff, Linear Finite Difference, Collocation, Nonlinear Finite Difference) using the linear tube law.

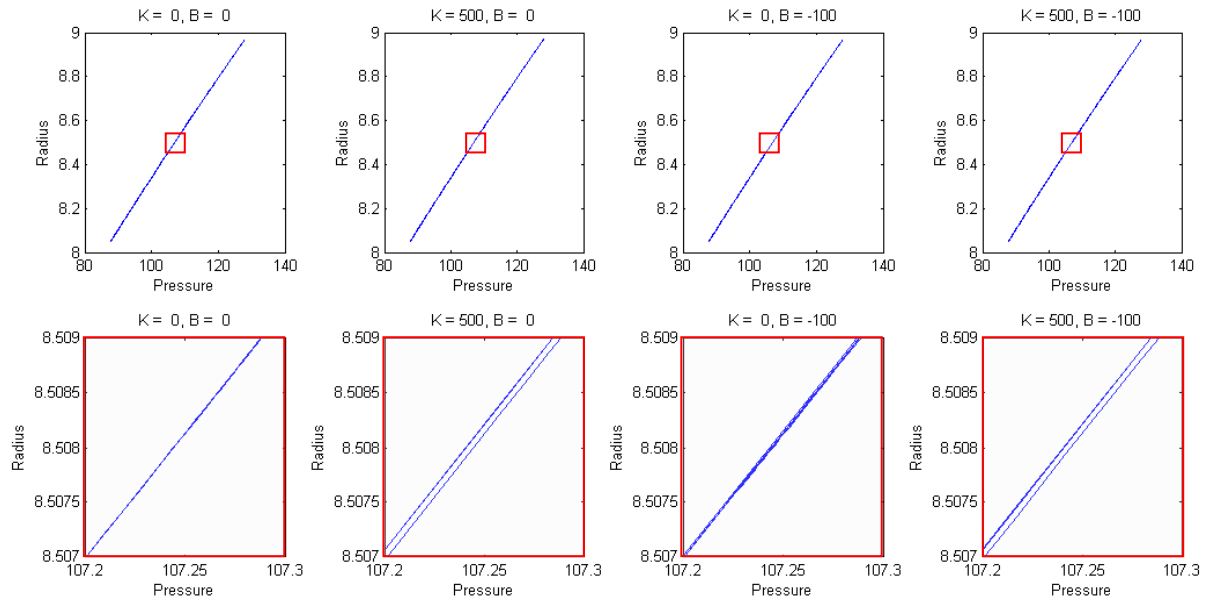


Figure 50 Sensitivity analysis of longitudinal stress, β , and damping term, κ , on the phase lag between the area and pressure, as shown in the state space diagram. The phase lag induced by the longitudinal stress term is small compared to the effects of the damping term.

The effects of employing the viscoelastic tube law are compared to the effects of using the longitudinal stress with damping tube law in Figure 51. This study show that the two tube laws produce very different results; the tube law of eq. 91, shown in column 1, gives a different radius-pressure state-space diagram than the tube law of eq. 90, shown in column 2. The phase lag between the area and pressure is much more sensitive to small changes to the τ_1 and τ_2 coefficients than the κ and β coefficients. The change in cross sectional area at comparable luminal blood pressure values demonstrates that the viscoelastic tube law is more sensitive to parametric changes than the longitudinal stress with damping tube law.

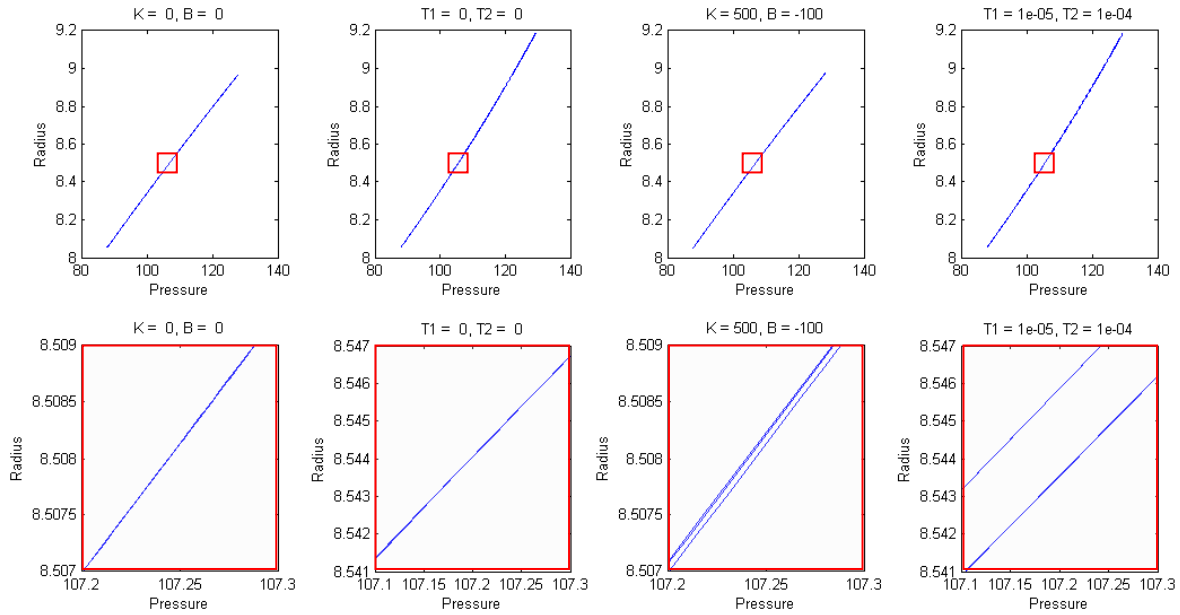


Figure 51 Comparison between damping and longitudinal stress model and viscoelastic model. A direct comparison is difficult as even the linear version of the two methods gives different results as shown in the first and second column. The pressure-radius state-space diagram is more sensitive to small changes in the viscoelastic parameters, τ_1 and τ_2 , than the damping and longitudinal stress coefficients, κ and β .

Bifurcation

The propagation of an oscillating pressure, area deformation, and flow signal was computed through an ovine (sheep) pulmonary arterial branch²⁷. The main arterial trunk, whose radius tapers from 10mm down to 9mm over a length of 6cm, has a small side branch 2cm from the inlet with a radius of 5mm which is 2.5cm long. The kinematic properties and fluid dynamic parameters of the problem are listed in Table XVII. The same blood fluid dynamic values of density and viscosity shown in Table XVI were used in the case study as well.

This bifurcation was only solved using the Collocation method and the Lax-Wendroff approach. Both the linear and nonlinear implicit finite difference approaches were dropped due to their long computational time which is discussed in more detail in the discussion section. The dynamic area, pressure and flow signal is compared between the Lax-Wendroff method, the Collocation approach and a Discontinuous Galerkin method employing a quasilinear viscoelastic tube law²⁷, QLV, at the proximal end of the parent vessel and main trunk daughter branch in Figure 52. This QLV model was not implemented; rather results from an implementation provided in the literature²⁷ were obtained for the purpose of comparison.

Table XVII Sheep Pulmonary Artery Case Study Parameters

Human Pulmonary Art.	Property	Symbol	Value	Unit	Reference
	Vessel Wall Young's Modulus	E_L	700	mmHg	²⁷
	Vessel Wall Thickness	h	1	mm	--
	Feeding Artery Proximal Radius	$R_{1,p}^0$	10.0	mm	²⁷
	Feeding Artery Distal Radius	$R_{1,d}^0$	9.7	mm	²⁷
	Feeding Artery Vessel Length	L_1	2.0	cm	²⁷
	Main Trunk Branch Proximal Radius	$R_{2,p}^0$	9.7	mm	²⁷
	Right Daughter Branch Distal Radius	$R_{2,d}^0$	9.0	mm	²⁷
	Right Daughter Branch Length	L_2	2.5	cm	²⁷
	Left Daughter Branch Proximal Radius	$R_{3,p}^0$	5.0	mm	²⁷
	Left Daughter Branch Distal Radius	$R_{3,d}^0$	4.0	mm	²⁷
	Left Daughter Branch Length	L_3	2.50	cm	²⁷
	Viscoelastic Damping Coefficient	κ	500	kg/m ³ /s	--
	Longitudinal Stress Coefficient	β	-100	kg/m/s ²	--
	Primary Outlet Resistance	R_1	20	MPa·s/m ³	--
	Secondary Outlet Resistance	R_2	1	kPa·s/m ³	--
	Outlet Compliance	C	1	cm ³ /Pa	--

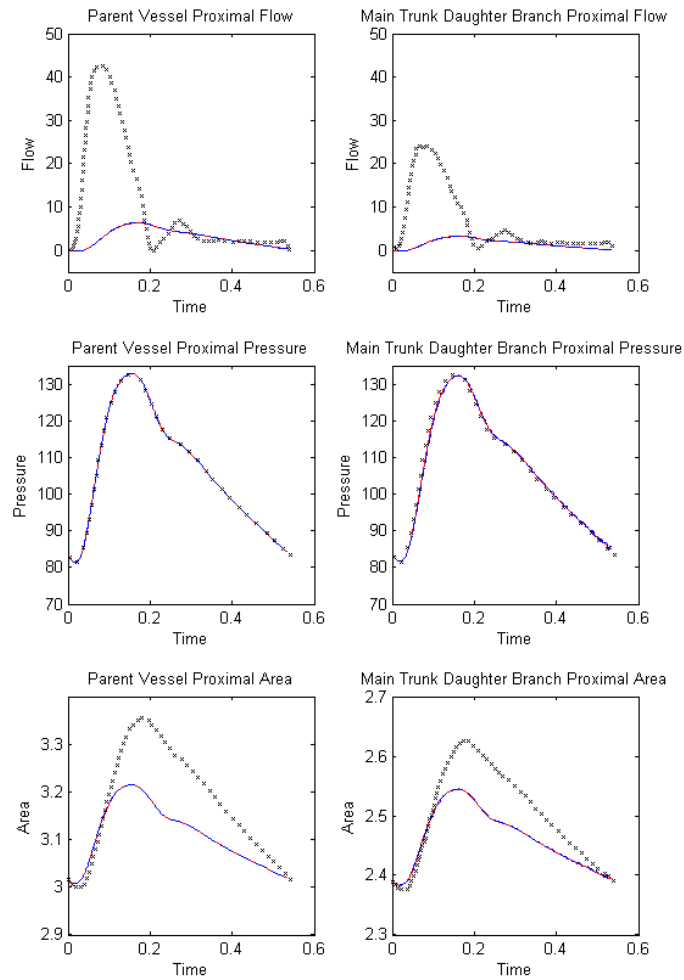


Figure 52 Dynamic trajectory of area, pressure, and flow at the proximal ends of the parent vessel and the main trunk bifurcation in the ovine arterial pulmonary bifurcation as computed by both the Lax-Wendroff (red) and Collocation (blue) method, compared to a QLV model²⁷. As the flow does not match between the methods presented in this report and computational results provided in the literature²⁷, a mass conservation analysis was undertaken as shown in Figure 53.

The wall displacement of the main trunk daughter branch smaller compared with the parent vessel and the pressure decrease slightly. Flow evenly splits between daughter branches, however the smaller side branch is not shown as no results from the implementation of QLV model were provided in the literature²⁷.

The Collocation method and the Lax-Wendroff method match each other with no significant deviation. However, the difference between these methods and the QLV model differ significantly. The difference in wall movement and flow predictions between the Collocation and Lax-Wendroff method and the QLV model may be possibly be due to differences in the material property, numerical integrator, or the use of an alternative momentum equation that incorporate the profile function of blood.

A mass conservation analysis shown in Figure 53 demonstrates that the results computed by the Lax-Wendroff method satisfy mass conservation for each vessel. The top row depicts the mass conservation at the proximal end of each vessel with a $dx=0.25\text{mm}$.

However, a similar analysis cannot be performed for the results of the QLV model, as only results are reported for the proximal and distal node of the parent vessel only. Analyzing the mass balance using the dynamic trajectory of flow at the proximal and distal node of the parent vessel and the change in area at the proximal node, as shown in the bottom row of Figure 53, indicates that an analysis with incomplete data would lead to misleading results.

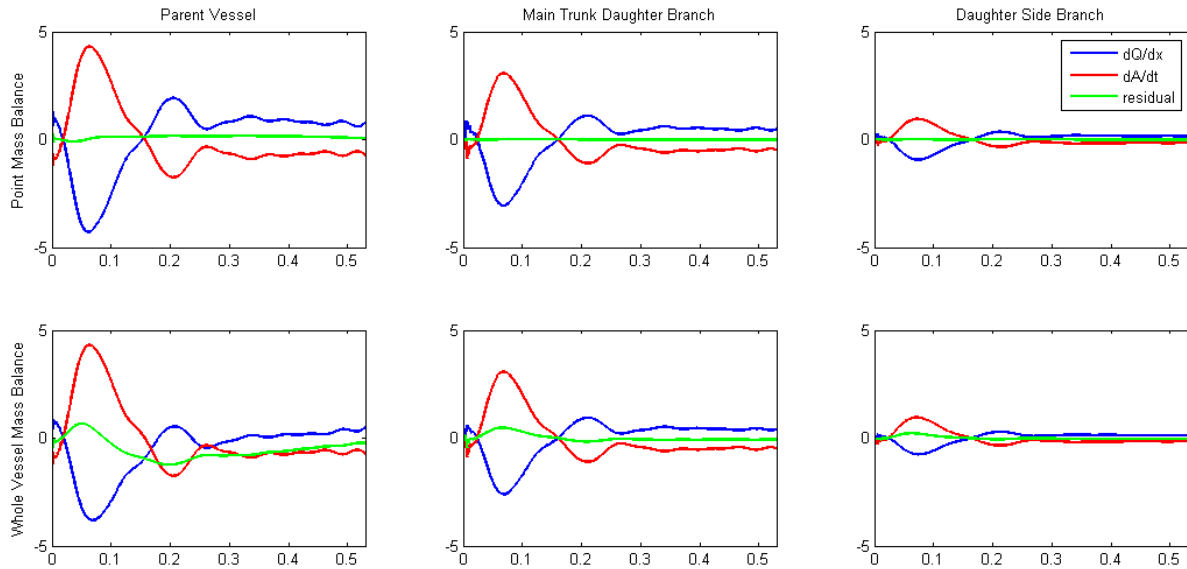


Figure 53 Mass Conservation of sheep pulmonary artery bifurcation as computed by the Lax-Wendroff method for the parent vessel, the main trunk daughter branch, and the smaller side branch. Analysis of a small vessel section with a $dx=0.25\text{mm}$ shows residual below numerical error, the green line, for each branch. However, extending the balance envelope to the entire vessel for the computation of Q while restricting the wall deformation measurement to either the proximal or distal node, as shown in the bottom row, results in a misleading analysis.

Network Simulations

The linear and nonlinear implicit one-step finite difference methods were dropped as a possible method for simulating bifurcations due to the low match between simulated values and recorded values in the single vessel case study. The nonlinear finite difference method also proved to be computationally infeasible based on its performance in the single vessel case study, with a simulation time more than twenty times longer than the competing methods. The linearized finite difference method was dropped from further analysis as its simulation time was also considerably longer than the Collocation or Lax-Wendroff method; simulation times ran for nearly ten times longer (results not shown).

As shown by the state-space diagrams for the single vessel case study, the results computed by the Collocation method and the Lax-Wendroff method do differ slightly. However, when compared against empirical data, both methods match the physiological measurements closely. Unlike the Collocation method, the Lax-Wendroff approach does not require the inversion of a matrix to solve each time step, and the solution of the dynamic state for each vessel at each time step is calculated algebraically.

Additionally, though the collocation method only requires solving a fraction of the elements needed for the single vessel as Lax-Wendroff method does (5 3rd order polynomials versus 50 finite difference elements), this may prove to be a disadvantage in the network simulations. Network structures of the vasculature, especially in the brain, are composed of many small segments to capture the tortuous vessel path. These segments may be small enough to be represented by a single finite difference element, but will still need to be represented by at least a single 3rd order polynomial for the Collocation method. This may artificially increase the number of elements needed to represent a network beyond what is needed to solve the same problem using the Lax-Wendroff method. The Lax-Wendroff method is therefore recommended as the method of choice for solving the distensible vessel problem on larger vascular networks.

The linear elastic model tube law was implemented to compute the vessel distension as a result of changes in lumen blood pressure.

Simplified Microvessel Network

A simplified cerebral microcirculation is proposed as shown in Figure 54. This single inlet single outlet microvessel network consists of a penetrating arteriole feeding a capillary bed which is then drained by a solitary ascending venule. The capillary bed consists of three bifurcations and three unions. Overall, the network has over six hundred vessels whose physiologic and hemodynamic properties can be found in the table embedded in Figure 54. The properties of the RCR outlet boundary conditions are the same as described in Table XVII.

Dynamic Results

Employing the Lax-Wendroff integrator, the blood pressure, velocity and lumen diameter was computed for every time step in response to an applied pressure signal (period = 0.6s) at the inlet of the penetrating arteriole. The system is initialized with velocity equal to zero and pressure equal to the extravascular lumen pressure ($P_{ex} = 88.86\text{mmHg}$) everywhere with a resting lumen diameter $16.15\mu\text{m}$ and harmonic steady state is reached by the fifth period. Repeated application of the input signal does not change the oscillatory fluctuations of the pressure after 3.0s as shown in Figure 55.

Property	Value
Blood Viscosity	3.5 g/m/s
Blood Density	1050 kg/m ³
Vessel Wall Young's Modulus	360 kPa
Vessel Lumen Diameter	16.15µm
Average Vessel Length	2.4±0.5µm
Vessel Wall Thickness	1µm
Number of Segments	608

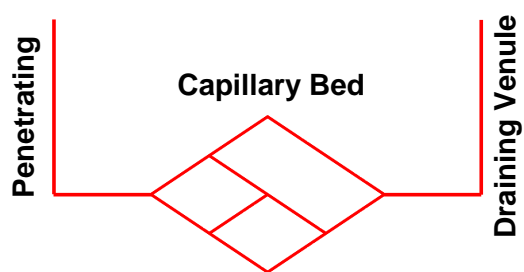


Figure 54 Simulation parameters and network properties of microvessel network. This cerebral microcirculatory single inlet / single outlet network model consists of a penetrating arteriole (left) a draining venule (right) and an interconnected capillary bed in the middle.

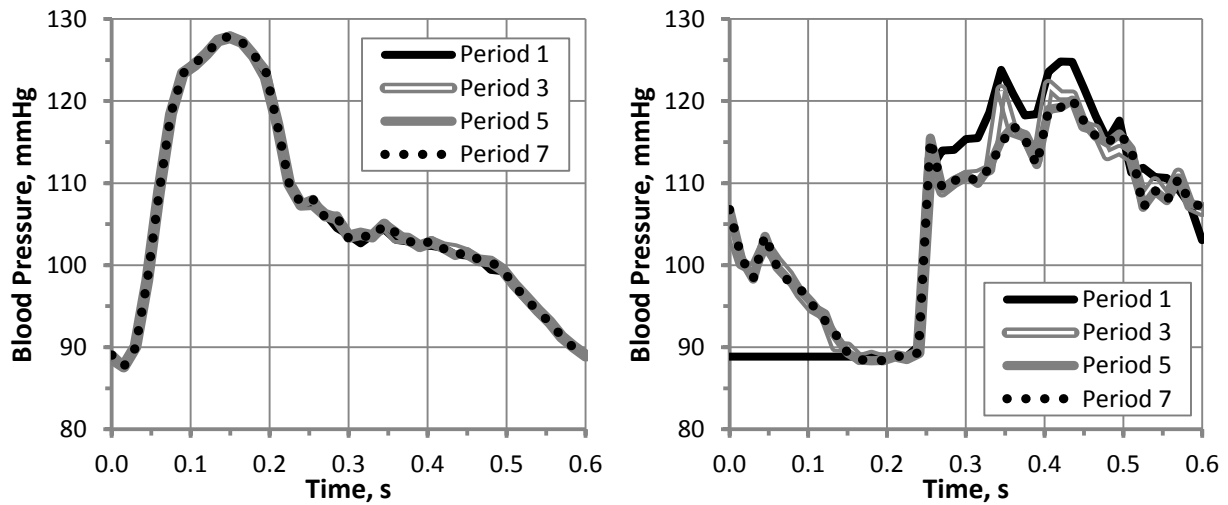


Figure 55 Harmonic steady state analysis of oscillatory signal in microcirculatory network. Blood pressure signal at **A.** penetrating arteriole inlet and **B.** descending venule outlet were compared for period 1, 3, 5 and 7. The blood pressure signals for periods 5 and 7 overlap for both the arteriole inlet and venule outlet, indicating that harmonic steady state is achieved by period 5. As each period is 0.6s, harmonic steady state is achieved at $t=3.0s$.

Dynamic blood pressure, velocity and percent lumen cross sectional area change was recorded at four key points in the microcirculatory structure as shown in Figure 56 starting at $t=3.6$, after harmonic steady-state is achieved.

Signals were recorded at the deep pre-capillary arteriole, Figure 56A, the post-arteriole and pre-venule vessels of the capillary bed, Figure 56A-B, and in the descending venule, Figure 56D. Though the peak to peak distance between each pressure signal does not change, the slope of the signal decay is steeper in the venules than in the arterioles. This increase in slope in signal decay in the descending venules is observed in the percent change in lumen cross sectional area as well. Amplitude of the blood velocity signal decreases in the capillary bed, which is expected following a bifurcation where the diameters of the daughter branches are equal to the parent branch. The blood velocity magnitude increases slightly in the descending venule and no longer exhibits high negative backflow as demonstrated in the penetrating arteriole.

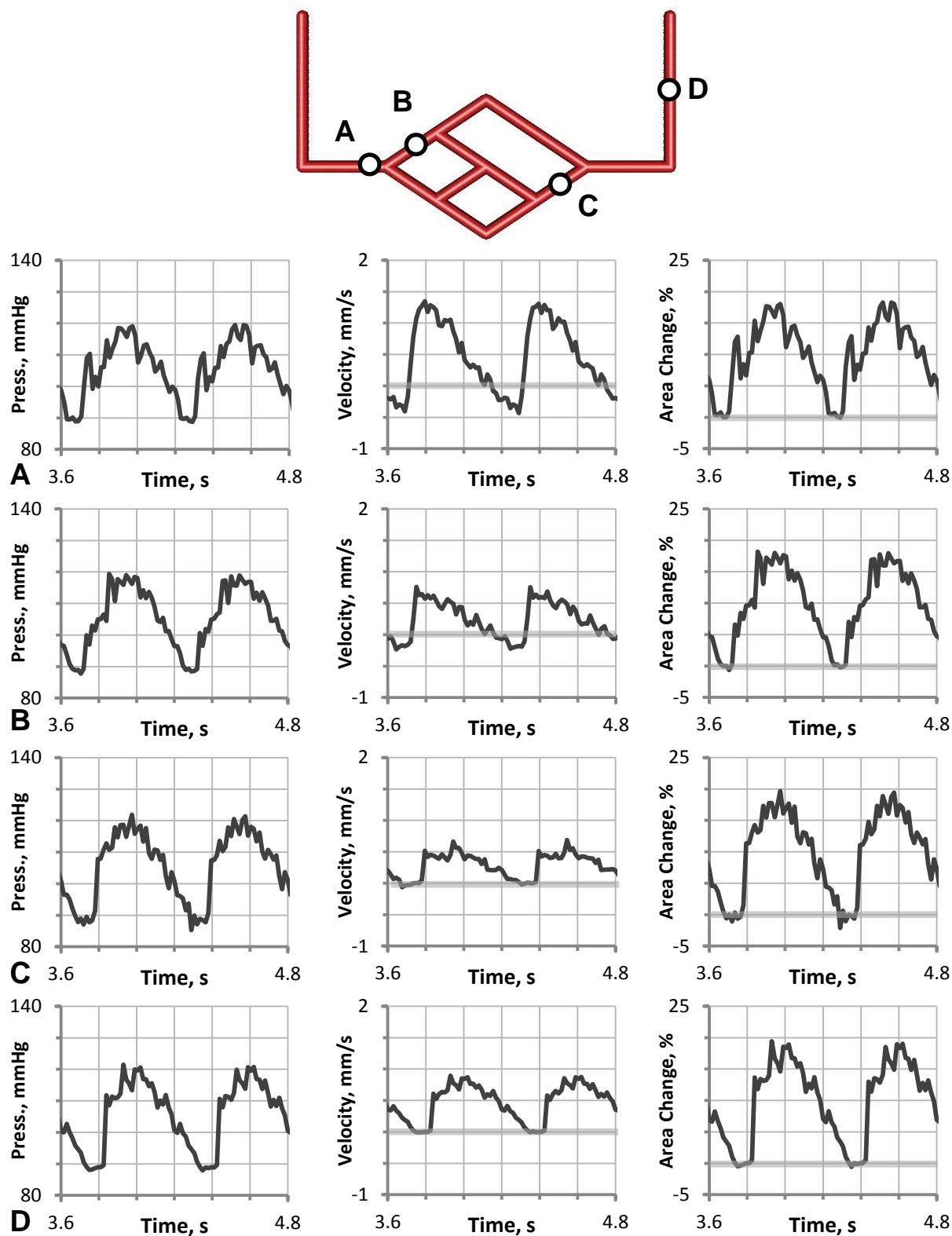


Figure 56 Dynamic blood pressure, velocity and percent change in cross sectional area at **A**. The deep penetrating pre-capillary arterioles, **B**, post-arteriole and **C**, pre-venule capillaries and **D**, the ascending venules. Gray bar in velocity and area plots indicates value of zero.

The spatial distribution of blood pressure at different time points is shown in Figure 57. At $t=3.6s$, the increase blood pressure from the previous period is still lingering in the ascending venule as shown in Figure 57A. As the pressure peak from the new period enters the penetrating arteriole, the ascending venule has returned to the resting exterior lumen pressure of $P_{ex} = 88.86\text{mmHg}$. As the peak of the pressure signal enters into the capillary bed by $t=3.90s$, there is some recirculation and backflow. This jagged signal is observed in Figure 57B-C. The peak of the pressure signal leaves the system by $t=4.20s$ as shown in Figure 57D and the new period begins as shown in Figure 57E. The relationship between the overall length of the microcirculatory system and the period of the input signal is such that one or zero signal peaks are present within the network at a time.

Validation of Continuously Differentiable Signal

The results shown in Figure 56 demonstrate jagged peaks and valleys for blood pressure, velocity and cross sectional area. These irregular peaks may be the product of signal reflection at bifurcations or recirculation in the capillary bed. However, these spikes may be artifacts introduced by the explicit Lax-Wendroff solver. To clarify whether the jaggedness of the results shown in Figure 56 are meaningful physiological results or integrator numerical errors, the shape of the signal was investigated in detail as shown in Figure 58.

Figure 58A depicts a signal spike at $t=0.25s$ which may be a real hemodynamic peak in blood pressure, or may be an integrator artifact. As the time step for the explicit Lax-Wendroff integration is very small ($\Delta t=150\mu s$) a filter was applied when recording time steps. By escalating the sampling rate of the filter and thereby heightening the signal resolution, as shown in Figure 58B, it is clear that the signal around the spike at $t=0.25s$ is continuously differentiable and therefore not a numerical artifact of the explicit integrator.

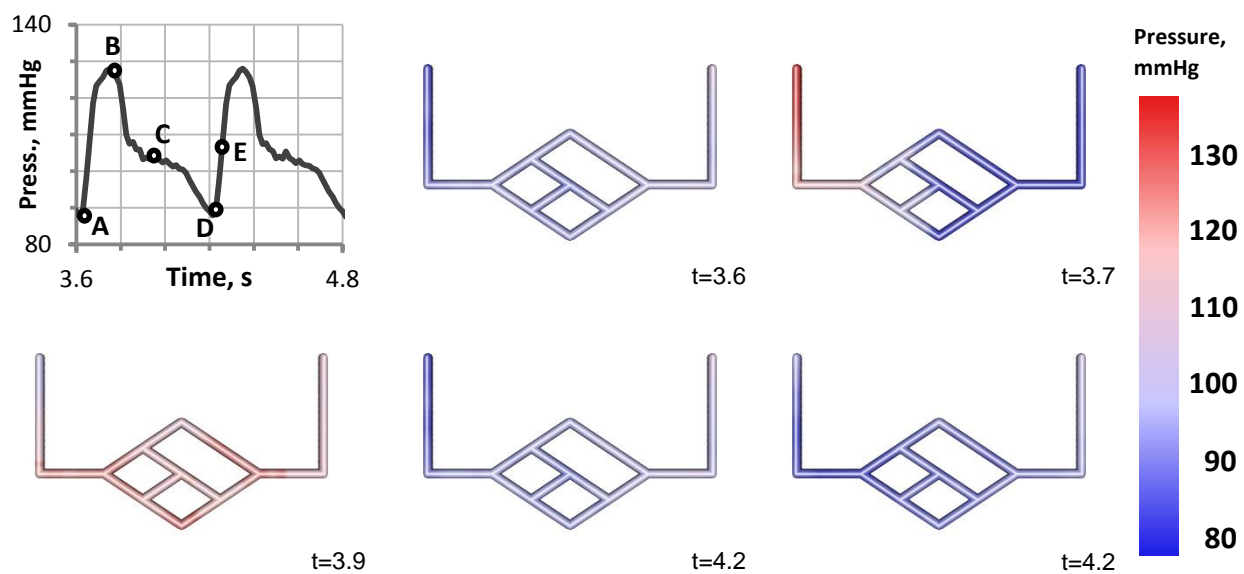


Figure 57 The dynamic blood pressure distribution in a small microcirculatory test network. Blood pressure throughout the test network was visualized at different time points as indicated by the empty circles on the input pressure signal shown in the top left corner. Blood pressure is shown from 130mmHg (red) to 80mmHg (blue) at each time point.

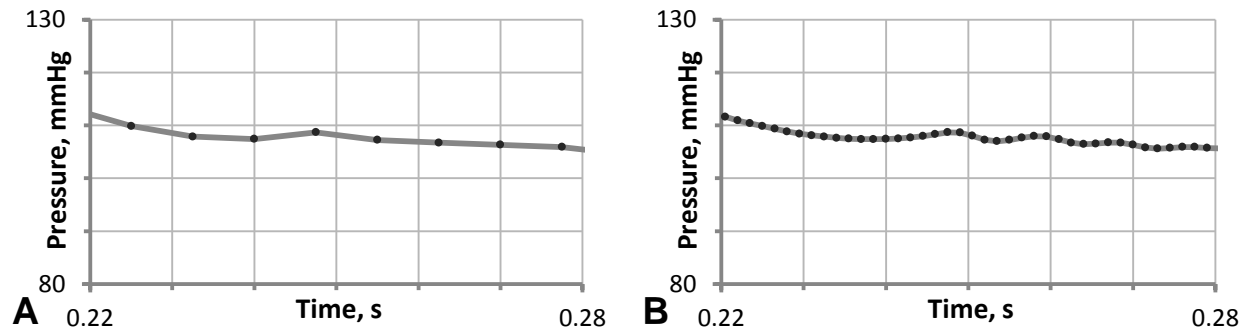


Figure 58 Investigation of signal smoothness at different sampling rates. **A.** At the coarse signal sampling rate of $\Delta t = 7.5\text{ms}$, it is unclear whether the peak at $t = 0.25\text{s}$ is real or an integrator artifact. Black dots indicate the actual data points extracted from the results of the Lax-Wendroff integration. **B.** A higher resolution sampling rate of $\Delta t = 1.5\text{ms}$ clarifies that the signal around this peak is continuously differentiable and smooth.

Discussion

This report compares the predictions of four separate numerical integrators for solving the distensible vessel problem; an Implicit Nonlinear One-Step Finite Difference method, an Implicit Linear One-Step Finite Difference method, the Two-Step Lax-Wendroff scheme, and the Collocation Method of Weighted Residuals. Each numerical integrator was tested on a single vessel case study of the canine aorta, and then only the Lax-Wendroff and Collocation method were compared for the bifurcation case study in the sheep arterial pulmonary branch.

Comparison of the performance of these four integrators when compared to measured results and the computational cost for each, the Lax-Wendroff method was determined to be the most accurate and efficient of the four methods. While both the Lax-Wendroff and Collocation MWR computed similar results in the canine aorta case study, the Collocation method is limited by matrix inversion, which is prohibitive in larger microcirculatory systems.

Simulation of the FSI problem was performed on a simplified cerebral microcirculation network. Analysis of the network simulation revealed a jagged dynamic blood pressure, velocity and cross sectional area profile at select vessels within the microcirculatory network. In this section, the effects of bifurcations are analyzed as a possible cause for these signal spikes. In addition, an open loop control mechanism is proposed as a possible model for blood flow distribution following a neuronal firing event.

Phase Lag between Pressure and Flow

In the single vessel case study, there was no appreciable lag between the pressure signal and the flow signal. Additionally, pressure, velocity and area signals in the network model are characterized by sharp peaks and valleys which are absent in the single vessel studies. Though these sharp peaks are shown to be differentiable in Figure 58, their presence remains unexplained. These jagged peaks may be due to signal reflections at the bifurcations. Though there has been much discussion over how the flow signal precedes the oscillatory pressure

signal^{17,29-30}, the pressure signal seemed to precede the flow signal in the single vessel model when the pressure signal was used as an input, as the flow field only arises from the pressure gradient in the momentum equation. This displacement between the pressure and flow signal in the daughter branch may lead to small accumulations in either pressure or velocity and create sharper gradients between adjacent vessels. Even though these systems reach harmonic equilibrium, these micro-gradients may persist, resulting in the jagged signals observed in the network models.

Determining Outlet RCR Parameters

For the network simulation, an alternate approach proposed by Alastruey et al. was undertaken to systematically compute the parameters of the outlet RCR circuit⁴⁵. This method specified setting the value of R_1 equivalent to the characteristic impedance of the terminal branch, Z_0 , which relies on the wave speed, c_0 . The derivative of cross sectional area to pressure at the terminal vessel was determined numerically from the inelastic tube law. Using this approach, the R_1 value was set to $3.71 \times \text{MPa} \cdot \text{s} \cdot \text{m}^{-3}$.

$$Z_0 = \frac{\rho c_0}{A_0} \qquad c_0 = \frac{1}{\sqrt{\frac{\rho}{A_0} \frac{dA}{dp}}}$$

In the approach described in Alastruey, the R_2 parameter was utilized to distribute flow accordingly between different outlets. As the network simulation presented here has only a single outlet, this term was assumed to be zero. The parameter C was assigned using the value prescribed in the paper of $9.45 \text{ mm}^3/\text{Pa}$. These new outlet boundary conditions resulted in a comparably small R_f of -0.079 at the terminal outlet to the system chosen by manual optimization, -0.013. Because the systematic approach performed comparably while avoiding the

arduous task of manual optimization, it is recommended that this approach be used to determine the parameters of the RCR circuit in future dynamic studies of the microvasculature.

Blood Flow Control

One of the most important functions of the cerebral vasculature is the dynamic redirection of blood flow following a change in the metabolic requirements of the brain. It is this change in blood flow, combined with a change in metabolic demand from the surrounding tissue that leads to the BOLD signal in fMRI. The ability of the cortical circulation to selectively supply choice sub-regions of the cortex is a critical function of the microcirculation.

Blood flow, pressure, velocity and cross sectional area were all computed following a closed-loop vasodilation event in the simplified network model presented in the Results. Analyzing the hemodynamic response to a vasodilation event requires a period averaging scheme to accurately assess whether blood flow, has changed meaningfully in response to a vessel caliber control event. The harmonic blood flow signal in a select vessel is shown in gray lines in Figure 60 with the corresponding period averaged values overlaid in black. Each blood flow signal is computed in response to an increase in the penetrating arterial input pressure, from the baseline signal (+0) to +30mmHg.

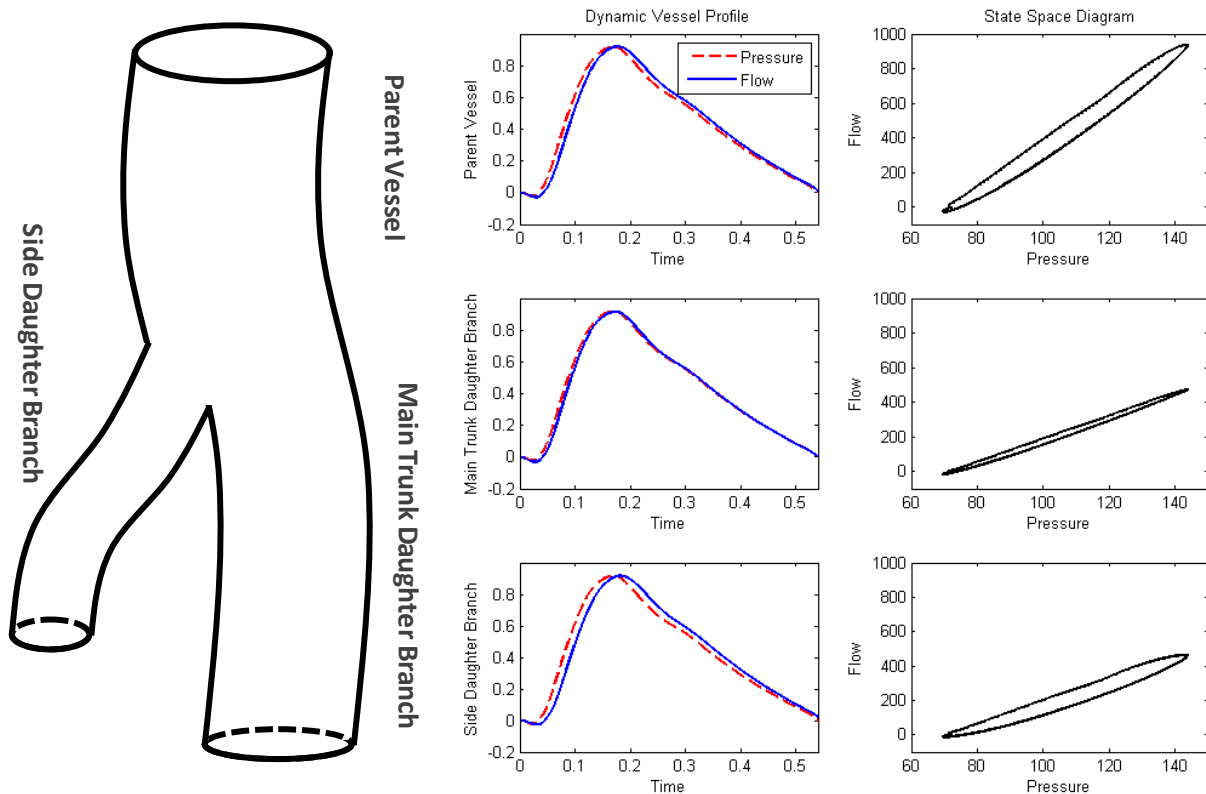


Figure 59 The effects of vessel bifurcation on phase lag between the pressure and flow signal and accompanying state space diagrams. In the parent vessel, the flow wave follows the pressure wave slightly. In the main trunk daughter branch, the phase lag between the flow and pressure signals is decreased, while in the side branch the phase lag is increased. This alignment in phase in the main trunk daughter branch is due to the similar area of the two vessels ($d=10\text{mm}$ in the parent vessel, $d=9\text{mm}$ in the daughter branch) that allows for the pressure signal to be passed through with little reflection while the flow signal is slightly reflected by the decreased change in flow. In the side daughter branch, the flow signal is reflected similarly to its sister branch, however the pressure wave is slowed down significantly more due to the large change in area ($d=10\text{mm}$ in the parent vessel, $d=5\text{mm}$ in the side branch).

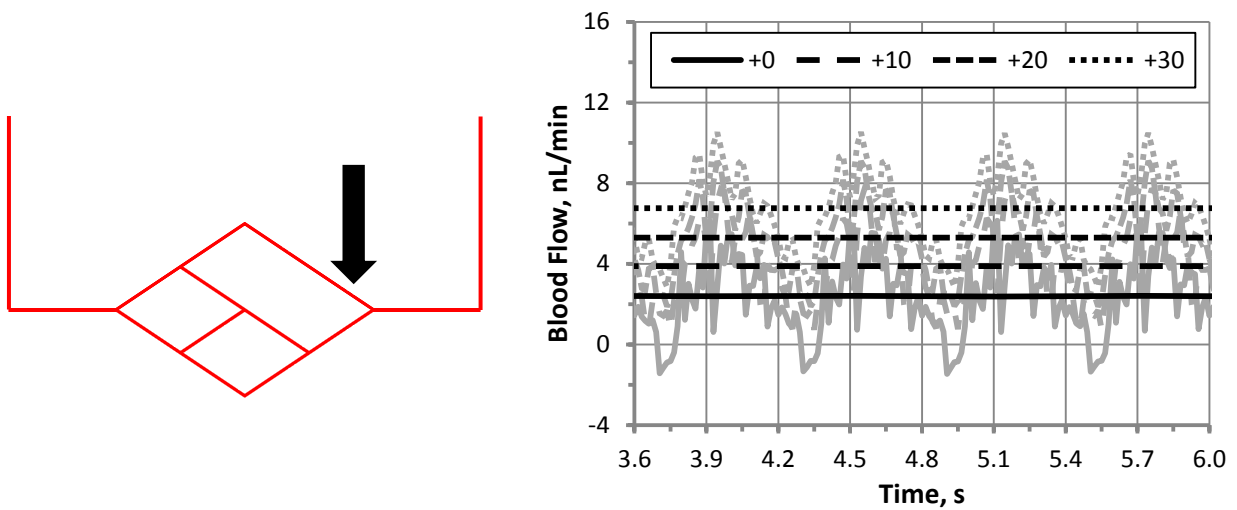


Figure 60 Four different blood flow signals in the upper branch of the cerebral microcirculation capillary bed indicated by the arrow as shown in the left panel. Each blood flow signal shown in gray is computed in response to a pressure input signal with an offset between +0 to +30mmHg in 10mmHg increments. The period averaged signal is shown in black lines for each flow signal. Flow increases by 4.37nL/min from 2.39 to 6.76nL/min in response to a 30mmHg increase in penetrating arterial input pressure.

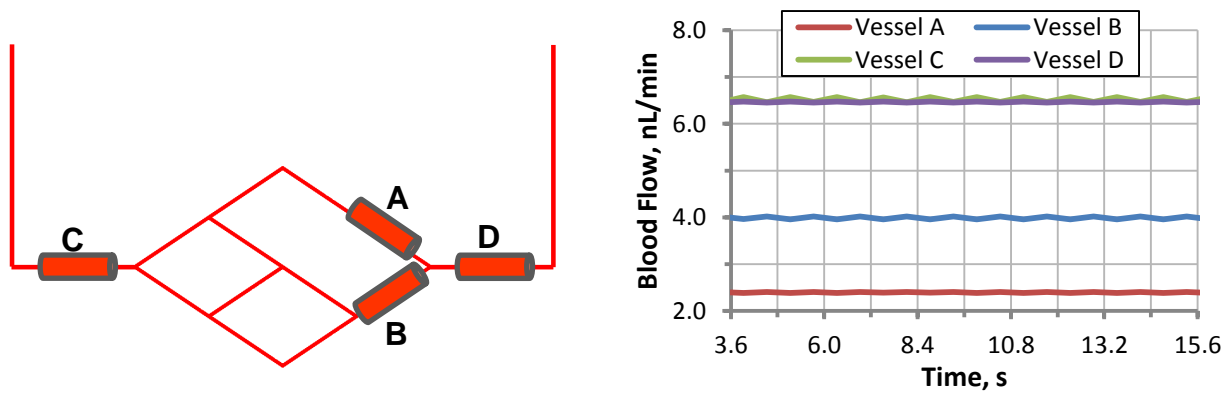


Figure 61 Fluctuations in period averaged flow measurements in four select vessels. The average blood flow through a vessel for a period may fluctuate from period to period at harmonic steady state. Average blood flow values have a two period cycle at harmonic steady state in these four select vessels. Mass is conserved between the arteriole inlet vessel C (6.46nL/min) and the venous outlet vessel D (6.46nL/min), as well as at the union of the upper capillary A (2.46nL/min) and the lower capillary B (4.00nL/min).

Even though the system has reached harmonic equilibrium, as demonstrated in Figure 55, the period averaged flow is not consistent from period to period. As demonstrated in Figure 61, the average blood flow has a cycle of two periods that it oscillates between. This pattern is exhibited in multiple vessels in the simplified microcirculatory system. These fluctuations of periodic blood flow averages are less in vessels that are farther away from the penetrating arteriole.

Open-loop control was implemented as a step function widening the resting lumen caliber, A_0 , at $t=6s$. The site of control is a single capillary indicated by the black arrow, its cross sectional area was increased by 10% (resting diameter = $16\mu m$). The resulting change in period averaged blood flow is shown in Figure 62 in the downstream capillary, sister vessel, feeding arteriole and draining venule. This change was measured in response to a 10%, 20% and 30% increase in A_0 . As the resting state cross sectional area of the capillary widens, blood flow through the downstream vessel initially decreases then climbs steadily to the new harmonic steady state level. Conversely, flow through the sister vessel in lower half of the capillary bed immediately increases and then drops steadily. Both the feeding arteriole and the draining venule experience perturbations less than 0.25nL/min and then resume to harmonic steady values prior to the step increase in A_0 . The period to period fluctuations in average blood flow do decrease after the control event.

The phenomenon of an initial decrease in blood flow in following a vasodilation event would not be observable in a rigid vessel model. Blood flow in non-distensible network models following a vasodilation open-loop control event establish to a new blood flow immediately. As this dynamic effect is lost, the blood flow signals produced here have not yet been observed in microvessel hemodynamic models.

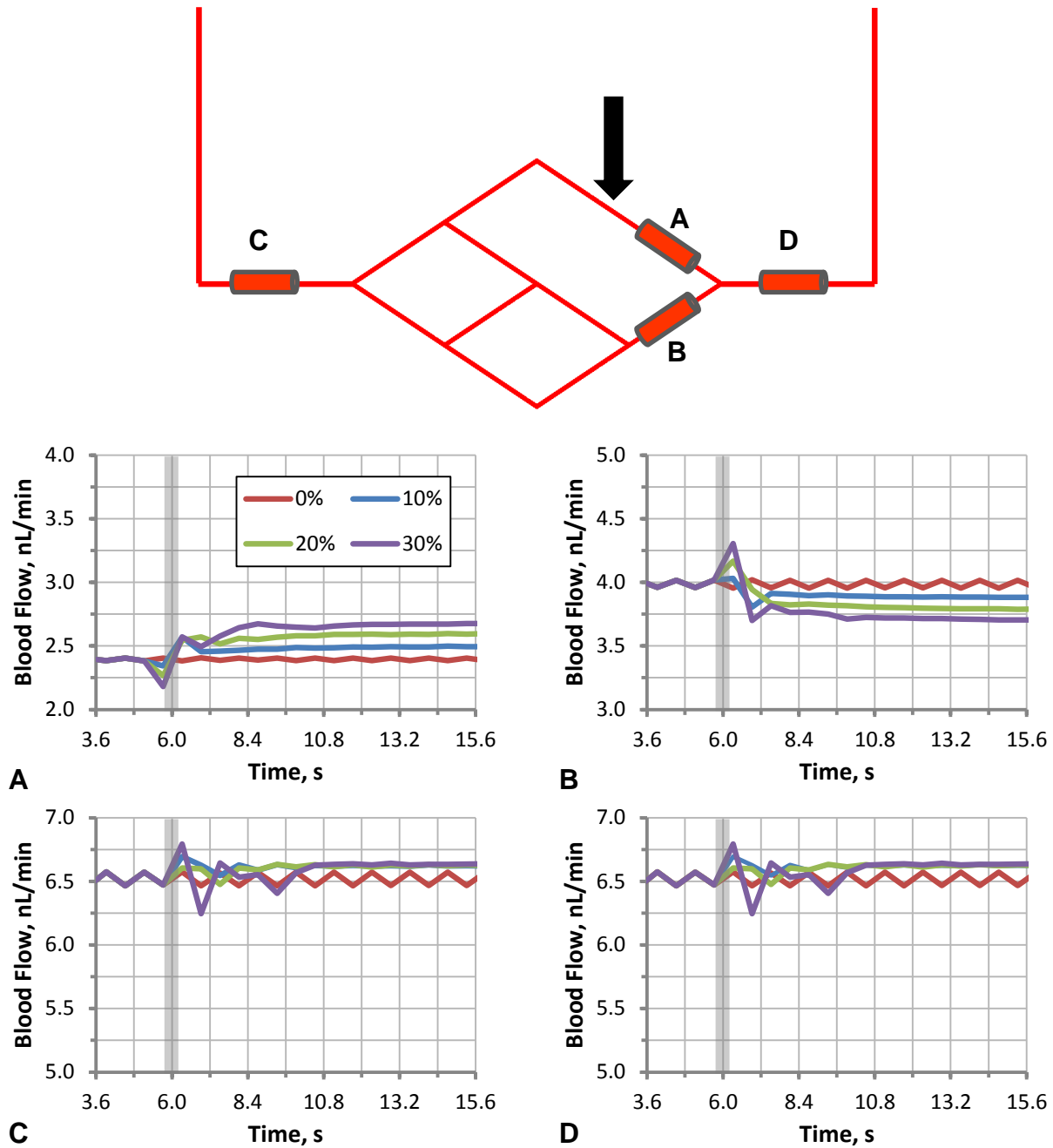


Figure 62 Dynamic blood flow response to an open-loop vasodilation event in the capillary bed at $t=6.0$ s. Dilation of a capillary in the upper half of the capillary bed, shown by the black arrow, affects the dynamic blood in **A**. downstream vessels, **B**. the lower half of the capillary bed, **C**. the pre-capillary feeding arteriole, and **D**. the post-capillary draining venule. Blood flow in the downstream vessel increases in response to the widening vessel, while blood flow correspondingly drops in the sister vessel in the lower half of the capillary bed. Period to period fluctuations are flattened by the Arteriole inflow and venule outflow are unaffected

Future Work

Currently, the parameters for these open-loop control mechanisms are not validated against physiologically measured data. This work has demonstrated the robustness of the two-step Lax-Wendroff integrator to compute FSI simulations over a distributed blood vessel network. The methodological validation presented here demonstrates that these simulated results can be meaningfully compared against a set of experimentally collected data. A study that compares simulated blood flow or area expansion to measured values in a distributed network could be used to predict measurements for blood pressure and velocity which are difficult to measure. Additionally, the modeling approach could be used to elucidate the sites of control in a distributed network. The work shown here only describes the effect on blood flow following a capillary expansion in a simplified network. However, the pial arteries, penetrating arterioles or pre-capillary arterioles are also potential sites for vasodilation to occur. By comparing vasodilation induced measured blood flow changes to a library of simulated responses in a more realistic network, the correct site of control can be identified. These simulated experiments may be instrumental in identifying the sites of control following functional activation, glial network stimulation, or injury leading to a significant contribution to better understanding cerebral hemodynamics.

Supplemental 1

Lax-Wendroff

The three equations describing the distensible vessel problem, the mass conservation of eq. 65, the second approach to the momentum balance in eq. 87, and the tube law of eq. 89, describe a quasi-linear first order hyperbolic system. The first two equations of this system, the mass conservation and momentum balance, can be written in the general form of hyperbolic partial differential equations described in eq. 101.

$$\frac{\partial u(x, t)}{\partial t} + \frac{\partial f(u(x, t))}{\partial x} = 0 \quad 114$$

The dynamic update of these equations can be written in the form of the two-step Richtmeyer-Morton Lax-Wendroff scheme¹⁸. This finite difference based numerical method for solving hyperbolic partial differential equations is second-order accurate in both space and time. The implementation of the Lax-Wendroff integrator for the distensible tube problem (including bifurcations and unions) is based off an understanding of the implementation proposed in Zagzoule⁹.

The simplicity of implementation is an attractive feature of this simple finite difference scheme. Even more so when one considers the strategy offered by the explicit formulation, in which the solution of the hyperbolic wave problem is propagated forward from inlet to outlet without the need for simultaneously solving large sets of algebraic equations. However, this method exhibits a nearly-discontinuous dispersive response in response to shocks¹⁹, which limits its usefulness in modeling impulse response problem. The implicit formulation is useful for smoothing the numerical shock profile³⁸⁻³⁹. Since the pulsatile pressure inlet for the distensible blood vessel problem is smooth and continuously differentiable, this formulation is not needed for this problem type.

The notation describing the Lax-Wendroff method is described in Figure 63, with the index t for each timeline and i for each spatial grid point from the proximal end of the vessel, $i = 0$, to the distal, $i = L$, where L is the length of the vessel. It should be noted that the function value at a grid midpoint is often evaluated as $f_{i+1/2}^n = \frac{f_i^n + f_{i+1}^n}{2}$.

As with any dynamic system, the entire system (A, U, P) must be known everywhere for i at the initial state $t = 1$. From this initial state, the update for the half time step at $t = 1\frac{1}{2}$ is determined for the cross sectional area, A , using the mass conservation in eq. 115, for the volumetric flow rate, Q , using the momentum balance in eq. 116, and for the blood pressure, P , using the tube law in eq. 118.

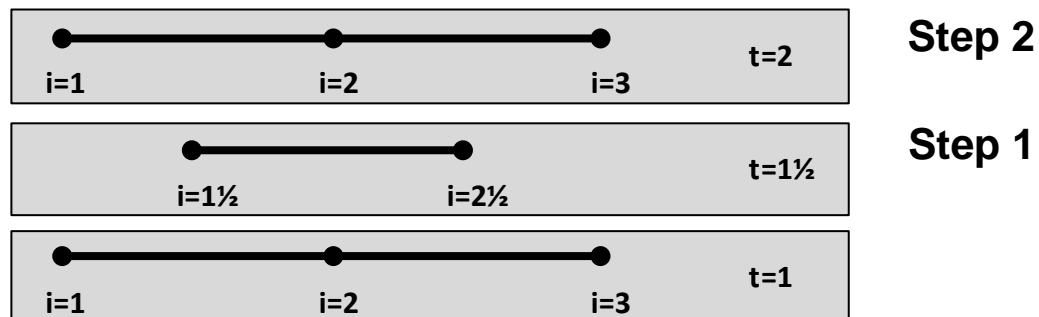


Figure 63 Schematic of Lax Wendroff Richten-Meyer two-step indexing scheme. The bottom row, the initial state, is the known states of A , U , and P at the nodes $I = 1, 2$ and 3 . Step 1 advances these values to the off-grid points $i = 1\frac{1}{2}$ and $2\frac{1}{2}$. Finally, Step 2 determines the values of A , U , and P at every node for the full advancement in time.

Step 1

Step 1 determines the value of A , Q , and P at the half step in both time and space, shown as the second row in Figure 63.

$$A_{i+1/2}^{t+1/2} = \frac{A_i^t + A_{i+1}^t}{2} - \frac{\Delta t}{2\Delta x} [(AU)_{i+1}^t - (AU)_i^t] \quad 115$$

$$U_{i+1/2}^{t+1/2} = \frac{U_i^t + U_{i+1}^t}{2} - \frac{\Delta t}{2\Delta x} \left\{ \left[\left(\frac{U^2}{2} \right) + \frac{P}{\rho} \right]_{i+1}^t - \left[\left(\frac{U^2}{2} \right) + \frac{P}{\rho} \right]_i^t \right\} - \frac{\Delta t}{2} \gamma \cdot \left(\frac{U}{A} \right)_{i+1/2}^t \quad 116$$

$$\left(\frac{U}{A} \right)_{i+1/2}^t = \frac{1}{2} \left[\left(\frac{U}{A} \right)_i^t + \left(\frac{U}{A} \right)_{i+1}^t \right] \quad 117$$

$$P_{i+1/2}^{t+1/2} = E_L \left(\frac{A_{i+1/2}^{t+1/2}}{A_{i+1/2}^1} - 1 \right) + \kappa \left(\frac{2}{\Delta t} A_{i+1/2}^{t+1/2} + \frac{A_i^t + A_{i+1}^t}{\Delta t} \right) + \frac{\beta}{\Delta x^2} (A_{i+1}^t - 2A_i^t + A_{i-1}^t) + P_{ex} \quad 118$$

Note that the value of A , Q , and P for the half step is explicitly dependent on the values at $t = 1$, each value can be found through algebraic substitution, it is no necessary to simultaneously solve a set of equations. For each determination of *Step 1*, the Area of for each index of i must be solved prior to determining the value of P due to the dependence of the tube law on the definition of $A_{i+1/2}^{t+1/2}$. The value of $A_{i+1/2}^1$ is the value of the initial conditions for A at the half spatial index, which can be found by geometric averaging.

Special Considerations at the Boundaries

All three equations require the definition of values from the previous time step at $i + 1$ to be known, which breaks down at the outlet, $i = N$, where N is the maximum number of nodal discretizations. However, there is no need to solve for $i = N + 1/2$, these half steps are only evaluated for the set $i = \{1, N - 1\}$.

The tube law requires the definition of $i + 1$ and $i - 1$, which is breaks down at the inlet where $i = 1$. In this case, a one-sided form of the second order differential is used, as shown in eq. 119.

$$P_{i+1/2}^{t+1/2} = E_L \left(\frac{A_{i+1/2}^{t+1/2}}{A_{i+1/2}^1} - 1 \right) + \kappa \left(\frac{2}{\Delta t} A_{i+1/2}^{t+1/2} + \frac{A_i^t + A_{i+1}^t}{\Delta t} \right) + \frac{\beta}{\Delta x^2} (A_{i+1}^t - A_i^t) + P_{ex} \quad 119$$

Step 2

Step 2 determines the value of A, Q, and P advancement from by “Leapfrogging” from the half time step to $t + 1$ at grid points of the original spatial indexing scheme³⁴, as shown as the third row of Figure 63.

$$A_i^{t+1} = A_i^t - \frac{\Delta t}{\Delta x} \left[(AU)_{i+1/2}^{t+1/2} - (AU)_{i-1/2}^{t+1/2} \right] \quad 120$$

$$U_i^{t+1} = U_i^t - \frac{\Delta t}{\Delta x} \left\{ \left[\left(\frac{U^2}{2} \right) + \frac{P}{\rho} \right]_{i+1/2}^{t+1/2} - \left[\left(\frac{U^2}{2} \right) + \frac{P}{\rho} \right]_{i-1/2}^{t+1/2} \right\} - \gamma \Delta t \cdot \left(\frac{U}{A} \right)_i \quad 121$$

$$\left(\frac{U}{A} \right)_i^{t+1/2} = \frac{1}{2} \left[\left(\frac{U}{A} \right)_{i+1/2}^{t+1/2} + \left(\frac{U}{A} \right)_{i-1/2}^{t+1/2} \right] \quad 122$$

$$P_i^{t+1} = E_L \left(\frac{A_i^{t+1}}{A_i^1} - 1 \right) + \kappa \left(\frac{A_i^{t+1} + A_i^t}{\Delta t} \right) + \frac{\beta}{\Delta x^2} (A_{i+1}^t - 2A_i^t + A_{i-1}^t) + P_{ex} \quad 123$$

As in Step 1, the value of A_i^{t+1} must be solved before the tube law is evaluated for the update of P .

Special Considerations at the Boundaries

At the inlet, $i = 1$, the pressure is assigned by the forcing function and the cross sectional area is evaluated by rearranging the tube law, as described in eq. 124.

$$A_1^{t+1} = \left(-P_1^{t+1} - E_L + \frac{\kappa}{\Delta t} A_1^1 - \frac{\beta}{\Delta x^2} A_{1+1}^t + \frac{\beta}{\Delta x^2} A_1^t + P_{ex} \right) / \left(-\frac{E_L}{A_1^1} + \frac{\kappa}{\Delta t} \right) \quad 124$$

As there is no value for $i - 1/2$ at the inlet boundary, where $i = 1$, an uncentered approximation⁴⁰ is enforced for the determination of Q at the inlet, as described in eq. 125.

$$U_1^{t+1} = U_1^t - \frac{\Delta t}{\Delta x} \left[\left(\frac{U^2}{2} \right)_{1+1}^t - \left(\frac{U^2}{2} \right)_1^t \right] - \frac{\Delta t}{\Delta x \rho} (P_{1+1}^t - P_1^t) + \gamma \Delta t \left(\frac{U}{A} \right)_1^t \quad 125$$

At the outlet, the area is determined by employing an explicit form of eq. 124. Outlet flow is determined by enforcing the momentum balance using the uncentered approximation shown in eq. 126.

$$U_N^{t+1} = U_N^t - \frac{\Delta t}{\Delta x} \left[\left(\frac{U^2}{2} \right)_N^t - \left(\frac{U^2}{2} \right)_{N-1}^t \right] - \frac{\Delta t}{\Delta x \rho} (P_N^t - P_{N-1}^t) + \gamma \Delta t \left(\frac{U}{A} \right)_N^t \quad 126$$

Parallel Computations

This two-step discretization in time and space explicitly solves blood pressure, velocity and vessel cross sectional area for each time step. This method relies exclusively on the values of each of these states in the previous time step at the node in question and the neighboring nodes. These values for the new time step can therefore be solved in any order and are not dependent on one another. Therefore, these computations can be easily solved in parallel, as the computation of each state for each time step can simply be distributed across multiple processors which compute the new time step independently. The ability of the two-step Lax-Wendroff integrator to independently compute the values of the new timeline extends to boundaries, bifurcations, and union as well as demonstrated in subsequent sections.

CFL Condition

At low magnitudes of the damping and longitudinal stress coefficients presented in the tube law, the system tends toward the behavior of a completely hyperbolic system. For the explicit formulation the stability of a hyperbolic system⁴¹ is shown dependent on the Courant-Friedrichs-Lewy (CFL) condition, shown in eq. 102 where C is the speed of the pressure wave velocity through the tube.

$$\left| \left(\left| \frac{Q}{A} \right| + C \right) \frac{\Delta t}{\Delta x} \right| \leq 1 \quad 127$$

As the system is not completely hyperbolic due to the presence of the damping and longitudinal stress terms, the ratio of Δt to Δx shown here is the upper limit that must lead to a

convergent solution; larger ratios of Δt to Δx may still converge. This criterion also assures the stability of the uncentered approximation⁴⁹ utilized at the boundary conditions. Application of the CFL convergence criterion

Supplemental 2

Bifurcations, Unions and Narrowing Channels

The vessels discussed so far are non-bifurcating, straight idealized cylinders. In realistic vascular networks propagating pressure and velocity waves are partially reflected at the junction and partially transmitted to both downstream daughter branches⁵⁰. At every vessel junction, the pressure, flow rate, and cross sectional area for the parent vessel and daughter branches must be computed by imposing suitable interface conditions^{9,26} that fulfill the following conditions⁵⁰;

- The pressure is a single value function, i.e. the distal pressure of the parent vessel is equal to the proximal pressure of the daughter branches.
- The flow must be continuous from the parent branch to both daughter branches; though the velocity can be discontinuous.

Using the same approach outlined in the literature⁹, only the two-step Lax-Wendroff integration method was used to solve these vessel junction case studies.

Bifurcations

Using the two-step Lax-Wendroff integrator to advance time steps, explicit knowledge is required of all neighboring nodes from the previous time step. Each vessel is discretized with a proximal node, distal node and a midway point. Therefore, each bifurcation is constructed as three nodes – one distal node of the parent vessel and two proximal nodes of both daughter branches. As the blood pressure, velocity and cross sectional area must be solved for each of these nodes, a total of nine algebraic equations must be solved, three for the parent vessel and three for each daughter branch.

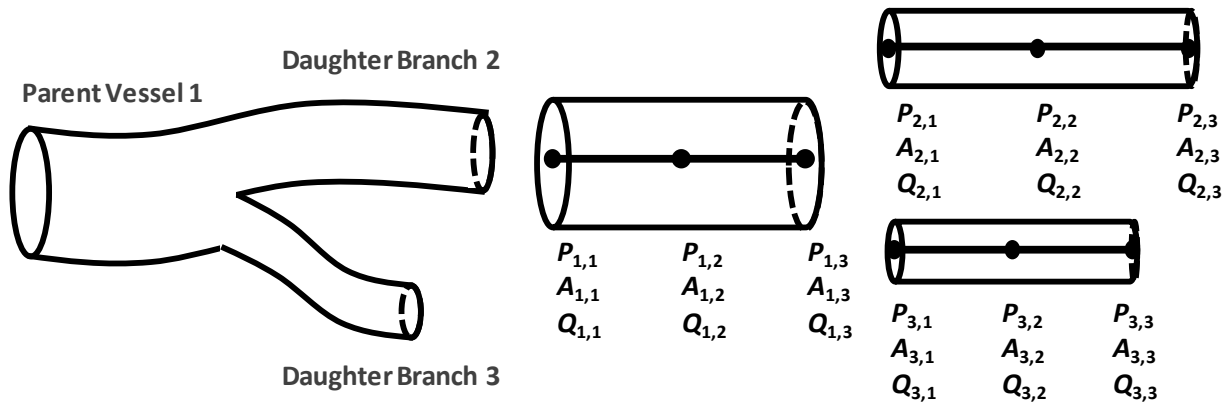


Figure 64 Schematic of bifurcation indexing scheme. Each vessel is assigned a local index from its proximal to distal end. The distal index of the parent vessel is in the same spatial position as the proximal node of both daughter branches. The value of P is the same between these three nodes, P_B , however the values of the cross sectional area, A , or the blood velocity, U , may not be as described in eq. 132-134. The length of each vessel is Δx_1 , Δx_2 , and Δx_3 .

For a single bifurcation, as shown in Figure 64, the volumetric flow rate across the bifurcation at each time step is conserved as described in eq. 128. By the principle of pressure continuity⁶ shown in eq. 129-130 are enforced, resulting in distal node of the parent vessel having the same pressure as the proximal node of the daughter vessels as show in Figure 64. The pressure at the bifurcation node is defined as P_B^{t+1} , defined in eq. 131.

$$(AU)_{1,3}^{t+1} - (AU)_{2,1}^{t+1} - (AU)_{3,1}^{t+1} = 0 \quad 128$$

$$P_{1,3}^{t+1} - P_{2,1}^{t+1} = 0 \quad 129$$

$$P_{1,3}^{t+1} - P_{3,1}^{t+1} = 0 \quad 130$$

$$P_B^{t+1} = P_{1,3}^{t+1} = P_{2,1}^{t+1} = P_{3,1}^{t+1} \quad 131$$

Though these vessel all have the same pressure, their area may not all be equivalent. Enforcing the linear elastic tube law presented in eq. 89, another three equations are obtained. Equal pressure for the parent and daughter branches at the vessel junction node may lead to large differences in vessel radius depending on the vessel's initial condition.

To obtain the final three equation need to solve this system, a face mass conservation⁹ was enforced across the parent and daughter branches as described in eq. 132-134.

$$\frac{\frac{A_{1,3}^{t+1} + A_{1,2}^{t+1}}{2} - \frac{A_{1,3}^t + A_{1,2}^t}{2}}{\Delta t} + \frac{(AU)_{1,3}^{t+1} - (AU)_{1,2}^{t+1}}{\Delta x_1} = 0 \quad 132$$

$$\frac{\frac{A_{2,2}^{t+1} + A_{2,1}^{t+1}}{2} - \frac{A_{2,2}^t + A_{2,1}^t}{2}}{\Delta t} + \frac{(AU)_{2,2}^{t+1} - (AU)_{2,1}^{t+1}}{\Delta x_2} = 0 \quad 133$$

$$\frac{\frac{A_{3,2}^{t+1} + A_{3,1}^{t+1}}{2} - \frac{A_{3,2}^t + A_{3,1}^t}{2}}{\Delta t} + \frac{(AU)_{3,2}^{t+1} - (AU)_{3,1}^{t+1}}{\Delta x_3} = 0 \quad 134$$

By rearranging eq. 132-134 equations to solve for flow, a mass conservation balance can be constructed as shown in eq. 135-140 from the mass conservation is eq. 128. The shorthand terms R and S in eq. 138-139 are introduced to simplify notation.

$$(AU)_{1,3}^{t+1} = (AU)_{1,2}^{t+1} - \frac{\Delta x_1}{2\Delta t} (A_{1,3}^{t+1} + A_{1,2}^{t+1} - A_{1,3}^t - A_{1,2}^t) \quad 135$$

$$(AU)_{2,1}^{t+1} = (AU)_{2,2}^{t+1} + \frac{\Delta x_2}{2\Delta t} (A_{2,1}^{t+1} + A_{2,2}^{t+1} - A_{2,1}^t - A_{2,2}^t) \quad 136$$

$$(AU)_{3,1}^{t+1} = (AU)_{3,2}^{t+1} + \frac{\Delta x_3}{2\Delta t} (A_{3,1}^{t+1} + A_{3,2}^{t+1} - A_{3,1}^t - A_{3,2}^t) \quad 137$$

$$R = (AU)_{1,2}^{t+1} - (AU)_{2,2}^{t+1} - (AU)_{3,2}^{t+1} \quad 138$$

$$S = \frac{\Delta x_1}{2\Delta t} (A_{1,3}^t + A_{1,2}^t - A_{1,2}^{t+1}) + \frac{\Delta x_2}{2\Delta t} (A_{2,1}^t + A_{2,2}^t - A_{2,2}^{t+1}) - \frac{\Delta x_3}{2\Delta t} (A_{3,1}^t + A_{3,2}^t - A_{3,2}^{t+1}) \quad 139$$

$$R + S = \frac{\Delta x_1}{2\Delta t} A_{1,3}^{t+1} + \frac{\Delta x_2}{2\Delta t} A_{2,1}^{t+1} + \frac{\Delta x_3}{2\Delta t} A_{3,1}^{t+1} \quad 140$$

In eq. 141-143 below, the inelastic tube law is used to define the area at the bifurcation node as a function of the resting area, the vessel's Young's modulus, the extravascular pressure and the blood lumen pressure.

$$A_{1,3}^{t+1} = \frac{A_{1,3}^0}{E_L} (P_{1,3}^{t+1} - P_{ex}) + A_{1,3}^0 \quad 141$$

$$A_{2,1}^{t+1} = \frac{A_{2,1}^0}{E_L} (P_{2,1}^{t+1} - P_{ex}) + A_{2,1}^0 \quad 142$$

$$A_{3,1}^{t+1} = \frac{A_{3,1}^0}{E_L} (P_{3,1}^{t+1} - P_{ex}) + A_{3,1}^0 \quad 143$$

Substituting eqs. 141-143 into eq. 140, and replacing the term P_B^{t+1} for each of the bifurcation pressure variables as defined in eq. 131. The term A_T is then introduced, as defined in eq. 144 to give the familiar form of the inelastic tube law shown in eq. 145, which can be rearranged to solve for P_B^{t+1} as shown in eq. 146.

$$A_T = A_{1,3}^0 + A_{2,1}^0 + A_{3,1}^0 \quad 144$$

$$E_L(R + S - A_T) = P_B^{t+1}A_T - P_{ex}A_T \quad 145$$

$$P_B^{t+1} = \frac{E_L}{A_T} (R + S - A_T) + P_{ex} \quad 146$$

Once the bifurcation pressure is solved, then the area of each vessel at the bifurcation can be solved by substitution using eq. 141-143, as well as the velocity using eq. 135-137.

Unions

Unions can be solved in a similar manner, with the branching junction pressure solved explicitly followed by solving the area and velocity by substitution. Solution of the blood pressure, velocity and cross sectional area change at the union requires explicit solution of each of these variables at the terminal nodes of the parent vessel and the proximal node of the single daughter branch, requiring nine separate equations.

Similar to the solution of the bifurcation, the steady state equation of mass conservation at the vessel junction is the first equation, as shown in eq. 147, followed by the two pressure continuity equations, eq. 148 and eq. 149.

$$(AU)_{1,3}^{t+1} + (AU)_{2,3}^{t+1} - (AU)_{3,1}^{t+1} = 0 \quad 147$$

$$P_{1,3}^{t+1} - P_{2,3}^{t+1} = 0 \quad 148$$

$$P_{1,3}^{t+1} - P_{3,1}^{t+1} = 0 \quad 149$$

The dynamic equations for mass conservation at the face are required to explicitly solve the area and velocity of the new step using the values from the old time step as shown in eq. 150-152.

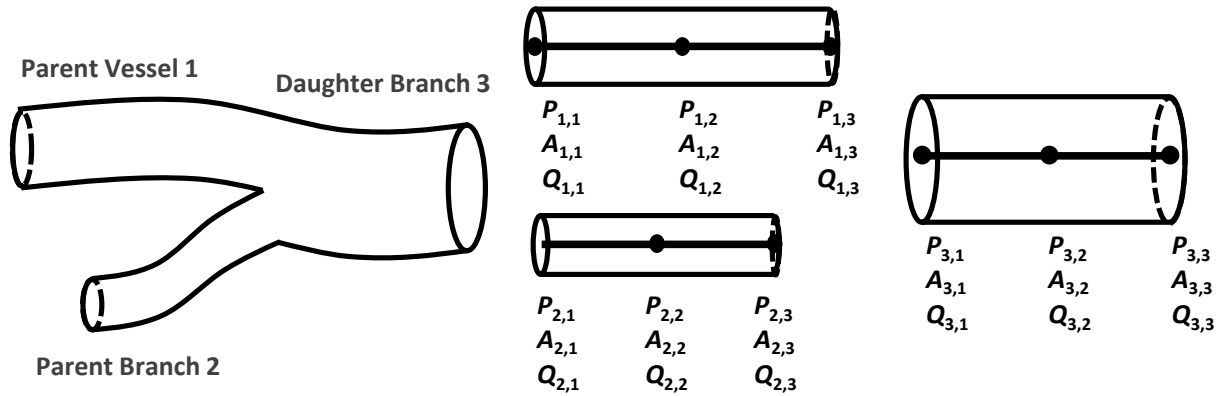


Figure 65 Schematic of union indexing. Each vessel is assigned a local index from proximal to distal end, where the distal index of both parent vessels has the same spatial coordinate as the proximal node of the daughter branch. The value of P is the same at all three nodes at the junction, however the values of A and U may not be. The length of each vessel is Δx_1 , Δx_2 , and Δx_3 .

$$\frac{\frac{A_{1,3}^{t+1} + A_{1,2}^{t+1}}{2} - \frac{A_{1,3}^t + A_{1,2}^t}{2}}{\Delta t} + \frac{(AU)_{1,3}^{t+1} - (AU)_{1,2}^{t+1}}{\Delta x_1} = 0 \quad 150$$

$$\frac{\frac{A_{2,3}^{t+1} + A_{2,2}^{t+1}}{2} - \frac{A_{2,3}^t + A_{2,2}^t}{2}}{\Delta t} + \frac{(AU)_{2,3}^{t+1} - (AU)_{2,2}^{t+1}}{\Delta x_2} = 0 \quad 151$$

$$\frac{\frac{A_{3,2}^{t+1} + A_{3,1}^{t+1}}{2} - \frac{A_{3,2}^t + A_{3,1}^t}{2}}{\Delta t} + \frac{(AU)_{3,2}^{t+1} - (AU)_{3,1}^{t+1}}{\Delta x_3} = 0 \quad 152$$

Finally, the bifurcation pressure equations are introduced to describe the relationship between pressure and cross sectional area as shown in eq. 153-155. As the pressure for the distal nodes of the parent branches and the proximal node of the daughter branch are identical, the bifurcation pressure can be solved explicitly.

$$A_{1,3}^{t+1} = \frac{A_{1,3}^0}{E_L} (P_{1,3}^{t+1} - P_{ex}) + A_{1,3}^0 \quad 153$$

$$A_{2,3}^{t+1} = \frac{A_{2,3}^0}{E_L} (P_{2,3}^{t+1} - P_{ex}) + A_{2,3}^0 \quad 154$$

$$A_{3,1}^{t+1} = \frac{A_{3,1}^0}{E_L} (P_{3,1}^{t+1} - P_{ex}) + A_{3,1}^0 \quad 155$$

Rearranging the conservation balance equations from eq. 147 and eq. 150-152, the substitution variables R and S can be defined to give the form shown in eq. 156 and eq. 157.

$$R = (AU)_{1,2}^{t+1} + (AU)_{2,2}^{t+1} - (AU)_{3,2}^{t+1} \quad 156$$

$$S = \frac{\Delta x_1}{2\Delta t} (A_{1,3}^t + A_{1,2}^t - A_{1,2}^{t+1}) + \frac{\Delta x_2}{2\Delta t} (A_{2,3}^t + A_{2,2}^t - A_{2,2}^{t+1}) - \frac{\Delta x_3}{2\Delta t} (A_{3,1}^t + A_{3,2}^t - A_{3,2}^{t+1}) \quad 157$$

$$R + S = \frac{\Delta x_1}{2\Delta t} A_{1,3}^{t+1} + \frac{\Delta x_2}{2\Delta t} A_{2,3}^{t+1} + \frac{\Delta x_3}{2\Delta t} A_{3,1}^{t+1} \quad 158$$

Combined the inelastic tube law shown in eq. 153-155, the bifurcation pressure can be solved directly as shown in eq. 159-161.

$$A_T = A_{1,3}^0 + A_{2,3}^0 + A_{3,1}^0 \quad 159$$

$$E_L(R + S - A_T) = P_B^{t+1}A_T - P_{ex}A_T \quad 160$$

$$P_B^{t+1} = \frac{E_L}{A_T}(R + S - A_T) + P_{ex} \quad 161$$

Narrowing or Widening Channels

As with the bifurcation and union, a special case must be constructed for vessel junctions where two vessels meet that do not have the same diameter. The distal node of the upstream vessel and the proximal node of the downstream vessel are assigned separate node indices and share the same spatial coordinate as shown in Figure 66.

As the pressure, velocity and cross sectional area must be determined for both upstream distal node and downstream proximal node, a total of six variables must be solved requiring six equations. As with bifurcations and unions, junction mass conservation, eq. 162, and pressure continuity, eq. 163, are the first set of equations.

$$(AU)_{1,3}^{t+1} - (AU)_{2,1}^{t+1} = 0 \quad 162$$

$$P_{1,3}^{t+1} - P_{2,1}^{t+1} = 0 \quad 163$$

Mass conservation equations for each face adjacent to the vessel junction are the second set of equations, shown in eq. 164-165.

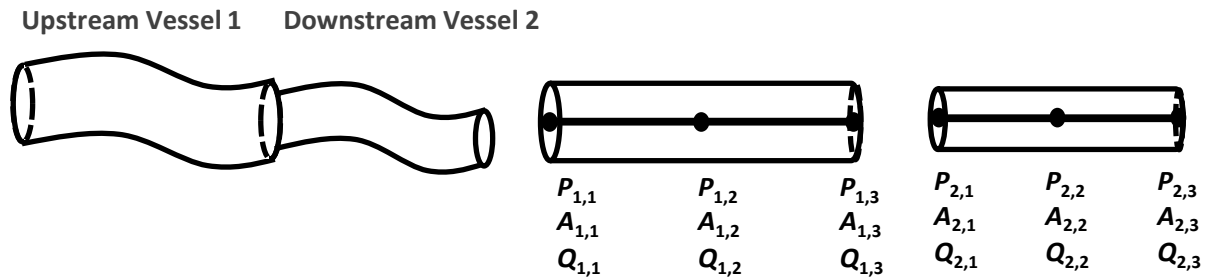


Figure 66 Schematic of narrowing or widening channel indexing. Each vessel is assigned a local index from proximal to distal end, where the distal index of the upstream vessels has the same spatial coordinate as the proximal node of the downstream vessel. The value of P is the same at both nodes at the junction, however the values of A and U may not be. Vessel length is Δx_1 and Δx_2 .

$$\frac{\frac{A_{1,3}^{t+1} + A_{1,2}^{t+1}}{2} - \frac{A_{1,3}^t + A_{1,2}^t}{2}}{\Delta t} + \frac{(AU)_{1,3}^{t+1} - (AU)_{1,2}^{t+1}}{\Delta x_1} = 0 \quad 164$$

$$\frac{\frac{A_{2,2}^{t+1} + A_{2,1}^{t+1}}{2} - \frac{A_{2,2}^t + A_{2,1}^t}{2}}{\Delta t} + \frac{(AU)_{2,2}^{t+1} - (AU)_{2,1}^{t+1}}{\Delta x_2} = 0 \quad 165$$

The final set of equations are the linear elastic tube law for both the distal node of the upstream vessel and the proximal node of the downstream vessel, as shown in eq. 166 and eq. 167.

$$A_{1,3}^{t+1} = \frac{A_{1,3}^0}{E_L} (P_{1,3}^{t+1} - P_{ex}) + A_{1,3}^0 \quad 166$$

$$A_{2,1}^{t+1} = \frac{A_{2,3}^0}{E_L} (P_{2,1}^{t+1} - P_{ex}) + A_{2,1}^0 \quad 167$$

Rearranging the conservation balance equations from eq. 162 and eq. 164-165, the substitution variables R and S can be defined to give the form shown in eq. 168 and eq. 169, whose sum is defined in eq. 170.

$$R = (AU)_{1,2}^{t+1} - (AU)_{2,2}^{t+1} \quad 168$$

$$S = \frac{\Delta x_1}{2\Delta t} (A_{1,3}^t + A_{1,2}^t - A_{1,2}^{t+1}) - \frac{\Delta x_2}{2\Delta t} (A_{2,1}^t + A_{2,2}^t - A_{2,2}^{t+1}) \quad 169$$

$$R + S = \frac{\Delta x_1}{2\Delta t} A_{1,3}^{t+1} + \frac{\Delta x_2}{2\Delta t} A_{2,1}^{t+1} \quad 170$$

Combined the inelastic tube law shown in eq. 166-167, the bifurcation pressure can be solved directly as shown in eq. 171-173.

$$A_T = A_{1,3}^0 + A_{2,1}^0 \quad 171$$

$$E_L (R + S - A_T) = P_B^{t+1} A_T - P_{ex} A_T \quad 172$$

$$P_B^{t+1} = \frac{E_L}{A_T} (R + S - A_T) + P_{ex} \quad 173$$

Supplemental 3

Radial Momentum Conservation

Conservation of radial momentum is shown below in eq. 174, the radial form of the incompressible axisymmetric Navier-Stokes equation assuming an angular velocity of zero.

$$\frac{\partial u_r}{\partial t} + u_x \frac{\partial u_r}{\partial x} + u_r \frac{\partial u_r}{\partial r} + \frac{1}{\rho} \frac{\partial P}{\partial r} = \frac{\nu}{r} \frac{\partial}{\partial r} \left(r \frac{\partial u_r}{\partial r} \right) \quad 174$$

Evaluating this equation requires conversion into dimensionless quantities as described in Canic and Kim⁴⁴. This conversion to non-dimensional variables requires a characteristic vessel inner radius, R_0 , vessel length, λ , radial velocity, U_0 , and axial velocity, V_0 .

$$\begin{aligned} r &= R_0 \tilde{r} & x &= \lambda \tilde{x} \\ t &= \frac{\lambda}{V_0} \tilde{t} & P &= \rho V_0^2 \tilde{p} \\ u_x &= V_0 \tilde{u}_x & u_r &= U_0 \tilde{u}_r \end{aligned}$$

A small parameter ε is introduced to signify a near-negligible number. The ratio of R_0/λ and U_0/V_0 can both be defined as ε .

Replacing these dimensionless variables into the radial momentum conservation equation gives the form shown in eq. 175.

$$\frac{V_0 U_0}{\lambda} \frac{\partial \tilde{u}_r}{\partial \tilde{t}} + \frac{V_0 U_0}{\lambda} \tilde{u}_x \frac{\partial \tilde{u}_r}{\partial \tilde{x}} + \frac{U_0^2}{R_0} \tilde{u}_r \frac{\partial \tilde{u}_r}{\partial \tilde{r}} + \frac{V_0^2}{R_0} \frac{\partial \tilde{p}}{\partial \tilde{r}} = \frac{\nu U_0}{R_0^2 \tilde{r}} \frac{\partial}{\partial \tilde{r}} \left(\tilde{r} \frac{\partial \tilde{u}_r}{\partial \tilde{r}} \right) \quad 175$$

Multiplying both sides by R_0 and dividing by V_0^2 the following form is obtained in eq. 176.

$$\frac{U_0 R_0}{V_0 \lambda} \frac{\partial \tilde{u}_r}{\partial \tilde{t}} + \frac{U_0 R_0}{V_0 \lambda} \tilde{u}_x \frac{\partial \tilde{u}_r}{\partial \tilde{x}} + \frac{U_0^2}{V_0^2} \tilde{u}_r \frac{\partial \tilde{u}_r}{\partial \tilde{r}} + \frac{\partial \tilde{p}}{\partial \tilde{r}} = \frac{\nu U_0}{\tilde{r} R_0 V_0^2} \frac{\partial}{\partial \tilde{r}} \left(\tilde{r} \frac{\partial \tilde{u}_r}{\partial \tilde{r}} \right) \quad 176$$

Considering that $\varepsilon = R_0/\lambda$ and $\varepsilon = U_0/V_0$, all of terms except for the pressure term have a coefficient of ε or ε^2 and can be ignored. The form eq. 177 emerges, demonstrating that the blood pressure remains constant in the radial direction over the vessel cross-sectional area.

$$\frac{\partial \tilde{p}}{\partial \tilde{r}} = 0$$

Cited Literature

1. Pontrelli, G. and E. Rossoni. "Numerical modelling of the pressure wave propagation in the arterial flow" *International Journal for Numerical Methods in Fluids* 43: 651-671, 2003.
2. Pontrelli, G. "A multiscale approach for modelling wave propagation in an arterial segment" *Comput Methods Biomech Biomed Engin* 7: 79-89, 2004.
3. Grinberg, L., E. Cheever, T. Anor, J. R. Madsen and G. E. Karniadakis. "Modeling blood flow circulation in intracranial arterial networks: a comparative 3D/1D simulation study" *Ann Biomed Eng* 39: 297-309, 2011.
4. Matthys, K. S., J. Alastruey, J. Peiro, A. W. Khir, P. Segers, P. R. Verdonck, K. H. Parker and S. J. Sherwin. "Pulse wave propagation in a model human arterial network: assessment of 1-D numerical simulations against in vitro measurements" *J Biomech* 40: 3476-86, 2007.
5. Figueroa, C. A., I. E. Vignon-Clementel, K. E. Jansen, T. J. R. Hughes and C. A. Taylor. "A coupled momentum method for modeling blood flow in three-dimensional deformable arteries" *Computer Methods in Applied Mechanics and Engineering* 195: 5685-5706, 2006.
6. Olufsen, M. S., C. S. Peskin, W. Y. Kim, E. M. Pedersen, A. Nadim and J. Larsen. "Numerical simulation and experimental validation of blood flow in arteries with structured-tree outflow conditions" *Annals of Biomedical Engineering* 28: 1281-1299, 2000.
7. van de Vosse, F. N. and N. Stergiopulos. "Pulse Wave Propagation in the Arterial Tree" *Annual Review of Fluid Mechanics, Vol 43* 43: 467-499, 2011.
8. Chorin, A. J. and M. J. E. *A Mathematical Introduction to Fluid Mechanics*. New York: Springer, 1998.
9. Zagzoule, M. and J. P. Marcvergnès. "A Global Mathematical-Model of the Cerebral-Circulation in Man" *Journal of Biomechanics* 19: 1015-1022, 1986.

10. Canic, S., C. J. Hartley, D. Rosenstrauch, J. Tambaca, G. Guidoboni and A. Mikelic. "Blood flow in compliant arteries: an effective viscoelastic reduced model, numerics, and experimental validation" *Ann Biomed Eng* 34: 575-92, 2006.
11. Jovanovic, M. and B. Bamieh. The spatio-temporal impulse response of the linearized Navier-Stokes equations. In *IEEE American Control Conference*, 2001.
12. Valdez-Jasso, D. *Modeling and Identification of Vascular Biomechanical Properties in Large Arteries*. North Carolina State University, 2010.
13. Formaggia, L., D. Lamponi and A. Quarteroni. "One-dimensional models for blood flow in arteries" *Journal of Engineering Mathematics* 47: 251-276, 2003.
14. Quarteroni, A., M. Tuveri and A. Veneziani. "Computational vascular fluid dynamics: problems, models and methods" *Computing and Visualization in Science* 2: 163-197, 2000.
15. Fung, Y. C. *Biomechanics: Mechanical Properties of Living Tissue*. New York Spring-Verlag, 1981.
16. Warming, R. F., B. R. M. and Y. H. C. *Stability of difference approximations for initial-boundary-value problems*. . Presented at Third International Symposium on Numerical Methods in Engineering, Paris, 1983.
17. Grinberg, L. and G. E. Karniadakis. "Outflow boundary conditions for arterial networks with multiple outlets" *Annals of Biomedical Engineering* 36: 1496-1514, 2008.
18. Kivity, Y. and R. Collins. "Nonlinear-Wave Propagation in Viscoelastic Tubes - Application to Aortic Rupture" *Journal of Biomechanics* 7: 67-76, 1974.
19. Collins, J. B., D. Estep and S. Tavener. "A posteriori error estimation for the Lax–Wendroff finite difference scheme" *Journal of Computational and Applied Mathematics* 236: 299-311, 2014.
20. Corre, C., Y. Huang and A. Lerat. A dramatic improvement of an implicit Lax-Wendroff scheme for steady compressible viscous flow calculations. In *Numerical Methods in Fluid Dynamics*. Berlin: Springer, 1997.

21. Kiuchi, T. "An Implicit Method for Transient Gas-Flows in Pipe Networks" *International Journal of Heat and Fluid Flow* 15: 378-383, 1994.
22. Rezolla, L. Numerical Methods for the Solution of Partial Differential Equations Lecture Notes for the COMPSTAR School on Computational Astrophysics. Potsdam: Albert Einstein Institute Max-Planck-Institute for Gravitational Physics, 2011.
23. Richtmeyer, R. D. and M. K. W. *Difference Methods for Initial-value Problems*. New York: Interscience, 1967.
24. Gottlieb, D. "Boundary conditions for multiscale P finite-difference methods for time-dependent equations" *J. Comput. Phys.* 26: 181-195, 1978.
25. Rajeev, K. *A least-squares/Galerkin split finite element method for incompressible and compressible Navier-Stokes equations*: ProQuest, 2008.
26. Sherwin, S. J., V. Franke, J. Peiro and K. Parker. "One-dimensional modelling of a vascular network in space-time variables" *Journal of Engineering Mathematics* 47: 217-250, 2003.
27. Steele, B. N., D. Valdez-Jasso, M. A. Haider and M. S. Olufsen. "Predicting Arterial Flow and Pressure Dynamics Using a 1d Fluid Dynamics Model with a Viscoelastic Wall" *Siam Journal on Applied Mathematics* 71: 1123-1143, 2011.
28. Armentano, R. L., J. G. Barra, J. Levenson, A. Simon and R. H. Pichel. "Arterial wall mechanics in conscious dogs. Assessment of viscous, inertial, and elastic moduli to characterize aortic wall behavior" *Circ Res* 76: 468-78, 1995.
29. Mills, C. J., G. I. T., D. Gault, J. Mason, J. Ross, E. Braunwald and J. P. Shillingford. "Pressure-flow relations and vascular impedance in man" *Cardiovasc. Res* 4: 405-417, 1970.
30. Nichols, W. W., M. F. O'Rourke and C. Hartley. *McDonald's Blood Flow in Arteries; Theoretical, Experimental and Clinical Principles*: Hodder Arnold Publication, 1998.

31. Gould, I. G. and A. A. Linninger. "Hematocrit distribution and tissue oxygenation in large microcirculatory networks" *Microcirculation* 22: 1-18, 2015.
32. Logothetis, N.K., "What we can do and what we cannot do with fMRI" *Nature* 453(7197), pp.869-878, 2008.
33. Kim, S.G. and Ogawa, S., Biophysical and physiological origins of blood oxygenation level-dependent fMRI signals. *Journal of Cerebral Blood Flow & Metabolism* 32(7), pp.1188-1206, 2012.
34. Gagnon, L., Sakadžić, S., Lesage, F., Musacchia, J.J., Lefebvre, J., Fang, Q., Yücel, M.A., Evans, K.C., Mandeville, E.T., Cohen-Adad, J. and Polimeni, J.R., Quantifying the microvascular origin of BOLD-fMRI from first principles with two-photon microscopy and an oxygen-sensitive nanoprobe. *Journal of Neuroscience* 35(8), pp.3663-3675, 2015.
35. Gagnon, L., Sakadžić, S., Lesage, F., Pouliot, P., Dale, A.M., Devor, A., Buxton, R.B. and Boas, D.A., Validation and optimization of hypercapnic-calibrated fMRI from oxygen-sensitive two-photon microscopy. *Phil. Trans. R. Soc. B* 371(1705), p.20150359, 2016.
36. Fang, Q., Sakadžić, S., Ruvinskaya, L., Devor, A., Dale, A.M. and Boas, D.A., Oxygen advection and diffusion in a three-dimensional vascular anatomical network. *Optics express* 16(22), pp.17530-17541, 2008.
37. Linninger, A.A., Gould, I.G., Marinnan, T., Hsu, C.Y., Chojecki, M. and Alaraj, A., Cerebral microcirculation and oxygen tension in the human secondary cortex. *Annals of biomedical engineering* 41(11), pp.2264-2284, 2013.
38. Huber, L. et al. Techniques for blood volume fMRI with VASO: From low-resolution mapping towards sub-millimeter layer-dependent applications. *NeuroImage* doi:10.1016/j.neuroimage.2016.11.039, 2016
39. Smirnakis, S. M. et al. Spatial Specificity of BOLD versus Cerebral Blood Volume fMRI for Mapping Cortical Organization. *J. Cereb. Blood Flow Metab.* 27, 1248–1261, 2007.

40. Warming, R. F., Beam, R. M. & Yee, H. C. Stability of difference approximations for initial-boundary-value problems. *Proceedings of the Third International Symposium on Numerical Methods for Engineering*, Paris, France. Vol. 1, 1983.
41. Richtmyer, R. D. & Morton, K. W. *Difference methods for initial-value problems*, 1994.
42. Gottlieb, D. Boundary conditions for multiscale P finite-difference methods for time-dependent equations. *J. Comput. Phys.* 26, 181–195, 1978.
43. Fung, Y. C. *Biomechanics: Mechanical Properties of Living Tissues*. Springer Science & Business Media, 2013.
44. Čanić, S. & Kim, E.H. Mathematical analysis of the quasilinear effects in a hyperbolic model blood flow through compliant axi-symmetric vessels. *Mathematical Methods in the Applied Sciences* 26(14), 1161-1186, 2003.
45. Alastruey, J., Parker, K. H., Peiró, J., Byrd, S. M., & Sherwin, S. J. Modelling the circle of Willis to assess the effects of anatomical variations and occlusions on cerebral flows. *Journal of biomechanics*, 40(8), 1794-1805, 2007.

VII. MODELING HEMODYNAMIC RESPONSE AND DIVERSION OF BLOOD FLOW FOLLOWING FUNCTIONAL HYPEREMIA IN THE CEREBRAL MICROCIRCULATION

Abstract

Neurovascular coupling between neuronal activity and functional hyperemia in the cerebral microcirculation has been qualitatively characterized by spatio-temporal fMRI measurements. However, quantitative (or calibrated) fMRI has not been established as a reliable technique, limiting its deployment as a research and clinical tool. It is unclear which dynamical features of the fMRI BOLD signal are governed by changes in CBV, blood flow or changes in deoxygenated hemoglobin. Mathematical models can delineate how these phenomena contribute to the composite signal in each vascular compartment (surface vessels, PA, AV, and capillary bed). We present a 3D cerebral microcirculatory nonlinear FSI blood flow model which accounts for both mass and momentum conservation. The architecture of the simplified blood flow network was automatically generated using a space-filling algorithm that accounts for all major structures in the cortical microangioarchitecture. Hemodynamic results are described at steady state and at harmonic equilibrium. Dynamical CBV and blood flow results were simulated in response to three vasodilatory scenarios: dilation of SMCs surrounding surface pial arterioles, dilation of a single PA and relaxation of all pre-capillary arteriole pericytes within a select region. Simulations reveal that the largest increase in flow follows vasodilation in the surface pial arteries; however dilation of small pre-capillary arterioles leads to a more local increase in blood flow. Additionally, a significant phase lag between PA and AV was recorded, which may affect fMRI BOLD signal in a way that has not yet been fully understood. These simulation results provide a descriptive and quantitative basis for deeper understanding of the features of the fMRI signal, distinguishing between changes in CBV, blood flow and hemoglobin deoxygenation. Conception of these metrics is necessary for establishing a quantitative basis for the fMRI BOLD signal.

Introduction

The cerebrovasculature is responsible for supplying, directing and regulating 20% of the systemic blood flow to the human brain³², however the distribution of cerebral blood flow and oxygen following neuronal stimulation is still poorly understood^{19,23}. Activation of neuronal territories and up regulation of blood flow is detectable by functional Magnetic Resonance Imaging (fMRI)^{9,10}. This measurement is acquired by detecting changes in the magnetic susceptibility of tissue, specifically as diamagnetic oxygenated hemoglobin unbinds oxygen in response to neuronal metabolism becoming paramagnetic deoxygenated hemoglobin. This change of magnetic susceptibility due to oxygen unbinding in the vasculature is referred to as the Blood Oxygen Level Dependent (BOLD) signal.

The BOLD signal is an indirect measurement of neuronal activity consisting of a wide array of physiological changes¹⁹. During neuronal firing, vasodilators are released which increases blood flow and oxygen is consumed within the neuronal soma. This increase in blood flow to microcirculation and decrease of oxygen tension in the tissue causes oxygen to unbind from hemoglobin. This increase in blood flow in response to neuronal activity is called *functional hyperemia*. However, efforts to extract *quantitative* cerebral blood flow (CBF) measurements from BOLD is hampered by poor understanding of how cerebral blood volume (CBV) and deoxygenated hemoglobin change during functional hyperemia^{8,11,22}. Additionally, it is not well established how sensitive fMRI is to CBV and blood flow changes in the different vascular compartments; surface pial arteries, penetrating arterioles, the capillary bed, or ascending venules. Changes in CBV during functional hyperemia independently affect the BOLD signal, as water protons in each compartment (including extravascular transport) have different MR relaxation times at baseline⁴⁰. These changes are independent of the concentrations of deoxygenated hemoglobin.

A review of what has been observed in each of these vessel structures and hypothesis of what role they play in functional hyperemia follows. The contribution of previous computational models to quantify CBV and CBF changes during neuronal activation is presented as well. Mechanisms of neurovascular coupling, release and distribution of neurotransmitters and deoxygenation of hemoglobin is outside of the scope of this paper

Changes in cerebral microcirculation compartments following functional hyperemia

The cerebral microcirculation is divided into five distinct compartments; pial arteries, penetrating arterioles, pre-capillary arterioles, capillaries, ascending venules and pial veins. These structures have been characterized in-depth in prior work^{12,16,40}. A brief overview of the properties of the cerebral microcirculation is included, focused on hemodynamic changes that affect the interpretation of the BOLD signal. Pial arteries and pial veins rest on the surface of the cortex as a bifurcating 2D graph. The terminal leaves of these surface pial trees penetrate the cortical parenchyma, becoming penetrating arterioles (PA) or ascending venules (AV), respectively. The capillary bed, an interconnected mesh-like vessel network embedded within the cortex, is connected to the PA by pre-capillary arterioles. The capillary bed is drained by AV.

Pial Vessels

Pial arteries undergo significant changes in CBV following neuronal stimulation^{7,9}. Pial veins CBV only respond to longer stimulations, and even then the response is lower than the changes measured in pial arteries. Pial arteries are surrounded with a thick layer of smooth muscle cells (SMC) which increase the vessel wall compliance, possibly acting as a low-pass filter dampening the pulsations of the heart⁴⁰. Pial veins are much stiffer than pial arteries, however they do undergo significant CBV changes from baseline during functional activation²⁶. Anastomoses in the pial arterial vasculature provide pathways for rapid flow

distribution following vessel vasodilation or micro occlusions^{2,36}, which may also account for more prolonged and farther reaching changes in CBV during functional hyperemia.

Penetrating vessels

It has been well established that PA supply a far larger region than a single whisker barrel cortex^{3,18,45}. Penetrating arterioles may not be specific enough to act as actuators for a distributed blood flow control system, as activation may lead to increased flow to multiple FBU columns. These smaller vessels deep within cortical tissue have been observed to undergo larger CBV changes than surface vessels^{9,17,26,39,43}. Simulated blood flow changes in a morphologically realistic vasculature model demonstrate that the affected territory increases the further upstream the vascular changes are³³, which has been reaffirmed in more recent studies on single PA²⁹.

Penetrating arterioles lose their SMC covering after the first or second branching order. Blood flow through these thinner vessels “pre-capillary” arterioles are controlled by pericytes, isolated contractile cells that have been demonstrated to respond to neurotransmitters and ischemic events^{28,42}. Blood flow through these small pre-capillary arterioles has a strong correlation with neuronal dynamics¹³.

Mathematical modeling

Comprehensive mathematical models of dynamical post-capillary vessel CBV and blood flow changes following neuronal activation are critical to understanding fMRI measurements. Network vascular models of the cerebral microcirculation have demonstrated the dynamic effects of oxygen extraction on the interpretation of the BOLD signal^{8,9,11}. Single and network vessel computational models have demonstrated that hematocrit distribution is necessary for computing the distribution of oxygen at baseline^{24,37} and following functional hyperemia. These models consist of modeling blood flow through a network of interconnected compliant

compartment governed by mass conservation and the Hagen-Poiseuille law^{4,12}. Quantitative models of fMRI signal following changes in CBV, oxygenation and magnetic field strength⁴¹ have determined that the fMRI signal is affected by hemodynamic changes in both the micro and macro vasculature.

Modeling fMRI BOLD signal

A quantitative model of fMRI signal and modeling for different MRI parameters has been simulated⁹ predicting CBV, blood flow and blood oxygenation values compared to the earlier established Davis model⁶. This study revealed that the largest CBV changes were measured within the cortical tissue and not at the surface of the cortex and that the largest CBV changes were in small arterioles. The lumped vascular compliance term in these fMRI models was used as a fitting parameter, and arterial lumen diameter was assigned as a sigmoidal input. Additionally, these models lack momentum conservation as flow is computed at each time step as a function of pressure distribution recalculation⁴. These compartmental models predict the BOLD signal response with high accuracy and compare well to previous work simulating fMRI signals. These models have yet to account for two dynamical features of the BOLD signal: initial dip and post-stimulus undershoot. Initial dip is a transient decrease in fMRI signal immediately following stimulus. Post-stimulation undershoot is the dip in BOLD signal below baseline following the end of stimulation which is then recovered. Inclusion of momentum conservation and a first-principles vessel compliance model may capture these spatiotemporal fluctuations in CBV and blood flow.

Modeling presented in this work

In this work, we present a fully dynamic nonlinear fluid structure interaction (FSI) blood flow network model of the human cerebral vasculature that accounts for mass and momentum conservation. Each blood vessel is modeled as a linearly elastic deformable cylinder, whose

lumen diameter responds to changes in blood pressure and velocity. A mathematical network model of the human cerebral microcirculation has been generated using an automatic geometric space-filling algorithm presented in an earlier work²². Blood pressure, velocity, flow and lumen caliber for each vessel is solved using a two-step Richtmeyer-Morton Lax-Wendroff solver. This two-step explicit method was selected over Runge-Kutta or Riemann solvers because it does not require computationally costly iterative matrix inversions.

This solver was programmatically implemented for each vessel, bifurcation and vessel union in the microvessel network. The details on model generation and the mathematical model are described in the Materials and Methods section. An investigation of hemodynamic values in different vessel types at harmonic equilibrium and after a vasodilation event is described in the Results section.

Materials and Methods

This section describes the generation of the 3D blood vessel networks and the equations of motion used to solve the fluid structure interaction (FSI) problem, including details on boundary conditions. The mathematical background for the solution of the FSI equations using the two-step Richtmeyer-Morton Lax-Wendroff solver is found in Supplemental 1 and Supplemental 2 of the previous chapter. This formulation was originally proposed by Zagzoule⁴⁴.

Model Generation

A 3D blood vessel network of the human cerebral microcirculation is shown in Figure 67 was generated as a set of interconnected cylindrical tubes with an assigned length and diameter. The generated network consists of a surface pial arterial network, PA, pre-capillary arterioles, an interconnected distributed capillary bed, AV and a surface pial venous network with 3.00 x 2.99 x 2.77mm dimensions (volume of 24.83mm³). This cyclic graph of logically connected cylindrical segments was generated using a modified Constrained Constructive Growth (CCO) algorithm³⁸ developed by our group, as described in detail in a previous work²².

The constraints of the generated tree presented here are the same as presented in earlier work; however the strategy of penetrating vessel generation and connection of capillary vessels has been revised. A brief overview of this vessel generation technique is described below.

The pial arterial vessel network was grown from a backbone vessel with a diameter of 50 μ m positioned at the top of the domain at the surface of the cortex. Pial arterial segments were added successively by selecting a random point limited to the top layer of the domain and connecting it to the existing tree. The location of the connection point was optimized to create an overall tree with the smallest luminal volume. This optimization includes selecting diameters and lengths of the two new daughter branches such that all terminal leaves discharged equal blood flow. Steady state blood flow was determined using a linear blood flow model described in eq. 178, where mass conservation of blood flow, Q , is conserved at each vessel junction.

$$\begin{aligned}\nabla \cdot Q &= 0 \\ \Delta P &= Q \cdot \alpha \\ \alpha &= \frac{128\mu L}{\pi d^4}\end{aligned}\tag{178}$$

The pressure drop across each blood vessel, ΔP , is a product of the blood flow and the hydraulic resistance, α , which is a function of the vessel lumen diameter, d , length, l , and blood viscosity, μ . Geometric constraints were enforced to prohibit vessel segment overlap, as well as enforce morphologically consistent bifurcation angles. The resulting surface arterial pial network was a bifurcating graph. No anastomoses were added to this structure.

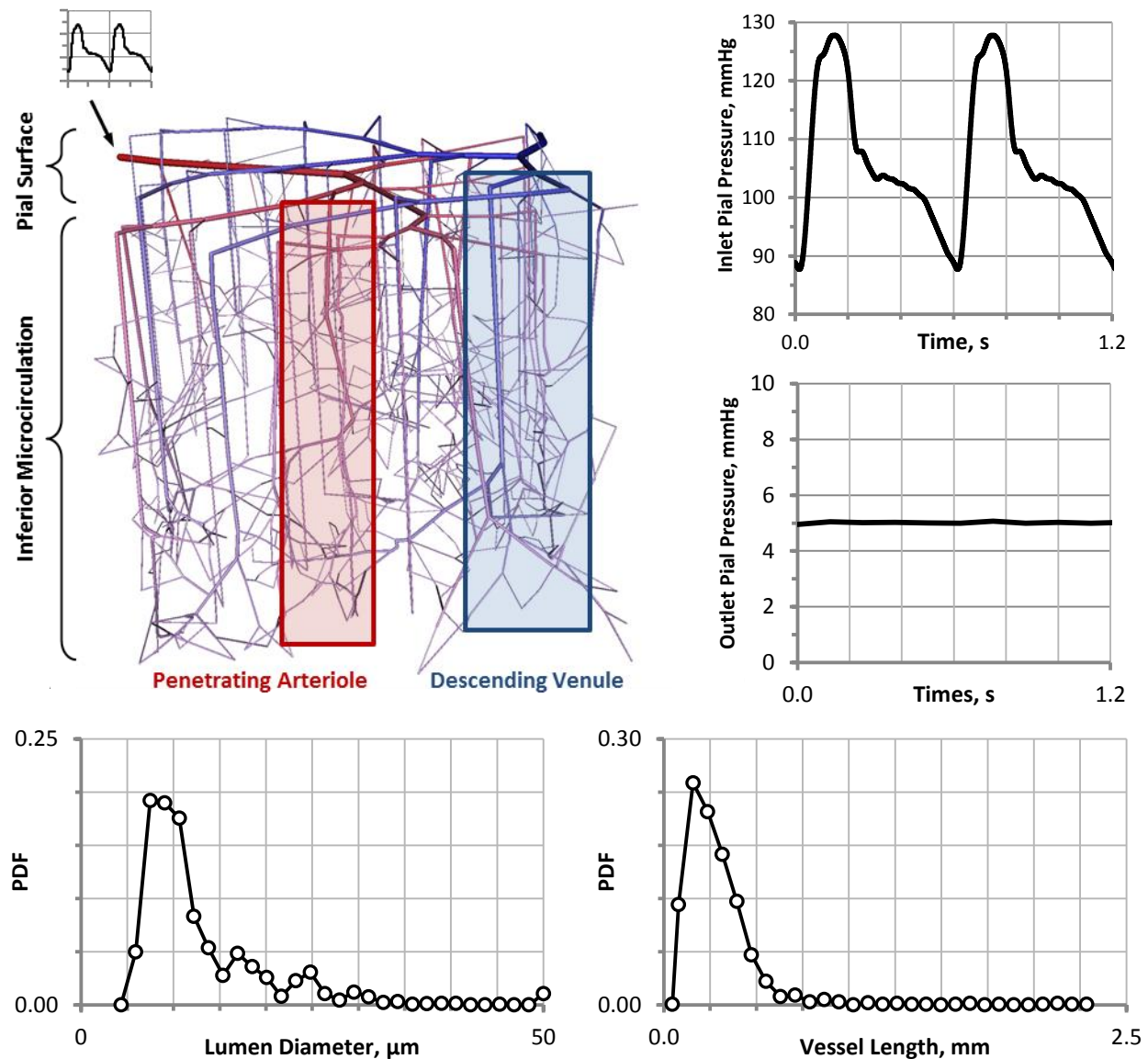


Figure 67 Angioarchitecture of cerebral microcirculation and pressure signal at pial arteriole entrance. **A.** Cerebral microvessels are either pial surface vessels located along the cortical exterior or inferior microcirculation embedded within the tissue of the cortex. The inferior microcirculation includes PA, pre-capillary arterioles, capillaries and AV. Arrow indicates the entrance of the model. **B.** The periodic inlet pressure boundary condition for the model ($T=0.6\text{ s}$) was captured using a 15 term Fourier series from patient Doppler measurements. **C.** Outlet pressure boundary condition of 5mmHg. **D.** Diameter probability distribution function (PDF) of generated microcirculation vessel network, mean diameter of 12.9 μm . **E.** Length PDF, mean length of 289 μm .

Pial vessels were successively bifurcated until 33 penetrating arterioles were achieved. From this coordinate, a penetrating arteriole backbone was sprouted with a variable depth of 0.5-2.77mm. Additional penetrating arteriole vessels were sprouted using the successive vessel addition approach described for the pial arteries. The process was continued until the terminal diameters of all penetrating arterioles, referred to as pre-capillary arterioles, were less than $6\mu\text{m}$. The venous drainage network was generated using the same method as described above with 28 AV and additional AV were sprouted until a post-capillary venule diameter of $6\mu\text{m}$ was achieved.

Constraints were enforced to ensure that none of the grown veins overlapped with existing vessel segments in the arterial tree. Capillaries were grown as an interconnecting acyclic graph linking pre-capillary arterioles to the nearest post-capillary venules. The Capillary connectivity was strictly limited to bifurcations only; higher order junctions were not permitted. The resulting network is an acyclic binary graph composed of cylindrical elements. Vessel wall thickness was assigned to each vessel using a diameter dependent formula¹⁴. The diameter and length probability distribution function (PDF) of the final microcirculatory vessel network is shown in Figure 67E-F.

Mathematical Formulation

In the formulation of the FSI problem, blood was considered to be incompressible viscous Newtonian fluid that flows through distensible vessels with a given cross-sectional area. Blood flow is governed by mass and momentum conservation which is coupled to vessel wall movement by a Hookean inelastic tube law. Hemodynamic values for blood velocity, pressure and vessel cross sectional area were solved using the set of nonlinear partial differential equations described below. Material properties are given in Table XVIII. A different material wall property was assigned to surface pial vessels, penetrating vessels and narrow capillaries.

Mass Conservation

Dynamic blood flow is governed by mass conservation at every vessel as shown in eq. 65, where the change in blood flow across a blood vessel is equal to the change in the lumen cross sectional area. Blood flow is defined as the product of the vessel cross sectional area, A , and blood velocity, U .

$$\frac{\partial}{\partial x}(U \cdot A) + \frac{\partial A}{\partial t} = 0 \quad 179$$

Momentum Conservation

Dynamic changes in blood velocity between vessels is driven by changes in lumen blood pressure, P , changes in velocity and viscous friction between the blood and the vessel wall as shown in eq. 87. Viscous friction is a function of blood viscosity, μ , and blood density, ρ . In this study, the blood viscosity, μ , is set to a constant value of 0.0035 Pa·s.

$$\frac{\partial U}{\partial t} + \frac{\partial}{\partial x} \left(\frac{U^2}{2} + \frac{P}{\rho} \right) + \frac{8\mu\pi}{\rho} \cdot \frac{U}{A} = 0 \quad 180$$

Tube Law

The instantaneous hydrostatic pressure difference between the vessel lumen, P , and the extravascular space, P_{ex} , drives wall deformations as governed by the inelastic tube law in eq. 89. Deformations are governed by the vessel wall Young's modulus, E , thickness, h , and the lumen resting radius, R_0 , and cross sectional area, A_0 .

$$P = \frac{Eh}{2R_0} \left(\frac{A}{A_0} - 1 \right) + P_{ex} \quad 181$$

The initial values for the hemodynamic simulation were initialized using values for pressure, velocity and cross sectional area obtained by executing steady state blood flow simulations wherein each vessel was assigned a hydraulic resistance by the Hagen-Poiseuille Law. The dynamic simulation was progressed from this initialized state until harmonic equilibrium was

achieved after 60 seconds of simulation time. Physiologic parameters for the FSI simulation are found in Table XVIII with references to the original work. A time step of 0.2s was chosen to satisfy the Courant-Freidrichs-Lewy (CFL) criterion³⁵ and ensure convergence.

Boundary Conditions

Inlet arterial blood pressure (ABP) was obtained from pressure microtransducer measurements in the canine aorta⁵, 127/88mmHg, with a period of $T=0.6s$. These systolic/diastolic values do not vary greatly from Doppler ABP measurements¹ in the middle cerebral artery in humans of 125/80mmHg. Input pressure signal was captured using a 15 term Fourier signal shown in Figure 67B. Outlet boundary pressure was set to 5mmHg, as shown in Figure 67C, and the extravascular tissue pressure was set to 40mmHg.

Table XVIII Values of physiologic parameters

Parameter	Symbol	Value	Unit	Reference
Blood Density	ρ	1050	kg/m ³	Canic ⁵
Blood Viscosity	μ	0.0035	Pa·s	Canic ⁵
Young's Modulus				
Pial Vessels	E_s	8.0e4	mmHg	--
Penetrating Vessels	E_p	6.0e4	mmHg	--
Capillaries	E_c	5.0e4	mmHg	--
Wall Thickness*	h	0.5-2.8	μm	Hart ¹⁴
Extravascular Pressure	P_{ex}	40	mmHg	--
Inlet Pial Arterial Pressure	--	Figure 67B	--	Canic ⁵
Pial Venous Pressure	--	5	mmHg	Oshio ³⁰

*Wall thickness is diameter dependent

Results

Steady state blood flow was computed using the system described in eq. 178. Dynamic blood pressure, velocity, flow and vessel caliper were computed by solving the system described by eq. 65-87 at each time step. Blood flow was computed as the product of blood velocity and cross sectional area for each vessel. Results at harmonic equilibrium are reported in each vessel compartment. Three vasodilation scenarios are investigated; relaxation of SMC surrounding surface pial arteries, penetrating arterioles or pericyte control of pre-capillary arterioles.

Steady State

Blood flow and pressure values at steady state were solved throughout the cerebral microcirculatory network using established blood flow models^{4,12,31}. Vascular resistance was assigned and mass conservation was enforced using the system described in eq. 178. A simplified blood viscosity approach was utilized; each vessel was assigned a flat viscosity value shown in Table XVIII. An inlet pressure was assigned of 107mmHg, the mean value of the pulsatile inlet pressure signal described in Figure 67. The outlet surface pial venous pressure of 5mmHg was assigned as shown in Table XVIII. This matrix problem was solved using an iterative Gauss-Seidel solver.

Blood Flow at Steady State

A blood flow of 13.07nL/min was computed through the inlet surface pial artery of the simplified cerebral microcirculatory network. An outlet surface pial venous blood flow of 13.07nL/min was computed, demonstrating that mass conservation was rigorously enforced. The smallest flow through the network was 26.21pL/min, through a capillary (dia=9.09 μ m). Flow through penetrating arterioles ranged from 0.10-1.53nL/min.

Blood Pressure at Steady State

Blood pressure decreased monotonically from the surface pial arterial inlet ($P_{in}=107\text{mmHg}$) to the surface pial venous outlet ($P_{out}=5\text{mmHg}$). The reduction in blood pressure was minimal across the surface pial arteries, $20.4\pm5.7\text{mmHg}$. Pressure drop through the PA was slightly higher, ranging from $10.8\text{-}26.3\text{mmHg}$. Decrease in blood pressure was greatest across the capillary bed, from pre-capillary arteriole pressure of $64.8\pm2.3\text{mmHg}$ to a post-capillary venule pressure of $27.9\pm6.1\text{mmHg}$. The AV and surface pial venules accounted for $20.1\pm2.9\text{mmHg}$ of the total loss in pressure through the cerebral microcirculation.

Harmonic Equilibrium

Dynamic hemodynamic simulations were initialized using steady state values for pressure and flow. The resting state of the cross sectional area was set using the assigned diameters of the vessel generation algorithm. Initial blood velocity through each vessel was calculated as the quotient of the flow and resting cross sectional area. The system reached harmonic equilibrium after 60s of simulation time (300,000 time steps). Oscillatory hemodynamic values are reported in select vessels throughout the microcirculation. Schematics of select vessels in pial arterioles, PA, pre-capillary arterioles, capillaries and AV are provided in to clarify vessel position, hierarchy and connectivity in the cerebral microvasculature in Figure 68.

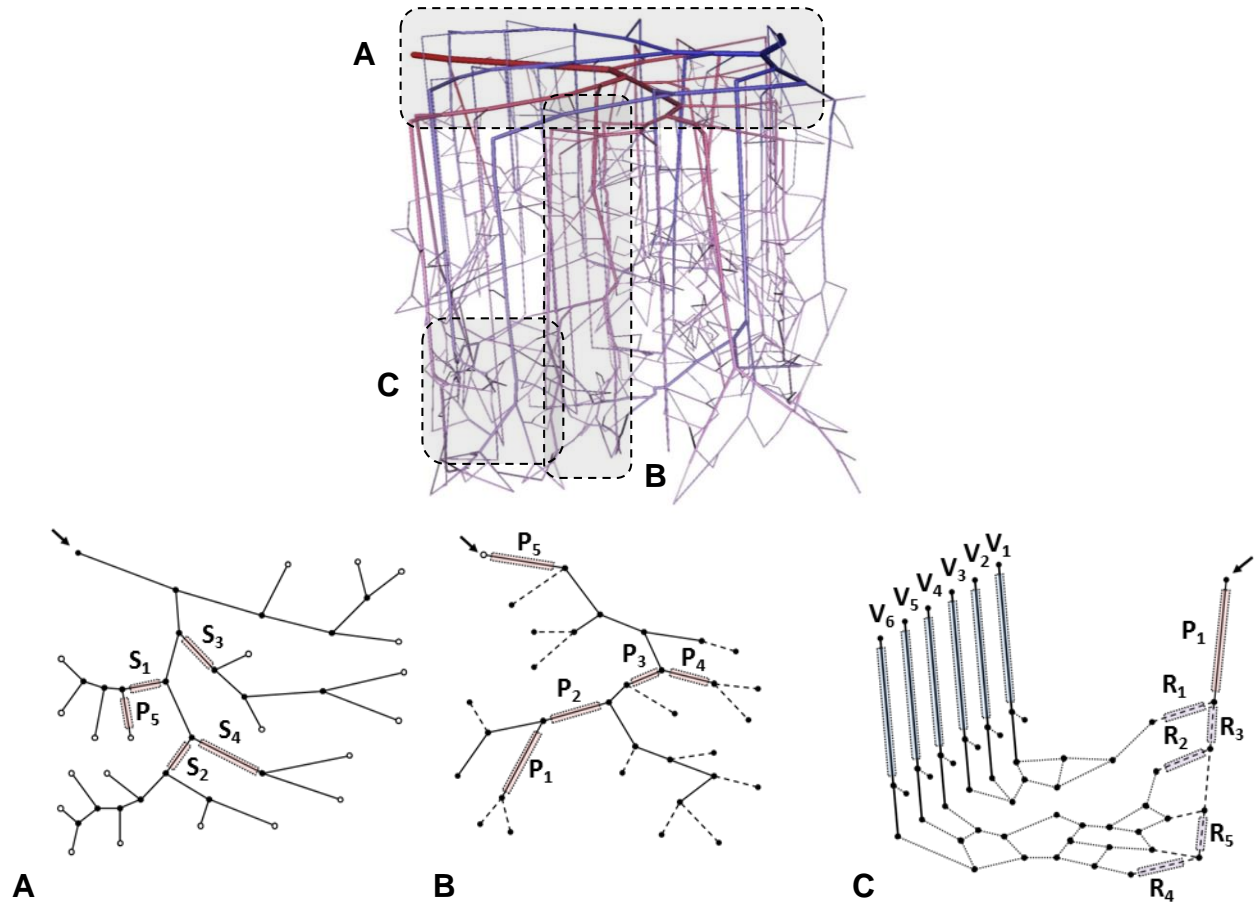


Figure 68 Schematic of microcirculatory vessel configuration and labels for **A.** pia surface arterioles, **B.** penetrating arterioles, **C.** pre-capillary arterioles, capillaries and draining ascending venules.

Blood Flow at Harmonic Equilibrium

The computed arterial blood flow of 14.28-16.72nL/min through the supplying pial artery (dia=50 μ m). The mean arterial blood flow of 15.36nL/min is comparable to steady state simulation. Blood flow decreases at each bifurcation as flow is distributed amongst smaller and smaller vessels. As blood flows from the surface pial arteries through the PA to the pre-capillary arterioles, the blood flow decreases to 119.77-171.75pL/min. As blood is drained from the capillary bed into the AV the flow steadily rises to 182.34-227.97pL/min. The mean flow from pial inlet to venous outlet is consistent (15.36nL/min), demonstrating rigorous enforcement of mass conservation. This systemic blood flow does not match steady state flow of 13.07nL/min as the systolic-diastolic average vessel diameter is larger at harmonic equilibrium than at the resting state. This blood flow is lower than values measured in the rat cortex²⁷ and in previous simulations¹², this discrepancy is addressed in the Limitations section of the Discussion.

Blood Velocity at Harmonic Equilibrium

Similar to flow, blood velocity exhibits amplitude dampening. Velocity signal amplitude is lower in the draining venules than in the penetrating arterioles. The computed capillary of velocity $29.13 \pm 8.92 \mu\text{m/s}$ is lower than previously reported RBC velocities measured in the rat cortex^{20,25} and in microcirculatory simulations^{12,37} of $0.93 \pm 0.29 \text{mm/s}$. This discrepancy is addressed in the Discussion section.

Blood Pressure at Harmonic Equilibrium

Blood pressure monotonically decreases from the pial arterial inlet to the outlet of the draining surface pial veins. The mean pressure drop from the feeding pial arteries to the penetrating arterioles is less than 1mmHg. The decrease in mean blood pressure from the PA to the pre-capillary arterioles is slightly larger, $12.3 \pm 8.3 \text{mmHg}$. The majority of the pressure loss occurs across between the pre-capillary arterioles to the AV, $20.1 \pm 6.6 \text{mmHg}$. These pressure drops are lower than steady state simulations in the simplified cerebral microcirculatory model.

Simulating Vasodilation

Vasodilatory stimulation of target vessels in response to a neuronal firing event was simulated in the cerebral microcirculation model. Three functional hyperemia case studies were conducted with different vasodilatory target sites; SMC surrounding a surface pial artery, a penetrating arteriole or pericyte sphincters on pre-capillary arterioles. Vasodilation was modeled as a relaxation of SMC or pericyte sphincters. This was accomplished by decreasing the material strength of the vessel wall by 30%, which increases vessel wall distensibility. Decrease in vessel wall distensibility was accomplished using a sigmoidal function. Change in blood flow and CBV in the target vessel and connected upstream and downstream vessels were measured before and after the vasodilatory event as shown in Figure 69-Figure 72. Schematics of the location and connectivity of each vessel is described in Figure 68. Change in CBV (ΔCBV) was measured as the ratio of the CBV at a given time compared to the resting vessel volume. Note that $\Delta\text{CBV}=1$ when the vessel lumen blood pressure is equivalent to the extravascular tissue pressure P_{ex} . Period-average blood flow and CBV trajectories before and after the vasodilatory event for each vasodilation scenario are shown in Supplemental 1 at the end of this chapter. These values are averaged over a one second interval.

Vasodilation of Surface Pial Arteries

Vasodilating surface pial artery S_1 ($d=34.68\mu\text{m}$, $l=158\mu\text{m}$) causes an 8.4% increase in mean blood flow through the inlet surface pial artery S_0 from 15.36nL/min to 16.65nL/min as shown in Figure 69A₁. This dilation leads to a slight divergence of blood flow from sister branch S_3 , which decreases in flow by 0.12nL/min. Downstream vessels S_2 and S_4 also lose flow by 1.27nL/min and 0.41nL/min respectively (results not shown). This vasodilation event also increases flow to downstream PA, elevating blood flow through vessel P_5 by 0.93nL/min described in Figure 69A₂. This increase in blood flow elevates downstream flow throughout the cortical tissue. Blood flow through downstream vessels P_3 increases from 1.35nL/min to 1.97nL/min and in vessel P_1 from

0.38nL/min to 0.54nL/min as shown in Figure 69A₃. The pre-capillary arterioles at the end of this tree elevate in blood flow by 46.7% in vessel R₂, 45.3% in R₅ and 45.5% and R₄ as described in Figure 69A₄. Blood flow did not increase significantly in pre-capillary arteriole R₁. Not all AV carried significantly more blood flow after the vasodilatory event. Ascending venules V₁ and V₅ increased in flow the most, 16.5% and 41.4% respectively as show in Figure 69A₅. Blood flow through AV V₃ and V₄ was not increased appreciably following vasodilation of the surface pial artery S₁. Of the three scenarios, the dilation of surface pial artery S₁ causes the largest redistribution of blood flow. Measurements of CBV increased in all vessels downstream of the vasodilatory site, with the vasodilating vessel increasing in volume by 150% as shown in Figure 69B₂. Downstream PA P₅ increases CBV by nearly 100%, whereas side vessels S₂ and S₄ do not change significantly in CBV. All downstream PA increase in CBV by $59.0 \pm 4.3\%$ as described in Figure 69B₃. Pre-capillary arterioles undergo an elevation in CBV as well, increasing from anywhere from 39.2%-50.4% in volume. The increase in CBV is similar between AV following surface pial artery dilation; AVs increase $39.4 \pm 6.4\%$ in volume shown in Figure 69B₅.

Vasodilation of Penetrating Arterioles

Vasodilating PA P₅ ($d=24.16\mu\text{m}$, $l=189\mu\text{m}$) causes a 1.4% increase in blood flow through the inlet surface pial artery as shown in Figure 70A₁. Figure 70A₂ shows that surface arteriole S₁ increases by 0.40nL/min, but S₁ and S₃ remain steady (S₃ not shown for clarity). Penetrating arteriole P₅ increases by 0.48nL/min, which branches into a 0.33nL/min increase through PA P₃ and a 0.04nL/min increase through P₄.

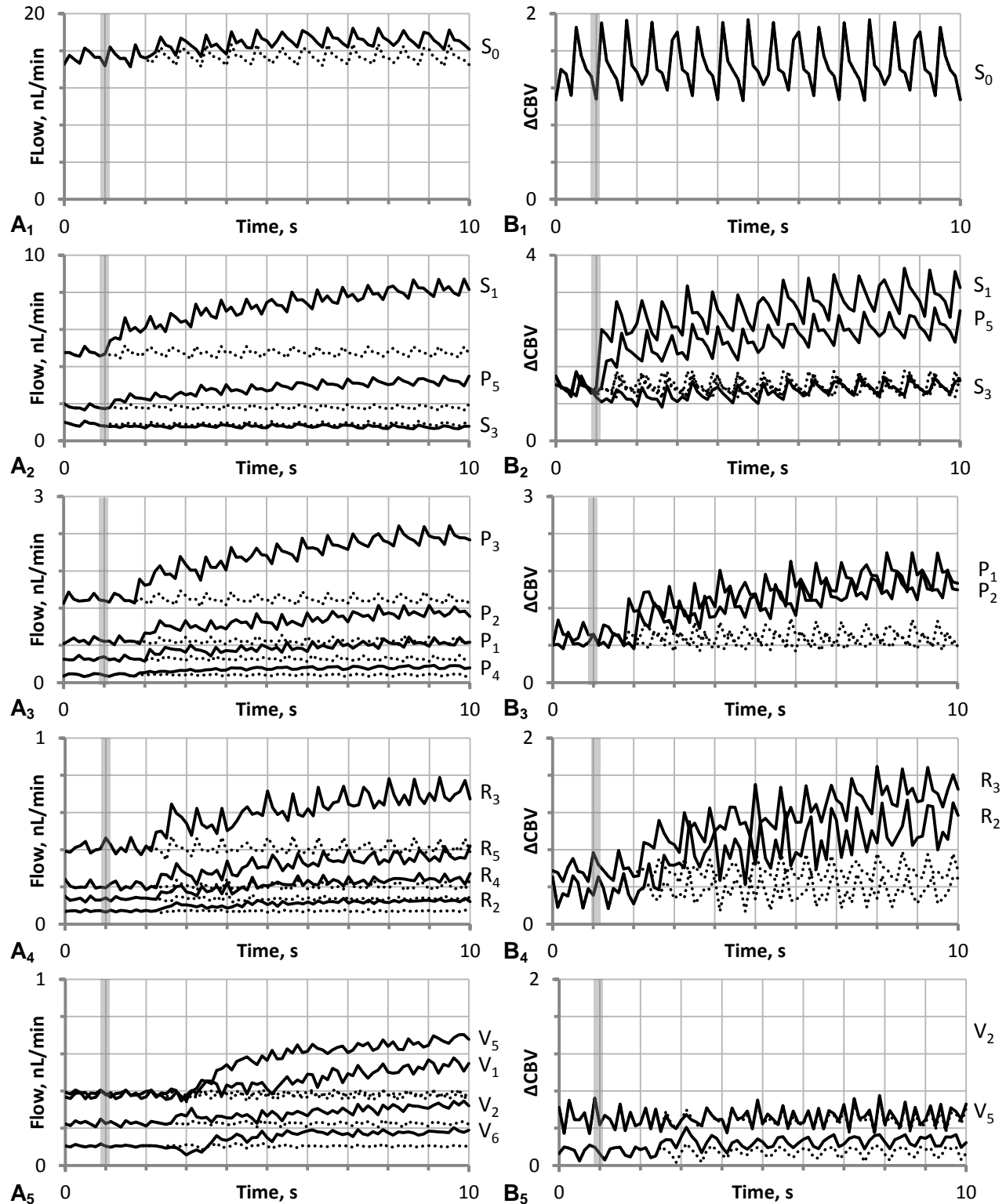


Figure 69 Vasodilation of surface pial arteriole S_1 leads to a hemodynamic changes in **A**. Blood flow and **B**. CBV. Values at harmonic equilibrium are shown as a dotted line, only select vessels shown. A 30% decrease in E of the pial artery S_1 led to a 1.4% increase in A_1 . upstream feeding arteriole S_0 and subsequently A_3 . PA, A_4 . capillaries and A_5 . AV. Increases in CBV were not limited to B_1 - B_2 . surface pial arteries, CBV increased significantly in B_3 - B_5 . vessels embedded in the cortical parenchyma.

Penetrating arteriole P_1 increases flow by 26.6%, which increases flow into downstream pre-capillary arterioles R_2 , +14.50pL/min and R_4 , +21.60pL/min. The increase in blood flow through pre-capillary arteriole R_1 (22.23pL/min) is not shown in Figure 70A₄ for clarity because its trajectory is similar R_4 . The dynamical trajectories for pre-capillary arteriole R_2 and R_4 are shown in Figure 70A₄. This increase of capillary blood flow is collected by the AV V_5 which increases in flow by 33.64pL/min (shown in Figure 70A₅) and V_4 which increases in flow by 23.31pL/min (not shown or clarity). Flow does not change significantly through either AV V_1 or V_3 . Blood flow slightly decreases in AV V_2 and V_6 by 6.19% and 17.82%, respectively.

Following a vasodilatory the PA P_5 , CBV does not change in the surface pial vessels as shown in Figure 70B₁-B₂. All CBV changes occur in downstream vessels within the parenchyma. All PA vessels downstream of the vasodilatory site increase in CBV by $23.7 \pm 2.6\%$, as shown in Figure 70B₃. Pre-capillary arterioles increase CBV by a similar trend, from 12.1-18.6% described in Figure 70B₄. There is a very small change in CBV change in AV. Ascending venule V_2 does not change in volume following PA vasodilation, which is representative of V_1 - V_3 . The collecting AV downstream of pre-capillary arterioles R_2 , R_4 and R_5 do increase in volume. Ascending venules V_4 - V_6 increase by 7.1-8.5%, V_5 is shown as a candidate vessel for this trend in Figure 70B₆.

Vasodilation of Pre-capillary Arterioles

Vasodilating pre-capillary arterioles R_1 , ($d=8.02\mu\text{m}$, $l=136\mu\text{m}$) R_2 ($d=8.27\mu\text{m}$, $l=160\mu\text{m}$) and R_4 ($d=11.59\mu\text{m}$, $l=163\mu\text{m}$) does not change blood flow through the inlet surface pial artery or through any of the surface pial arterioles or penetrating arterioles as shown in Figure 72A₁-A₃. Flow redistribution occurs in the pre-capillary arterioles to different regions in the capillary bed. Flow through R_3 , R_5 , and R_8 increased, siphoning flow away from R_2 , 3.31pL/min, and R_1 , 2.41pL/min (data not shown). Total flow through vessel R_4 increased by 10.83pL/min as shown in Figure 72A₄. This flow redistribution was reflected in collection in AV. Figure 72A₆ shows an

increase in V_5 by 42.93pL/min, and decreases in V_6 by 5.80pL/min. Ascending venule V_4 does not undergo any change in flow following vasodilation (data not shown). Flow through V_1 decreases by 143.06pL/min, and flow does not change significantly through vessel V_2 and V_3 .

Following vasodilation of pre-capillary arterioles, there is no change in CBV for upstream surface pial arterioles of penetrating arterioles as shown in Figure 72B₁-B₃. Pre-capillary arterioles embedded within the parenchyma did not undergo a large change in CBV (R_1 - R_3 , R_5) except for vessel R_4 which increased CBV by 56.8% as shown in Figure 72B₃. None of the AV V_1 - V_6 changed in CBV as shown in Figure 72B₆.

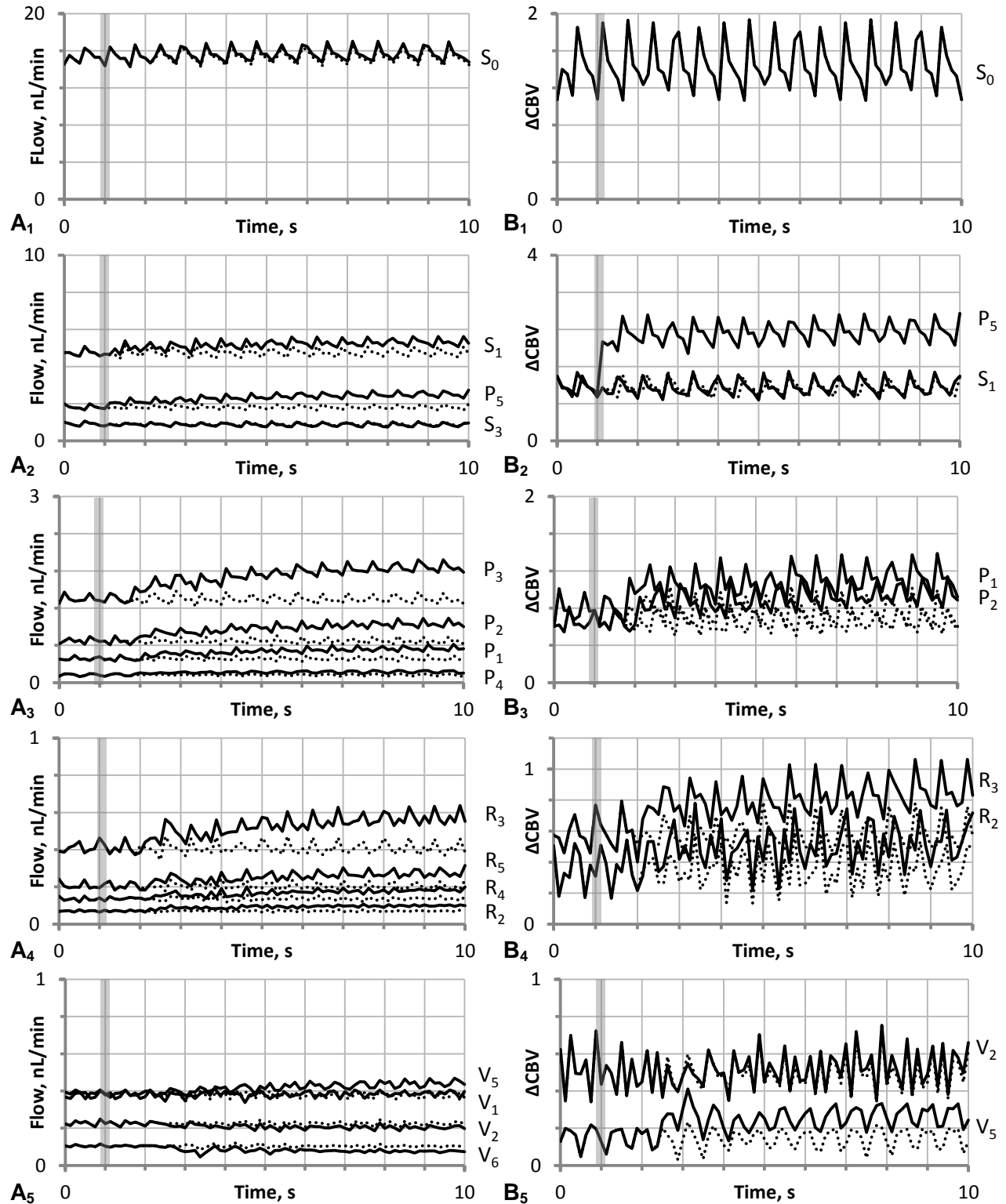


Figure 70 Vasodilation of PA P_5 leads to an increase in **A**. Blood flow and **B**. CBV. Harmonic equilibrium values are shown as a dotted line. A 30% decrease in E of the PA P_5 leads to an increase in flow through **A**₁. The upstream feeding pial artery S_0 by 1.4%, leading to an increase in **A**₃. PA, and **A**₄. capillaries and **A**₅. AV. Increases in CBV occurred mostly at **B**₁-**B**₂. surface pial arteries, CBV increased slightly in **B**₃. PA and **B**₄. capillaries. **B**₅. AV CBV did not increase appreciably.

Discussion

In this work we investigate the passive compliance of the cerebral microcirculation in a simplified 3D blood vessel network from surface pial arterioles, penetrating arterioles, pre-capillary arterioles, the capillary bed, ascending venules and pial surface veins. This investigation was conducted using a fully coupled FSI model of vascular compliance which computes blood pressure, velocity and change in vessel caliber. The hemodynamic response of the blood flow and changes in CBV were investigated following three separate vasodilation scenarios where a surface pial artery, a PA or a collection of pre-capillary arterioles were dilated by relaxing vessel compliance. This approach allowed us to study the effects of different vasodilation mechanisms on CBV and blood flow in different vessel compartments.

Baseline microcirculation hemodynamics

Blood pressure amplitude decreased significantly from the inlet surface pial arteries to the outlet surface pial veins. Input arterial pressure signal varied from 88.30-127.88mmHg, outlet venous pressure signal was only 4.96-5.06mmHg. This depression in signal amplitude was reflected in systole to diastole CBV changes from the arterial, 87%, to the venous signal, <1%. The low compliant capillaries dampen the pressure signal that passes through them. This attenuation of the pressure signal decreases the amplitude of cross sectional area fluctuations. A decrease in both pressure and area amplitude drives down the oscillations of the velocity signal, which affects blood flow.

A peak-to-peak lag was observed from across the cerebral microcirculation of 1.5s from the pial arterial inlet to the pial venous outlet. The majority of the phase lag occurs across the capillary bed from the pre-capillary arterioles to the AV, 0.88s.

Vasodilation Study

As the primary site of vasodilation accompanying functional hyperemia is currently unknown^{13,15}, we elected to study how different vasodilatory sites affected CBV and blood flow changes in larger surface vessels and smaller vessels embedded in the cortical parenchyma. Vasodilation of surface arterioles had the greatest effect on blood flow, a 30% decrease of vessel compliance resulted in a 71.4% increase in blood flow to the cortical microcirculation, compared to the 40.5% increase in response to dilation of a penetrating arteriole as shown in Figure 71A₁. Active dilation of blood vessels in the surface accounted for only 5.7% of the overall 17.0% increase in blood flow through the pial arteries following dilation of surface vessels. Active increase in blood flow is defined as increase in blood flow through the targeted vessel.

Dilation of pre-capillary arterioles has no measurable effect on overall blood flow. Dilation of PA affected flow to a wide region. Not only was flow elevated through the targeted vasodilated PA, affecting all downstream vessels, but flow was diverted from neighboring PA. This redistribution of flow following vasodilation of a PA decreased perfusion to neighboring territories while elevating flow. Additionally, a single PA feeds a wide territory³, far larger than a single column or FBU.

Vasodilation of pre-capillary arterioles in a select region affected flow locally and did not increase flow through the main supplying surface pial artery. This mechanism of vasodilation causes a very local redistribution of blood flow from one sub-region to another. It is feasible that in a more realistic microcirculatory network with a capillary density equivalent to morphologically accurate studies^{12,37}, the flow following pre-capillary arteriole vasodilation would be higher than the elevation described here. Dilation of more vessels in a denser space may increase local blood flow.

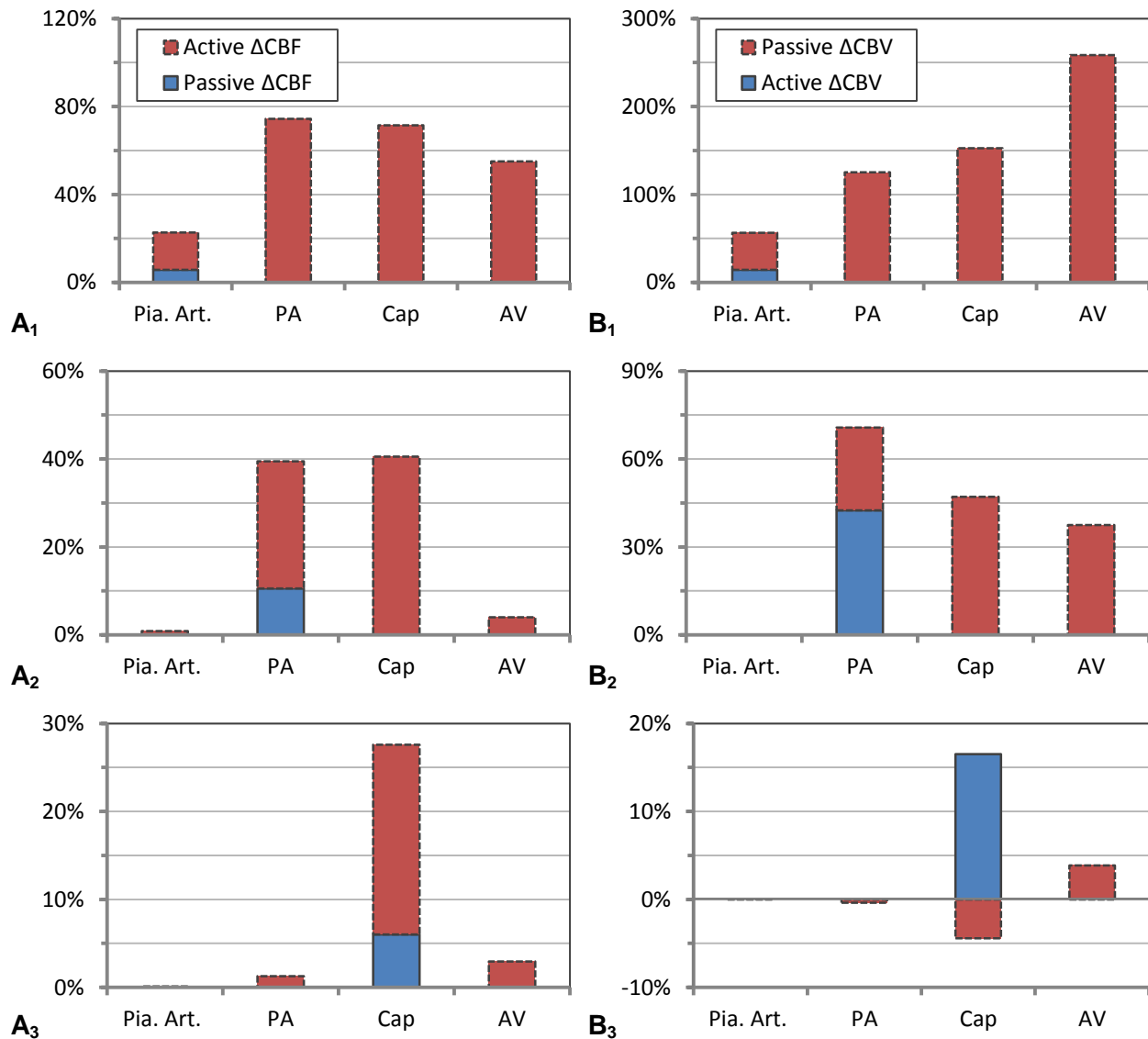


Figure 71 Comparison of active and passive changes in **A.** CBF and **B.** CBV for all three vasodilation scenarios, **1.** Surface pial arteries, **2.** Penetrating arterioles and **3.** Pre-capillary arterioles. Hemodynamic changes in blood flow and volume were measured for surface pial arteries, PA, capillaries and AV vessel groups. **A₁-B₁** Passive Δ CBF and Δ CBV dominated active changes during vasodilation of surface pial arteries, while active Δ CBV dominated during PA dilation as shown in **B₂**. Vasodilation of pre-capillary arterioles led to the smallest Δ CBF and CBV as shown in **A₃-B₃**, and led to diversion of blood volume from capillaries that were not actively dilated, resulting in passive Δ CBV < 0.

The increase in flow to downstream vessels following vasodilation leads to an increase in CBV. As flow increases through vessels, vessel lumen caliber (and hence volume) passively increased to maintain mass conservation. Vasodilation of a surface pial arteriole led to a passive elevation of CBV at the cortical as well as within the parenchyma (PA, capillaries, and AV). Passive increase in CBV dominated increase in blood volume following vasodilation of the surface pial arteries, with the majority of CBV elevation occurring in the microcirculation, as shown in Figure 71A₂. During vasodilation of PA, passive CBV increase, 28.3%, was less than active dilation, 42.5%, for those vessels, while surface arterioles did not change in volume. Vasodilation of pre-capillary arterioles had little effect on volume changes in surface vessels, PA or veins. Nearby capillaries that were not directly fed by dilating pre-capillary arterioles lost volume, shrinking by 4.4%, whereas downstream capillaries widened by 16.5% as shown in Figure 71C₃. On average, passive CBV increase was higher within the tissue, $70.6 \pm 59.7\%$ than at the cortical surface, $18.8 \pm 26.6\%$ for the three vasodilation case studies described here.

Recent fMRI studies have measured a larger change in CBV within the parenchyma than at the surface^{9,17,26} indicating that pial arteries may not be the exclusive site of vasodilation during functional hyperemia. Additionally, of the three scenarios studied here, dilation of a surface pial artery was the only scenario that produced a large change in venous CBV. A baseline decrease in CBV, such as the reduction of capillary volume during vessel rarefaction, would decrease BOLD signal intensity following neuronal activity. Patients exhibiting decreased capillary density may not exhibit a strong BOLD signal since a decrease in hemodynamic reserve would inhibit vascular CBV response and hence limit CBF changes.

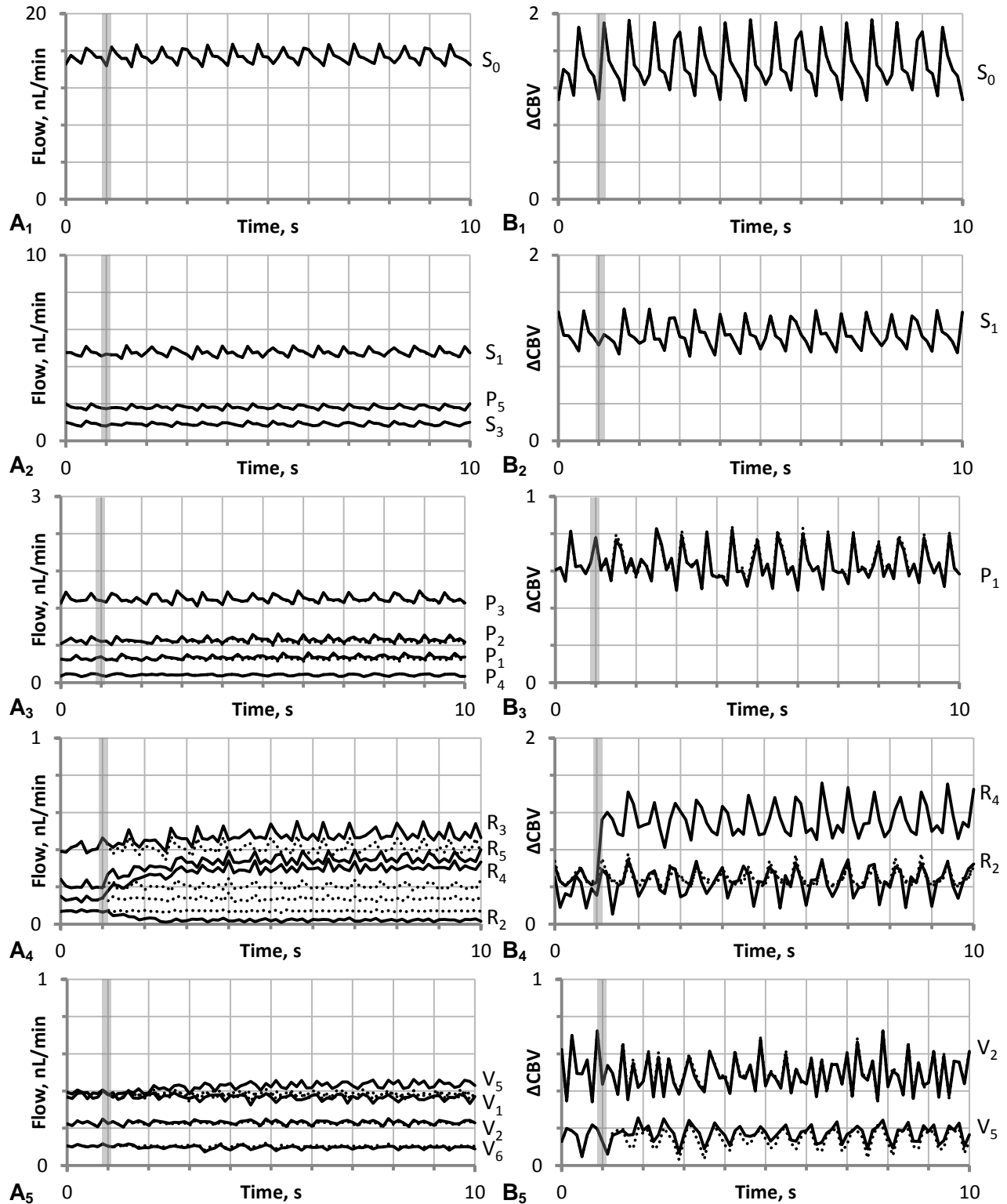


Figure 72 Vasodilation of pre-capillary arterioles R₁, R₂, and R₄ leads to a slight increase in **A**. Blood flow and little change to **B**. CBV. Harmonic equilibrium values are shown as a dotted line. A 30% decrease in E of the pre-capillary arterioles R₁, R₂, and R₄ leads to an increase in flow **A**₄. capillaries R₃, R₄, and R₅ only. CBV increased in capillaries embedded within the cortical parenchyma only, R₄ shown as a candidate vessel. Some vessels (such as R₂) did not increase in diameter even though E was decreased.

Vasodilation of PA did not cause a change in CBV at the cortical surface, and produced a much smaller passive CBV increase in the tissue. Blood volume in AV was increased slightly. Pre-capillary arteriole vasodilation caused the least passive CBV increase, elevating the volume in only a few narrow capillary vessels. Surface vessels, PA, and AV were unaffected by this vasodilation mechanism. From this investigation, it appears that none of these vasodilatory mechanisms are active in isolation; rather that a combination of mechanisms is necessary to produce the effects measured by fMRI.

Limitations

The simplified microcirculation presented here has a very low period averaged blood flow at harmonic equilibrium of $5.7\mu\text{L}/\text{min}/100\text{g}$. This perfusion value is considerably lower than the expected perfusion of $80\text{mL}/\text{min}/100\text{g}$ reported in previous studies¹², due to the high microcirculatory resistance of this sparse cerebral microcirculatory model. In order to achieve a more physiologically meaningful microcirculatory resistance, the volumetric ratio of blood vessels to tissue would have to be increased from the current sparse value of 0.2% to a more realistic^{3,33,46} density of 0.8-1.5%. Even with these limitations however, the current model accurately depicts the percent changes of surface to embedded microcirculation CBV during vasodilation. Additionally, the fractional changes in local and overall CBF can be used to guide future vasodilation studies both *in vivo* and *in silico*.

This model also neglected to account for the non-Newtonian properties of blood, specifically plasma skimming and the Fahraeus-Lindqvist effect. Note that implementing an *in vivo* or *in vitro* model of diameter and hematocrit dependent viscosity would increase vascular resistance and decrease perfusion. This low blood flow also affected blood velocity, which was similarly depressed.

Distensible vessel dynamics were governed by an infinitely fast tube law which determined cross sectional area as a Hookean spring response to changes to luminal blood pressure. The

absence of a dampening term in the tub law leads to instability in the dynamic system. These instabilities were limited by applying a sigmoidal signal for vasodilation; using a step or ramp signal to increase vessel wall distensibility led to instability in the cross sectional area term. These instabilities are apparent at bifurcations, where discontinuities in vessel distensibility computations (changes in resting cross sectional area) led to the creation of high-order frequencies in the pressure signal, i.e. shocks. Aliasing occurs when high-frequency components are higher than the Nyquist frequency of the input Fourier Transform sampling rate ($f_2/2 = 2500$). This aliasing may cause shocks in the pressure, area and velocity signal. These shocks may be eliminated by applying an anti-aliasing bandpass filter to the simulation results. Additionally, accounting for inertial and axial viscoelastic forces could also eliminate these higher order frequencies before they arise. Explicit solvers, like the two-step Lax-Wendroff solver used in this study, are also susceptible to generating higher-order frequency artifacts. Riemann solvers, such as Roe Solvers, are ideal for handling systems shocks and contact discontinuities²¹.

Future Work

Future work should include expanding this approach to solving nonlinear dynamic blood on larger, morphologically accurate microcirculation network models. These models could incorporate nonlinear non-Newtonian blood flow dynamics, i.e. plasma skimming and diameter and hematocrit dependent blood viscosity. These models could also be used in hypothesis testing of how changes in RBC content could change the BOLD signal following vasodilation or at harmonic equilibrium. These improvements would be necessary to predict physiologically blood oxygenation patterns, specifically predicting the rate of hemoglobin de-oxygenation following neuronal activation. Such a model that was capable of predicting oxygen distribution patterns during functional hyperemia could answer questions regarding vessel activation or

inactivation, the effects of vessel rarefaction, or postulate mechanisms for feed forward signal processing and the location of oxygen-sensing chemo-receptors in the brain.

Cited Literature

1. Aaslid, R., D. W. Newell, R. Stooss, W. Sorteberg, and K. F. Lindegaard. Assessment of cerebral autoregulation dynamics from simultaneous arterial and venous transcranial Doppler recordings in humans. *Stroke* 22:1148–1154, 1991.
2. Blinder, P., A. Y. Shih, C. Rafie, and D. Kleinfeld. Topological basis for the robust distribution of blood to rodent neocortex. *PNAS* 107:12670–12675, 2010.
3. Blinder, P., P. S. Tsai, J. P. Kaufhold, P. M. Knutsen, H. Suhl, and D. Kleinfeld. The cortical angiome: an interconnected vascular network with noncolumnar patterns of blood flow. *Nat Neurosci* 16:889–897, 2013.
4. Boas, D. A., S. R. Jones, A. Devor, T. J. Huppert, and A. M. Dale. A vascular anatomical network model of the spatio-temporal response to brain activation. *NeuroImage* 40:1116–1129, 2008.
5. Canic, S., D. Lamponi, A. Mikelic, and J. Tambaca. Self-Consistent Effective Equations Modeling Blood Flow in Medium-to-Large Compliant Arteries. *Multiscale Model. Simul.* 3:559–596, 2005.
6. Davis, T. L., K. K. Kwong, R. M. Weisskoff, and B. R. Rosen. Calibrated functional MRI: Mapping the dynamics of oxidative metabolism. *PNAS* 95:1834–1839, 1998.
7. Drew, P. J., A. Y. Shih, and D. Kleinfeld. Fluctuating and sensory-induced vasodynamics in rodent cortex extend arteriole capacity. *PNAS* 108:8473–8478, 2011.
8. Fang, Q., S. Sakadžić, L. Ruvinskaya, A. Devor, A. M. Dale, and D. A. Boas. Oxygen advection and diffusion in a three-dimensional vascular anatomical network. *Opt. Express, OE* 16:17530–17541, 2008.
9. Gagnon, L., S. Sakadžić, F. Lesage, J. J. Musacchia, J. Lefebvre, Q. Fang, M. A. Yücel, K. C. Evans, E. T. Mandeville, J. Cohen-Adad, J. R. Polimeni, M. A. Yaseen, E. H. Lo, D. N. Greve, R. B. Buxton, A. M. Dale, A. Devor, and D. A. Boas. Quantifying the Microvascular Origin of BOLD-fMRI from First

- Principles with Two-Photon Microscopy and an Oxygen-Sensitive Nanoprobe. *J. Neurosci.* 35:3663–3675, 2015.
10. Gagnon, L., S. Sakadžić, F. Lesage, P. Pouliot, A. M. Dale, A. Devor, R. B. Buxton, and D. A. Boas. Validation and optimization of hypercapnic-calibrated fMRI from oxygen-sensitive two-photon microscopy. *Phil. Trans. R. Soc. B* 371:20150359, 2016.
 11. Gould, I. G., and A. A. Linninger. Hematocrit Distribution and Tissue Oxygenation in Large Microcirculatory Networks. *Microcirculation* 22:1–18, 2015.
 12. Gould, I. G., P. Tsai, D. Kleinfeld, and A. Linninger. The capillary bed offers the largest hemodynamic resistance to the cortical blood supply. *Journal of Cerebral Blood Flow & Metabolism* 37:52–68, 2017.
 13. Hall, C. N., C. Reynell, B. Gesslein, N. B. Hamilton, A. Mishra, B. A. Sutherland, F. M. O’Farrell, A. M. Buchan, M. Lauritzen, and D. Attwell. Capillary pericytes regulate cerebral blood flow in health and disease. *Nature* 508:55–60, 2014.
 14. Hart, M. N., D. D. Heistad, and M. J. Brody. Effect of chronic hypertension and sympathetic denervation on wall/lumen ratio of cerebral vessels. *Hypertension* 2:419–423, 1980.
 15. Hill, R. A., L. Tong, P. Yuan, S. Murikinati, S. Gupta, and J. Grutzendler. Regional Blood Flow in the Normal and Ischemic Brain Is Controlled by Arteriolar Smooth Muscle Cell Contractility and Not by Capillary Pericytes. *Neuron* 87:95–110, 2015.
 16. Hirsch, S., J. Reichold, M. Schneider, G. Székely, and B. Weber. Topology and Hemodynamics of the Cortical Cerebrovascular System. *Journal of Cerebral Blood Flow & Metabolism* 32:952–967, 2012.
 17. Huber, L., D. Ivanov, D. A. Handwerker, S. Marrett, M. Guidi, K. Uludağ, P. A. Bandettini, and B. A. Poser. Techniques for blood volume fMRI with VASO: From low-resolution mapping towards sub-millimeter layer-dependent applications. *NeuroImage* .doi:10.1016/j.neuroimage.2016.11.039

18. Keller, A. L., A. Schüz, N. K. Logothetis, and B. Weber. Vascularization of Cytochrome Oxidase-Rich Blobs in the Primary Visual Cortex of Squirrel and Macaque Monkeys. *J. Neurosci.* 31:1246–1253, 2011.
19. Kim, S.-G., and S. Ogawa. Biophysical and Physiological Origins of Blood Oxygenation Level-Dependent fMRI Signals. *Journal of Cerebral Blood Flow & Metabolism* 32:1188–1206, 2012.
20. Kleinfeld, D., P. P. Mitra, F. Helmchen, and W. Denk. Fluctuations and stimulus-induced changes in blood flow observed in individual capillaries in layers 2 through 4 of rat neocortex. *PNAS* 95:15741–15746, 1998.
21. LeVeque, R. J. Finite Volume Methods for Hyperbolic Problems. Cambridge University Press, 2002, 542 pp.
22. Linninger, A. A., I. G. Gould, T. Marinnan, C.-Y. Hsu, M. Chojecki, and A. Alaraj. Cerebral Microcirculation and Oxygen Tension in the Human Secondary Cortex. *Ann Biomed Eng* 41:2264–2284, 2013.
23. Logothetis, N. K. What we can do and what we cannot do with fMRI. *Nature* 453:869–878, 2008.
24. Lückner, A., B. Weber, and P. Jenny. A dynamic model of oxygen transport from capillaries to tissue with moving red blood cells. *American Journal of Physiology - Heart and Circulatory Physiology* 308:H206–H216, 2015.
25. Lyons, D. G., A. Parpaleix, M. Roche, and S. Charpak. Mapping oxygen concentration in the awake mouse brain. *eLife* 5:e12024, 2016.
26. Ma, Y., M. A. Shaik, S. H. Kim, M. G. Kozberg, D. N. Thibodeaux, H. T. Zhao, H. Yu, and E. M. C. Hillman. Wide-field optical mapping of neural activity and brain haemodynamics: considerations and novel approaches. *Phil. Trans. R. Soc. B* 371:20150360, 2016.

27. Maeda, K., G. Mies, L. Oláh, and K.-A. Hossmann. Quantitative Measurement of Local Cerebral Blood Flow in the Anesthetized Mouse Using Intraperitoneal [14C]Iodoantipyrine Injection and Final Arterial Heart Blood Sampling. *Journal of Cerebral Blood Flow & Metabolism* 20:10–14, 2000.
28. Mishra, A., J. P. Reynolds, Y. Chen, A. V. Gourine, D. A. Rusakov, and D. Attwell. Astrocytes mediate neurovascular signaling to capillary pericytes but not to arterioles. *Nat Neurosci* 19:1619–1627, 2016.
29. O’Herron, P., P. Y. Chhatbar, M. Levy, Z. Shen, A. E. Schramm, Z. Lu, and P. Kara. Neural correlates of single-vessel haemodynamic responses in vivo. *Nature* 534:378–382, 2016.
30. Oshio, K., H. Watanabe, Y. Song, A. S. Verkman, and G. T. Manley. Reduced cerebrospinal fluid production and intracranial pressure in mice lacking choroid plexus water channel Aquaporin-1. *FASEB J* 19:76–78, 2005.
31. Pries, A. R., T. W. Secomb, P. Gaehtgens, and J. F. Gross. Blood flow in microvascular networks. Experiments and simulation. *Circulation Research* 67:826–834, 1990.
32. Raichle, M. E., and D. A. Gusnard. Appraising the brain’s energy budget. *PNAS* 99:10237–10239, 2002.
33. Reichold, J., M. Stampanoni, A. L. Keller, A. Buck, P. Jenny, and B. Weber. Vascular Graph Model to Simulate the Cerebral Blood Flow in Realistic Vascular Networks. *Journal of Cerebral Blood Flow & Metabolism* 29:1429–1443, 2009.
34. Rezzolla, L. Numerical methods for the solution of partial differential equations. , 2011.
35. Richtmyer, R. D., and K. W. Morton. Difference methods for initial-value problems. 1994.at <<http://adsabs.harvard.edu/abs/1994dmiv.book.....R>>
36. Schaffer, C. B., B. Friedman, N. Nishimura, L. F. Schroeder, P. S. Tsai, F. F. Ebner, P. D. Lyden, and D. Kleinfeld. Two-Photon Imaging of Cortical Surface Microvessels Reveals a Robust Redistribution in Blood Flow after Vascular Occlusion. *PLOS Biology* 4:e22, 2006.

37. Schmid, F., P. S. Tsai, D. Kleinfeld, P. Jenny, and B. Weber. Depth-dependent flow and pressure characteristics in cortical microvascular networks. *PLOS Computational Biology* 13:e1005392, 2017.
38. Schreiner, W., R. Karch, M. Neumann, F. Neumann, P. Szawlowski, and S. Roedler. Optimized arterial trees supplying hollow organs. *Medical Engineering & Physics* 28:416–429, 2006.
39. Smirnakis, S. M., M. C. Schmid, B. Weber, A. S. Talias, M. Augath, and N. K. Logothetis. Spatial Specificity of BOLD versus Cerebral Blood Volume fMRI for Mapping Cortical Organization. *Journal of Cerebral Blood Flow & Metabolism* 27:1248–1261, 2007.
40. Uludağ, K., and P. Blinder. Linking brain vascular physiology to hemodynamic response in ultra-high field MRI. *NeuroImage* .doi:10.1016/j.neuroimage.2017.02.063
41. Uludağ, K., B. Müller-Bierl, and K. Uğurbil. An integrative model for neuronal activity-induced signal changes for gradient and spin echo functional imaging. *NeuroImage* 48:150–165, 2009.
42. Underly, R. G., M. Levy, D. A. Hartmann, R. I. Grant, A. N. Watson, and A. Y. Shih. Pericytes as Inducers of Rapid, Matrix Metalloproteinase-9-Dependent Capillary Damage during Ischemia. *J. Neurosci.* 37:129–140, 2017.
43. Vazquez, A. L., M. Fukuda, J. C. Crowley, and S.-G. Kim. Neural and Hemodynamic Responses Elicited by Forelimb- and Photo-stimulation in Channelrhodopsin-2 Mice: Insights into the Hemodynamic Point Spread Function. *Cereb Cortex* 24:2908–2919, 2014.
44. Zagzoule, M., and J.-P. Marc-Vergnes. A global mathematical model of the cerebral circulation in man. *Journal of Biomechanics* 19:1015–1022, 1986.
45. Zheng, D., A. S. LaMantia, and D. Purves. Specialized vascularization of the primate visual cortex. *J. Neurosci.* 11:2622–2629, 1991.
46. Lauwers F, Cassot F, Lauwers-Cances V, Puwanarajah P, Duvernoy H. Morphometry of the human cerebral cortex microcirculation: general characteristics and space-related profiles. *NeuroImage* 39: 936-48, 2008.

Supplemental 1

Period averaged blood flow and CBV trajectories are shown for each of the three vasodilation case studies in the following figures. These values were averaged over one second interval for each of the vessels of interest in the surface pial arterioles, penetrating arterioles, pre-capillary arterioles and ascending venules. Each blood flow and CBV trajectory is shown in thick lines compared to the signal at harmonic equilibrium shown a dotted line.

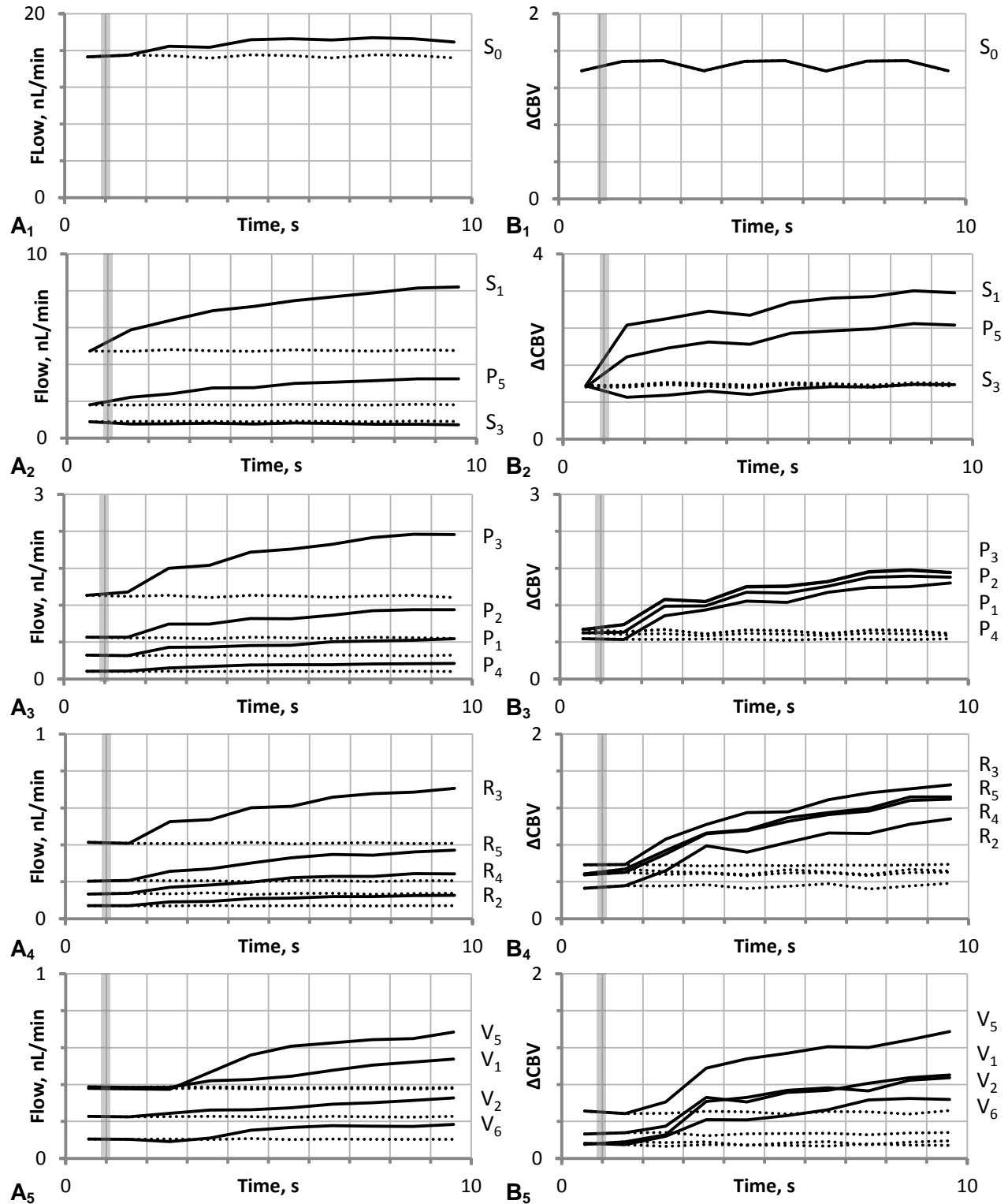


Figure 73 Vasodilation of pial arteriole S_1 leads to a changes in **A.** Blood flow and **B.** CBV in select vessels. Signals displayed as values averaged over one-second intervals. Harmonic equilibrium shown as a dotted line. A 30% decrease in E of the pial artery S_1 led to a 1.4% increase in **A₁**, upstream feeding arteriole S_0 and subsequently **A₃**, PA, **A₄**, capillaries and **A₅**, AV. CBV increases in **B₁-B₂**, surface pial arteries, were significantly higher than changes in **B₃-B₅**, vessels embedded in the cortical parenchyma.

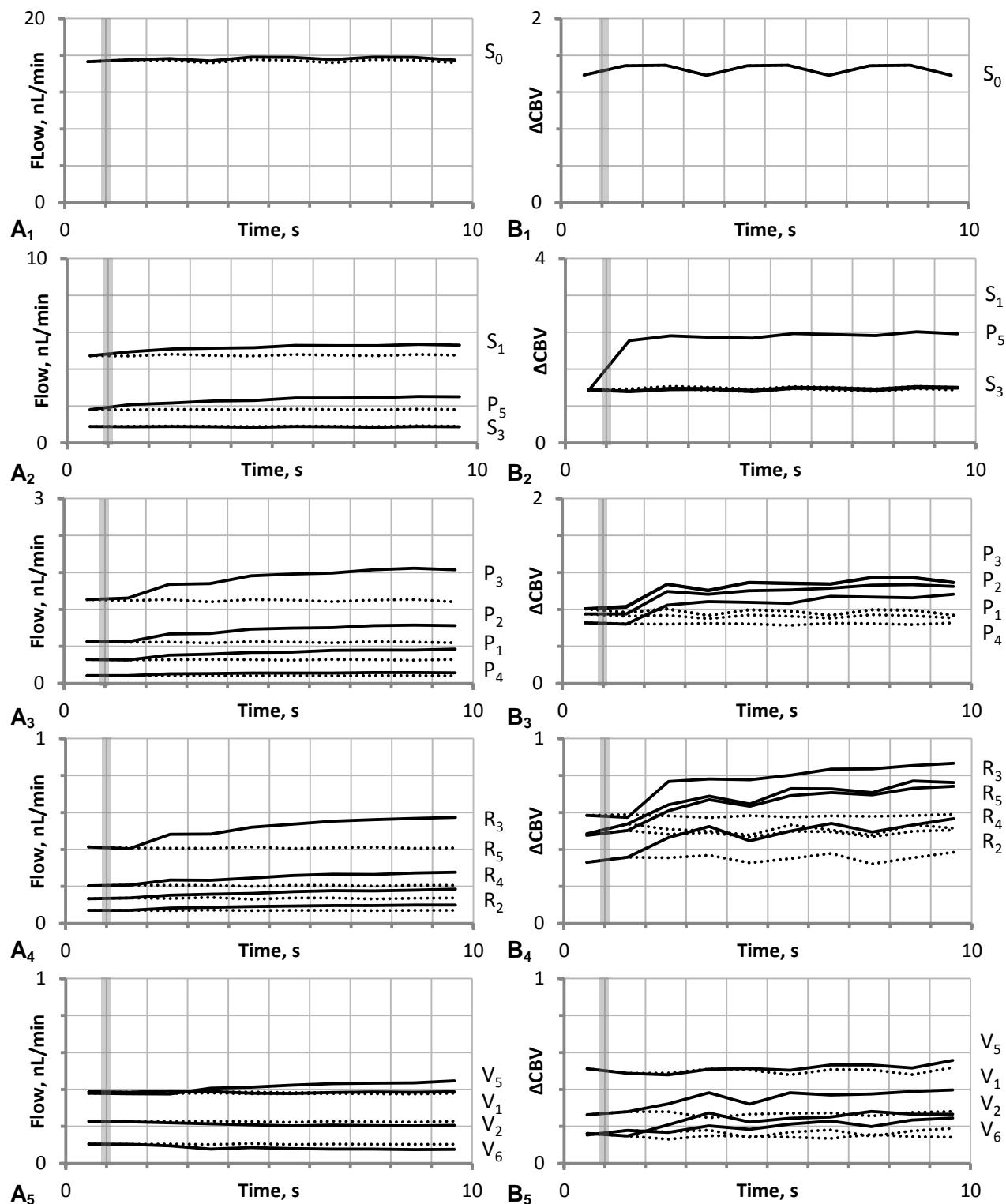


Figure 74 Vasodilation of PA P₅ leads to an increase in **A**. Blood flow and **B**. CBV. Signals displayed as values averaged over one-second intervals and harmonic equilibrium values are shown as a dotted line. **A₁**. A 30% decrease in E of P₅ increases flow through upstream feeding pial artery S₀ by 1.4%, leading to an increase in **A₃**. PA, and **A₄**. capillaries and **A₅**. AV. Increases in CBV occurred mostly at **B₁-B₂**. surface pial arteries, and increased slightly in **B₃**. PA and **B₄**. capillaries. **B₅**. AV CBV did not increase appreciably.

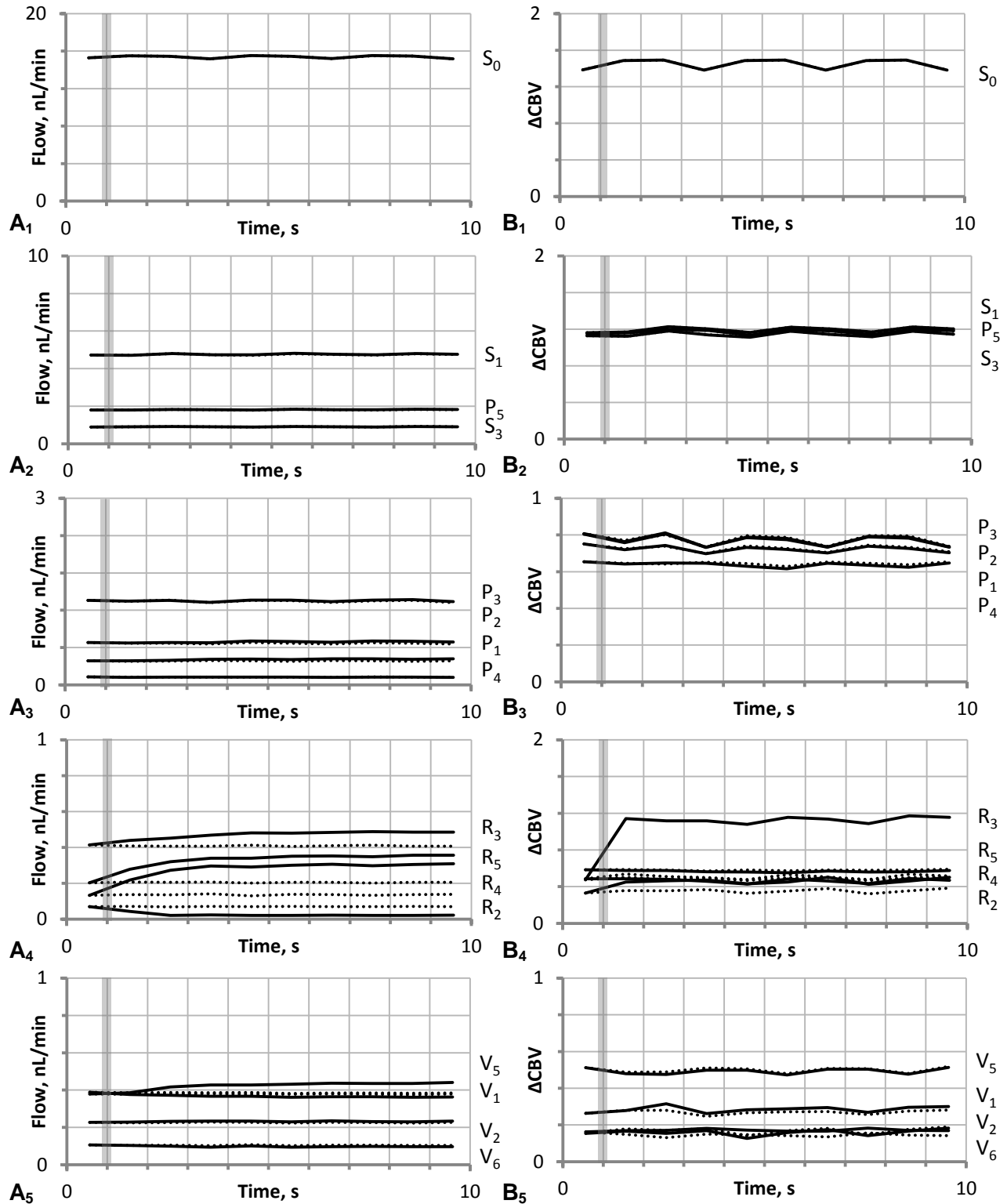


Figure 75 Vasodilation of pre-capillary arterioles R_1 , R_2 , and R_4 leads to a slight increase in **A**. Blood flow and **B**. CBV. Signals displayed as values averaged over one-second intervals and harmonic equilibrium is shown as a dotted line. A 30% decrease in E of pre-capillary arterioles R_1 , R_2 , and R_4 increases flow **A**₄, capillaries R_3 , R_4 , and R_5 only. CBV only increased in some capillaries, R_4 shown as a candidate vessel. Other capillaries, such as R_2 , did not increase in diameter even though E was decreased.

This page is left intentionally blank.

APPENDIX A**APPENDICES****APPENDICE A****Permission for use of previously published work****Publisher Permissions for Chapter II**

See following page.

APPENDIX A



01_03

PERMISSION LETTER

January 12, 2017

Springer reference

Annals of Biomedical Engineering

November 2013, Volume 41, Issue 11, pp. 2264-2284

First online: 11 July 2013

Cerebral Microcirculation and Oxygen Tension in the Human Secondary Cortex

Authors: A. A. Linninger, I. G. Gould, T. Marinnan, C.-Y. Hsu, M. Chojecki, A. Alaraj

© Biomedical Engineering Society 2013

DOI 10.1007/s10439-013-0828-0

Print ISSN 0090-6964

Online ISSN 1573-9686

Journal no. 10439

Your project

Requestor: Ian Gopal Gould

PhD Candidate

Dr. Andreas Linninger

Bioengineering Department

University of Illinois at Chicago

iangopal@gmail.com

University: University of Illinois at Chicago

Purpose: Dissertation/Thesis

With reference to your request to reuse material in which Springer controls the copyright, our permission is granted free of charge under the following conditions:

Springer material

- represents original material which does not carry references to other sources (if material in question refers with a credit to another source, authorization from that source is required as well);
- requires full credit (Springer book/journal title, chapter/article title, volume, year of publication, page, name(s) of author(s), original copyright notice) to the publication in which the material was originally published by adding: "With permission of Springer";
- may not be altered in any manner. Abbreviations, additions, deletions and/or any other alterations shall be made only with prior written authorization of the author;
- Springer does not supply original artwork or content.

This permission

- is non-exclusive;
- is valid for one-time use only for the purpose of defending your thesis and with a maximum of 100 extra copies in paper. If the thesis is going to be published, permission needs to be reobtained.
- includes use in an electronic form, provided it is an author-created version of the thesis on his/her own website and his/her university's repository, including UMI (according to the definition on the Sherpa website: <http://www.sherpa.ac.uk/romeo/>);
- is subject to courtesy information to the co-author or corresponding author;
- is personal to you and may not be sublicensed, assigned, or transferred by you to any other person without Springer's written permission;
- is only valid if no personal rights, trademarks, or competitive products are infringed.

This license is valid only when the conditions noted above are met.

APPENDIX A



01_03

PERMISSION LETTER

Permission free of charge does not prejudice any rights we might have to charge for reproduction of our copyrighted material in the future.

Rights and Permissions
Springer
Tiergartenstr. 17
69121 Heidelberg
Germany

APPENDIX APublisher Permissions for Chapter III

See the following page.

APPENDIX A

2/20/2017

RightsLink Printable License

JOHN WILEY AND SONS LICENSE TERMS AND CONDITIONS

Feb 20, 2017

This Agreement between Ian G Gould ("You") and John Wiley and Sons ("John Wiley and Sons") consists of your license details and the terms and conditions provided by John Wiley and Sons and Copyright Clearance Center.

License Number	4053261164444
License date	Feb 20, 2017
Licensed Content Publisher	John Wiley and Sons
Licensed Content Publication	Microcirculation
Licensed Content Title	Hematocrit Distribution and Tissue Oxygenation in Large Microcirculatory Networks
Licensed Content Author	Ian G. Gould, Andreas A. Linninger
Licensed Content Date	Jan 6, 2015
Licensed Content Pages	18
Type of use	Dissertation/Thesis
Requestor type	Author of this Wiley article
Format	Print and electronic
Portion	Full article
Will you be translating?	No
Title of your thesis / dissertation	COMPUTATIONAL MATHEMATICS ELICIDATES THE DEPENDENCE OF BRAIN PERFUSION ON MICROCIRCULATION
Expected completion date	May 2017
Expected size (number of pages)	250
Requestor Location	Ian G Gould 3721 W Belmont Ave Apt 2F Chicago, IL 60618 United States Attn: Ian G Gould
Publisher Tax ID	EU826007151
Billing Type	Invoice
Billing Address	Ian G Gould 3721 W Belmont Ave Apt 2F Chicago, IL 60618 United States Attn: Ian G Gould
Total	0.00 USD
Terms and Conditions	

TERMS AND CONDITIONS

APPENDIX A

2/20/2017

RightsLink Printable License

This copyrighted material is owned by or exclusively licensed to John Wiley & Sons, Inc. or one of its group companies (each a "Wiley Company") or handled on behalf of a society with which a Wiley Company has exclusive publishing rights in relation to a particular work (collectively "WILEY"). By clicking "accept" in connection with completing this licensing transaction, you agree that the following terms and conditions apply to this transaction (along with the billing and payment terms and conditions established by the Copyright Clearance Center Inc., ("CCC's Billing and Payment terms and conditions"), at the time that you opened your RightsLink account (these are available at any time at <http://myaccount.copyright.com>).

Terms and Conditions

- The materials you have requested permission to reproduce or reuse (the "Wiley Materials") are protected by copyright.
- You are hereby granted a personal, non-exclusive, non-sub licensable (on a stand-alone basis), non-transferable, worldwide, limited license to reproduce the Wiley Materials for the purpose specified in the licensing process. This license, and any **CONTENT (PDF or image file)** purchased as part of your order, is for a one-time use only and limited to any maximum distribution number specified in the license. The first instance of republication or reuse granted by this license must be completed within two years of the date of the grant of this license (although copies prepared before the end date may be distributed thereafter). The Wiley Materials shall not be used in any other manner or for any other purpose, beyond what is granted in the license. Permission is granted subject to an appropriate acknowledgement given to the author, title of the material/book/journal and the publisher. You shall also duplicate the copyright notice that appears in the Wiley publication in your use of the Wiley Material. Permission is also granted on the understanding that nowhere in the text is a previously published source acknowledged for all or part of this Wiley Material. Any third party content is expressly excluded from this permission.
- With respect to the Wiley Materials, all rights are reserved. Except as expressly granted by the terms of the license, no part of the Wiley Materials may be copied, modified, adapted (except for minor reformatting required by the new Publication), translated, reproduced, transferred or distributed, in any form or by any means, and no derivative works may be made based on the Wiley Materials without the prior permission of the respective copyright owner. **For STM Signatory Publishers clearing permission under the terms of the [STM Permissions Guidelines](#) only, the terms of the license are extended to include subsequent editions and for editions in other languages, provided such editions are for the work as a whole in situ and does not involve the separate exploitation of the permitted figures or extracts.** You may not alter, remove or suppress in any manner any copyright, trademark or other notices displayed by the Wiley Materials. You may not license, rent, sell, loan, lease, pledge, offer as security, transfer or assign the Wiley Materials on a stand-alone basis, or any of the rights granted to you hereunder to any other person.
- The Wiley Materials and all of the intellectual property rights therein shall at all times remain the exclusive property of John Wiley & Sons Inc, the Wiley Companies, or their respective licensors, and your interest therein is only that of having possession of and the right to reproduce the Wiley Materials pursuant to Section 2 herein during the continuance of this Agreement. You agree that you own no right, title or interest in or to the Wiley Materials or any of the intellectual property rights therein. You shall have no rights hereunder other than the license as provided for above in Section 2. No right, license or interest to any trademark, trade name, service mark or other branding

APPENDIX A

2/20/2017

RightsLink Printable License

("Marks") of WILEY or its licensors is granted hereunder, and you agree that you shall not assert any such right, license or interest with respect thereto

- NEITHER WILEY NOR ITS LICENSORS MAKES ANY WARRANTY OR REPRESENTATION OF ANY KIND TO YOU OR ANY THIRD PARTY, EXPRESS, IMPLIED OR STATUTORY, WITH RESPECT TO THE MATERIALS OR THE ACCURACY OF ANY INFORMATION CONTAINED IN THE MATERIALS, INCLUDING, WITHOUT LIMITATION, ANY IMPLIED WARRANTY OF MERCHANTABILITY, ACCURACY, SATISFACTORY QUALITY, FITNESS FOR A PARTICULAR PURPOSE, USABILITY, INTEGRATION OR NON-INFRINGEMENT AND ALL SUCH WARRANTIES ARE HEREBY EXCLUDED BY WILEY AND ITS LICENSORS AND WAIVED BY YOU.
- WILEY shall have the right to terminate this Agreement immediately upon breach of this Agreement by you.
- You shall indemnify, defend and hold harmless WILEY, its Licensors and their respective directors, officers, agents and employees, from and against any actual or threatened claims, demands, causes of action or proceedings arising from any breach of this Agreement by you.
- IN NO EVENT SHALL WILEY OR ITS LICENSORS BE LIABLE TO YOU OR ANY OTHER PARTY OR ANY OTHER PERSON OR ENTITY FOR ANY SPECIAL, CONSEQUENTIAL, INCIDENTAL, INDIRECT, EXEMPLARY OR PUNITIVE DAMAGES, HOWEVER CAUSED, ARISING OUT OF OR IN CONNECTION WITH THE DOWNLOADING, PROVISIONING, VIEWING OR USE OF THE MATERIALS REGARDLESS OF THE FORM OF ACTION, WHETHER FOR BREACH OF CONTRACT, BREACH OF WARRANTY, TORT, NEGLIGENCE, INFRINGEMENT OR OTHERWISE (INCLUDING, WITHOUT LIMITATION, DAMAGES BASED ON LOSS OF PROFITS, DATA, FILES, USE, BUSINESS OPPORTUNITY OR CLAIMS OF THIRD PARTIES), AND WHETHER OR NOT THE PARTY HAS BEEN ADVISED OF THE POSSIBILITY OF SUCH DAMAGES. THIS LIMITATION SHALL APPLY NOTWITHSTANDING ANY FAILURE OF ESSENTIAL PURPOSE OF ANY LIMITED REMEDY PROVIDED HEREIN.
- Should any provision of this Agreement be held by a court of competent jurisdiction to be illegal, invalid, or unenforceable, that provision shall be deemed amended to achieve as nearly as possible the same economic effect as the original provision, and the legality, validity and enforceability of the remaining provisions of this Agreement shall not be affected or impaired thereby.
- The failure of either party to enforce any term or condition of this Agreement shall not constitute a waiver of either party's right to enforce each and every term and condition of this Agreement. No breach under this agreement shall be deemed waived or excused by either party unless such waiver or consent is in writing signed by the party granting such waiver or consent. The waiver by or consent of a party to a breach of any provision of this Agreement shall not operate or be construed as a waiver of or consent to any other or subsequent breach by such other party.
- This Agreement may not be assigned (including by operation of law or otherwise) by you without WILEY's prior written consent.

APPENDIX A

2/20/2017

RightsLink Printable License

- Any fee required for this permission shall be non-refundable after thirty (30) days from receipt by the CCC.
- These terms and conditions together with CCC's Billing and Payment terms and conditions (which are incorporated herein) form the entire agreement between you and WILEY concerning this licensing transaction and (in the absence of fraud) supersedes all prior agreements and representations of the parties, oral or written. This Agreement may not be amended except in writing signed by both parties. This Agreement shall be binding upon and inure to the benefit of the parties' successors, legal representatives, and authorized assigns.
- In the event of any conflict between your obligations established by these terms and conditions and those established by CCC's Billing and Payment terms and conditions, these terms and conditions shall prevail.
- WILEY expressly reserves all rights not specifically granted in the combination of (i) the license details provided by you and accepted in the course of this licensing transaction, (ii) these terms and conditions and (iii) CCC's Billing and Payment terms and conditions.
- This Agreement will be void if the Type of Use, Format, Circulation, or Requestor Type was misrepresented during the licensing process.
- This Agreement shall be governed by and construed in accordance with the laws of the State of New York, USA, without regards to such state's conflict of law rules. Any legal action, suit or proceeding arising out of or relating to these Terms and Conditions or the breach thereof shall be instituted in a court of competent jurisdiction in New York County in the State of New York in the United States of America and each party hereby consents and submits to the personal jurisdiction of such court, waives any objection to venue in such court and consents to service of process by registered or certified mail, return receipt requested, at the last known address of such party.

WILEY OPEN ACCESS TERMS AND CONDITIONS

Wiley Publishes Open Access Articles in fully Open Access Journals and in Subscription journals offering Online Open. Although most of the fully Open Access journals publish open access articles under the terms of the Creative Commons Attribution (CC BY) License only, the subscription journals and a few of the Open Access Journals offer a choice of Creative Commons Licenses. The license type is clearly identified on the article.

The Creative Commons Attribution License

The [Creative Commons Attribution License \(CC-BY\)](#) allows users to copy, distribute and transmit an article, adapt the article and make commercial use of the article. The CC-BY license permits commercial and non-

Creative Commons Attribution Non-Commercial License

The [Creative Commons Attribution Non-Commercial \(CC-BY-NC\) License](#) permits use, distribution and reproduction in any medium, provided the original work is properly cited and is not used for commercial purposes. (see below)

Creative Commons Attribution-Non-Commercial-NoDerivs License

The [Creative Commons Attribution Non-Commercial-NoDerivs License \(CC-BY-NC-ND\)](#) permits use, distribution and reproduction in any medium, provided the original work is properly cited, is not used for commercial purposes and no modifications or adaptations are made. (see below)

Use by commercial "for-profit" organizations

APPENDIX A

2/20/2017

RightsLink Printable License

Use of Wiley Open Access articles for commercial, promotional, or marketing purposes requires further explicit permission from Wiley and will be subject to a fee.

Further details can be found on Wiley Online Library

<http://olabout.wiley.com/WileyCDA/Section/id-410895.html>

Other Terms and Conditions:

v1.10 Last updated September 2015

Questions? customercare@copyright.com or +1-855-239-3415 (toll free in the US) or +1-978-646-2777.

APPENDIX A

Publisher Permissions for Chapter IV

from: **Ian Gould** <iangopal@gmail.com>
 to: permissions@sagepub.com
 date: Tue, Jan 10, 2017 at 9:52 AM
 subject: Thesis Re-printing Permission

SAGE Journal
 via RightsLink,

I am in the process of submitting my dissertation for internal review at my home university and I require written permission to include my previously published article (Gould, Ian Gopal, Philbert Tsai, David Kleinfeld, and Andreas Linninger. "The capillary bed offers the largest hemodynamic resistance to the cortical blood supply." *Journal of Cerebral Blood Flow & Metabolism* 37, no. 1 (2017): 52-68.) in your journal.

What information is required to receive explicit consent for this article to be re-printed in my dissertation? Best,
 -Ian Gould

--
 Ian Gopal Gould
 PhD Candidate
 Dr. Andreas Linninger
 Bioengineering Department
 University of Illinois at Chicago

from: **PermissionsUK** <PermissionsUK@sagepub.com>
 to: Ian Gould <iangopal@gmail.com>
 date: Tue, Jan 10, 2017 at 11:06 AM
 subject: RE: Thesis Re-printing Permission

Dear Ian Gould,

Thank you for your email. I am pleased to report we can grant your request without a fee as part of your dissertation.

Please accept this email as permission for your request as detailed below. Permission is granted for the life of the edition on a non-exclusive basis, in the English language, throughout the world in all formats provided full citation is made to the original SAGE publication.

The permission is subject to approval from any co-authors on the original project. Please note approval excludes any graphs, photos, excerpts, etc. which required permission from a separate copyright holder at the time of publication. If your material includes anything which was not your original work, please contact the rights holder for permission to reuse those items.

If you have any questions or require additional information, please let me know.

Best Wishes,

APPENDIX A

Craig Myles
on behalf of SAGE Ltd. Permissions Team

SAGE Publishing
1 Oliver's Yard, 55 City Road
London, EC1Y 1SP
UK
www.sagepublishing.com
SAGE Publications Ltd, Registered in England No.1017514
Los Angeles | London | New Delhi
Singapore | Washington DC

CURRICULUM VITAE

Education

- B.S., Biochemistry, Case Western Reserve University, Cleveland, Ohio, 2007
- Ph.D., Bioengineering, University of Illinois at Chicago, Chicago, Illinois, 2017

Awards and Honors

- Outstanding TA award, 2010. UIC Department of Bioengineering, BIOE 440, Biological Systems Analysis
- Honorable Mention, 2011. Sweetman B, Gould IG, and Linninger AA. "Vasculature-brain tissue interaction and cerebrospinal fluid flow in the brain (Multi-scale modeling of biomechanical interactions in the brain)." UIC Student Research Forum, Chicago IL, April 19.
- Best Poster. Honorable Mention for Scientific Visualization, 2012. Marrinan T, Gould IG, Hsu CY, Linninger AA. "Whole-Brain Vascular Reconstruction, Simulation, and Visualization." *VisWeek* (2012), Seattle WA, Oct 13-18.
- NSF Nuggets to US Congress, 2013. State-of-the-Art Virtual Reality System is Key to Medical Discovery.

Industrial Experience

- Chemist I, Ben Venue Laboratories, Bedford OH, 2007-2008.
- Research Technologist, University of Illinois at Chicago, Department of Endocrinology and Metabolism, Chicago IL, Prof. Papsani Subbaiah, 2008-2010.

Publications

- **Gould, IG**, Tsai, P, Kleinfeld, D, & Linninger, AA. "The capillary bed offers the largest hemodynamic resistance to the cortical blood supply." *Journal of Cerebral Blood Flow & Metabolism* 37.1 (2017): 52-68.
- **Gould IG**, and Linninger AA. "Hematocrit distribution and tissue oxygenation in large microcirculatory networks." *Microcirculation* 22.1 (2015): 1-18.
- Buishas J, **Gould IG**, and Linninger AA. "A computational model of cerebrospinal fluid production and reabsorption driven by Starling forces." *Croatian medical journal* 55.5 (2014): 481-497.
- Linninger AA, **Gould IG**, Marinnan T, Hsu CY, Chojecki M, and Alaraj A. "Cerebral Microcirculation and Oxygen Tension in the Human Secondary Cortex." *Ann Biomed Eng*, 41.11 (2013): 2264-2284.
- Subbaiah PV, **Gould IG**, Lal S, Aizezi B. "Incorporation profiles of conjugated linoleic acid isomers in cell membranes and their positional distribution in phospholipids." *BBA - Molecular and Cell Biology of Lipids*, 1811.1 (2011):17-24.

Refereed Proceedings Articles

- Marrinan T, Gould IG, Hsu CY, Linninger AA. "Whole-Brain Vascular Reconstruction, Simulation, and Visualization." *VisWeek* (2012), Seattle WA, Oct 13-18. Best Poster. Honorable Mention for Scientific Visualization.

Abstract, Posters and Presentations at Technical Conferences and Meetings

- Gould IG, Tsai P, Kleinfeld D, Linninger AA. "Complex Cerebral Angioarchitecture and Neuronal Metabolism Lead to Wide Variations of Hematocrit, RBC Saturation in the Capillary Bed." XVIIth International Symposium on Cerebral Blood Flow, Metabolism and Function (2015), Vancouver, Canada, June 27-30.
- Buishas J, Gould IG, and Linninger AA. "Water Homeostasis in the Brain: The Effects of Osmotic Pressure Gradients on Intracranial Volume Shifts." UIC Student Research Forum (2015), Chicago IL, April 2.
- Buishas J, Romero R, Gould IG, and Linninger AA. "The Accumulation of CSF due to Hyperosmolarity of the Parenchymal Interstitial Fluid." UIC Student Research Forum (2014), Chicago IL, April 8.
- Gould IG, Hsu CY, and Linninger AA. "Parametric Cerebral Blood Flow Predictions." AIChE Annual Meeting (2013), San Francisco CA, Nov. 3-8.
- Gould IG and Linninger AA. "Systems Approach to Nonlinear Microvasculature Blood Flow." AIChE Annual Meeting (2013), San Francisco CA, Nov. 3-8.
- Gould IG, Marinnan T, Chojecki M, Qader M, Henry B, Pervais M, Vaičaitis N, Zhu Y, Rogers A, and Linninger AA. "Hemodynamics of cerebral vasculature." Proceedings of the 11th International Symposium on Process Systems Engineering. (2012) Singapore, July 15-19.
- Marrinan T, Gould IG. "Artificially Created Cortical Functional Blood Unit." UIC Image of Research (2012), Chicago IL. First Place.
- Alaraj A, Hsu CY, Gould IG, Marrinan T, Charbel F, Linninger AA. "The Use of Angiography to Quantify Relative Cortical Cerebral Blood Flow." Congress of Neurological Surgeons (2012) Chicago IL, Oct 6-10.
- Chojecki M, Qader M, Gould IG, and Linninger AA. "Insights into cerebral hemodynamics of microvasculature." UIC Student Research Forum (2012), Chicago IL, April 17.
- Sweetman B, Gould IG, and Linninger AA. "Vasculature-brain tissue interaction and cerebrospinal fluid flow in the brain (Multi-scale modeling of biomechanical interactions in the brain)." UIC Student Research Forum (2011), Chicago IL, April 19. Honorable Mention.